Beamforming and Source Quantification in Complex Environments Using In-Band and Out-of-Band Methods

by

Alexander Scott Douglass

A dissertation submitted in partial fulfillment
of the requirements for the degree of
Doctor of Philosophy
(Mechanical Engineering)
University of Michigan
2019

Doctoral Committee:

Professor David Dowling, Chair
Professor Karl Grosh
Assistant Professor Raj Rao Nadakuditi
Assistant Professor Bogdan Popa
Associate Professor Gregory Wakefield

Alexander Scott Douglass
asdougl@umich.edu
ORCID iD: 0000-0001-6778-4207

DEDICATION

To Christina. For being yourself, above all else.

ACKNOWLEDGMENTS

I'd first like to acknowledge my research advisor, Professor David Dowling, for his mentorship, guidance, patience, and constructive advice throughout graduate school. Much of what I've learned through this process has been a direct result of our collaboration and the experienced feedback that he brought to our work.

I would also like to thank the other members of my committee, Professors Karl Grosh, Bogdan Popa, Gregory Wakefield, and Raj Nadakuditi, for their willingness to devote their time to my thesis and defense. Their questions, suggestions, and input on my thesis has been valuable and much appreciated.

Outside of the University of Michigan, there were a number of collaborators that I need to thank who were critical to much of this work's success. Dr. Heechun Song of the Scripps Institute for sharing useful ocean data and collaborating on work with this data. Dr. Shima Abadi of the University of Washington - Bothell, for her collaboration on multiple research topics and for her thesis work, which set the foundation for most of the work presented here. Drs. Jason Smoker and Natasha Chang for their support of the NEEC projects within our research team.

In addition, multiple sponsors for this work provided me with the neces-

sary resources to focus on my research. The Office of Naval Research (Award Number N00014-16-1-2975), the Naval Sea Systems Command through the Naval Engineering Education Consortium (Contract Number N00174-16-C-0021), and the Rackham Graduate School (Rackham Merit Fellowship).

Nothing as long and demanding as graduate school would have been possible without the support of friends. I will almost inevitably (but unintentionally) leave somebody out of this section and apologize to whomever that may be. First, I want to acknowledge my two closest friends, Roy and Alan, who despite living far from me, have been there for me in every aspect of my life. In addition to these two, Kashif, Maya, Anna, Kristin, Jessie, Aaron, Greg, and Nancy have been wonderful and supportive friends since before and throughout graduate school. I've met many friends as a result of graduate school that have shaped the day-to-day experience: Brian, T. J., Brandon P., Kely, Marc, Harish, Brandon L., Dave, Anubhav, Daniel, Louise, Adaleena, Joel, Kevin, Phil, Suyash, Siddesh, Lauren, John, Jane, and all of the others that were a part of the experience.

I need to thank my parents, Scott and Joan, who have always been supportive of my goals and decisions - their endless support and encouragement shaped much of who I am and where I am today. Also my brother, Andrew, for sparking my interest in science and critical thinking at a young age, and my grandmother, Barbara, for being a constant inspiration in life.

Finally, I want to thank Christina, for the constant love and support in our lives both before and during graduate school. But more than that, for showing me what true strength looks like, helping me discover what is most important in life, and demonstrating the importance of being true to and embracing oneself.

TABLE OF CONTENTS

LIST OF FIGURES

LIST OF TABLES

ABSTRACT

Acoustic array signal processing in the ocean faces challenges due to multipath propagation, scattering from objects or surfaces, geometric uncertainty, and limitations from array geometry - all of which can harm conventional beamforming outputs. Frequency-difference and frequency-sum beamforming are out-of-band signal processing techniques that exploit signal bandwidth to beamform at below- or above-band frequencies. The work described here evaluates frequency-difference beamforming's ability to reduce the undesirable effects associated with array sparseness, strong random scattering, or geometric uncertainty, and examines the array coherence properties of both techniques. Frequency-difference beamforming has also been used with Synthetic Time Reversal (STR) for blind deconvolution, and is extended to underwater communications here.

The performance of frequency-difference beamforming is evaluated using simulations and experiments in a laboratory water tank and a shallow-ocean environment (KAM11 experiment[1] [73]). The method is shown to mitigate the effects of array sparseness, with results comparable to conventional beamforming when the in-band frequency matches the difference frequency (Δf), despite frequency-difference beamforming using a higher frequency signal. Shallow ocean results show agreement when comparing expected directions-of-arrival (DOAs) and the frequency-difference DOAs, with a reduced-χ^2 = 0.91 in experiments, despite notable multipath and array element spacing of 27-80 in-band wavelengths. Horizontal array simulations indicate that frequency-difference beamforming is robust to random variation in ray-path arrival times when $\Delta f \sigma \leq 0.20$ (σ

[1]Experimental data provided by Dr. HeeChun Song of the Scripps Institute of Oceanography

= arrival time standard deviation). Additional water tank simulations and experiments show that frequency-difference beamforming mitigates strong scattering effects by utilizing frequencies where Δka is small (k = wavenumber, a = spherical scatterer radius). Here, frequency-difference beamforming localizes a source with a factor of 4 reduction in error and 5 dB peak-to-sidelobe ratio improvement compared to conventional in-band techniques using the same signals.

The coherence lengths of frequency-difference and -sum autoproducts are considered using recordings of a bottom-reflected path with an 8 km towed array (COAST 2012 experiment [74]), showing coherence extending below and above the signal band. Here, averaged coherence lengths were 7.0λ for conventional fields from 1-200 Hz, 12.4λ for frequency-difference autoproducts from 1-100 Hz, and 8.6λ for frequency-sum autoproducts from 40-400 Hz (both using a 10-200 Hz signal band).

Blind deconvolution of a communication signal (from KAM11 data) is considered using an Overlapping STR (OSTR) technique that provides real-time channel updates. OSTR is shown to be useful for long-duration signals in time-varying environments and is compared to a standard Time Reversal (TR) method. Here, the TR method yields a bit error rate (BER) = 0.34% and an SNR = 8.5 dB (average bit error in the complex plane). For the same signal, OSTR yields BER = 0.0% and SNR = 12.2 dB.

An additional experiment[2] considers acoustic measurements of aeroacoustic noise in a wind tunnel. Conventional beamforming and the Spectral Estimation Method with cross spectral density matrix (CSDM) subtraction, and Robust Principal Component Analysis with a subspace denoising technique are considered for noise removal using a reference measurement. In a $\leq$-15 dB SNR environment, localization and source level estimation of field changes are possible when the source level is louder than noise resulting from experimental variation. Here, source level increments from 0.05 to 0.15 dB are determined with average error of 0.013 dB or less. This work demonstrates that simple

[2]Experimental data provided by Dr. Natasha Chang and Dr. Jason Smoker of the Naval Surface Warfare Center - Carderock

CSDM subtraction is effective when a robust noise reference exists.

CHAPTER 1

Introduction

This content of this thesis is focused on techniques in acoustic array signal processing, and branches into several areas within this topic. All of the topics covered here are related in that they ultimately aim to learn something about an acoustic source based on array-recorded signals - its location, the broadcast signal, the source level, or detecting changes to the source. The success of these tasks will be based on localization error, peak-to-sidelobe ratio, beamformer dynamic range, and source level error. This chapter provides an overview of the topics to be covered in the rest of the document, the prior work in each topic, and the areas in the existing literature to which this work contributes.

1.1 Acoustic Source Localization

A common task in array signal processing is source localization. In a typical source localization scenario, a signal is measured across a receiving array with a known geometry and the relative characteristics of the signal across the array – phase, amplitude, time of arrival, etc. – are exploited for the purposes of estimating the source location or direction-of-arrival (DOA). In acoustic remote sensing, particularly for underwater applications, all of these characteristics can be exploited in different ways, but in the work presented here, recorded-signal phase is generally the most critical. A common localization method for array signal processing that relies on exploiting phase across the array is beamforming, which is the focus of a large portion of this thesis. In all of the work

considered here (except where explicitly stated), a single source is assumed to be broadcasting the measured signal.

1.1.1 Beamforming

Beamforming is a widely used technique within acoustics, but is also used extensively in applications utilizing electromagnetic and seismic waves. The goal of beamforming can be to determine the DOA of a wave (plane-wave beamforming), the specific location of a source (spherical-wave beamforming), or to be used as a method of array gain to improve on other signal processing methods to follow. Both passive and active beamforming techniques are of interest, with active scenarios being those in which the user has control of the source signal, while the signal is generally unknown in a passive scenario. The method consists of "steering" a receiver array by imparting phase shifts (or time delays) to individual receivers based on a steering angle (or test location, for spherical-wave beamforming) and receiver locations. A variety of methods have been developed over decades of research and are thoroughly documented in various review papers and textbooks [156] [89] [80], and yet beamforming continues to be a significant area of research [47] [63] [36]. The most basic beamformer, known as the conventional or the Bartlett beamformer, has been in use for decades. Its use today attests to its reliability and robustness, particularly in the presence of noise and array uncertainty. However, conventional beamforming techniques do face challenges, such as when frequencies are too high or low for the given array geometry, environmental conditions, or application.

1.1.1.1 Advanced Beamforming Methods

Improvements to beam resolution, precision, and sidelobe suppression have been a significant area of interest and are widely studied in the beamforming literature. In this document, "precision" will primarily be used to reflect the size of the beamforming lobes (i.e. more precise corresponds to a smaller lobe), while "resolution" will refer to the ability to distinguish two nearby sources, though in some cases the two definitions have similar implications. Two of the most well-studied

methods in this area include the Capon beamformer [26], also known as the Minimum Variance Distortionless Response (MVDR) beamformer, and the Multiple Signal Classification (MUSIC) beamformer [124]. The MVDR beamformer provides a much higher resolution output than conventional beamforming and minimizes the power contributions from noise or other sources. However, MVDR is sensitive to uncertainty and error in the array steering process, often making practical implementation difficult. Recent research into this method has generally involved working towards improvements in MVDR's robustness [144] [52] [162] [126], attempting to make it more reliable for use in practice. MUSIC is a subspace method which, much like MVDR, improves the beamforming resolution. MUSIC utilizes the eigenstructure of the Cross Spectral Density Matrix (CSDM) to separate the signal and noise subspaces and seeks to minimize the contribution from the noise subspace, relying on the assumption that all signal and noise sources in the field are uncorrelated. Similarly, many extensions to this method have been developed to improve on some of MUSIC's shortcomings [84] [142]. Both MUSIC and MVDR may yield a similar output, with performance varying between different environments, assumptions, and parameters, thus one does not appear to be consistently preferred over the other.

Other classes of DOA algorithms and beamformers have been developed over many years to address a variety of problems and applications, including time-domain methods [53] [141], a variety of Maximum Likelihood (ML) methods [184] [143] [33], adaptive beamformers [59] [183] [159] [35], subspace methods such as ESPRIT [109] [116] and WSF [158], eigenstructure-based algorithms [15], iterative algorithms [175] [176], statistical Bayesian methods [16] [90], and those utilizing vector sensor arrays [106]. These various methods of beamformers are, in some cases, designed specifically for an application of interest, while others have the potential for implementation in a variety of fields.

Recently, significant attention has been given to methods in compressive sensing (CS). Methods in CS have only been applied to acoustic beamforming in roughly the past decade [96] [68] [127] [51] to provide high resolution outputs based on sparse matrix approximations. Though the outputs are precise, the robustness of compressive beamforming in the presence of noise, multiple

sources, basis mismatch, array uncertainty, various array geometries, etc., are prominent problems and a continuing area of active research. Several papers have studied the performance with multiple arrivals or multiple source signals and generally found that compressive methods are capable of handling these scenarios [170] [44]. Others have considered the effects of multiple and single snapshot datasets [64] and overcoming basis mismatch [79] [169]. Utilizing the cross-spectral-density matrix and exploiting the lack of coherence between sources and background noise provided improvement in compressive DOA in the presence of white noise [179]. Furthermore, compressive methods have been extended beyond simple beamforming to techniques including Matched Field Processing (MFP) [97] [60] and Bayesian methods [30]. The volume of research in this area has been increasing over the past decade and continues to be a growing area of interest.

Frequency-sum beamforming [4], a technique considered further herein, provides a means of enhancing beamforming precision by processing a signal at a frequency above the signal band. While the gains are not as significant as some high precision methods may be in the absence of noise, such as MVDR, MUSIC, or Compressive Beamforming, the method has a comparable robustness to that of conventional beamforming and with nearly the same complexity of implementation. However, an important caveat exists for frequency-sum beamforming, in which additional, non-existent sources appear in the beamforming output when two or more sources or propagation paths are present and unaccounted for. This is a result of the cross terms that appear in the standard implementation of frequency-sum autoproduct, and special care must be taken for these to not corrupt the result. The mitigation of this phenomena has not been thoroughly investigated yet. The frequency-sum method has thus far been considered primarily for use in acoustic imaging [1]. The counterpart, frequency-difference beamforming, which is much of the focus of this document, has previously been used in conjunction with blind deconvolution techniques [2] and for source localization or DOA estimation in both laboratory and shallow ocean environments [45] (the results of which are presented as part of this document).

Much of the literature also considers the design of arrays to be used in beamforming. While equally-spaced array elements are common, many techniques are improved with intentional design

variations. Random arrays are often considered and have been shown to be both detrimental or beneficial, depending on the application [169] [39]. Spiral arrays have been shown to perform well, but resolution and precision may be sacrificed without adding additional receiving elements [91] [11].

Beamforming spans a wide variety of applications. Source localization is a common use for beamforming, which may be utilized underwater for locating acoustic sources such as ships, marine mammals, etc. Other applications of acoustic beamforming include improving array gain for recovering unknown signals (see section 1.2), underwater communications [131], AUV tracking and localization [24], the localization of gas leaks [178] [78], medical imaging and ultrasound [150], [83] [146] [76], among others. In addition, radar applications are abound [156]. Coprime arrays provide a means of increasing array aperture, thus improving spatial resolution, with the same number of elements as a comparable linear array; these are often utilized due in part to their design and processing simplicity [182] [99] [181].

1.1.1.2 Beamforming with Sparse Arrays

Despite this wide array of beamforming research, methods for overcoming the effects of spatial aliasing are notably sparse in the literature. Mitigation of the negative effects of sparse arrays have consisted of both signal processing solutions and array design and implementation solutions. Moving arrays were investigated as a method of obtaining additional, continuous spatial information to reduce aliasing [40]. Compressive sensing was used to develop an iterative method of DOA estimation using sparse arrays, with promising, though inconsistent results [122]. Accounting for expected aliasing patterns to perform aliasing cancellation also showed some increase in performance [6], but becomes difficult as the element spacing grows to more than just a few signal wavelengths in magnitude. Array elements with large, pressure sensitive areas provided more spatial information from a single hydrophone [102], while continuous, directional spherical sensors [5] and other types of directional sensors [153] were used to provide a vector output from each sensor.

Frequency-difference beamforming [3] is a beamforming method that utilizes signal bandwidth to beamform at lower, out-of-band frequencies that are not actually present in the signal. By doing this, arrays that are sparse in the signal band can be used at frequencies where sparseness is no longer a concern. This was originally introduced for use with Synthetic Time Reversal (STR) [117] [118] as a method of blind deconvolution [2], but left largely uninvestigated. This method was later extended to matched-field processing [166] [167] and the crux of the method, the autoproduct, was investigated more thoroughly [165].

1.1.1.3 Beamforming in the Shallow Ocean

The shallow ocean is an environment of interest for many applications, but comes with a unique collection of challenges. The depth of the channel compared to the signal wavelength will dictate which acoustic modeling techniques are applicable – for example, ray models are not valid if the wavelength and depth are comparable in magnitude, and for high frequencies, modal methods may be cumbersome due to the number of modes required for an accurate solution, thus rays may be preferred. Refraction due to spatially-dependent sound speed and reflections from both the surface and ocean floor lead to significant multipath propagation. Objects and rough surfaces cause unwanted scattering (except in some active scenarios where scattering is desired). Bottom conditions vary significantly, leading to varying reflection and scattering characteristics. Significant noise levels, some of which is anthropogenic, leads to poor SNRs in many recorded signals. Attenuation is frequency-dependent and high frequencies have a higher transmission loss than lower frequencies when propagating over long distances. These challenges, among others [80] [154], can make beamforming in the shallow ocean difficult.

In general, arrays are deployed either in a vertical or horizontal orientation (or some combination of the two). Vertical arrays may be bottom or surface mounted (or both), while horizontal arrays may be deployed on the ocean floor or towed by a moving ship. Vertical arrays can collect information from various depths in the water channel, which can be both beneficial or challenging, depending on the desired information. Many major acoustic experiments make use of mounted ver-

tical arrays, such as the Kauai Acomms MURI 2011 (KAM11) experiment [74] (discussed herein), the KauaiEx experiment [110], and the Focused Acoustic Field (FAF06) experiment [136], among others.

Horizontal arrays, particularly towed arrays, are often more practical to deploy in the field and have been studied and used in underwater acoustics for the past century [92]. Often, the research problems addressed with horizontal arrays and vertical arrays focus on the same (or a similar) problem, but are applied to the relevant array geometry. Research areas such as adaptive beamforming [62], underwater communications [173] [82], compressive sensing [51] [169] and source localization [37] are all areas of interest with horizontal arrays. Additionally, horizontal arrays come with their own research areas specific to their geometry, such as coherence length limitations [27] and performance during maneuvering [62].

1.1.1.4 Beamforming in Inhomogeneous Environments

Beamforming methods may struggle at high frequencies where signal wavelengths are small relative to features of or objects in the environment that the waves interact with. Acoustic scattering, while sometimes desirable (particularly in active array processing applications such as ultrasound imaging), can be detrimental to beamforming in both active and passive scenarios. Scattering can result from acoustic illumination of rough boundaries (ocean surface or bottom), inhomogeneities in the environment (manmade objects, bubbles, schools of fish, etc.), or changes in medium properties (sound speed, density, etc.). The resulting scattered field can vary significantly from the direct-path field in both phase and amplitude. When the scattering features are small relative to the signal wavelength (e.g. $ka < 1$ for a spherical scatterer, where $k = \omega/c$ is the acoustic wave number, c is the medium's sound speed near the scatterer, and a is the scatterer radius), the scattered field is weak and minimally disruptive. When ka and the acoustic impedance difference between the medium and the scatterer are both large, the scattered field becomes significant and its effects on conventional beamforming methods are not negligible. For high ka ($ka >> 1$) and high contrast scatterers, frequency-difference beamforming may provide improvements over

in-band conventional beamforming by effectively reducing ka when the difference frequency is chosen such that $\Delta ka = \Delta\omega a/c$ is sufficiently small.

Scattering by ideal-shape objects has been studied extensively for acoustic waves [19], having been extended to multiple scattering from point scatterers decades ago [58]. Plane- and spherical-wave scattering from simple geometries is well understood and can be modeled accurately for pressure release, rigid, and finite impedance boundary conditions [19] [104] and for a variety of configurations, frequencies, or mediums of interest [155] [56] [107] [69].

Source localization and near-field beamforming in inhomogeneous environments has been addressed through a variety of methods, including extensions to MFP [71], Time-Reversal and MUSIC [98] [34], and statistical methods [105] [120] [161] [85]. The frequency-difference beamforming counterpart, frequency-sum beamforming, has also been shown to improve localization of a source in an inhomogeneous medium relative to the comparable in-band frequencies [4] [1], but no prior work has been published on the possible scattering-suppression available from below-band methods.

1.1.2 Array Coherence

As acoustic environments become more variable and complex, the acoustic field's coherence between spatially-separated receivers in such environments commonly decreases. Predicting field coherence between two points in space is a difficult task, as it is a function of the locations of the two points, the propagating frequency, and the characteristics of the environment between the sound source and the two points. In general, coherence improves with decreasing receiver separation and decreasing frequency, as well as with decreased environmental complexity [154], although coherence in the presence of certain environmental characteristics has been shown to behave unintuitively [72].

Limited coherence length can be problematic for array signal processing in the ocean, especially for towed horizontal arrays or deep ocean vertical arrays, where the array aperture can easily exceed the field's coherence length at the frequencies of interest. Coherence length is directly re-

lated to the array gain and thus has strong implications in beamforming [103] [28] and matched field processing applications [12]. When an array is nominally shorter than the field's coherence length, all its elements should contribute positively to the achievable array gain, but adding array elements that extend the array's aperture beyond the coherence length generally does not provide improvements, and can potentially reduce the performance of array signal processing techniques. In particular, prior work has shown that for shallow water environments, coherence length is a primary factor in predicting performance [114]. For a known finite coherence, the theoretical limitations of conventional beamforming methods are understood and readily calculated [42]. Coherence length has been studied in a variety of experimental scenarios, including both vertical and horizontal arrays [160], in the presence of internal waves [49] [95], with varying channel depth [29], and at long ranges [10], in order to understand the influence of various environmental characteristics.

1.1.3 Other Localization Methods

1.1.3.1 MFP

Matched field processing [20] is a generalization of beamforming which aims to localize a source by incorporating environmental characteristics into the propagation model, rather than assuming a direct plane or spherical wave as is generally done in beamforming [80]. While it will not be examined in this document, work in MFP has had significant implications in beamforming, and vice versa, such that an understanding of the literature in both areas is important. In a near-perfect model of an environment, MFP will perform with high accuracy, but as environmental mismatch increases, particularly at high frequencies, the performance declines. Fortunately, techniques have been investigated for overcoming this issue over the decades since its development [12].

Similar to conventional beamforming, MFP has been extended to MVDR [111] [55] [13] and MUSIC [108], but other noteworthy MFP techniques have been developed in addition. Multiple Constraint (MCM) processing allows for environmental uncertainty by relaxing the single-point constraint of MVDR [125]. Matched Mode Processing (MMP) provides a means for normal mode

decomposition [172]. Subarray methods reduce the aperture of individual arrays, addressing some of the mismatch issues that grow with increasing spatial sampling of a single array and improving the plane-wave arrival assumption [43]. Focalization [41] attempts to simultaneously determine the environmental and signal parameters using a parameter optimization method.

More recent work in MFP has lead to improvements by exploiting sidelobe behavior [149], using the CLEAN method [135], Bayesian learning techniques [61], and compressive sensing methods [60] [97]. Recent work has implemented the frequency-difference technique with MFP as a means of suppressing the effects of environmental mismatch by downshifting the signal frequency in both shallow ocean [166] [167] and deep ocean environments.

Reviews of MFP methods are readily available in the literature, and thus the more thorough overview of the techniques is left to those publications [12] [152] [80] [47].

1.1.3.2 Other Methods

Aside from beamforming and matched field processing, a number of other techniques exist for source localization, most of which won't be considered here. If available, time-difference-of-arrival (TDOA) provides a means of geometrically determining possible source locations, requiring, at minimum, four receivers in a three-dimensional environment for absolute localization, though the convenience of knowing time-of-arrival is often not available in some applications, and becomes more complicated in environments where the sound speed is varying [123] [121]. In ocean environments in particular, the direct path may not be the first to arrive, if there is a direct path, and most paths will arrive at an angle that is highly dependent on range, depth, and sound speed profile, and thus is not a good indicator of its broadcast angle. If a probe signal is available (in order to estimate the source to receiver impulse response function), time reversal focusing of a passive signal can be used to focus the signal onto a specific location [87]. Without a probe signal, synthetic time reversal (STR) is able to determine signal and impulse response information. The relative time of arrival and signal phase between receivers can be estimated with STR and exploited for source range and depth estimation [2]. Another technique utilizes the waveguide

invariant, which describes the frequency- and range-dependent behavior of a field's interference pattern when propagating through a sound channel and interacting with the ocean surfaces [66]. Because the waveguide invariant is frequency- and range-dependent, it can be exploited for passive range estimation and localization [48] [148]. Energy-based localization methods can use the acoustic energy and the relative energy decay between receivers to estimate source location based on a modeled decay [93]. Acoustic holography provides a near-field technique for reconstructing an acoustic field, providing a high level of detail dependent on frequency [101] [157]. The Spectral Estimation Method (SEM) is based on the same weighting vectors and propagation models as plane- and spherical-wave beamforming, but seeks to minimize the difference between measured and modeled cross-spectral-density matrices (CSDMs) rather than solving the L_2-norm minimization that leads to conventional beamforming [18]. SEM is discussed in more detail later in this chapter and is utilized in Chapter 7.

1.2 Underwater Communication

Underwater communications has been studied extensively for decades. Due to the poor propagation capabilities of electromagnetic waves in water, acoustics is necessary for practical underwater communication applications. Unfortunately, acoustic waves face many problems underwater as well. Higher frequency acoustic signals attenuate much faster than low frequencies [88], but are more useful in high-rate communication. The presence of noise and other environmental factors such as reverberation, scattering, diffraction, etc. cause additional problems with recovering the original communication signals due to signal corruption. Much of the research in this area has focused on suppressing the effects of one or more of these factors in a wide variety of ocean environments and scenarios. One of the key issues with underwater acoustics is that the problem of signal recovery is often ill-posed – the array output is known, but the source signal(s) and the Green's function(s) are unknown.

Blind deconvolution refers to the process of estimating a source signal and/or an impulse re-

sponse function with only knowledge of the received signal. The problem is fundamentally ill-posed since the equation $P_j(\omega) = S(\omega)G_j(\omega)$ contains two unknowns, the source signal, $S(\omega)$, and impulse response between the source and the j^{th} receiver, $G_j(\omega)$. The technique has applications in many fields and, fortunately, a diverse literature. A number of methods have been developed that utilize additional known information about an environment, the acoustic propagation, or take advantage of a numerical method to determine an optimum solution. Some of the methods used in acoustic applications include minimum entropy methods [23] [164], parallel deconvolution method based on using Monte-Carlo optimization [129], using a strategically placed guide source to remove some of the distorting effects of the environment from the unknown source [128], taking advantage of multiple sources, the number of which is determined by Principal Component Analysis, for a blind source separation technique [171], adaptive multichannel blind equalization [163], time-frequency matched filter processing [100], and by utilizing sparse structures of channels with large time-delay spreads using a least-squares approach [177], matching pursuit, orthogonal matching pursuit, basis pursuit, and a variety of compressive methods [177] [9] [180]. The basic Time Reversal implementation requires the use of a probe signal, and thus is not capable of blind deconvolution with conventional implementation, but Synthetic Time Reversal (STR) [117] uses assumptions about the type of acoustic propagation and the output of a conventional beamformer [118] or frequency-difference beamforming [3] to solve the blind deconvolution problem and has been applied to blind source localization [2] and localization using sources of opportunity to learn information about the environment [22]. Through this work, STR has been shown to be effective in underwater sound channels where multipath propagation is prominent. Both modal- and ray-based versions of STR exist, but in this document, only ray-based STR will be discussed. By assuming ray-based propagation, one can use a conventional beamformer to identify an individual ray path and obtain signal phase information by combining receiver array outputs based on the beamforming result, effectively eliminating one of the two unknowns. This process is explained in more detail in Chapter 6.

A prominent method of demodulating underwater communication signals is through adaptive

equalization using a multichannel decision feedback equalizer (M-DFE) [145] [112]. M-DFEs work well in practice but suffer from computational complexity, particularly as the number of array elements and/or signal taps increases. Time reversal based approaches to underwater communication were first proposed in the early 2000s [115] [50] and have progressed substantially since [57] [137] [138] [174] [65]. Time reversal methods utilize a known intermittent probe signal sent prior to the communication signal to determine the Green's function of the environment, which is then used to recover the original communication signal, and a single-channel DFE is applied at the end to remove residual inter-symbol interference (ISI). The intermittent probe signals lead to a reduced data rate, particularly for time-varying channels (where they are required more frequently) and risks an increase in error by not providing a method for adapting to a dynamic environment between probe signals. Recent work has mitigated this loss by utilizing smaller, overlapping time windows and updates to the channel impulse response (CIR) using known DFE taps, rather than with a probe signal [132]. Additional work in the area has been done on a variety of topics, including mobile sources [81] [133], multiuser communication [140] [134] [38] [130], and long-range communication [139] [134].

1.3 Localization and Source Level Estimation in Noisy Environments with Noise References

A variety of techniques, particularly higher resolution and higher precision techniques, have been developed for source localization applications. MVDR and MUSIC, discussed previously, have been researched for decades and continue to be investigated. Compressive sensing, also discussed above, has received significant attention in acoustics over the last decade. Another technique, the Spectral Estimation Method (SEM) [18] was developed using a similar approach to conventional beamforming methods, but the problem is formulated as an L_2-minimization of CSDM subtraction between a measured and modeled CSDM. This method results in a higher resolution localization compared to conventional beamforming methods, and may also yield improved

source level estimation capabilities. An L_1-minimization version of SEM has been studied as well and showed improvements over a standard compressive beamforming technique for localization, but was not compared directly to conventional SEM [179]. Unfortunately, many of these higher resolution methods are sensitive to uncertainty and noise. As a result, though they can perform exceptionally well under the right conditions, they often lack robustness and are difficult to implement effectively.

The mitigation of noise is important since many environments are characterized by low SNRs. The SEM method was extended to a noise subtraction version, SEM with Additive Noise (SEMWAN), as one way of mitigating the noise influence [17]. Here, by assuming that the source(s) of interest and source(s) of noise are uncorrelated, and if a noise-only measurement is available for reference, the noise CSDM can be subtracted from the signal-plus-noise CSDM. Generally, CSDMs are obtained by averaging over many signal snapshots to improve robustness. The resulting CSDM ideally now has the source(s) of interest location and source level information, which can then be obtained through the L_2-minimization procedure. For comparison purposes, the simple CSDM subtraction can also be applied to conventional beamforming methods.

Another background removal technique of interest is Robust Principal Component Analysis (RPCA), which is a relatively new but commonly used method in image processing [168] [25]. The technique relies on assuming that a matrix of signal measurements can be reduced to a sum of a low-rank matrix and a sparse matrix. In image processing, this breaks down to a steady background image over many measurements (low-rank) and a foreground image that appears in very few measurements (sparse). This technique has shown strong performance capabilities in image processing, but has only recently been extended to the field of acoustics and hasn't been thoroughly researched here. In one case, RPCA was used to separate components of fan noise [54]. In another, RPCA was used to estimate source location and source spectrum in a hydrodynamic tunnel, separating the source from two types of noise generated by flow convection and from turbulent flow [7]. These techniques demonstrate the possibility of using RPCA for the purposes of source level estimation, source localization, and detection of source changes in a noisy field.

1.4 Thesis Motivation and Goals

There are several areas of acoustics investigated in this thesis, all related to source localization or characterization. One primary focus of the document is the examination out-of-band beamforming methods in ocean environments. In particular, frequency-difference beamforming methods are capable of reducing some of the negative impacts that result from processing high frequency signals. With a decreased wavelength, the effects of environmental mismatch, array sparseness, scattering from objects or rough boundaries, or geometric uncertainties can be detrimental to beamforming. Frequency-difference methods process the field via its autoproduct as if it were at a lower, typically out-of-band frequency (longer wavelength), and despite the genuine in-band signal being at a higher frequency, the autoproduct field behaves similarly to the comparable lower-frequency field. In addition to frequency-difference methods, frequency-sum methods are considered, but less thoroughly. The main advantage of frequency-sum methods is improved precision as a result of producing a higher frequency field, but the method struggles in the presence of unknown multiple sources. These out-of-band methods, and the techniques used for comparison, are spectral-based techniques and thus are computationally advantageous when compared with parametric methods (such as compressive beamforming) [89].

Two other topics are covered in two of the chapters of this thesis. In one chapter, a technique for dealing with time-varying, multipath environments is introduced. Again, frequency-difference methods are utilized, here for both beamforming and signal phase estimation. In the other, source level estimation and source localization in noisy environments are considered for scenarios where a noise reference is available.

The thesis document is organized into eight chapters. The current chapter provides a literature review of the topics relevant to and motivating the thesis content. The second chapter provides an overview of acoustic fundamentals and a review of conventional and out-of-band beamforming methods and the results of applying these methods to a free-space environment. The third chapter considers out-of-band coherence length, since this is a significant predictor of beamforming perfor-

mance, using a long, towed horizontal array. The fourth chapter implements out-of-band methods in shallow ocean environments using both vertical and horizontal arrays. The fifth chapter considers frequency-difference beamforming methods for a source in the presence of strong scatterers. The sixth chapter implements an overlapping STR method for blind deconvolution of communication signals in time-varying environments in the shallow ocean. The seventh chapter examines and compares noise subtraction methods for source level estimation and source localization in both laboratory experiments with a discrete source and noise fields generated by turbulent air flow, as well as to detect changes to a source in a wind tunnel. The eighth and final chapter provides a summary of the completed research and the conclusions of the research presented herein.

CHAPTER 2

Out-of-Band Beamforming

Conventional beamforming methods are well understood array signal processing techniques that often provide robust and reliable source localization or direction-of-arrival (DOA), but with limitations. For beamforming, many of these limitations depend on the receiver array design and the environment through which the acoustic wave is propagating. In many environments of interest, such as the shallow ocean, which is much of the focus of this thesis, reverberation, environmental and/or wavefront mismatch, rough boundary conditions, small and large obstructions, and low signal-to-noise ratio (SNR) can all be factors contributing to the degradation of a beamformer output. In particular, obstructions (scatterers), environmental fluctuations, and boundary conditions cause problems that vary based on the signal frequency – when the wavelength is much larger than these features they can generally be ignored, but at lower wavelengths that are comparable to or smaller than the sizes of these features, they become more significant.

The receiver array is also a significant factor in beamforming performance. Uncertainty in the receiver element positions is important when the location uncertainty is comparable to the signal wavelength or larger. Array sparseness – when the receiver elements are spaced by more than a half signal wavelength – causes spatial aliasing that can lead to false source locations, particularly as the sparseness becomes much greater than unity. Alternatively, an array with appropriately spaced elements but that has a low aperture will yield a potentially robust result, but with poor resolution and precision, failing to resolve multiple sources or give a precise indication of source location or DOA.

This chapter introduces and explores the performance of two methods of out-of-band beamforming that can be used to suppress some of the negative effects described above. Frequency-difference beamforming is a technique that utilizes signal bandwidth to process a high frequency signal as if it were a genuine field at a lower frequency. This chapter specifically considers the performance of frequency-difference beamforming for arrays with a receiver-spacing-to-signal-wavelength ratio of roughly 5.7 and compares these results to conventional beamforming with both high frequency signals and a low frequency signal matching the difference frequency used with the high frequency signal, providing a genuine field leading to a ratio of 0.51. Both simulations and water tank experiments are used to validate the performance of frequency-difference beamforming. Frequency-sum beamforming is the counterpart to frequency-difference beamforming which processes a signal as if it were at a higher frequency, improving the beam precision. Simulations and experiments using the same geometry as that for frequency-difference beamforming, but with lower frequency signals, are considered. The goal of the chapter is to demonstrate that out-of-band methods behave comparably to in-band methods in free-space environments when the frequency-difference or frequency-sum autoproduct is formed at a difference frequency, Δf, or sum frequency, Σf, matching the genuine in-band frequency, f. The metric for success in this comparison will be the source localization error and the comparison of beam widths in the angular and range directions.

2.1 Mathematical Formulation

2.1.1 Fundamentals

Acoustic wave propagation can be assumed to approximately obey the linearized acoustic wave equation,

$$\nabla^2 p(\vec{r}, t) - \frac{1}{c^2} \frac{\partial^2 p(\vec{r}, t)}{\partial t^2} = 0, \tag{2.1}$$

where $p(\vec{r}, t)$ is a time-domain acoustic field, and c is the speed of sound. The acoustic field at any given point in a field and any given point in time is a convolution of the source signal, $s(t)$, and the time-domain Green's function, $g(\vec{r_s}, \vec{r}, t)$, which contains all of the environmental information for the propagation between the source and point of interest

$$p(\vec{r}, t) = s(t) * g(\vec{r_s}, \vec{r}, t). \tag{2.2}$$

Here, $\vec{r_s}$ is the source position vector, $\vec{r}$ is the field point of interest, and * represents a convolution operation. For many signal processing techniques, and generally for beamforming, the processing is completed in the frequency domain. A time domain signal is converted into the frequency domain using a Fourier transform, which represents the same information, but as a function of frequency, where each value is now a complex number, providing a magnitude and phase in each bin. A Fourier transform of a time domain signal is given by

$$S(\omega) = \frac{1}{2\pi} \int_{-\infty}^{\infty} s(t) e^{i\omega t} dt = |S(\omega)| e^{i\varphi(\omega)}, \tag{2.3}$$

where $i = \sqrt{-1}$, ω is the temporal radian frequency, and $\varphi(\omega)$ is the frequency-dependent signal phase. This same function can be applied to $p(\vec{r}, t)$ and $g(\vec{r_s}, \vec{r}, t)$ to obtain the corresponding $P(\vec{r}, \omega)$ and $G(\vec{r_s}, \vec{r}, \omega)$ functions. One particular convenience of working in the frequency domain is that convolutions in the time domain correspond to simple multiplication in the frequency domain, thus Eq. 2.2 can be rewritten as

$$P(\vec{r}, \omega) = S(\omega) G(\vec{r_s}, \vec{r}, \omega). \tag{2.4}$$

Green's functions can become very complicated since they include all of the information in a given environment. However, one of the simplest forms of a Green's function, which is often assumed for the most basic plane- and spherical-wave beamforming operations described in the next section, is

a simple free-space propagation through an unchanging medium. This function is given as

$$G(\vec{r_s}, \vec{r}, \omega) = \frac{e^{ik|\vec{r_s} - \vec{r}|}}{|\vec{r_s} - \vec{r}|}, \tag{2.5}$$

where k is the acoustic wavenumber, $k = \omega/c$.

2.1.2 Conventional Beamforming

Both conventional plane- and spherical-wave beamforming can be defined simply as the magnitude-squared of a weighted sum of array-recorded signals. If the time-domain pressure recorded by the j^{th} array element is $p_j(t)$ with temporal Fourier transform $P_j(\omega)$, then the conventional beamformed output, $B_{conv}(\omega)$, from an array of N transducers is

$$B_{conv}(\omega) = |b_{conv}(\omega)|^2 = \left| \sum_{j=1}^{N} P_j(\omega) w_j(\omega) \right|^2, \tag{2.6}$$

where $w_j(\omega)$ is the complex weighting for the j^{th} array element. The weighting vector chosen for beamforming is the crux of a successful beamforming output. For simple plane- and spherical-wave beamforming, the weighting vectors are given by

$$w_j(\omega) = e^{-i\omega \hat{e}_s \cdot \vec{r}_j / c} \tag{2.7}$$

and

$$w_j(\omega) = \frac{e^{-i\omega |\vec{r}_s - \vec{r}_j| / c}}{\left|\vec{r}_s - \vec{r}_j\right|} \tag{2.8}$$

respectively, where $\hat{e}_s$ is a unit vector that points in the search direction for plane-wave beamforming and $\vec{r}_j$ is the location of the j^{th} receiver. The $1/\left|\vec{r}_s - \vec{r}_j\right|$ factor for spherical-wave beamforming provides a weighting that increases the influence of receivers closer to the source, but is not required for successful spherical-wave beamforming. For the purposes of the work in this chapter, this weighting is not included, for simplicity in comparing each beamforming method. In general,

$B_{conv}(\omega)$ depends on ω, the array configuration, the characteristics of the acoustic environment, the source coordinate(s), and the steering coordinate(s). For plane-wave beamforming, the source and field coordinates are angles, and for spherical-wave beamforming, they are field points. Conventional beamforming is considered successful when the maxima of B coincide with true wave propagation directions at the receiving array, or with true source locations. In addition, a beamforming scheme is known as linear when w_j does not depend on P_j. Thus, Eqs. 2.7 and 2.8 together with Eq. 2.6 define linear beamforming schemes. When a signal has nonzero bandwidth, Eq. 2.6 can be incoherently averaged through the signal bandwidth, $\Omega_L \leq \omega \leq \Omega_H$, to improve performance

$$\bar{B}_{conv}(\omega) = \langle B_{conv}(\omega) \rangle_\omega = \left\langle \left| \sum_{j=1}^{N} P_j(\omega) w_j(\omega) \right|^2 \right\rangle_\omega \tag{2.9}$$

where $\langle\ \rangle_\omega$ indicates an average over ω from Ω_L to Ω_H.

Conventional plane- and spherical-wave beamforming schemes are successful when the recorded signals are composed of plane or spherical waves, respectively, and when the spacing between array elements is small enough to prevent strong side lobes from appearing in $B_{conv}(\omega)$. For example, strong side lobes in $B_{conv}(\omega)$ are avoided in plane-wave beamforming using a linear array with uniform spacing d between elements when $d \leq \lambda/2$, where $\lambda = 2\pi c/\omega$ is the acoustic wavelength at frequency ω. However, the utility of both conventional schemes deteriorates when the recorded-signal wavefront geometry does not match the assumed wavefront shape, and when the spacing between array elements is multiple wavelengths, i.e., when the array is sparse.

2.1.3 Frequency-Difference and Frequency-Sum Beamforming

Frequency-difference and frequency-sum beamforming are unconventional, out-of-band beamforming methods used for identifying source locations or DOAs for non-zero bandwidth signals[1]. Frequency-difference beamforming is utilized when the array geometry or environmental parameters aren't suitable for conventional beamforming methods due to high frequencies, but sacrifices

[1]Relevant MATLAB code can be found at https://github.com/dougl122/outofband.

beam resolution and precision. Frequency-sum beamforming generates an output using an above-band frequency for cases where improved precision is desired, perhaps due to a lack of array aperture. Here, precision is referring to the width of the beam in the beamformer output, while resolution refers to the ability to distinguish multiple nearby sources; while the two definitions are related, it is important to distinguish them. The two out-of-band methods utilize the frequency-difference and frequency-sum autoproducts, $AP_{\Delta,j}$ and $AP_{\Sigma,j}$, defined by

$$AP_{\Delta,j} = P_j(\omega_2)P_j^*(\omega_1) \tag{2.10}$$

and

$$AP_{\Sigma,j} = P_j(\omega_2)P_j(\omega_1), \tag{2.11}$$

respectively. Recent work has shown that the fields generated by the autoproducts defined in Eqs. 2.10 and 2.11 mimic solutions to the Helmholtz equation at the difference frequency, $\Delta\omega = \omega_2 - \omega_1$, and the sum frequency, $\Sigma\omega = \omega_2 + \omega_1$, if sufficient bandwidth averaging is available [165]. Equations (2-10) and (2-11) can be considered a signal-internal heterodyning step that preferentially produces the lower- and higher-frequency heterodyne components. However, a local oscillator at either frequency is not needed. The frequency-difference and frequency-sum concepts consider $AP_{\Delta,j}$ and $AP_{\Sigma,j}$ as acoustic fields at $\Delta\omega$ and $\Sigma\omega$, respectively, and apply established array signal processing schemes at the appropriate difference or sum frequency to obtain potentially desirable results that cannot be produced by processing $P_j(\omega)$ with the same schemes evaluated at ω. For a given set of recorded signals $P_j(\omega)$, frequency-difference beamforming is not a replacement for conventional techniques. Instead, it provides results that are complementary to those available from conventional techniques. Interestingly, quadratic products of signal amplitudes have been considered for blind signal separation as well [77].

Three modifications to conventional beamforming, Eqs. 2.6 - 2.9, are needed to implement the frequency-difference approach. First, $P_j(\omega)$ in Eq. 2.6 is replaced by $AP_{\Delta,j}$ or $AP_{\Sigma,j}$ since it mimics the not-directly-available acoustic field at the lower difference frequency or higher sum frequency.

Second, the array-element weights defined by Eqs. 2.7 and 2.8 are evaluated at the difference frequency, $\Delta\omega$, or sum frequency, $\Sigma\omega$, rather than the in-band frequency, ω. Thus, the frequency-difference and frequency-sum equivalents of Eq. B_{conv} are

$$B_{\Delta}(\Delta\omega) = \left| \sum_{j=1}^{N} AP_{\Delta,j} w_j(\Delta\omega) \right|^2 \tag{2.12}$$

and

$$B_{\Sigma}(\Sigma\omega) = \left| \sum_{j=1}^{N} AP_{\Sigma,j} w_j(\Sigma\omega) \right|^2 \tag{2.13}$$

respectively. Since $w_j(\Delta\omega)$ and $w_j(\Sigma\omega)$ are simply Eqs. 2.7 and 2.8 with ω replaced by the corresponding difference or sum frequency, the beamforming algorithm is still a linear processing scheme, but with an unconventional field product. Both $\Delta\omega$ and $\Sigma\omega$ are user selectable frequencies, with the only constraint being that the two frequencies used to form them, ω_1 and ω_2, lie within the signal bandwidth, $\Omega_L \leq \omega \leq \Omega_H$. Thus, within these constraints, the sum and difference frequencies can be chosen to accommodate the user's requirements or the limitations of the array or environment present. For frequency-difference beamforming in the work presented in this chapter, $\Delta\omega$ is chosen well below the signal bandwidth, specifically at a difference frequency that should result in a well-populated array, eliminating the effects of spatial aliasing. Frequency-sum beamforming will be chosen so that the sum frequency is twice that of the intended signal center frequency, to illustrate a predictable precision enhancement.

Third, the frequency averaging specified by Eq. 2.9 can be extended to difference frequency averaging and sum frequency averaging. First, an incoherent average is generally completed throughout the full signal bandwidth available. That is, for frequency-difference beamforming, an incoherent average is completed across all available $\bar{\omega}$ values (frequency-difference), which is the average of each frequency pair, $\bar{\omega} = \frac{(\omega_1+\omega_2)}{2}$, for a given difference frequency. For a given sum frequency, the incoherent average is completed across all available difference frequency pairs that yield the same sum frequency, i.e. $\Delta\omega = \omega_2 - \omega_1$, where $\Sigma\omega = \omega_2 + \omega_1 = \bar{\omega} \pm \Delta\omega/2$. In addition to this average, an incoherence average can be completed over multiple difference and sum frequencies.

Thus, the frequency-difference and frequency-sum equivalents of Eq. 2.9 are given by

$$\bar{B}_{\Delta} = \langle B_{\Delta}(\bar{\omega}, \Delta\omega)\rangle_{\bar{\omega},\Delta\omega} = \left\langle \left| \sum_{j=1}^{N} AP_{\Delta,j} w_j(\Delta\omega) \right|^2 \right\rangle_{\bar{\omega},\Delta\omega} \tag{2.14}$$

and

$$\bar{B}_{\Sigma} = \langle B_{\Sigma}(\Delta\omega, \Sigma\omega)\rangle_{\Delta\omega,\Sigma\omega} = \left\langle \left| \sum_{j=1}^{N} AP_{\Sigma,j} w_j(\Sigma\omega) \right|^2 \right\rangle_{\Delta\omega,\Sigma\omega} \tag{2.15}$$

where $\langle\ \rangle_{\bar{\omega},\Delta\omega}$ and $\langle\ \rangle_{\Delta\omega,\Sigma\omega}$ indicate double averages through the signal bandwidth and a specified range of difference frequencies and sum frequencies, respectively. The additional averaging implied in Eqs. 2.14 and 2.15 increases the robustness of the beamformed results and suppresses the unintended consequences of the quadratic nonlinearity inherent in Eqs. 2.10 and 2.11.

2.1.4 Frequency-Difference and Frequency-Sum Autoproduct Fields

As stated above, the fields generated by the frequency-difference and frequency-sum autoproducts behave like a genuine field at the corresponding frequency if enough bandwidth averaging is available. Though this has been previously examined in other works [3, 165], it is briefly explored here to understand the assumptions included in this statement. First, a propagation model is assumed for the in-band acoustic field – in this case a sum of acoustic ray paths will be used since the beamforming algorithms discussed previously assume ray-based propagation

$$P_j(\omega) = S(\omega) \sum_{l=1}^{L} A_{lj} e^{i\omega r_{lj}/c}, \tag{2.16}$$

where L is the number of propagation paths between the source and j^{th} receiver, A_{lj} is the complex amplitude of the l^{th} path, which will include any $1/r$ decay, and r_{lj} is the length of the l^{th} path. Any phase shifts caused by reflection and change in media are incorporated into the phase of A_{lj}. Taking the frequency-difference autoproduct of Eq. 2.16 yields

$$AP_{\Delta,j} = P_j(\omega_2)P_j^*(\omega_1) = S(\omega_2)S^*(\omega_1) \sum_{l=1}^{L} \sum_{m=1}^{L} A_{lj} A_{mj}^* e^{i(\omega_2 r_{lj} - \omega_1 r_{mj})/c}, \tag{2.17}$$

which can be rewritten with the diagonal and off-diagonal terms separated

$$AP_{\Delta,j} = S(\omega_2)S^*(\omega_1)\left\{ \sum_{l=1}^{L} |A_{lj}|^2 e^{i\Delta\omega r_{lj}/c} + \sum_{\substack{l,m=1 \\ l\neq m}}^{L,L} A_{lj}A_{mj}^* e^{i(\omega_2 r_{lj} - \omega_1 r_{mj})/c} \right\} \tag{2.18}$$

By extension, it is easy to determine that the frequency-sum autoproduct field is given by

$$AP_{\Sigma,j} = S(\omega_2)S(\omega_1)\left\{ \sum_{l=1}^{L} |A_{lj}|^2 e^{i\Sigma\omega r_{lj}/c} + \sum_{\substack{l,m=1 \\ l\neq m}}^{L,L} A_{lj}A_{mj} e^{i(\omega_2 r_{lj} + \omega_1 r_{mj})/c} \right\} \tag{2.19}$$

In both Eqs. 2.18 and 2.19, the first bracketed term is clearly the desired term that would be expected to behave usefully with the beamforming algorithms discussed above, due to the difference and sum frequency dependencies. However, the second bracketed term is undesired. Fortunately, if sufficient bandwidth is available to average through when calculating the beamforming output, the cycling of the phase angle as the in-band frequencies are varied generates an effectively random phase term, which does not yield false source localizations, but rather will create an effective noise floor that will reduce the dynamic range of the output. Both autoproducts require bandwidth to average through to behave robustly, but their limitations with respect to bandwidth are different. For the frequency-difference autoproduct, the difference frequency can approach 0 Hz on the low end (limited only by the frequency resolution), but cannot exceed the total bandwidth, $\Omega_H - \Omega_L$, on the high end. In addition, if the difference frequency exceeds half of the total bandwidth, i.e. $\Delta\omega \geq (\Omega_H - \Omega_L)/2$, frequency bins near the center of the bandwidth will go unused. Frequency-sum beamforming is limited by the actual values of the frequencies within the bandwidth. The minimum sum frequency is twice the minimum in-band frequency, while the maximum sum frequency is twice the maximum in-band frequency. Again, these extreme cases are less than ideal due to the lack of available bandwidth to average over, so a sum frequency closer to $\Sigma\omega = (\Omega_L + \Omega_H)/2$ is typically desirable. Figure 2.1 illustrates the available difference and sum frequency bands based on a range of in-band frequencies. The solid gray box corresponds to the in-band frequencies between Ω_L and Ω_H, the gray triangle with vertical lines corresponds to the range of available difference

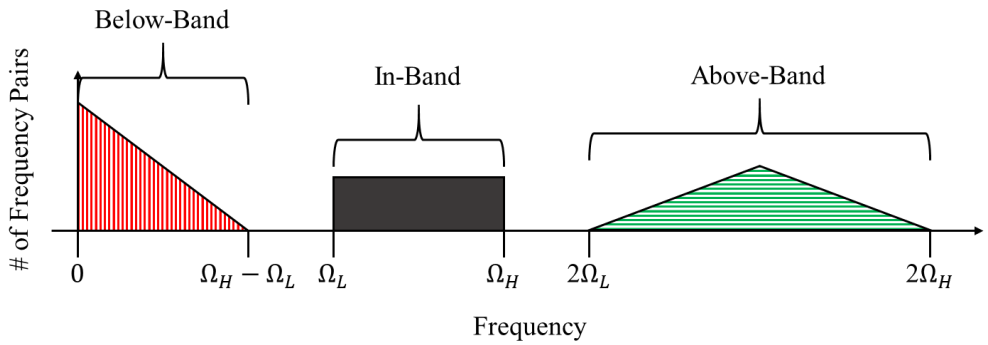

Figure 2.1: Difference frequencies and sum frequencies available from a signal with a bandwidth of $\Omega_L \leq \omega \leq \Omega_H$. The solid black box corresponds to in-band frequencies, the triangle with vertical red lines to the below-band difference frequencies, and the triangle with horizontal green lines to the above-band sum frequencies. The vertical axis indicates the number of available frequency pairs, which decreases with increased difference frequencies, as well as sum frequencies extending away from the center sum frequency (the gray box representing the in-band fields is at an arbitrary height for visual purposes).

frequencies, and the gray triangle with horizontal lines corresponds to the range of available sum frequencies. The vertical axis indicates the number of available frequency pairs for each choice of difference or sum frequency (with the in-band box at arbitrary height not corresponding to this axis).

The effects of the non-linearity introduced by the autoproduct will impact the results differently for specific cases. The undesired terms introduced in Eqs. 2.18 and 2.19 are suppressed with bandwidth averaging, but a minimum amount of bandwidth is generally required. When considering the autoproduct near a surface boundary, the interaction between the incident and reflected waves does not behave as a conventional field would at a frequency matching the difference or sum frequencies, and the interference layer (i.e. the distance from the boundary in which the field behaves unintuitively) is dependent on the bandwidth and the difference or sum frequencies considered, as well as the incident angle [165]. In addition, the quadratic product will turn a negative reflection coefficient (-1 for a pressure release boundary) into a positive one when sufficiently outside of the interference layer (which is not necessarily a harmful outcome). Furthermore, the nonlinearity will favor the higher amplitude portions of a signal measurement. For example, if the SNR is below 0 dB, the influence of the noise present in the measurement may increase. Or, if multiple arrivals or

sources exist, the quieter arrivals/sources may be partially suppressed.

2.2 Frequency-Difference Beamforming

2.2.1 Free Space Simulations and Experiments

The performances of Eqs. 2.9, 2.14, and 2.15 were first examined in simulated and experimental free-space environments (uniform sound speed and no boundaries). The simulations utilized the free-space Green's function and were geometrically- and frequency-matched to experiments conducted in a 1.07 m diameter 0.90 m deep cylindrical laboratory water tank. Two 0.1 ms Gaussian-enveloped pulses, one 15 kHz and one 165 kHz, were broadcast from ITC-1032 and ITC-1094A transducers, respectively, to an array of 14 Reson TC4013 receiving hydrophones spaced $d = 5.08$ cm apart. The broadcast and receiving transducers were all located in a single horizontal plane at a depth of 53 cm. The output from each array element was amplified, appropriately bandpass filtered, and then digitized and recorded at a rate of 1.0 MHz. Figure 2.2 shows a schematic of the experimental setup with the source at the first of nine near-field positions. The array mounting hardware was discretely (not continuously) adjustable, so the array center was located at $x = 0$ cm and $y = 0.7$ cm in the coordinate system shown in Fig. 2.2. With this array geometry, $d/\lambda = 0.51$ at 15 kHz and $d/\lambda = 5.7$ at 165 kHz; thus, the array is well populated at the lower frequency but is sparse at the higher frequency.

Nine source positions were considered for both the simulations and experiments, and all recorded signals were time-windowed to eliminate (to the extent possible) surface, bottom, or sidewall reflections. The time windowing was adjusted for each source location, but was the same for both the low and high signal pulses. Figure 2.3 shows sample time traces from all 14 transducers for the 15kHz (Fig. 2.3(a) and 2.3(c)) and 165 kHz signal pulses (Fig. 2.3(b) and 2.3(d)) for the first source location in both simulation (Fig. 2.3(a) and 2.3(b)) and experiment (Fig. 2.3(c) and 2.3(d)). Except for minor artifacts left from time windowing, the experimental signals are nearly ideal at the lower frequency. At the higher frequency, hydrophone-to-hydrophone scattering caused a

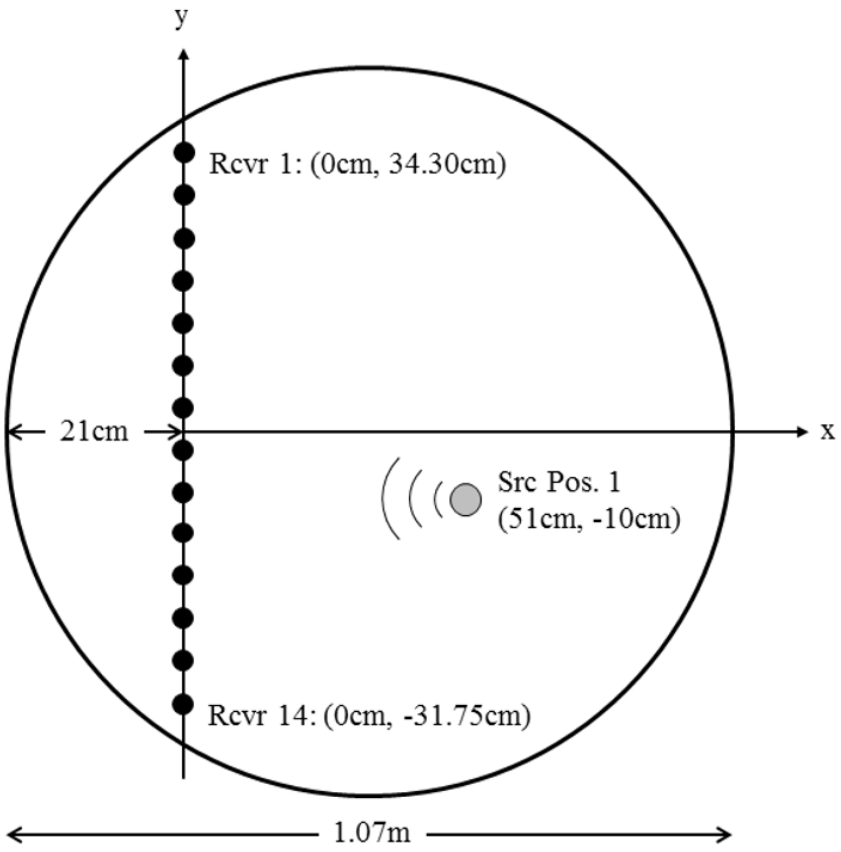

Figure 2.2: Simulation and experimental setup. A 14-element receiver array with 5.08 cm spacing was placed 21 cm from the edge of a 1.07 m diameter, 0.90 m deep cylindrical water tank at a depth of 0.53 m. The array center was offset from the centerline of the tank by 0.7 cm in the positive y direction. Two sources were used to broadcast 15 and 165 kHz pulses with 0.1 ms duration from 9 different source locations.

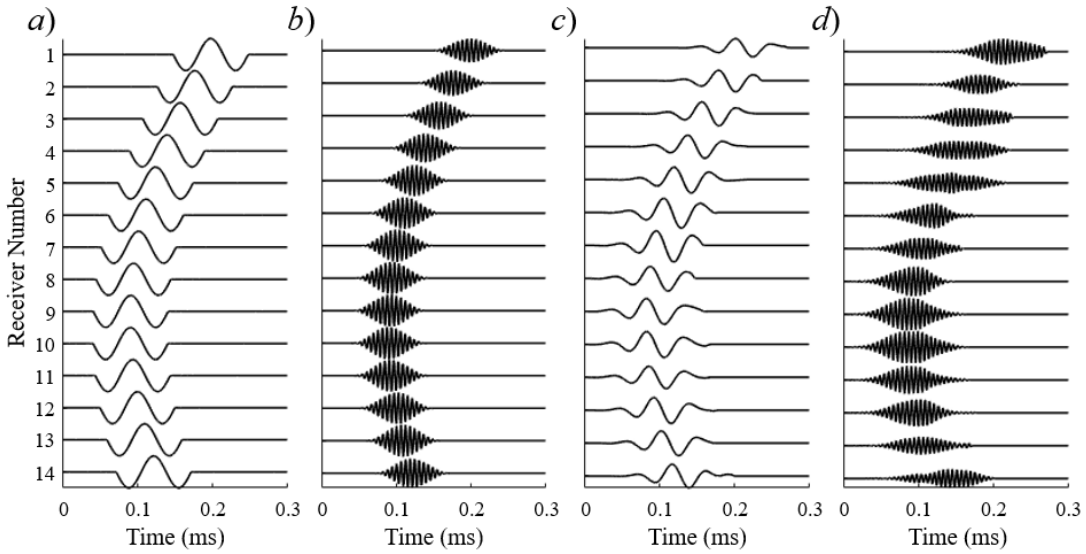

Figure 2.3: Receiver array recordings in simulation (a,b) and experiments (c,d) with the source in the position shown in Fig. 2.2 for the 15 kHz pulse (a,c) and the 165 kHz pulse (b,d). For the experiments, first reflections and additional reverberation have been removed from the signals via time windowing.

noticeable variation in the recorded signals' envelopes.

Sample spherical-wave beamforming results from the source location in Fig. 2.2 are shown in Fig. 2.4 for both simulated and experimental cases. In all six panels of Fig. 2.4, the dynamic range is 10 dB, and a small white 'x' marks the source location. Figures 2.4(a) and 2.4(d) provide conventional beamforming results for B_{conv} from Eqs. 2.6 and 2.8 at $f = \omega/2\pi = 15$ kHz without any signal bandwidth averaging for the simulated and experimental cases, respectively. Here, as expected, the source is localized via a single broad maximum (main lobe) of B_{conv} without ambiguity, and the simulation and experimental results are nearly identical. Figures 2.4(b) and 2.4(e) provide conventional beamforming results for B_{conv} using Eqs. 2.8 and 2.9 for $f = \omega/2\pi = 165$ kHz with 60 kHz of signal-bandwidth averaging, 135 kHz $\leq f \leq$ 195 kHz, for the simulated and experimental cases, respectively. In the simulated case, the beamforming is successful and precise, but additional side lobes exist, which suggest that any added uncertainty, noise, reverberation, etc., would be detrimental to these results. As expected, in the experimental case, conventional beamforming is unsuccessful because of ambiguity; there are many possible maxima of B_{conv}, but only one lies near the actual source location. Experimental conventional beamforming results for the

other eight source locations using this technique were similarly ambiguous. When taken together, these results indicate the expected limitation of conventional spherical-wave beamforming with a sparse array where $d/\lambda = 5.7$. However, as shown in the simulation case in Fig. 2.4(c) and the experimental case in Fig. 2.4(f), the 165 kHz signal pulse recordings can be used to localize the source using B_Δ from Eqs. 2.8 and 2.12 with Δf-averaging from 142.5 to 187.5 kHz and Δf = 15 kHz alone (no difference frequency averaging). These specifications for f and Δf cause B_Δ in Figs. 2.4(c) and 2.4(f) to use precisely the same signal-bandwidth as is used for B_{conv} in Figs. 2.4(b) and 2.4(e). The results shown in Fig. 2.4(c) are nearly identical to those in Fig. 2.4(a) even though different signals were used to create these figures, and Δf = 15 kHz is well below the signal band of the 165 kHz pulse. This result indicates that frequency-difference beamforming of high-frequency signals can perform comparably to conventional beamforming of low-frequency signals when the difference frequency Δf used to determine B_Δ matches the absolute frequency used to determine B_{conv}. In the experimental case, the findings are similar between Figs. 2.4(d) and 2.4(f), though the performance of frequency-difference beamforming is degraded slightly, primarily due to the between-phone scattering of the higher frequency signal. However, the fairer comparisons are actually between Figs. 2.4(c) and 2.4(e), and Figs. 2.4(d) and2.4(f), since these pairs of results were both created from the same signal recordings using the same signal bandwidth. Overall, Fig. 2.4 illustrates how frequency- difference beamforming can be used with a high-frequency signal to improve localization robustness when the array is sparse.

A quantitative listing of results for all nine source-array geometries is provided in Table 2.1. Conventional beamforming B_{conv} from Eqs. 2.6 and 2.8 uses the 15 kHz signal. Frequency-difference beamforming B_Δ from Eqs. 2.8 and 2.9 uses the 165 kHz signal, with f-averaging from 142.5 to 187.5 kHz and a constant Δf = 15 kHz (no difference frequency averaging). The results from in-band B_{conv} with the 165 kHz signal provided an accurate peak near the source in most cases, but with much more ambiguity due to many additional maxima located throughout the search field. The first section of Table 2.1 lists the true range (r) and angle (θ) from the center of the receiving array to the source, with $\theta = 0°$ defining the broadside direction. For the experiments, the

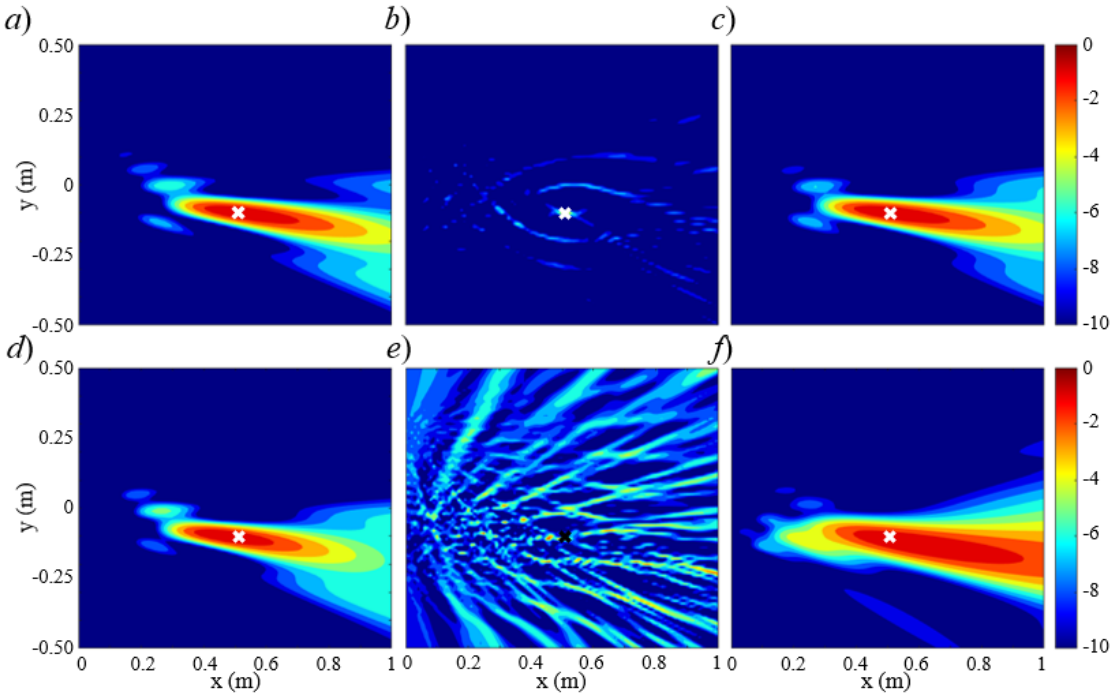

Figure 2.4: Simulated and experimental beamforming output for the geometry shown in Fig. 2.3. Conventional beamforming of the (a) simulated and (d) experimental 15 kHz signal, conventional beamforming of the (b) simulated and (e) experimental 165 kHz signal processed between 135 and 195 kHz, and frequency-difference beamforming at Δf = 15 kHz using the simulated (c) and experiment (f) 165 kHz signal processed between 135 and 195 kHz. The actual source location is indicated by a white or black 'x'.

metrology-determined range and angle uncertainties of the actual source location were nominally $+/-1.9$ cm, and between $+/-2$ and 7 degrees, with the smaller angle uncertainties corresponding to the longer range cases. These were calculated by combining the estimated uncertainties for each component used in the experimental setup for all three dimensions. The tabulated entries in the remainder of the table are source range and angle errors and the beam width (abbreviated "Res.") achieved from the beamformed outputs for both the simulations (top) and experiments (bottom). For these entries, the beam width numbers are the distances or angular widths to the -3 dB points of the ambiguity surface's main lobe. Average range and angle errors are also listed in the final row of each section in the table. The locations for the simulations were determined by the measured positions in experiments. The results would be expected to obtain perfect localization, but in general, these positions did not fall on integer centimeter values, thus the error associated with each case is a result of each method's performance response to an imperfectly resolved window. For two experimental cases, a combination of the geometry, scattering effects, and sidewall reflections contributed to a near-plane wave result for B_Δ with no -3 dB range border within the $x - y$ search plane. Thus, the beam width as a function of range for these source locations are not listed in Table 2.1.

In addition to comparing frequency-difference beamforming with conventional methods, the capabilities of several common advanced beamforming techniques - MVDR, MUSIC, and Compressive Beamforming - are considered for the experiments performed here. In general, these techniques have been designed for the purposes of improving precision and resolution, rather than correcting for the negative effects associated with beamforming at high frequencies. Nevertheless, it is important to understand whether existing techniques provide a viable solution to the problems investigated herein. For these purposes, the most basic implementations of MVDR, MUSIC [89], and compressive beamforming [63] will be utilized. A sample output for the experiment corresponding to Trial 3 is shown in 2.5 for conventional beamforming (a), MVDR (b), MUSIC (c), and compressive beamforming (d), all utilizing a 135 kHz $\leq f \leq$ 195 kHz bandwidth. Here, the black or white circle indicates the expected source location. MVDR and MUSIC have nearly identical

Table 2.1: Summary of spherical beamforming results. Trial numbers preceded by an "S" (upper half of the table) indicate simulation results. The corresponding experimental trials (lower half of the table) use approximately the same source position. The actual source range and angle are provided in the next two columns. The results for conventional beamforming at 15 kHz are listed in the section labeled "conventional," and the results for frequency-difference beamforming using Δf = 15 kHz for the 165 kHz signal are listed in the section labeled "Frequency-Difference." The error is provided for range and angle in each case. The range and angular beam widths (abbreviated "Res.") are provided for each case and are defined by the B-contour-edge at -3 dB.

	Actual		Conventional				Frequency-Difference			
Trial	Range (m)	Angle (°)	Range Error (m)	Angle Error (°)	Range Res. (m)	Angle Res. (°)	Range Error (m)	Angle Error (°)	Range Res. (m)	Angle Res. (°)
S1	0.519	12	0.002	0	0.613	8	0.002	0	0.553	8
S2	0.340	37	0.015	-1	0.305	9	0.016	-1	0.374	11
S3	0.508	1	0.012	0	0.569	8	0.002	0	0.430	8
S4	0.272	-48	0.007	1	0.180	10	0.007	1	0.168	12
S5	0.175	19	0.004	-1	0.139	12	0.014	-2	0.247	16
S6	0.587	10	0.023	0	0.811	8	0.022	0	0.598	8
S7	0.490	-44	0.001	1	0.768	8	-0.006	0	0.724	8
S8	0.312	-14	0.003	0	0.254	9	0.003	0	0.238	11
S9	0.282	31	0.008	-1	0.214	9	0.013	1	0.271	10
AVG			**0.008**	**0.6**			**0.009**	**0.6**		
1	0.519	12	0.037	1	0.491	8	0.076	1	1.316	12
2	0.340	37	0.007	-1	0.307	10	0.030	-1	0.466	10
3	0.508	1	0.038	1	0.507	10	0.012	1	Plane	13
4	0.272	-48	0.015	5	0.178	11	0.000	5	0.265	18
5	0.175	19	0.003	6	0.136	12	0.002	6	0.235	12
6	0.587	10	0.046	1	0.683	8	0.003	0	Plane	11
7	0.490	-44	0.019	4	0.582	9	0.112	2	0.445	11
8	0.312	-14	0.026	-5	0.236	10	0.006	-5	0.440	10
9	0.282	31	0.018	3	0.223	9	0.035	1	0.366	10
AVG			**0.023**	**3.0**			**0.031**	**2.4**		

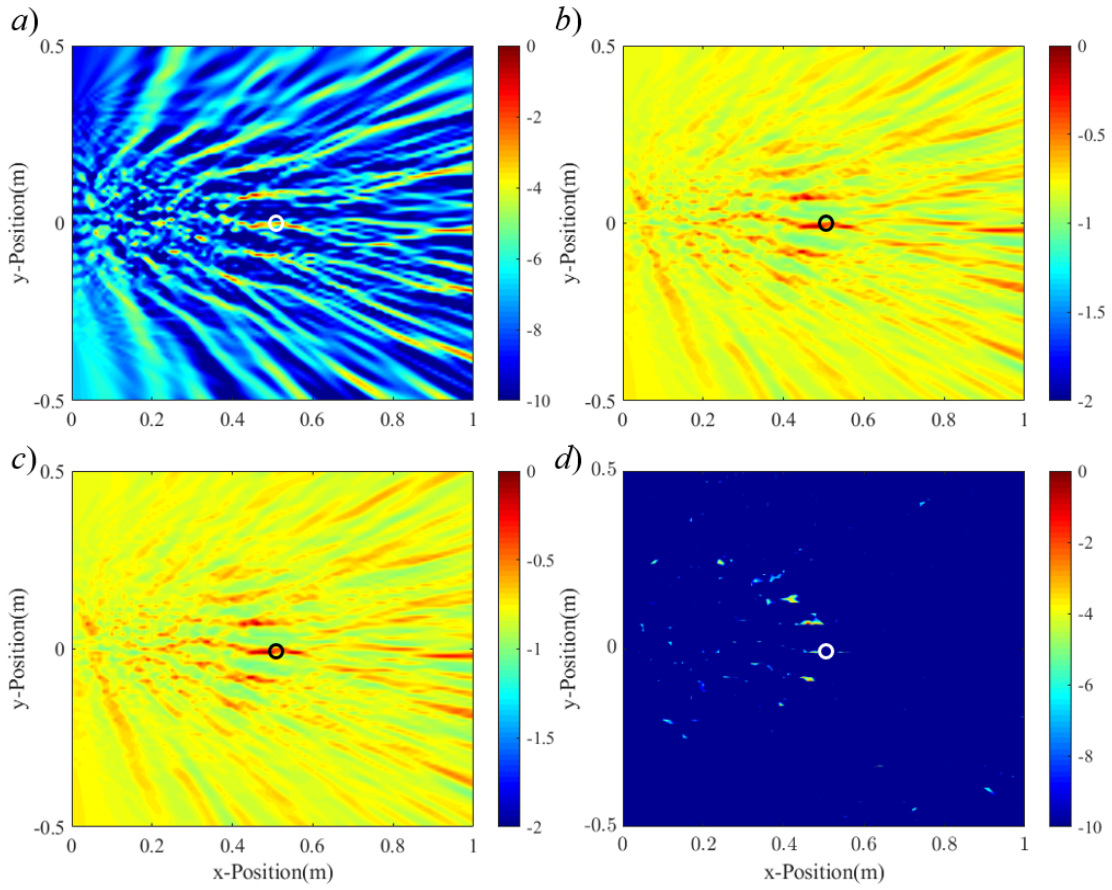

Figure 2.5: Beamforming outputs of Trial 3 for conventional beamforming (a), MVDR (b), MUSIC (c), and compressive beamforming (d), all utilizing a 135 kHz $\leq f \leq$ 195 kHz bandwidth. The black or white circle indicates the expected source location. Note that the color bars vary between figure panels.

outputs, which is expected in a noise-free, single source scenario such as this [119], and notably have very poor dynamic range and poor localization (the color bars vary between figure panels for clarity). Compressive beamforming has a large dynamic range, but many sidelobes and again, a higher error than desired.

A results summary is provided in Table 2.2 for conventional beamforming, MVDR, MUSIC, and compressive beamforming. Conventional beamforming has comparable performance to frequency-difference beamforming, with a slightly higher error overall (when considering Euclidean distance), which is an unsurprising result in a simple environment like this. However, the baseline versions of MVDR, MUSIC, and compressive beamforming, all notably worse at the

Table 2.2: Summary of experimental results for conventional beamforming, MVDR, MUSIC, and compressive beamforming, using the same 9 cases as in 2.1 and a bandwidth of 135 kHz $\leq f \leq$ 195 kHz.

Trial	**Conventional Beamforming**		**MVDR**		**MUSIC**		**Compressive Beamforming**	
	Range Error (m)	Angle Error (°)	Range Error (m)	Angle Error (°)	Range Error (m)	Angle Error (°)	Range Error (m)	Angle Error (°)
1	0.028	0.7	0.006	1.3	0.006	1.3	0.016	1.6
2	0.022	2.8	0.007	1.0	0.007	1.0	0.036	2.4
3	0.028	1.2	0.055	8.7	0.055	8.7	0.041	1.0
4	0.009	8.8	0.024	4.4	0.024	4.4	0.207	63.4
5	0.020	4.9	0.005	7.2	0.005	7.2	0.181	0.4
6	0.086	1.8	0.251	8.1	0.251	8.1	0.157	8.4
7	0.014	4.3	0.040	1.9	0.040	1.9	0.052	31.0
8	0.005	5.1	0.024	3.8	0.024	3.8	0.174	13.3
9	0.036	0.4	0.027	4.7	0.027	4.7	0.120	9.5
AVG	**0.028**	**3.3**	**0.049**	**4.6**	**0.049**	**4.6**	**0.109**	**14.6**

source localization task. This is unsurprising, since these techniques are not expected to be robust to uncertainty, mismatch, and scattering, in their basic implementation. Thus, the remainder of the work with out-of-band beamforming methods will use conventional beamforming as a baseline for comparisons.

As mentioned previously, the user can choose the difference frequency to be used with frequency-difference beamforming within the constraints of the signal bandwidth. To generate a more robust beamforming output, these difference frequency outputs can be averaged together through the frequency-difference bandwidth using Eq. 2.14. This is demonstrated in Fig. 2.6 using the same data as above, but choosing Δf = 10 kHz (a), 20 kHz (b), 30 kHz (c), and averaging difference frequencies between 10 and 30 kHz at 1 kHz increments (d) for simulations. The same cases are shown for experimental results in (e)-(h), in the same order. The simulations clearly demonstrate that as difference frequency increases, beam width decreases, and in the case of simulation, source localization is not sacrificed. In addition, the difference frequency averaging case reduces any side-lobes from difference frequencies that would potentially lead to aliasing, such as the lobes seen for

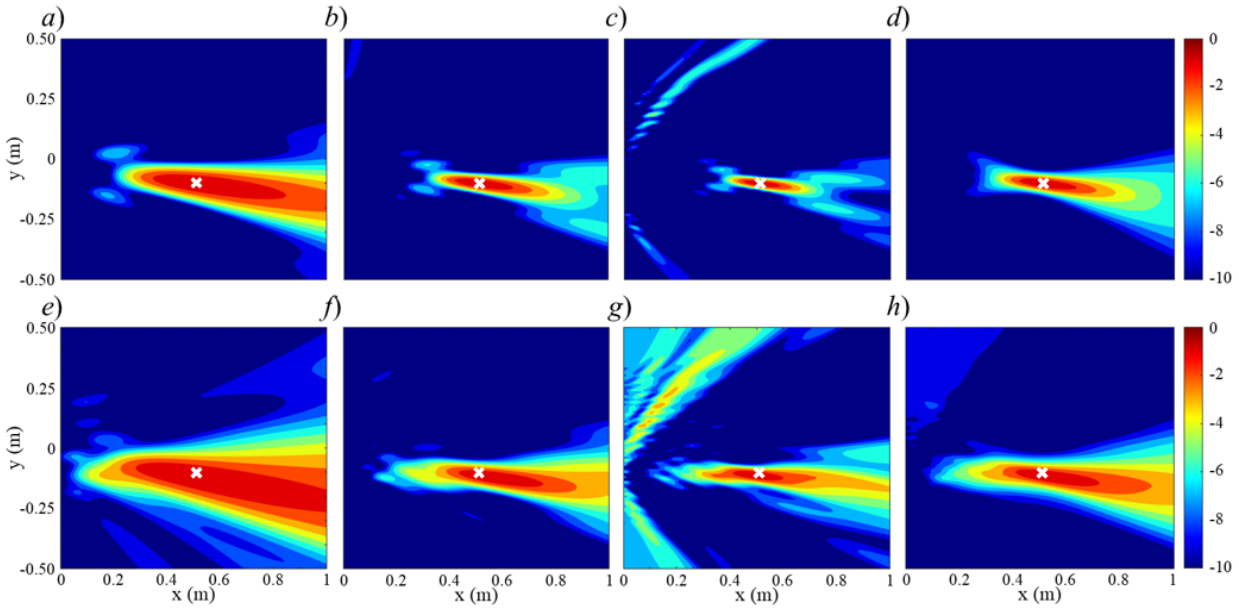

Figure 2.6: Simulated and experimental beamforming output for the geometry shown in Fig. 2.2. All results are frequency-difference beamforming outputs for simulations (top row) and experiments (bottom row). Four cases are shown using the same signal measurement but with varying difference frequencies: Δf = 10 kHz (a,e), Δf = 20 kHz (b,f), Δf = 30 kHz (c,g), and Δf = averaged from 10 to 30 kHz at 1 kHz increments (d,h). The white 'x' corresponds to the expected source location.

the 30 kHz case (c). Interestingly, the experimental results show some variation in the peak location dependent on the chosen difference frequency, but by averaging the results across difference frequencies, a more robust localization results. Another benefit of difference frequency averaging is the suppression of sidelobes, such as those shown in the Δf = 20 kHz case.

As mentioned before, the undesired cross-terms from Eq. 2.18 are expected to be suppressed by bandwidth averaging when multiple sources are present. This is demonstrated through a simulation using the same setup and signals as in Fig. 2.4, but with an additional source placed at (x, y) = (0.5 m,0.3 m), broadcasting a white noise signal with an SNR = 0 dB over each signal's bandwidth. Figure 2.7 shows the output of this scenario using conventional beamforming at 15 kHz (a), conventional beamforming from 135-195 kHz (b), and frequency-difference beamforming from 135-195 kHz, using a difference frequency of Δf = 15 kHz (the markers are left out of panel (b) for clarity). The output suggests that the cross terms are sufficiently suppressed, such that

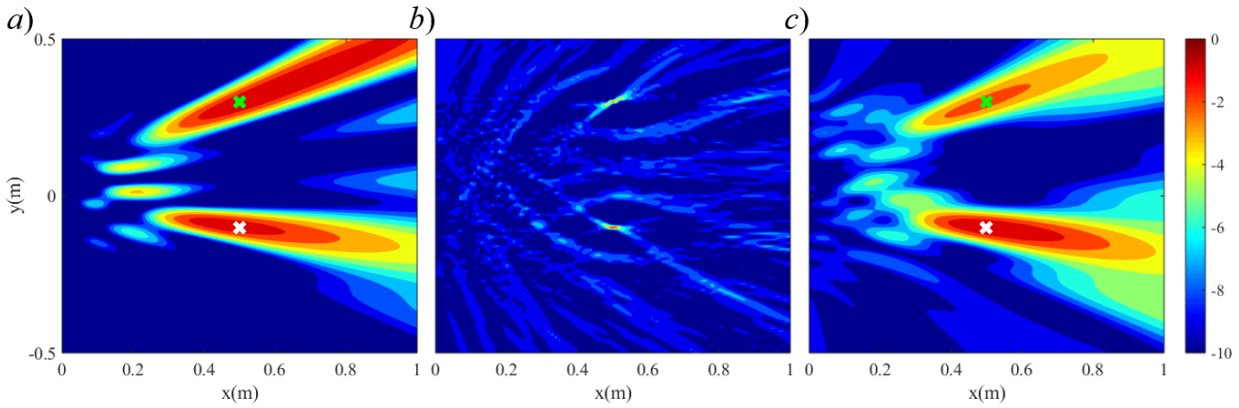

Figure 2.7: Conventional beamforming at f = 15 kHz (a), conventional beamforming from 135 kHz $\leq f \leq$ 195 kHz (b), and frequency-difference beamforming at Δf = 15 kHz using a bandwidth of 135 kHz $\leq f \leq$ 195 kHz (c), for a two-source case. One source is a 15 kHz or 165 kHz pulse (same as above), the other is an unknown noise source with an SNR = 0 dB. The source of interest is indicated by a white 'x' and the noise source by a green 'x' (markers are left out in panel (b) for clarity).

the beamformed outputs in (a) and (c) are comparable and no false sources appear, indicating that no significant structure exists in the cross terms over the signal bandwidth. Frequency-difference beamforming does provide a slightly different output for the noise source, due to the variation of SNRs over frequency pairs.

Overall, the results from Fig. 2.4 and Table 2.1 indicate that frequency-difference beamforming provides superior results to conventional beamforming when both techniques are applied at a higher frequency, where the array is considered sparse. Frequency-difference beamforming's capabilities are further exploited when some additional undesired effects exist in a dataset, such as array geometry uncertainty or signal scattering. Additionally, the results above indicate that frequency-difference beamforming at a chosen Δf can be expected to behave similarly and provide similar results to a conventional beamforming field at a frequency matching the difference frequency, Δf. Finally, Fig. 2.6 illustrates the flexibility provided to the user in choosing the difference frequency and demonstrates capabilities and benefits of frequency-difference beamforming for various difference frequencies.

2.3 Frequency-Sum Beamforming

2.3.1 Free Space Simulations and Experiments

In this section, the performance of frequency-sum beamforming, Eqs. 2.13 and 2.15, is evaluated. As the counterpart to frequency-difference beamforming, the process of constructing a frequency-sum field is very similar. The only difference in the autoproduct calculation is that the complex conjugate is dropped from the equation. As a result, instead of the $\Delta\omega = \omega_2 - \omega_1$ result, $\Sigma\omega = \omega_2 + \omega_1$ is obtained. Theoretically, bandwidth is not required to generate a frequency-sum autoproduct, since a single frequency can be doubled, but as discussed before, for a robust field, some bandwidth averaging should be included. Ultimately, frequency-sum beamforming is expected to improve the precision of the beamforming output, as if the signal was an actual in-band signal matching the sum frequency, Σf.

The same setup as in the previous section will be used to evaluate frequency-sum beamforming, as shown in Fig. 2.2. In addition, the same low-frequency 15 kHz signal will be utilized for this analysis, as shown in Fig. 2.3. The high frequency signal is not needed for this analysis, since array sparsity isn't a concern, but simply beamforming precision. Conveniently, the 15 kHz signal bandwidth has a small amount of signal energy at 30 kHz, and due to the very high SNR achieved in the water tank, this information is usable without broadcasting a new signal. Figure 2.8 demonstrates the capabilities of frequency-sum beamforming for a single source. Here, conventional beamforming for a 15 kHz signal is shown for simulation (a) and experiments (d). Using the same signal, conventional beamforming is processed at 30 kHz, again for a simulated case (b) and an experimental case (e). Frequency-sum beamforming uses the same 15 kHz signal, but utilizes signal bandwidth to generate the frequency-sum field. Specifically, a 10 kHz bandwidth centered around 15 kHz is utilized to generate a 30 kHz frequency-sum autoproduct, with all frequency pairs that sum to 30 kHz being utilized. The beamforming output for this case is shown for simulation (c) and experiment (f) as well, and compares nicely with the conventional beamforming

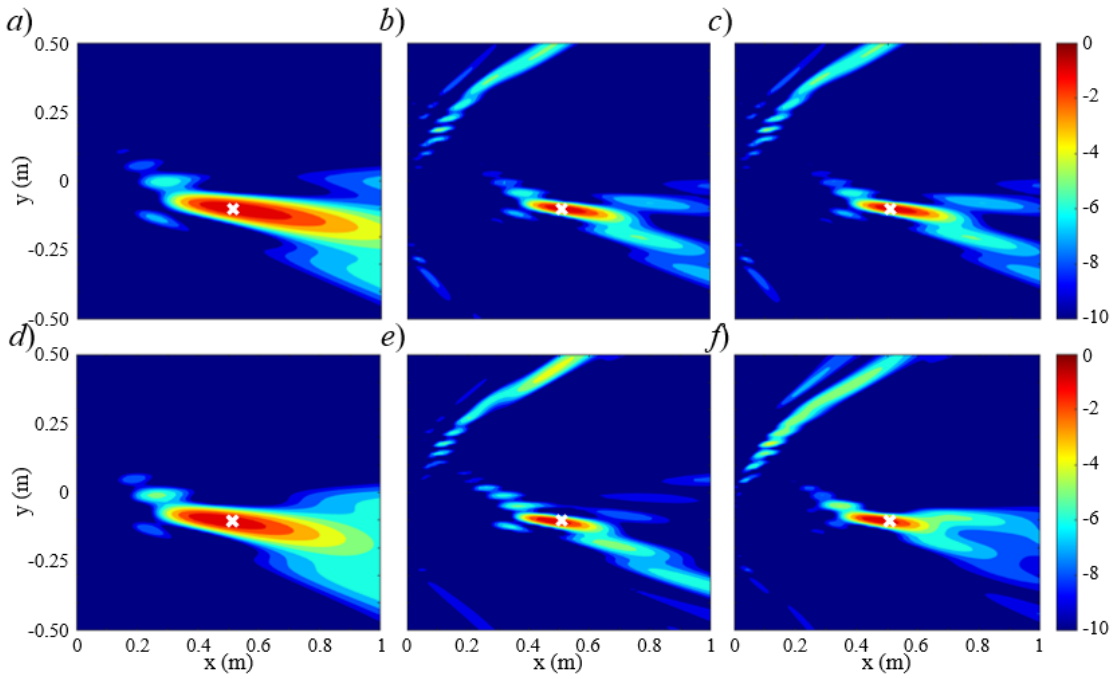

Figure 2.8: Conventional beamforming and frequency-sum beamforming comparison, all using the same, wideband 15 kHz pulse in simulations (top row) and experiments (bottom row). The cases shown are for conventional beamforming at 15 kHz (a and d), conventional beamforming at 30 kHz (b and e), and frequency-sum beamforming with Σf = 30 kHz but generated using frequencies between 10 and 20 kHz. The expected source location is indicated with a white 'x'.

cases at 30 kHz. In simulation, the two appear nearly identical, whereas in the experimental case, differences are easily found, but they are minimal and have little impact on performance. This suggests that for a single-path environment, with sufficient bandwidth averaging, frequency-sum can localize comparably to conventional beamforming when the sum frequency, Σf, matches the in-band frequency used with conventional beamforming.

As was done above for frequency-difference beamforming, multiple source locations are tested in both simulation and experiment. The exact same datasets were used as in the previous section, thus the performance of conventional beamforming at 15 kHz is not repeated here. Instead, the table provides the actual source location, the performance of conventional beamforming at 30 kHz, and the performance of frequency-sum beamforming with Σf = 30 kHz, but using only frequencies between 10 and 20 kHz. On average, the source localization error for frequency-sum beamforming is comparable to that of conventional beamforming at 30 kHz, with only a slightly

higher error for frequency-sum in simulation and slightly improved results in experiments (note that the average is calculated using the absolute errors, but the negative signs are left in the table to indicate the direction of the found peak). Again, as before, the simulations are performed with source locations placed in non-centimeter increments, hence why precise source locations are not found, as may be expected in simulation. Also notable is that the range and angle beam width estimates between the two methods is almost identical in simulation, and only slightly worse for frequency-sum in experiments, indicating that frequency-sum does provide the precision benefits of a higher frequency field, despite using lower frequencies as inputs.

Finally, frequency-sum beamforming provides the use the capability to select a specific sum frequency for the processing, constrained by the available frequencies in the signal bandwidth. In general, to utilize the full bandwidth available, a sum frequency that is twice the signal center frequency must be used. For a higher sum frequency, the lower end of the signal bandwidth is not available, and the opposite is true for a lower sum frequency. Figure 2-7 demonstrates frequency-sum beamforming in simulation (top row) and experiment (bottom row) for four different cases - $\Sigma f = 22$ kHz using a bandwidth of 10 kHz $\leq \Omega \leq$ 12 kHz (a, e), $\Sigma f = 30$ kHz using a bandwidth of 10 kHz $\leq \Omega \leq$ 20 kHz (b, f), $\Sigma f = 38$ kHz using a bandwidth of 18 kHz $\leq \Omega \leq$ 20 kHz (c, g), and an average of sum frequencies from 22 to 38 kHz at 1 kHz increments (d, h). The precision of the method behaves predictably as the sum frequency is varied, and side lobes appear where expected. An interesting and important result is in the sum frequency averaging cases (d, h), where the sum frequency averaging significantly reduces the sidelobes.

An important caveat exists for frequency-sum beamforming. Here, the performance is considered specifically for one source. The nature of the frequency-sum beamforming formulation results in an undesired feature – when more than one source exist, additional peaks are formed between the sources. For example, with two sources present, a third peak is formed directly between the two, with its amplitude sometimes larger than either individual peak. Fortunately, this is a predictable feature of frequency-sum beamforming and can potentially be accounted for, but doing so would likely require some additional knowledge, such as the number of sources present, unless a

Table 2.3: Frequency-sum beamforming performance for nine source locations in simulation (top row) and experiment (bottom row). The actual source location is shown in the 2nd and 3rd columns, followed by the results from conventional beamforming at 30 kHz, and finally the results from frequency-sum beamforming at Σf = 30 kHz, but processed using frequencies between 10 and 20 kHz. The average range and angle error are provided for both simulation and experiment.

	Actual		Conventional (30 kHz)				Frequency-Sum (30 kHz)			
Trial	Range (m)	Angle (°)	Range Error (m)	Angle Error (°)	Range Res. (m)	Angle Res. (°)	Range Error (m)	Angle Error (°)	Range Res. (m)	Angle Res. (°)
S1	0.519	12	0.001	0.9	0.250	4	0.011	1.1	0.249	4
S2	0.340	37	-0.004	-0.5	0.137	7.2	0.004	-1.5	0.139	4.5
S3	0.508	1	0.002	1	0.242	3.9	0.012	1	0.245	3.9
S4	0.272	-48	0.004	1.4	0.088	3.5	0.011	-0.1	0.089	4.2
S5	0.175	19	0.002	2.6	0.057	5.2	0.011	-3.5	0.068	5.6
S6	0.587	10	0.002	-0.2	0.316	3.8	0.011	-0.4	0.321	4
S7	0.490	-44	0.027	-1.4	0.303	4.7	0.012	-1.4	0.309	4.5
S8	0.312	-14	0.008	0.5	0.124	4.1	0.018	0	0.125	4.4
S9	0.282	31	0.004	-0.7	0.105	4.3	0.002	1.8	0.106	4.5
AVG			**0.006**	**1.0**			**0.010**	**1.2**		
1	0.519	12	-0.038	0	0.209	3.9	-0.038	0	0.233	4.4
2	0.340	37	0.026	-2	0.149	4.5	0.004	-1.5	0.167	5.3
3	0.508	1	-0.038	0.2	0.218	4.9	-0.038	0.2	0.256	4.5
4	0.272	-48	-0.010	-4.5	0.086	4.4	-0.010	-4.5	0.118	4.9
5	0.175	19	0.013	6.2	0.079	5.1	0.000	4.6	0.095	6.8
6	0.587	10	-0.067	1.1	0.263	3.9	-0.057	0.9	0.309	3.8
7	0.490	-44	-0.025	-3.3	0.244	4.6	0.037	-3.6	0.240	4
8	0.312	-14	-0.033	7	0.112	6.5	-0.024	6.3	0.127	4.4
9	0.282	31	0.015	1.6	0.589	5.4	0.015	1.6	0.604	5.6
AVG			**0.029**	**2.9**			**0.025**	**2.6**		

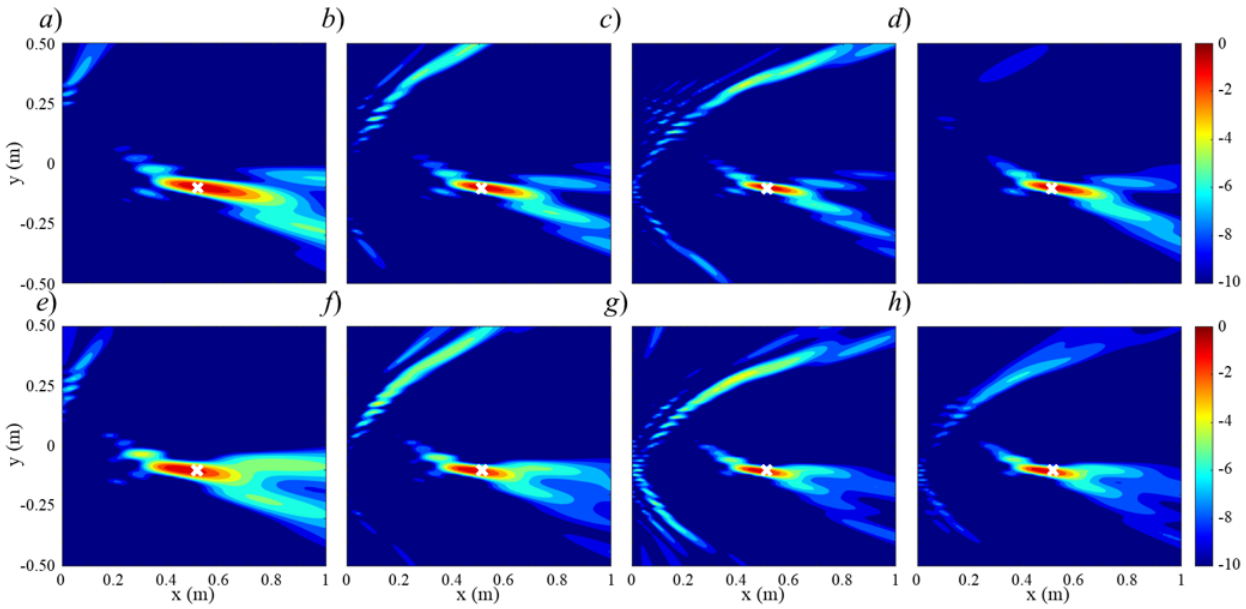

Figure 2.9: Frequency-sum beamforming in simulation (top row) and experiment (bottom row) for Σf = 22 kHz (a, e), Σf = 30 kHz (b, f), Σf = 38 kHz (c, g), and Σf outputs averaged from 22 to 38 kHz, at 1 kHz increments. In each case, as much bandwidth as possible is used between 10 and 20 kHz (but only the full bandwidth can be utilized for the 30 kHz case). The expected source location is indicated by a white 'x'.

simple scenario is considered. For the purposes of active array signal processing, a potential fix exists. When the signal is known, a coherent version of frequency-sum beamforming can be implemented, simultaneously improving the accuracy of the localization and reducing the influence of the undesired source and extra peak. Coherent beamforming utilizes the knowledge of the source signal to perform bandwidth averaging prior to taking the magnitude of the beamformer. That is, rather than Eq. 2.9, the beamforming formulation is

$$\bar{B}_{conv,coh}(\omega) = \left| \left\langle \sum_{j=1}^{N} \frac{P_j(\omega)}{S(\omega)} w_j(\omega) \right\rangle_{\omega} \right|^2 . \tag{2.20}$$

By removing the source term from the array output, one is effectively beamforming with the Green's function alone. For a perfect weighting vector at the correct DOA or source location, the product of the weighting vector and Green's function should yield a real number. Thus, by averaging across bandwidth before squaring the output, phase discrepancies are ignored. For incorrect source locations, this will yield a low-magnitude sum across bandwidth, further emphasizing the correct source location. Similarly, the out-of-band implementation can be constructed by swapping in the appropriate autoproducts, resulting in

$$\bar{B}_{\Delta,coh}(\Delta\omega) = \left| \left\langle \sum_{j=1}^{N} \frac{AP_{\Delta,j}(\omega, \Delta\omega)}{S(\bar{\omega} + \frac{\Delta\omega}{2}) S^*(\bar{\omega} - \frac{\Delta\omega}{2})} w_j(\Delta\omega) \right\rangle_{\bar{\omega}} \right|^2 \tag{2.21}$$

or

$$\bar{B}_{\Sigma,coh}(\Sigma\omega) = \left| \left\langle \sum_{j=1}^{N} \frac{AP_{\Sigma,j}(\bar{\omega}, \Delta\omega)}{S(\bar{\omega} + \frac{\Delta\omega}{2}) S(\bar{\omega} - \frac{\Delta\omega}{2})} w_j(\Sigma\omega) \right\rangle_{\Delta\omega} \right|^2 \tag{2.22}$$

A simple example of Eq. 2.22 is demonstrated in Fig. 2.10. Here, the same array geometry previously utilized is implemented, but two sources are placed in the field. A known source, a Gaussian-enveloped linear frequency sweep from 10 to 20 kHz, is placed at (x, y) = (0.50 m, -0.10 m). An "unknown" noise source (known for the purposes of the simulation, but processed as if it were not known) is placed at (x, y) = (0.50 m, 0.30 m). The noise source amplitude is adjusted

such that over the bandwidth of interest, the signal energy in the noise and known source match (i.e. the SNR = 0 dB). The figure demonstrates the performance of conventional beamforming (a), coherent conventional beamforming (b), frequency-sum beamforming at Σf = 30 kHz (c), and coherent frequency-sum beamforming at Σf = 30 kHz (d). In all four cases, the full 10 to 20 kHz bandwidth is utilized. The source of interest is indicated by a white 'x' and the noise source is indicated by a green 'x'. It is clearly demonstrated here that when the signal of interest is not known, frequency-sum beamforming yields an undesired lobe between the two sources, whereas conventional beamforming does not. However, frequency-sum beamforming clearly provides improved precision, making it desirable to use. Coherent conventional beamforming (b) provides enhanced precision and suppresses the noise source, and when extending this to frequency-sum beamforming, the same result is achieved but with enhanced precision and the undesired center lobe suppressed.

Based on the results presented in this section, frequency-sum beamforming can be expected to enhance beamforming precision without sacrificing localization capability. However, frequency-sum beamforming generates undesirable center lobes when multiple signals are present, meaning it may only be useful for single-source and single-path environments, or in cases where the number of sources is known a priori. For active array signal processing cases, frequency-sum beamforming may be useful since the broadcast signal should be known and a coherent version can be implemented, which is shown to suppress the undesired center lobe in addition to undesired noise sources. Unfortunately, this does not address a multipath scenario where multiple arrivals may originate from the same source signal.

2.4 Summary and Conclusions

This chapter provides an overview of out-of-band beamforming methods. The formulation of the autoproduct generates an acoustic field that can be expected to exhibit similar behavior to that of a conventional field at the corresponding difference or sum frequency. Signal band-

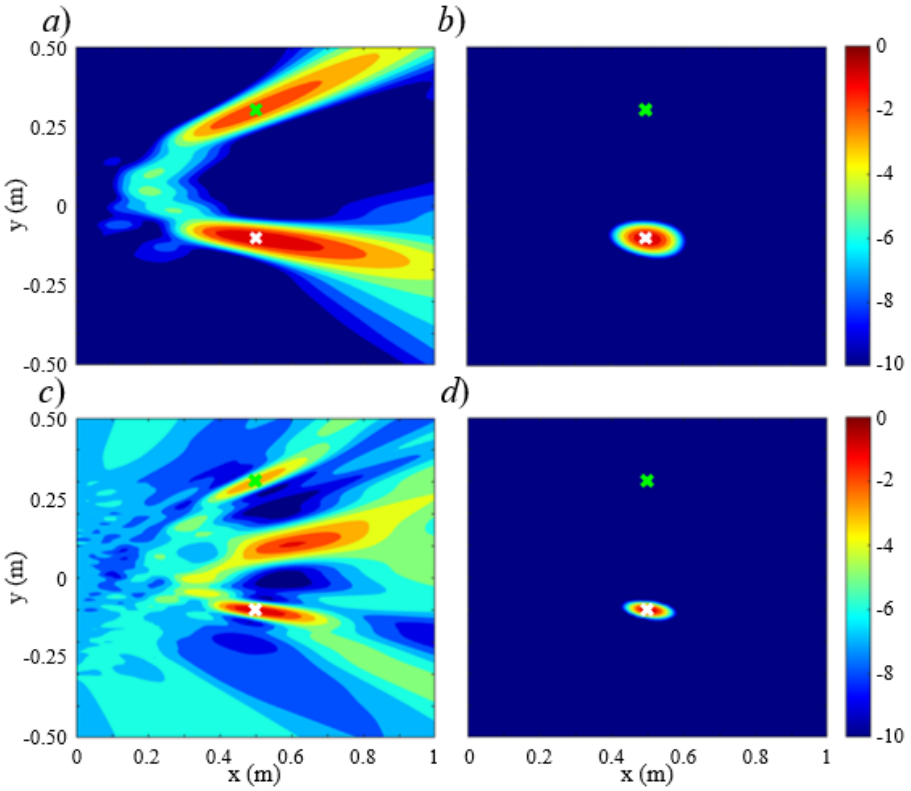

Figure 2.10: Conventional beamforming (a), coherent conventional beamforming (b), frequency-sum beamforming at Σf = 30 kHz (c), and coherent frequency-sum beamforming at Σf = 30 kHz (d) for a two-source case. One source is a known linear frequency sweep from 10 to 20 kHz, the other is an unknown noise source with an SNR = 0 dB. Each method utilizes the full 10 to 20 kHz of bandwidth available in the signal. The source of interest is indicated by a white 'x' and the noise source by a green 'x'.

width is required to generate an autoproduct, and the available bandwidth determines the possible frequency-difference autoproducts, while the absolute frequencies and bandwidth determine the possible frequency-sum autoproducts.

Frequency-difference beamforming provides a solution to the spatial aliasing problem faced with sparse array signal processing. By processing the signal as if it were at a lower frequency, undesired side lobes are suppressed and source localization is reliable, including in cases with experimental uncertainty and undesired scattering. Furthermore, frequency-difference beamforming provides the user with the flexibility to choose a difference frequency, within the constraints of the signal bandwidth, and to average difference frequencies for a more robust solution.

Frequency-sum beamforming improves the precision of a beamformer output based on the chosen sum frequency, processing the signal as if it were at a higher frequency. Again, the user has some flexibility over the choice of sum frequency, and sum frequency averaging can provide a more robust solution. The method increases precision without sacrificing accuracy and robustness for a single path environment. For multiple-source cases, frequency-sum beamforming generates undesirable center lobes. These lobes can be suppressed in active array signal processing scenarios where the source signal is known, providing the capability to perform coherent frequency-sum beamforming.

Both out-of-band methods discussed here provide the potential for improving on many of the common problems seen in conventional beamforming methods. The chapters that follow expand on these techniques and examine their performance in shallow water and in the presence of scatterers. Applications in underwater acoustic source localization (see chapters 4 and 5), communications (see chapter 6), medical ultrasound, and other potential areas of acoustics may benefit from implementation of these methods and thus understanding their capabilities and robustness is an important step in implementation.

Several conclusions can be made from the results shown above regarding out-of-band methods in a near free-space environment. (1) Frequency-difference beamforming can provide useful beamforming outputs in scenarios where conventional beamforming is unsuccessful because of sparsity

of the receiving array. Here, frequency-difference beamforming was found to be successful in a free-space environment with an array-element-spacing to signal-center-frequency-wavelength ratio of 5.7. (2) Frequency-sum beamforming can provide enhanced precision over conventional beamforming. Here, frequency-sum beamforming was tested in a free-space environment with a well designed array, showing a decrease in lobe size and increasing the accuracy of localization. However, when multiple sources are present, the basic implementation of frequency-sum beamforming yields additional, undesired peaks. (3) Both frequency-difference beamforming and frequency-sum beamforming with a single source behave similarly to conventional beamforming in a free-space environment when the in-band frequencies used with conventional methods match the out-of-band difference or sum frequencies.

CHAPTER 3

Out-of-Band Coherence Length

For signal processing techniques such as beamforming to be successful, particularly in complex environments like the shallow ocean, adequate coherence across the receiving array is a requirement. Coherence length describes the separation between two points in space over which a predetermined level of coherence is maintained. The concept of coherence length has been studied for a variety of environments and configurations for in-band fields, as well as its implications in many signal process techniques. In this chapter, the coherence length of the field measured across a roughly 8 km towed array in approximately 2 km deep water is considered, for both in-band fields, and for the autoproduct fields described in the previous chapter. Of interest is the comparison between in-band coherence and autoproduct coherence, rather than the absolute coherence, so several simplifications are made to the analysis where arguably environmental knowledge could be exploited to increase coherence. The goal of this chapter is to demonstrate that coherence is maintained, and potentially improved, in-band, and extends below- and above-band, when autoproducts are utilized, suggesting that their extension to beamforming and other general array signal processing techniques may be successful. The success will be determined by comparisons of coherence length to those measured or expected from a genuine field.

3.1 Background

3.1.1 Coherence

In general, for Q independent field samples recorded at locations $\vec{r}_m$ and $\vec{r}_n$, the complex coherence of the field at frequency ω between these locations can be estimated from a double-average (indicated by $\langle,\rangle$-brackets) over Q and the number of reference receivers, M, of a product of normalized field amplitudes:

$$\langle\gamma(\Delta\vec{r},\omega)\rangle = \frac{1}{MQ}\sum_{m=1}^{M}\sum_{q=1}^{Q}\frac{P_q(\vec{r}_m,\omega)P_q^*(\vec{r}_n,\omega)}{\left|P_q(\vec{r}_m,\omega)\right|\left|P_q(\vec{r}_n,\omega)\right|}, \tag{3.1}$$

where $\vec{r}_m$ is the location of the reference receiver, $\vec{r}_n$ is the receiver a distance of $\Delta r = |\vec{r}_n - \vec{r}_m|$ away from the reference, and $P_q(\vec{r}_j,\omega)$ is the q^{th} field sample from the receiver located at $\vec{r}_j$ [31]. For a Δr that yields a number of receiver pairs less than the number of chosen reference receivers, M should be reduced to the number of pairs available when calculating $\langle\gamma(\vec{r}_m,\Delta\vec{r},\omega)\rangle$. The normalization in Eq. 3.1 ensures that each coherence sample resides on the unit circle in the complex plane. Thus, the magnitude of $\langle\gamma(\vec{r}_m,\Delta\vec{r},\omega)\rangle$ falls below unity when the phase of $P_q(\vec{r}_m,\omega)P_q^*(\vec{r}_n,\omega)$ varies for $1 \leq q \leq Q$. In this investigation, equally spaced sample locations in the horizontal direction pointing away from a known-location source are of interest, so $R\hat{e}_r = jd\hat{e}_r$, where $j(\geq 0)$ is the sample location index relative to the reference receiver, d is the separation between neighboring receivers, $\hat{e}_r$ is the horizontal range unit vector, and $R = jd$ is the total horizontal separation between any two receiver locations. Thus,

$$\gamma(R,\omega) = \left|\langle\gamma(\Delta\vec{r},\omega)\rangle\right| \tag{3.2}$$

defines the coherence function for the ordinary acoustic field. The highest possible value of $\gamma(R,\omega)$ is unity (perfect coherence between field samples separated by R), while the minimum magnitude of $\gamma(R,\omega)$ is zero (complete lack of coherence between field samples separated by R). While the coherence length is a property of the propagating environment, the definition of coherence used

here will include the influence of noise, meaning at SNRs below 0 dB, the coherence length may result from noise measurements in the field, rather than the desired signal.

The coherence length is a measure of the distance over which a predetermined level of coherence is maintained, though the exact mathematical definition of coherence length varies between scientific areas, applications, and authors. For the present purposes, the coherence length is determined from the decay of $\gamma(R, \omega)$ with increasing receiver-separation distance R. The normalization in Eq. 3.1 requires $\gamma(0, \omega) = 1$, and $\gamma(R, \omega)$ typically decreases monotonically with increasing R. Thus, the coherence length, $L(\omega)$, may then be defined as the receiver separation where $\gamma(R, \omega)$ falls below a specified threshold. No strict rules exist for this threshold value, but e^{-1} (≈ 0.368) is a common choice and is used here as well, but with a slight modification intended to suppress statistical fluctuations. The coherence lengths reported in the following sections are determined from fitting a decaying exponential of the form $\exp([-R/(L(\omega))])$ to $\gamma(R, \omega)$ out to distances where $\gamma(R, \omega)$ first falls below e^{-2} (≈ 0.135). When the coherence did not fall below e^{-2} for any receiver separation, the decaying exponential was instead fit to all the available data. The exponential decay model for coherence was considered by Cox [42] to examine the effect of coherence on SNR gain of a line array and has been commonly used as a model for coherence decay in the literature [103] [29] [72] [49].

In prior work, coherence lengths have been determined from analysis, from simulated data, and from experimental measurements in a variety of acoustic environments and with a variety of signals. All such results consider only in-band signal frequencies. Interestingly, recent work [165] has shown that the frequency-difference and frequency-sum acoustic-field autoproducts constructed from non-zero-bandwidth field recordings may mimic genuine acoustic fields at (user selectable) frequencies below and above, respectively, the recorded signal's bandwidth, and that the autoproducts can be used to obtain unique results in acoustic remote sensing [46]. The frequency-difference autoproduct, $AP_{\Delta,q}$, and frequency-sum autoproduct, $AP_{\Sigma,q}$, from Eqs. 2.10 and 2.11, can be rewritten as follows, for the q^{th} acoustic recording at the j^{th} element of a receiving array through Fourier

transformation and multiplication, with or without complex conjugation of the second field-factor:

$$AP_{\Delta,q}(\vec{r}_j, \omega, \Delta\omega) = P_q(\vec{r}_j, \omega + \frac{\Delta\omega}{2})P_q^*(\vec{r}_j, \omega - \frac{\Delta\omega}{2}) \tag{3.3}$$

and

$$AP_{\Sigma,q}(\vec{r}_j, \omega, \Delta\omega) = P_q(\vec{r}_j, \omega + \frac{\Delta\omega}{2})P_q(\vec{r}_j, \omega - \frac{\Delta\omega}{2}), \tag{3.4}$$

respectively. Prior work has shown that $AP_{\Delta,q}$ and $AP_{\Sigma,q}$ may mimic genuine acoustic fields at the difference, $\Delta\omega$, and sum, $\Sigma\omega = 2\omega$, frequencies [165] [94].

The definition of the frequency-difference autoproduct's coherence follows directly from Eqs. 3.1 and 3.2 with $AP_{\Delta,q}(\vec{r}_j, \omega, \Delta\omega)$ replacing $P_q(\vec{r}_j, \omega)$ with an additional average over the possible in-band frequencies, ω_s ($1 \leq s \leq S$), consistent with the chosen $\Delta\omega$:

$$\gamma_\Delta(R, \Delta\omega) = \left| \frac{1}{MQS} \sum_{m=1}^{M} \sum_{q=1}^{Q} \sum_{s=1}^{S} \frac{AP_{\Delta,q}(\vec{r}_m, \omega_s, \Delta\omega)AP^*_{\Delta,q}(\vec{r}_n, \omega_s, \Delta\omega)}{\left|AP_{\Delta,q}(\vec{r}_m, \omega_s, \Delta\omega)\right| \left|AP^*_{\Delta,q}(\vec{r}_n, \omega_s, \Delta\omega)\right|} \right|, \tag{3.5}$$

where $\Omega_L \leq \omega_s \pm \Delta\omega/2 \leq \Omega_H$, and the low- and high-frequency limits of the signal bandwidth are Ω_L and Ω_H, respectively. The definition of the frequency-sum autoproduct coherence similarly follows from Eqs. 3.1 and 3.2 with $AP_{\Sigma,q}(\vec{r}_j, \omega, \Delta\omega)$ replacing $P_q(\vec{r}_j, \omega)$, but here the additional average is over all possible difference frequencies $\Delta\omega_s$ ($1 \leq s \leq S$) consistent with the chosen $\Sigma\omega = 2\omega$:

$$\gamma_\Sigma(R, \Sigma\omega) = \left| \frac{1}{MQS} \sum_{m=1}^{M} \sum_{q=1}^{Q} \sum_{s=1}^{S} \frac{AP_{\Sigma,q}(\vec{r}_m, \omega, \Delta\omega_s)AP^*_{\Sigma,q}(\vec{r}_n, \omega, \Delta\omega_s)}{\left|AP_{\Sigma,q}(\vec{r}_m, \omega, \Delta\omega_s)\right| \left|AP^*_{\Sigma,q}(\vec{r}_n, \omega, \Delta\omega_s)\right|} \right|, \tag{3.6}$$

where $\Omega_L \leq \omega \pm \Delta\omega_s/2 \leq \Omega_H$. The same caveat discussed earlier, that M should be reduced to the number of available pairs of $\vec{r}_m$ and $\vec{r}_n$ if that number is less than M, applies to Eqs. 3.5 and 3.6. Averaging through the signal bandwidth with a constant difference or sum frequency suppresses undesired multipath cross terms in the autoproducts [165] and leads to higher autoproduct coherence.

Coherence lengths, $L_\Delta(\omega)$ and $L_\Sigma(\omega)$, for AP_Δ and AP_Σ, respectively, were then determined

from the spatial decay of $\gamma_\Delta(R, \Delta\omega)$ and $\gamma_\Sigma(R, \Sigma\omega)$, respectively, using the same threshold and fitting strategy employed for the in-band field.

3.1.2 Beamforming

A field's coherence length has significant implications in array signal processing, and this is examined herein for the specific case of spherical-wave beamforming of the in-band field and its autoproducts. The beamforming formulation in Chapter 2 still applies here, but is reformulated here to incorporate subarray averaging. Here, spherical-wave beamforming is specified with a triple sum

$$B_q(\vec{r}, \omega) = \sum_{l=1}^{N_A} \sum_{\substack{m,n= \\ 1+(l-1)N_L}}^{lN_L} w_m^*(\vec{r}, \omega) K_{qmn}(\omega) w_n(\vec{r}, \omega), \tag{3.7}$$

where N_A is the number of independent sub-arrays having N_L elements, N_L is the number of array elements need to reach the coherence length of the field used to construct $K_{qmn}(\omega)$, the cross spectral density matrix for the q^{th} field sample,

$$K_{qmn}(\omega) = P_q(\vec{r}_m, \omega) P_q^*(\vec{r}_n, \omega), \tag{3.8}$$

and $w_n(\vec{r}, \omega)$ is the spherical-wave-beamforming weight vector define in 2.8. When plotted as a function of the search coordinate $\vec{r}$, B_q is typically normalized by its maximum value and presented as a decibel value: $10 \log_{10} \left\{ (B_q(\vec{r}, \omega)) / [B_q(\vec{r}, \omega)]_{max} \right\}$.

When beamforming with the autoproducts, Eqs. 3.7, 3.8, and 2.8 were again used, except $P_q(\vec{r}_j, \omega)$ was replaced by $AP_{\Delta,q}(\vec{r}_j, \omega, \Delta\omega)$ or $AP_{\Sigma,q}(\vec{r}_j, \omega, \Delta\omega)$ and the cross spectral density matrix was averaged through the available signal or difference frequency bandwidths:

$$K_{\Delta,qmn}(\Delta\omega) = \frac{1}{S} \sum_{s=1}^{S} AP_{\Delta,q}(\vec{r}_m, \omega_s, \Delta\omega) AP_{\Delta,q}^*(\vec{r}_n, \omega_s, \Delta\omega), \tag{3.9}$$

or

$$K_{\Sigma,qmn}(\Sigma\omega) = \frac{1}{S}\sum_{s=1}^{S} AP_{\Sigma,q}(\vec{r}_m, \omega, \Delta\omega_s) AP^*_{\Sigma,q}(\vec{r}_n, \omega, \Delta\omega_s), \tag{3.10}$$

and the weight vector was evaluated at the difference or sum frequency, as appropriate. The $1/|\vec{r}-\vec{r}_n|$ amplitude factor specified Eq. 2.8 could have been changed to $1/|\vec{r}-\vec{r}_n|^2$ when beamforming with the autoproducts to compensate for their quadratic nature, but this change was not made for simplicity.

3.2 COAST 2012 Experiment

The Cascadia Open Access Seismic Transects (COAST) experiment [75] was conducted off the coast of Washington state in July of 2012. The goal of this experiment was to collect two-dimensional seismic reflection profiles and other geophysical data. In this experiment, a research vessel towed an approximately 8-km-long array at 9 m depth containing a receiver array with N = 636 elements spaced d = 12.5 m apart. In the data considered here, the output of the receiver closest to the source exhibited behavior inconsistent with neighboring receivers (low amplitude and SNR), and is left out from the analysis, thus N = 635 for the purposes of this manuscript. Also attached to the streamer was an array of 36 airguns towed 240 m behind the ship at either 9 m or 15 m depth. This airgun array was used as a single directional acoustic source that preferentially broadcast a wide-band impulsive signal with frequency content from below 10 Hz to above 200 Hz toward the ocean floor. The ship towed the streamer at approximately 4.5 knots along 11 separate transects, during which the airgun array was fired approximately every 50 m while the receiving array recorded for 16.384 s with a 500 Hz sampling rate. The timing of the source broadcasts and receiving-array recording window provided ample time to record direct-path and multiple-reflected-path sounds at both the closest and furthest receiver in the deepest ocean locations. For the present study, no corrections for ship motion during the data recording interval were made in the data processing. In addition, a single source will be assumed in all of the work presented here, with no adjustments made for multiple arrivals.

Figure 3.1a) shows the layout of the experiment, with solid bold lines indicating each of the 11 transects. For the current study, data from the primarily shore-parallel transect number 10 was used since the depth variation along this track was the smallest of the eleven available and the number of usable signal samples was far greater than the other primarily shore-parallel transect, number 11. Figure 3.1b) shows the depth profile over the extent of transect 10, which was traversed from north to south. The average depth along this transect is slightly more than 1.9 km and varies by less than 300 m. To ensure that array curvature did not significantly influence the results, the first 200 and the last 60 airgun signal pulses along this track were not used in the analysis. This left Q = 701 signal pulses from the middle 70% of this transect for analysis. These data were collected on July 22, 2012 between 01:30:06 and 05:56:03. The dashed vertical lines in Fig. 3.1b) are 35 km apart and indicate the ship location for the first (10 km) and last (45 km) analyzed signal pulses.

The airgun array was designed so that acoustic energy was primarily focused towards the ocean floor. As a result, direct-path sound recorded by the array was significantly weaker than both the first and second bottom reflections over most of the array. Figure 3.2 shows a range-depth schematic of the experiment with the nominal horizontal and vertical dimensions. The bottom reflected (solid lines) and bottom-surface reflected (dashed lines) propagation paths to a single receiver are shown. These two paths convey most of the signal energy from the airgun array to the receivers. Thus, as the receiving array is towed along transect number 10, reductions in measured coherence arise from the varying bathymetry, ocean surface roughness, and other propagation fluctuations along these paths.

Figure 3.3a) shows a waterfall plot of the receiver array output for one signal pulse with a 1972 m depth at the airgun array taken at 05:16:36 (only every 10th recorded waveform is shown for clarity). Here receiver number 1 is closest to the airgun array and receiver number 635 is furthest from it. A weak direct path can be seen on the first few receivers closest to the airgun array within the first 100 to 200 ms. The strong signal arriving at the various receivers between 2.5 and 6.0 seconds is the first bottom reflection. A second bottom reflection is also visible in the recordings. Figure panels 3.3b) and 3.3c) show spectrograms recorded by receivers 1 and 635, respectively,

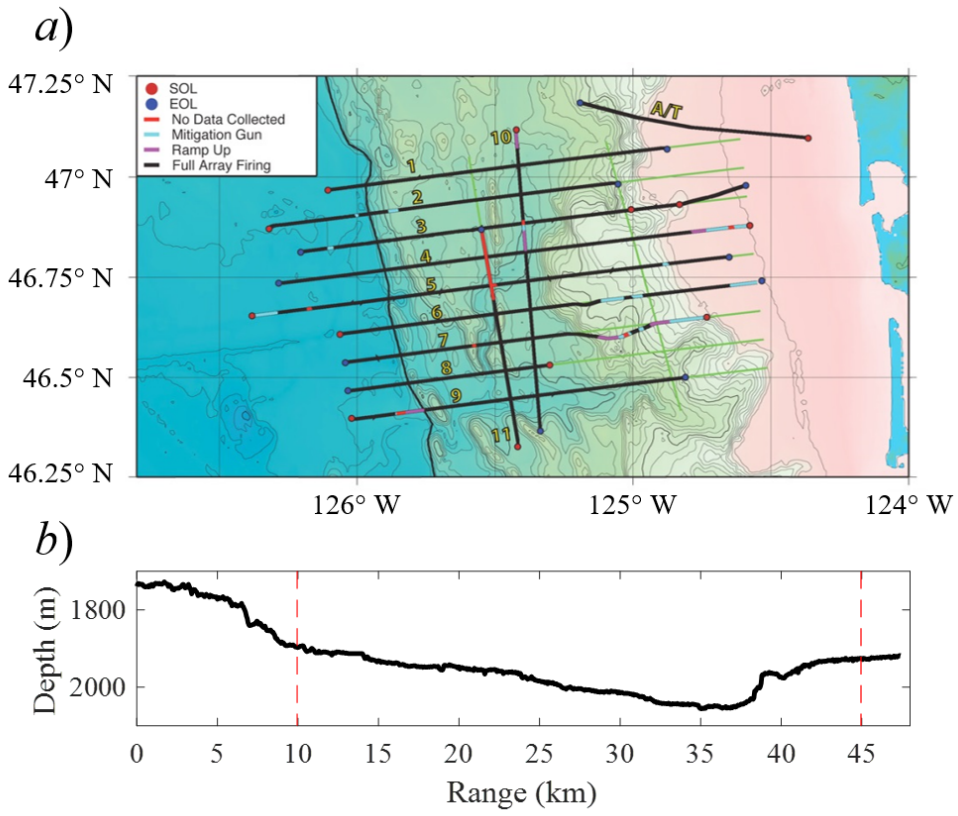

Figure 3.1: (a) Layout of the COAST experiment, conducted off the coast of Washington state in July, 2012. Each line represents the ship's path while towing a roughly 8 km streamer with 636 receivers spaced 12.5 m and a source array of 36 airguns. Data were collected by simultaneously firing the airgun array approximately every 50 m and recording for 16.384 s. (b) The bathymetry of line 10 is shown here with dashed vertical lines indicating the ship location for the first (10 km) and last (45 km) analyzed signal pulses.

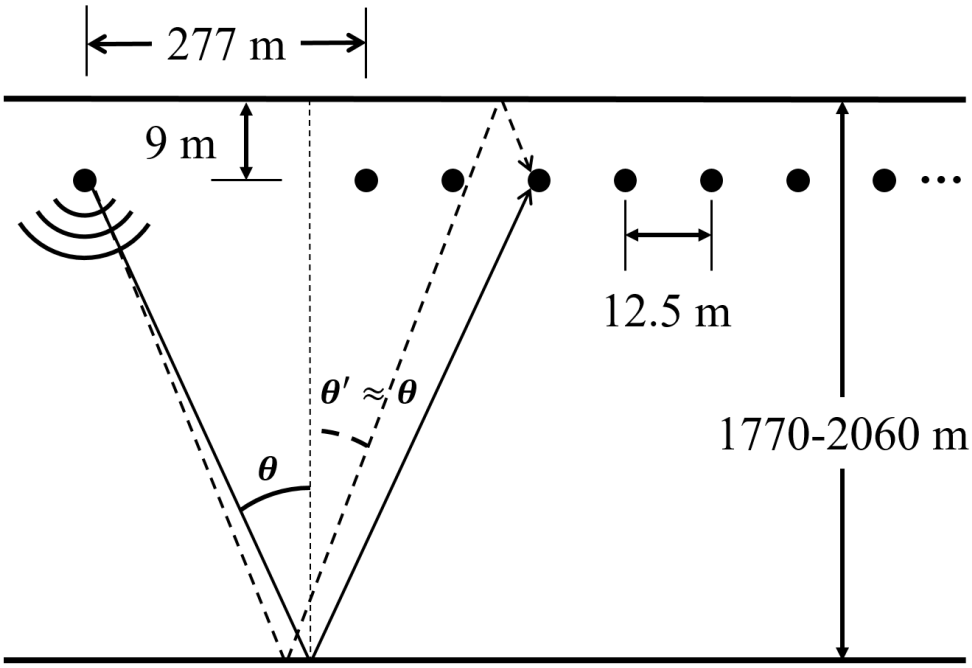

Figure 3.2: Experimental geometry showing the approximate experimental. The first bottom reflection (solid line) and bottom-top reflection (dashed line) account for most of the signal energy recorded by the array.

for the field sample shown in Fig. 3.3a). In the closest receiver's spectrogram, the direct path is visible (red vertical stripe) in the first 200 ms, followed by several bottom reflections with a time spacing of 2.5 to 3 seconds. In the farthest receiver's spectrogram, there is no indication of a direct path but two bottom reflections are clearly apparent and a possible third path is indicated as well. These spectrograms show that substantial signal energy exists across most of the available frequency range, with noise being more prominent in the lower frequency range. Plus, some dips in signal amplitude are apparent in Fig. 3.3b) around 80-90 and 150-170 Hz. Nevertheless, the airgun signal pulses provide a healthy signal-to-noise ratio (SNR) of roughly 20 and 50 dB through most of the recorded-signal's bandwidth. Spectrograms from other positions along the array are similar, and show the variations expected with increasing source-to-receiver range and variations in water column depth.

The dips in signal amplitude around 80-90 Hz and 150-170 Hz in Fig. 3.3b) are both predictable based on the experimental geometry and receiving array's depth below the ocean's re-

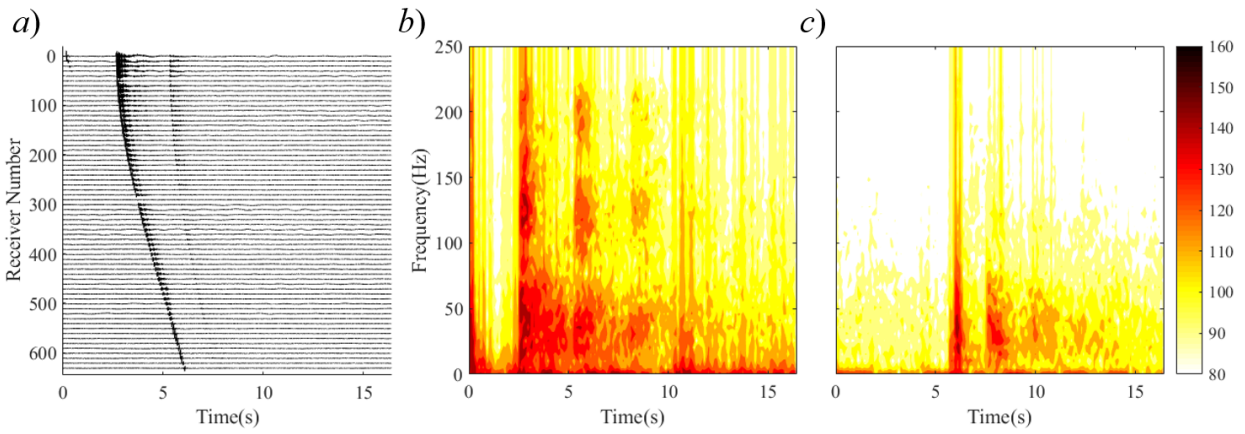

Figure 3.3: Waterfall plot showing the time-series output of every 10th receiver for the dataset recorded at 05:16:36 on July 22, 2012 (a). Spectrogram outputs for the closest (b) and furthest (c) receivers with 200 ms windows with 100 ms window overlap.

flecting surface. These are the frequency ranges where upward-propagating sea-floor reflected sound destructively interferes with downward-propagating sea-surface reflected sound, and this phenomenon causes some variation in SNR across the frequencies of interest for this experiment. This is demonstrated in a simulation shown in Fig. 3.4, with the source signal equal to unity for simplicity. Here, conventional fields for 43 Hz (a) and 86 Hz (c) resulting from a combination of a bottom reflected path and bottom-top reflected path are shown (direct path is ignored here), where the channel depth is 2 km, the source and receiver depths are 9 m, and the first receiver is 277 m from the source. The dark regions correspond to areas where the two paths constructively interfere, which corresponds well with the position of the closest receiver in the $f = 43$ Hz case, while the lighter regions correspond to areas where the two paths destructively interfere, which corresponds well with the position of the closest receiver in the $f = 86$ Hz case. When a 10-200 Hz signal is broadcast and a frequency-difference autoproduct field is constructed for $\Delta f = 43$ Hz (b) and $\Delta f = 86$ Hz (d), using the full bandwidth, these minimums and maximums switch positions. The pressure-release boundary must be maintained, which explains the odd behavior of the field near the surface, but moving a short distance from the surface, the field begins to behave as if this boundary were rigid. This explains the dips in signal amplitude seen in Fig. 3.3(b,c) for the

conventional field, and predicts where these should be expected in the autoproduct fields.

Figure 3.5 shows the measured SNR for receivers 1 (a) and 635 (b) array as a function of frequency. Here, the SNR is calculated for each receiver at each frequency, $\omega = 2\pi f$, as the average recorded signal variance divided by the average noise variance for the 701 the airgun pulses:

$$\mathrm{SNR}(\vec{r}_j, \omega) = 10 \log_{10} \left(\frac{\sum_{q=1}^{Q} \left| P_q(\vec{r}_j, \omega) \right|^2}{\sum_{q=1}^{Q} \left| N_q(\vec{r}_j, \omega) \right|^2} - 1 \right) \tag{3.11}$$

The '-1' within the logarithm ensures that $\mathrm{SNR}(\vec{r}_j, \omega)$ tends to the appropriate limit when the recorded complex field amplitudes, $P_q(\vec{r}_j, \omega)$, which contain signal and noise, become increasing dominated by noise. Additionally, each point on the curve in Fig. 3.5 is averaged over multiple points with a 1 Hz sliding window to increase smoothness. To evaluate Eq. 3.11, the complex field amplitudes, $P_q(\vec{r}_j, \omega)$, were determined from a 4 s time segment within each recording that started at the beginning of the first bottom reflection's arrival, while the noise-only amplitudes, $N_q(\vec{r}_j, \omega)$, were determined from a 4 s time segment within each recording that was least likely to contain any signal, typically either the recording's final or initial 4 s. The dips in SNR seen in Fig. 4, particularly for the closest receiver, occur at the frequencies expected to produce destructive interference between bottom-reflected upward-propagating sound and bottom-surface-reflected downward-propagating sound for the COAST 2012 experimental geometry, as shown in 3.4. A reduction in coherence length is expected at these SNR dips as well. In addition, the SNR drops below 0 dB for frequencies below roughly 5 Hz. Thus, at the lowest frequencies considered here, the ordinary field's coherence will be dominated by noise. A notable comparison between the first and last receiver SNRs is the prominence of the first major dip. For the further receiver, this SNR dip occurs at frequency that is approximately 15 Hz higher than that for the close receiver. This SNR-dip frequency variation arises from propagation angle variations in the experimental geometry that occur between the receivers 1 and 635.

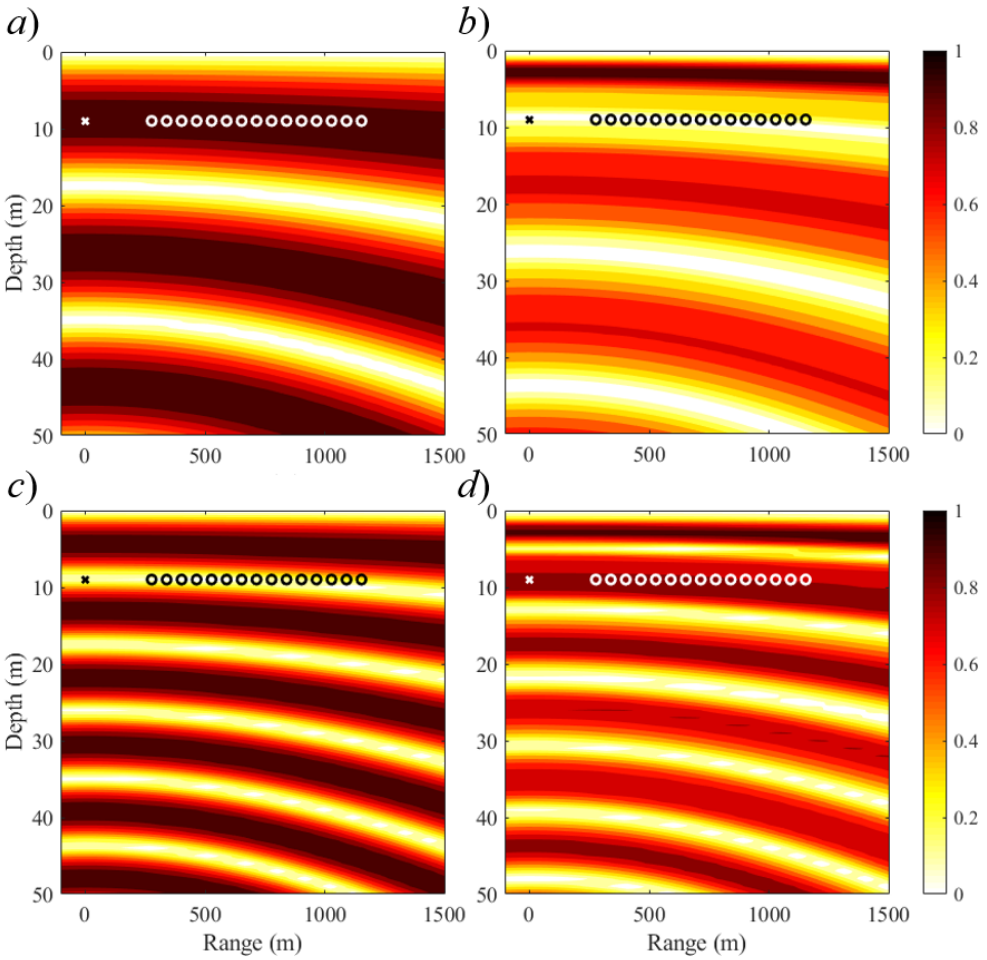

Figure 3.4: Simulated conventional fields (a,c) and autoproduct fields (b,d) for 43 Hz (a,b) and 86 Hz (c,d). Here, the propgation of a bottom reflection and a bottom-surface reflection are simulated at the given frequencies for a source and array located at 9 m depth ('x') in a 2 km deep channel. Notably, the maximums and minimums switch locations for the autoproduct fields, with the behavior close to the surface being an exception. This is expected to influence the outputs of the receivers (black circles).

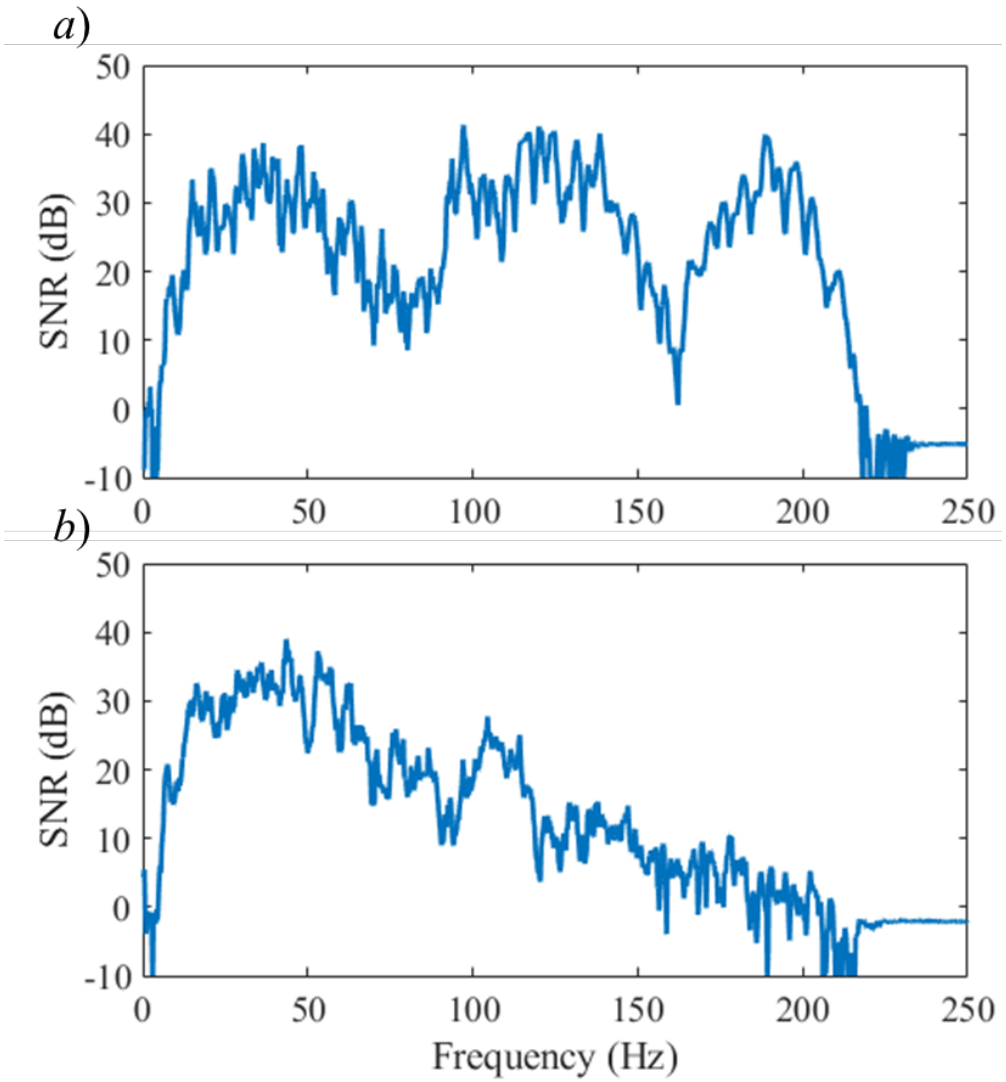

Figure 3.5: Signal-to-Noise Ratio (SNR) from Eq. (10) for the closest receiver (a) and the furthest receiver (b) for 701 signal pulses. The dips in SNR, particularly for the nearest receiver, occur at the frequencies predicted for destructive interference of upward- and downward-propagating sounds at the depth of the receiver array as shown in 3.4.

3.3 Coherence Length

As described in Section II, in-band, frequency-difference, and frequency-sum coherence lengths, $L(\omega)$, $L_\Delta(\Delta\omega)$, and $L_\Sigma(\Sigma\omega)$, were determined from fitting decaying exponential functions to the measured coherences, $\gamma(R,\omega)$, $\gamma_\Delta(R,\Delta\omega)$, and $\gamma_\Sigma(R,\Sigma\omega)$, respectively. In all cases, receivers 1-10 were used as the reference receivers. Additional reference receivers weren't included due to the experimental geometry - the angle of reflection from the ocean bottom varies significantly across the array, but the difference in the first 10 is small enough to maintain benefits from averaging, which reduces influence from other experimental artifacts, such as receiver malfunctions. The recording time for each signal pulse nominally provides 0.061 Hz frequency resolution; however, coherence lengths as functions of cyclic frequency (f) are reported here in 1 Hz increments by calculating these lengths for each resolved frequency and then averaging length results for all such frequencies that round to the same integer-Hz frequency value. For simplicity and consistency, the signal bandwidth limits were defined as $\Omega_L/2\pi = 10$ Hz and $\Omega_H/2\pi = 200$ Hz for all the results provided here. Plus, given that the results for each coherence length – $L(\omega)$, $L_\Delta(\Delta\omega)$, and $L_\Sigma(\Sigma\omega)$ – all come from exactly the same data and that comparisons between these lengths are the primary topic of this manuscript, no geometrical or environmental corrections based on the known experimental parameters were made to improve or alter any of the measured coherences. However, five receivers in the array (receivers 47, 53, 75, 188, and 287) consistently provided dramatic (anywhere from 30% to 80%) drops in coherence relative to neighboring receivers. This finding likely indicates malfunction of these receivers and is evident in their recorded time traces. Similar instances of receiver malfunction are mentioned in the field report [75]. Thus, recordings from these receivers were excluded from the analysis.

Figure 3.6 shows three coherence function samples and the associated exponential fitting results. The experimental airgun source-array provided sufficiently broadband data so that ordinary-field, frequency-difference, and frequency-sum coherences were all be computed from 40 to 100 Hz. In particular, Fig. 3.6a) shows results for γ at $f = 60$ Hz; Fig. 3.6b) shows results for γ_Δ at

Δf = 60 Hz; and Fig. 3.6c) shows results for γ_Σ at Σf = 60 Hz. Here, the horizontal axis is the scaled receiver spacing R/λ, where λ is the wavelength (24.75 m) computed from the frequency (60 Hz) and the reference sound speed for the COAST 2012 experiment (1485 m/s). Within each Fig. 3.6 panel, the jagged black curve is the measured coherence function, the smooth solid curve is the exponential fit of the measured coherence down to the point where it first falls to e^{-2}, and the dashed horizontal line marks the e^{-1} threshold. At this frequency of 60 Hz, the coherence lengths determined from the curve fitting are: L/λ = 7.7, L_Δ/λ = 9.9, and L_Σ/λ = 16.7; and both autoproduct coherence lengths are longer than that of the in-band field.

Interestingly, this finding of more extensive coherence available from the autoproducts is generally true across the entire frequency range of the experiment, and persists into the below-band range (1 Hz $\leq f \leq$ 10 Hz) possible with the frequency-difference autoproduct and into the above-band range (200 Hz $\leq f \leq$ 400 Hz) possible with the frequency-sum autoproduct. Notably, the frequency-sum autoproduct provides coherence results above the signal bandwidth and above the Nyquist frequency limit (250 Hz) dictated by the experimental sampling rate. Complete results for the three coherence lengths (divided by the nominal acoustic wavelength) are plotted vs. frequency in log-log coordinates in Fig. 3.7. Here, black crosses indicate $L(f)$; red diamonds indicate $L_\Delta(\Delta f)$, blue circles indicate $L_\Sigma(\Sigma\omega)$, and data points for experimentally-determined coherence lengths less than 0.1λ are plotted on the horizontal axis. In the in-band frequency range (10 to 200 Hz), both autoproduct coherence lengths generally exceed that of the in-band field and display more modest dips. When averaged through their respective frequency ranges (provided in parentheses), the frequency-difference autoproduct's coherence length is 12.4 wavelengths (1 Hz $\leq \Delta f \leq$ 100 Hz), the ordinary field's coherence length is 7.0 wavelengths (10 Hz $\leq f \leq$ 200 Hz), and the frequency-sum autoproduct's coherence length is 8.6 wavelengths (40 Hz $\leq \Sigma f \leq$ 400 Hz). In the below-band (1 Hz $\leq \Delta f \leq$ 10 Hz) and above-band (200 Hz $\leq \Sigma f \leq$ 400 Hz) frequency ranges, the autoproducts provide coherence lengths of approximately 6 to 20 wavelengths, despite the fact that apparently-incoherent noise provides the majority of the signal energy below 10 Hz, and many of the above-band frequencies are unreachable with conventional methods. Taken to-

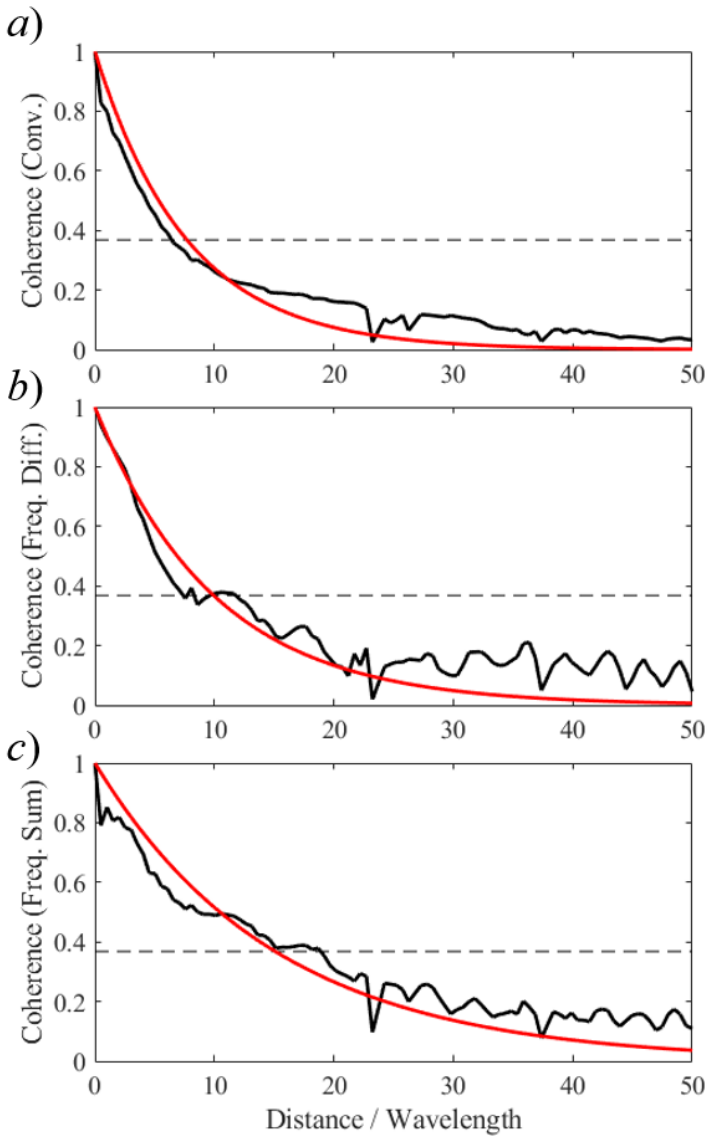

Figure 3.6: Coherence vs. distance (normalized by wavelength) for $f = 60$ Hz using a conventional field (a), $\Delta f = 60$ Hz with 10-200 Hz bandwidth using a frequency-difference field (b), and $\Sigma f = 60$ Hz with 10-50 Hz bandwidth using a frequency-sum field (c). The black curve is the coherence calculated using Eqs. 3.1 and 3.2 and the red curve is an exponential fit to the data. The coherence length is taken at the point where the red curve crosses the dashed horizontal line (corresponding to e^{-1}). The resulting coherence lenghts are $L/\lambda = 7.7$, $L_\Delta/\lambda = 9.9$, and $L_\Sigma/\lambda = 16.7$.

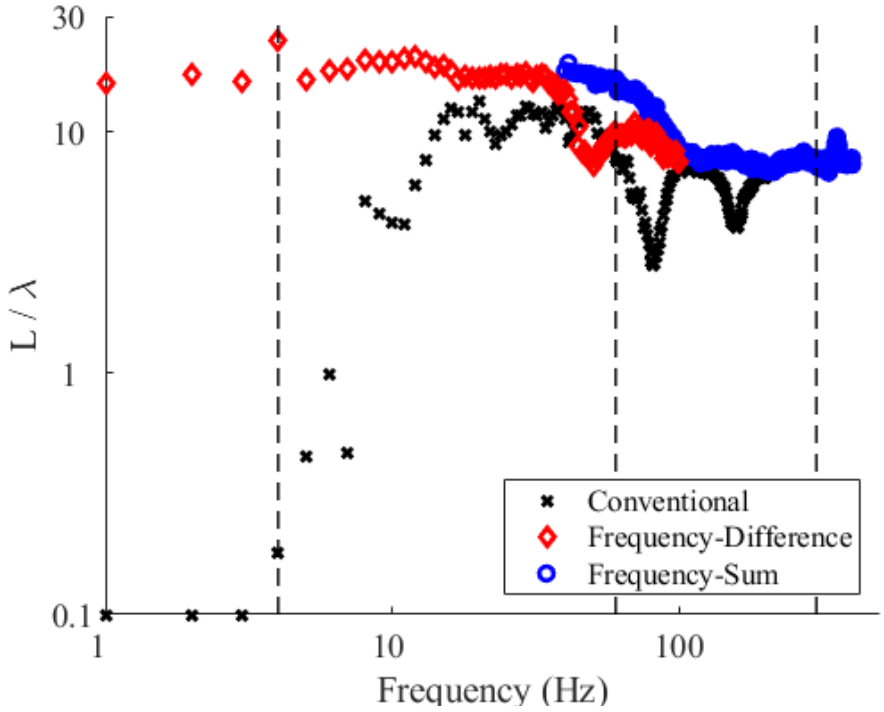

Figure 3.7: Coherence length vs. frequency (with logarithmic axes) for conventional fields (black crosses) from $f = 1$ to 200 Hz, frequency-difference fields (red diamonds) from $\Delta f = 1$ to 100 Hz, and frequency-sum fields (blue circles) from $\Sigma f = 40$ to 400 Hz. When averaged through their respective frequency ranges, the ordinary field's coherence length is 7.0 wavelengths, the frequency-difference autoproduct's coherence length is 12.4 wavelengths, and the frequency-sum autoproduct's coherence length is 8.6 wavelengths. The vertical dashed line indicates the 60 Hz frequency bin, to be used for beamforming in the next section.

gether, these results strongly suggest that the autoproducts might enhance coherent array signal processing when they can be calculated at in-band frequencies, and that they can extend coherent array signal processing to out-of-band frequencies. And, as a simple note, the accuracy of the frequency-difference coherence-length data at $\Delta f \leq 4$ Hz on Fig. 3.7 may be compromised by the finite length (8 km) of the COAST 2012 array, as these coherence lengths exceed 8 km.

As mentioned earlier, the coherence length dips seen in the various curves on Fig. 3.7 are caused by destructive interference of upward- and downward-traveling sound at the depth of the receiving array. However, the frequencies of these dips differ between the ordinary field and the autoproducts because the quadratic character of the autoproducts causes them to respond to the ocean surface's pressure release boundary as if it were a hard boundary, as shown in Fig. 3.4 (see

Worthmann and Dowling 2017). In addition, the depth of these coherence-length dips is lessened for the autoproducts because they benefit from the in-band- or difference-frequency averaging specified in Eqs. 3.5 and 3.6 that does not appear in 3.1 and 3.2.

3.4 Extension to Spherical-Wave Beamforming

Spherical-wave beamforming is a straightforward array signal processing method that is beneficially impacted by increased coherence length. Thus, it was chosen to illustrate the impact of the autoproducts' improved coherence on array signal processing. The results provided in the prior section suggest that the autoproducts typically provide longer coherence lengths than in-band fields while also providing worthwhile coherence at above- and below-band frequencies. Therefore, the autoproducts may also provide a way to improve signal processing outcomes at low-coherence and low-SNR frequencies within and outside the signal bandwidth. However, the COAST 2012 experiment was not designed as a beamforming or source-localization experiment; thus, some geometric adjustments to the standard implementation of spherical-wave beamforming are needed, and the shapes and character of the various lobes in the beamformed output are unusual. Nevertheless, the results presented here illustrate the benefits of the greater coherence possible with the autoproducts.

To properly implement spherical wave beamforming within the COAST 2012 experimental scenario, the element weight vector specified by Eq. 2.8 must be geometrically adjusted because of the dominance of the first bottom reflection and the endfire location of the source with respect to the nominally-straight and horizontal array. Thus, Eq. 2.8 was modified to:

$$w_j(\vec{r},\omega) = \frac{\exp\left(\frac{i\omega|\vec{r}-\vec{r}_j|}{c\sin(\theta_j)}\right)}{|\vec{r}-\vec{r}_j|/\sin(\theta_j)}, \tag{3.12}$$

where (as before) $\vec{r}$ is the search coordinate, $\vec{r}_j$ is the location of the j^{th} array element, c is the nominal speed of sound, and $\theta_j = \tan^{-1}(|\vec{r}-\vec{r}_j|/2D)$ is the incidence angle (from vertical) on the ocean floor for the first bottom reflection, D is the depth of the ocean, and ω may be the in-band,

difference, or sum frequency (in rad./s). The factors of $\sin\theta_j$ in Eq. 3.12 appear because $|\vec{r}-\vec{r}_j|$ is a purely horizontal distance while the dominant propagation path includes vertical travel to and from the ocean floor. Here, D is the ocean depth at the location of the tow vessel which may not be the ocean depth where the acoustic reflection occurs, so Eq. 3.12 introduces some mismatch. In light of this, correction of θ_j for the depth of the source and receiving array was neglected for simplicity. The impact of spherical-wave beamforming with the bottom reflection, as embodied by Eq. 3.12, is a relatively accurate range estimation of the end-fire source, but with increased angular ambiguity. This adjusted spherical-wave beamforming technique can also be considered a simple version of matched-field processing. For the three frequencies (4, 60, and 300 Hz) considered in this section, only a single representative airgun signal pulse (q = 750) was beamformed; the horizontal search plane is coincident with the source and array; and the receiving array is primarily extended in the north-south direction. This experiment was chosen because the ship location hasn't yet reached the comparatively-sharp depth change seen at around 39 km in Fig. 3.1b).

The first set of beamforming results are for the in-band frequency of 60 Hz, indicated by the vertical dashed line in Fig. 3.7. At this frequency, the ordinary field's coherence length is L = 191 m, the frequency-difference autoproduct's coherence length is L_Δ = 246 m, and the frequency-sum autoproduct's coherence length is L_Σ = 209 m. When using Eq. 3.2, these coherence lengths suggest the full COAST 2012 array (d = 12.5 m) should be broken into 18-element, 19-element, and 32-element subarrays for the ordinary, frequency-difference autoproduct, and frequency-sum autoproduct fields, respectively. An average of these coherence lengths is used to provide a more direct comparison between methods, resulting in 26 subarrays of 24 elements for each technique. Beamformed results at 60 Hz for the ordinary field are shown in Fig. 3.8a), for the frequency-difference autoproduct in Fig. 3.8b), and for the frequency-sum autoproduct in Fig. 3.8c). In both panels, the 'x' marks the known location of the source (the origin of coordinates), the 'o' marks the peak of the beamformed output, and the nearly-vertical black segment (many overlapping black circles) is the receiving array. Since all techniques yield long coherence length here, beamforming with all methods locate the source successfully; the 'x' and 'o' marks lie close to one another in

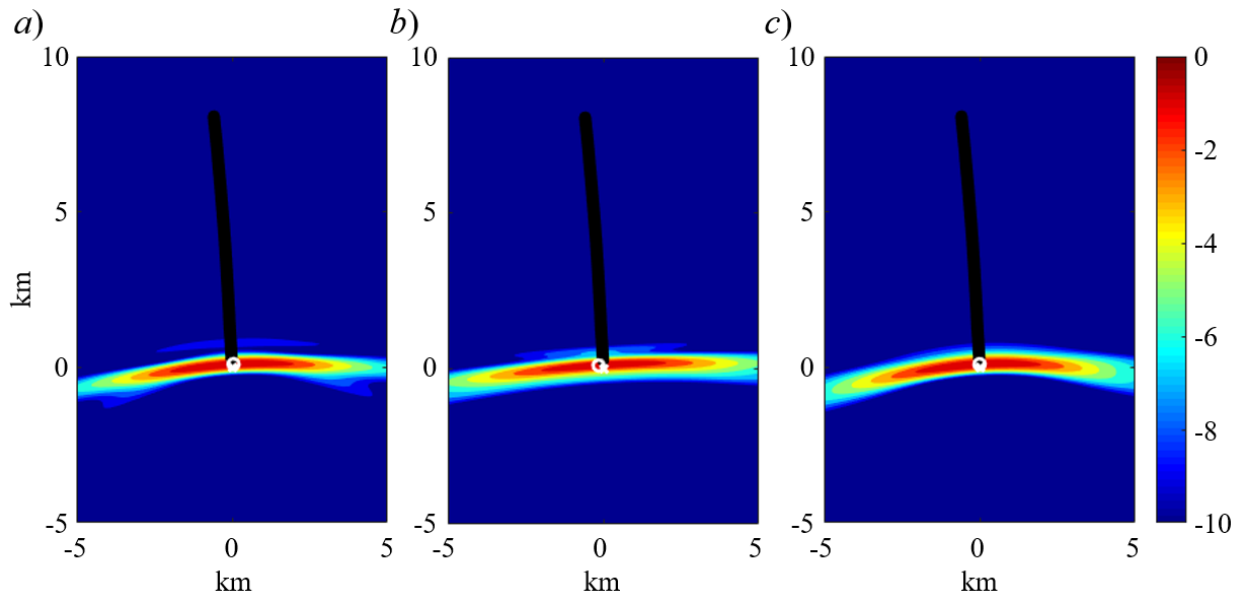

Figure 3.8: Beamformed outputs at 60 Hz in the horizontal plane containing the COAST 2012 source and array for the ordinary field (a), a frequency-difference field (b), and the frequency-sum field (c), each using 24-element subarrays (26 in total). The true source location is indicated by a white 'x' and the beamformed peak is indicated by an white circle. The array is the nearly vertical stripe of overlapping black circles (one for each element). The horizontal (east-west) and vertical (north-south) axes show distances in km from the true source location

each figure panel.

The second set of beamforming results are for the below-band frequency of 4 Hz. At this frequency, the ordinary field's coherence length, L = 61 m, is determined by noise, while the frequency-difference autoproduct's coherence length, L_Δ = 8.6 km, is determined using the full signal bandwidth. When using Eq. 3.7, these lengths cause the full COAST 2012 array (d = 12.5 m) to be broken into 105 subarrays of 6 elements for the ordinary field, and into 1 subarray of 635 elements for the frequency-difference autoproduct. Beamformed results at 4 Hz for the ordinary field are shown in Fig. 3.9a) with 6-element subarrays, Fig. 3.9b) with the full array, and for the frequency-difference autoproduct in Fig. 3.9c) with the full array. In both panels, the 'x' marks the known location of the source (the origin of coordinates), the 'o' marks the peak of the beamformed output, and the nearly-vertical black segment (many overlapping black circles) is the receiving array. As expected, beamforming the ordinary field measurements fails to localize the source,

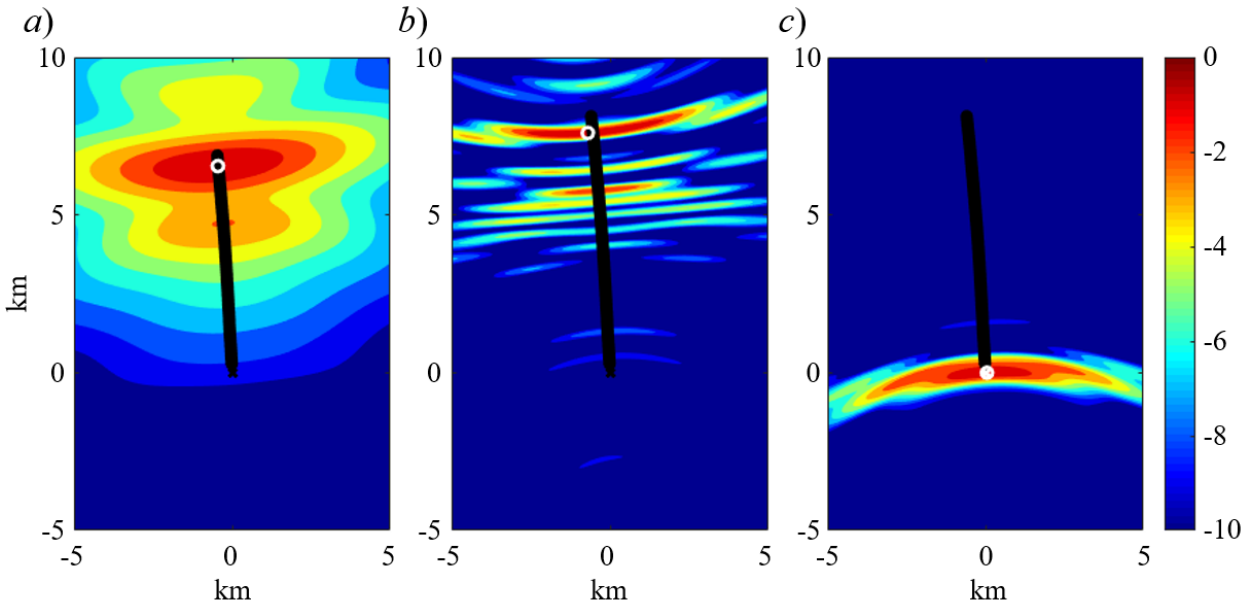

Figure 3.9: Beamformed outputs at 4 Hz in the horizontal plane containing the COAST 2012 source and array for the ordinary field with 6-element subarrays (105 in total) (a), with a single 635-element array (b), and the frequency-difference autoproduct for a single 635-element array (c). The true source location is indicated by a white 'x' and the beamformed peak is indicated by a white o. The array is the nearly vertical stripe of overlapping black circles (one for each element). The horizontal (east-west) and vertical (north-south) axes show distances in km from the true source location.

and instead places it near the trailing end of the array, roughly 7-8 km from its actual location. However, beamforming the frequency-difference autoproduct at the same frequency is successful; the 'x' and 'o' marks overlap in Fig. 3.9c). In addition, the side lobe structure in Fig. 3.9c) results from the multiple bottom reflections in the measurements.

The final beamforming results are for the above-band and Nyquist-exceeding frequency of 300 Hz. Thus, there are no comparable ordinary field results available for comparison. At this frequency, the frequency-sum autoproduct's coherence length is L_Σ = 35 m. Thus, when using Eq. 3.2, this length causes the full COAST 2012 array to be broken into 210 subarrays of 3 elements. Beamformed results at 300 Hz for the frequency-sum autoproduct are shown in Fig. 3.10 where again 'x' marks the known location of the source, 'o' marks the peak of the beamformed output, and the nearly-vertical black segment is the receiving array. Here, beamforming the frequency-

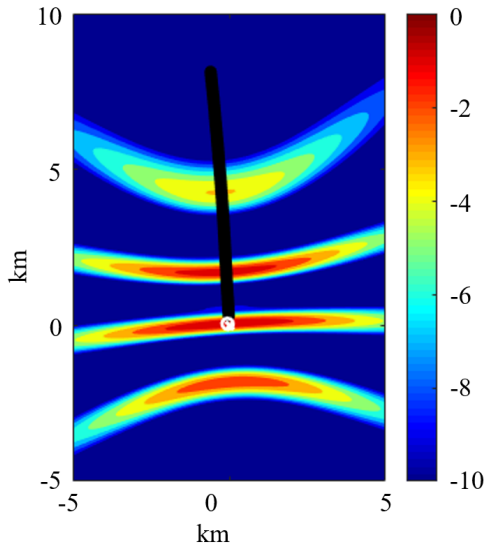

Figure 3.10: Same as Fig. 7, except here the beamformed output is for 300 Hz using the frequency sum autoproduct and 4-element subarrays (158 in total). The true source location is indicated by a white 'x' and the beamformed peak is indicated by a white o. The array is the nearly vertical stripe of overlapping black circles (one for each element). The horizontal (east-west) and vertical (north-south) axes show distances in km from the true source location. This localization result is accurate, but strong side lobes appear because of spatial aliasing of the recorded signal.

sum autoproduct provides a good localization result; 'x' and 'o' marks overlap. However, at this frequency the receiving array is sparse, $d/\lambda \approx 2.5$, so several strong side lobes appear because of spatial aliasing of the recorded signal.

3.5 Summary and Conclusions

Prior work has shown that autoproduct-based methods can be effective for correcting array-signal-processing problems associated with array sparseness, unknown random scattering, wavefront mismatch, and inadequate resolution. Given that such corrections are only possible for coherent fields, the goals of this investigation were to determine and compare the horizontal coherences of the acoustic field, its frequency-difference autoproduct, and its frequency-sum autoproduct from ocean recordings collected on a north-to-south transect during the COAST 2012 experiment. In particular, this investigation considered 701 airgun pulses recorded by 635 receivers uniformly spaced along an 8-km-long horizontal array towed at a depth of 9 m where the ocean depth was

approximately 2 km. Variations in water depth, surface reflections, and acoustic propagation along the 35-km-long tow path lead to coherence loss between the first and any subsequent receiver along the array. The nominal frequency range of the airgun signals was 10 Hz to 200 Hz. Nevertheless, coherence results were obtained for frequencies from 1 Hz to 400 Hz, including a substantial range (40 to 100 Hz) where all three types of coherence and coherence lengths could be determined. Spherical-wave beamforming results from recordings of a single airgun pulse successfully illustrate coherent array-signal processing at frequencies below and above the nominal signal band, and verify the utility of the autoproducts for such tasks based on their superior coherence lengths. The work presented here provides five key conclusions. First, the frequency-difference autoproduct can extend coherent array-signal processing capabilities to frequencies below the signal band, where the signal no longer exists and noise dominates the recorded field. In the current investigation, the frequency-difference autoproduct provided coherence lengths of 7.3 to 23.8 difference-frequency wavelengths, $c/\Delta f$, for 1 Hz $\leq \Delta f \leq$ 10 Hz. Second, the frequency-sum autoproduct can similarly extend signal processing to frequencies above the signal band and above the Nyquist frequency set by the sampling rate. In the current investigation, the frequency-sum autoproduct provided coherence lengths of 6.8 to 19.2 sum frequency wavelengths, $c/\Sigma f$, for 200 Hz $\leq \Sigma f \leq$ 400 Hz. Third, utilizing the full signal bandwidth for frequency- or difference-frequency averaging generally increases the coherence length of the autoproducts compared to that of the corresponding ordinary acoustic field from which they are derived. In this investigation, the frequency-averaged coherence lengths were 7.0, 12.4, and 8.6 wavelengths for the ordinary field, frequency-difference autoproduct, and frequency-sum autoproduct, respectively. However, destructive interference from surface reflections at the 9 m depth of the receiving array in the COAST 2012 experiment did reduce coherence length calculations for all three fields at predictable frequencies. Fourth, the autoproducts maintain their coherence at frequencies where the ordinary field suffers from destructive interference and reduced coherence length. This occurs because the quadratic nature of the autoproducts causes the ocean surface to appear as a rigid boundary, and this alters the autoproducts' interference pattern below the surface when compared to that of the ordinary field. And finally,

the improved coherence lengths provided by the autoproducts can support coherent array signal processing performance improvements at below-band, above-band, and potentially even in-band frequencies. Such performance improvements were illustrated with spherical-wave beamforming applied to a single representative signal pulse from COAST 2012 experiment.

CHAPTER 4

Frequency-Difference Beamforming in the Shallow Ocean

Shallow ocean environments often yield complex acoustic fields due to many factors, including non-smooth and non-ideal boundaries, range- and depth-dependent sound speed profiles, multipath propagation, low SNRs due to ocean noise and signal attenuation, etc. Each of these factors will generally reduce localization capabilities, unless the user has accurate knowledge of them, which is challenging and unlikely. In addition, capabilities can be limited by the receiving array geometry, if the array lacks the required aperture, spatial sampling, or certainty in the array element positions. The impacts of each of these characteristics depends on the signal frequencies. For higher frequencies, attenuation is stronger, scattering from objects or rough boundaries is more pronounced, array uncertainty becomes more significant as the errors become comparable to signal wavelength, and spatial aliasing will occur if the field is not sampled with enough spatial resolution. As the frequency drops, it is more robust to most of these characteristics, but will lose resolution and precision, which is improved with increased frequency or increased array aperture.

Chapter 2 demonstrated that frequency-difference beamforming can be successful in a nominally free-space environment in both simulations and experiments. In addition to successful localization, frequency-difference methods were shown to behave similarly to conventional methods, when the difference frequency, Δf, matched a comparable in-band frequency, f. In this chapter, frequency-difference beamforming is implemented in shallow ocean channels for both vertical and horizontal arrays. The frequency downshift is exploited to reduce the impacts of spatial aliasing

and geometric uncertainty in a multipath environment, both in simulations and experiments. No adjustments will be made for multipath propagation - a single source/arrival model will be used in all cases. The goal of the chapter is to demonstrate that frequency-difference beamforming is successful in the presence of multipath, experimental uncertainty, and sparse arrays in shallow ocean environments. This will be evaluated by considering the DOA outputs of frequency-difference beamforming vs. expected DOAs in both simulation and experiment.

4.1 KAM11 Experiment

The Kauai Acomms Multi-University Research Initiative (MURI) 2011 (KAM11) Experiment was an extensive study carried out off the coast of Hawaii for the purposes of obtaining data relevant to acoustical oceanography and underwater communications. The experiment is summarized in detail in Hodgkiss and Presig, 2012 [74], but a brief summary of the information relevant to this chapter's work is repeated here.

The KAM11 experiment took place from June 23rd to July 12th, 2011, and was conducted entirely in shallow water, ranging from depths of 80-200 m. Various sources and arrays were used between ranges of 1-8 km and covering frequencies between 3.5 and 35 kHz. The various positions of sources, receivers, and instrumentation are laid out in Fig. 4.1, borrowed from [74]. For the data considered in this chapter, which was collected on JD 183 and 184, the source at MPL-SRA1/SRA2 and the vertical array at MPL-VLA1 are of interest, both of which were deployed by the Marine Physical Laboratory (MPL) at the Scripps Institute of Oceanography. The source array used is an 8-element vertical array with 7.5 m spacing between each source, spanning 38 m to 90 m depth on JD 183, and 36 m to 88 m depth on JD 184. The receiver array was a 16-element vertical array with 3.75 m element spacing, spanning 41 m to 97 m depth, and placed 3 km from the source array. The average column depth over this range was approximately 106 m. The experimental data considered here consisted of a single broadcast from each source on each of the two days, yielding 16 total data sets. The broadcast signal was a 100 ms, 11.2-32.8 kHz Gaussian-enveloped linear

frequency sweep. The intent of this signal was to act as a probe signal for a BPSK communication sequence that followed, but the communication portion of the experiment will not be considered in this chapter (see Chapter 6).

For conventional beamforming methods, the array is not well designed for these signals. The ratio of the array element spacing to the signal wavelength is ideally 0.5 or less, but in this case it is between $d/\lambda = 27$ and 80, making for an extremely sparse array. As a result, conventional methods are expected to unsuccessfully beamform in this scenario.

4.2 Shallow-Water Simulations with Sparse Arrays

The focus of this section is to provide comparisons of conventional and frequency-difference plane-wave beamforming in a simulated ocean sound channel where refraction, reflection, and multipath propagation are prevalent. The simulations were conducted with the ray propagation code BELLHOP (available from HLS Research, Inc.). Here, the simulations were performed in a computational environment intended to mimic the experimental KAM11 environment.

4.2.1 Vertical Arrays

The first simulations are conducted based on the KAM11 geometry and signals. The source-array and channel geometry is shown in Fig. 4.2. Sound was broadcast in a downward refracting, 106 m deep sound channel from a single source placed at 8 different depths uniformly distributed between 38 and 90 m. In both the simulations and the experiments, a 100 ms linear frequency sweep from 11.2 to 32.8 kHz was broadcast by the source to a linear vertical receiving array 3 km away that had 16 elements spaced 3.75 m apart over approximately 41 to 97 m depth.

The simulation results allow direct comparisons of: (i) $\bar{B}_{conv}$ from Eq. 2.9 using the high-frequency signal (11.2 kHz $\leq f \leq$ 32.8 kHz), (ii) $\bar{B}_{conv}$ from Eq. 2.9 using an equivalent mid-frequency signal (1.12 kHz $\leq f \leq$ 3.28 kHz), and (iii) $\bar{B}_{\Delta}$ from Eq. 2.14 using the high-frequency signal with mid-frequency difference frequencies (1.7 kHz $\leq \Delta f \leq$ 2.3 kHz). Here, the mid-

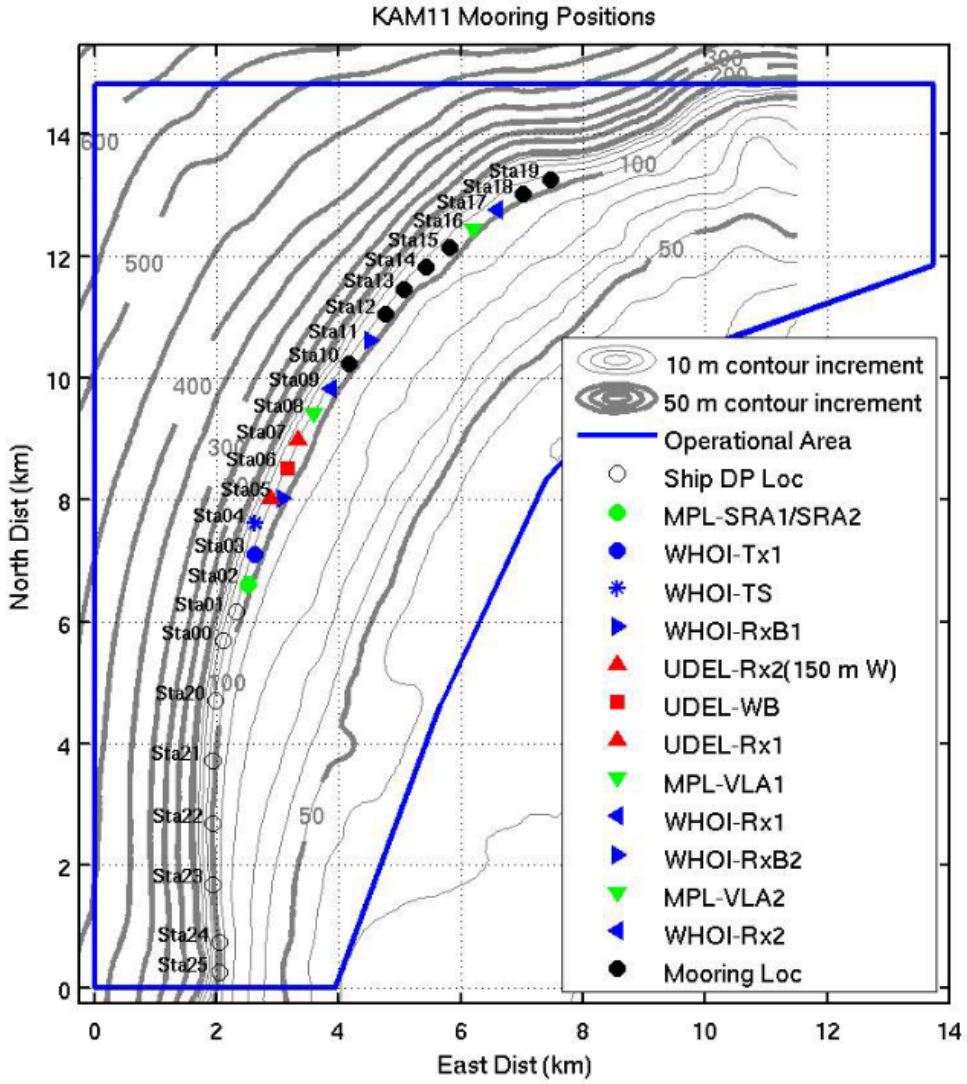

Figure 4.1: Deployment locations for various sources, receiver arrays, and other instrumentation in the KAM11 experiment. MPL-SRA1/SRA2 and MPL-VLA1 are relevant for the work presented here.

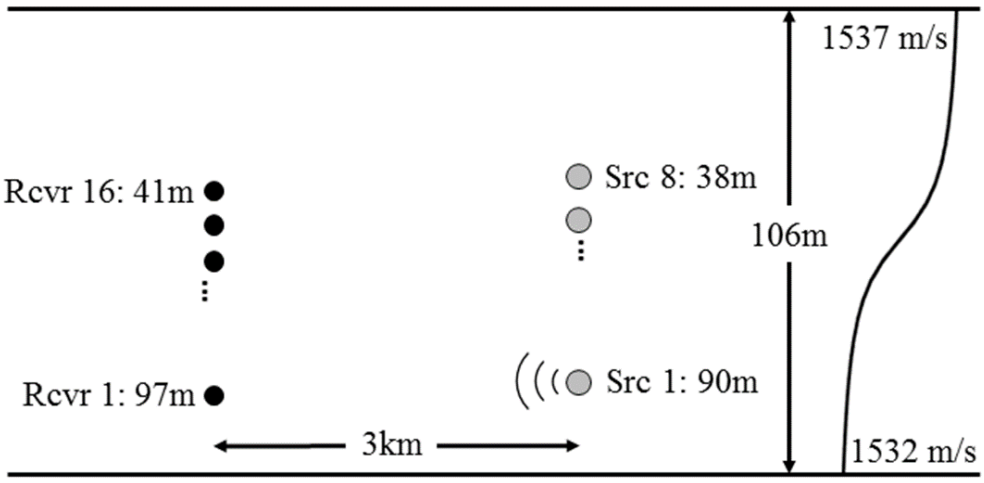

Figure 4.2: Sound channel geometry for shallow-water simulations based on the KAM11 experiment. The source signals used are linear frequency sweeps from 1.12 to 3.28 kHz and 11.2 to 32.8 kHz. Eight source depths, equally spaced between 38 and 90 m, were considered. The 16-element vertical receiver array is 3 km away and spans an approximate depth of 41 to 97 m with 3.75 m element spacing. The sound channel has a depth of 106 m and has a smooth downward-refracting sound speed profile fitted to data measured near the experiment location.

frequency signal was identical to the high-frequency signal except the frequencies were 1 decade lower, but it is only processed over a band equivalent to that used for frequency-difference beamforming (1.7 kHz $\leq f \leq$ 2.3 kHz). Unfortunately, mid-frequency signal recordings were not available from the KAM11 experiment, but these simulations provide a scenario in which wavefront arrival angles are known and environmental parameters can be varied in a controlled manner so that the accuracy, precision, and resolution of the three techniques [(i), (ii), and (iii) above] can be assessed.

For all simulations shown here, the sound channel was range-independent and the ocean's upper and lower surfaces were modeled as pressure-release and rigid, respectively. The sound speed profile was either a 1535 m/s isospeed profile, or a downward-refracting arctangent profile (see right side of Fig. 4.2) that was fit to sound speed measurements made near the KAM11 experiment site, yielding

$$c(z) = 1.923 \tan^{-1}(4.683 - 0.0893z) + 1534.15 \tag{4.1}$$

for depth z measured in meters. The source-to-receiver impulse responses were calculated using the outputs of the BELLHOP ray-tracing code based on the experimental geometry and the two sound speed profiles. BELLHOP outputs include the ray-path arrival amplitude, arrival time, number of bottom and top bounces, and arrival angle for each acoustic ray. These first three pieces of information are used to construct an impulse response as a sum of L impulses

$$h_j(t) = \sum_{l=1}^{L} a_{lj}\delta(t - t_{lj}) \quad \text{or} \quad H_j(\omega) = \sum_{l=1}^{L} a_{lj}e^{i\omega t_{lj}} \tag{4.2}$$

Here, a_{lj} is the arrival amplitude, including any phase shifts from top bounces, t_{lj} is the arrival time, and $\delta(t)$ is the Dirac delta function. This impulse response was convolved with the high- and mid-frequency signals to generate the receiver array outputs. Beamformed results from all eight source depths were then analyzed with and without refraction as a function of the number of wavefront arrivals (up to eight).

For frequency-difference beamforming, averages through a fixed bandwidth of difference frequencies were computed. The upper and lower difference frequency limits for this averaging were chosen to achieve 1/2-degree beam width at -6 dB and to avoid major side lobes in the angular range of interest. The -6 dB beam width is chosen so that coherent arrivals can be resolved when separated by 1° or more. For a linear array with N elements uniformly spaced a distance d apart, the angular half-width, $\theta_{1/2}$, of the array's main beam near broadside is approximately

$$\theta_{1/2} = \frac{1.9c}{\pi\Delta f(N-1)d}, \tag{4.3}$$

where sinc(1.9) $\approx$ 0.50. To achieve $\theta_{1/2} \approx 1/2°$ (0.0087 rad) with c = 1535 m/s, N = 16, and d = 3.75 m, a difference frequency of approximately 1.9 kHz is needed. Since a bandwidth will be utilized, this is dropped to 1.7 kHz, assuming the averaging with higher frequencies will yield a beam width closer to the average frequency's. The angles of interest from the KAM11 experiment are estimated from experimental matched filter impulse response plots, two samples of which are shown in 4.3 from JD 183, source number 4, and from JD 184, source number 1. This is done

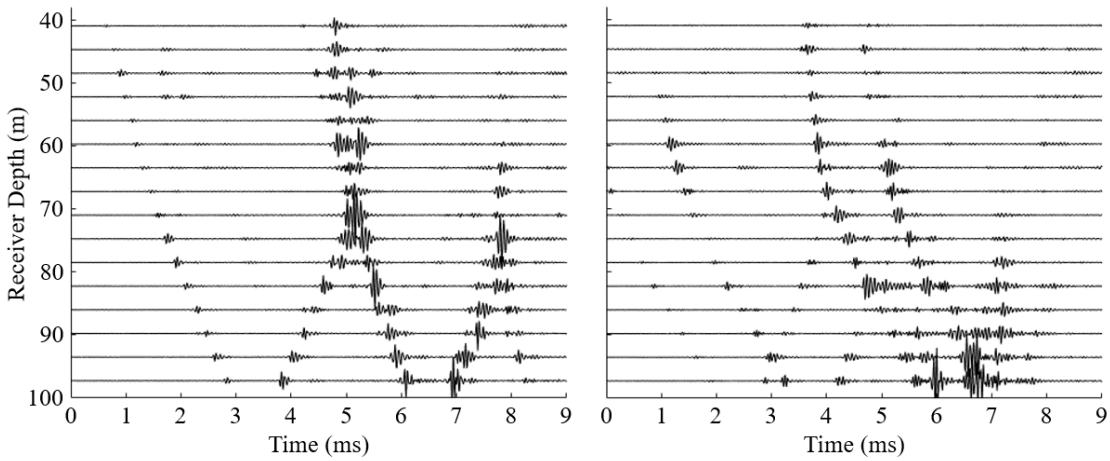

Figure 4.3: Impulse response plots generated using a matched filter with a modeled broadcast signal. The are produced using data broadcast from source number 4 on JD 183 (a), and source number 1 on JD 184 (b).

by roughly fitting a line through each visually identifiable path and calculating an angle of arrival based on the distance between receivers and time between arrival peaks on each receiver. These angles span approximately ±5° , so the upper limit for the frequency difference was chosen to prevent major side lobes from appearing within a 10° angular range. The angular location of the m^{th} major side lobe of a linear array, steered to broadside with element spacing d, is given by

$$\sin(\theta_m) = \frac{mc}{\Delta f d} \tag{4.4}$$

when the frequency is Δf [88]. Thus, setting $m = 1$ and $\theta_m = 10°$ produces a maximum frequency of approximately 2.3 kHz. Based on these calculations, a 600 Hz frequency-difference bandwidth centered on 2 kHz (1.7 kHz $\leq \Delta f \leq$ 2.3 kHz) with a 25 Hz difference frequency step between calculations was utilized when evaluating $\bar{B}_\Delta$ from Eq. 2.14. And, for direct comparison purposes, the mid-frequency conventional beamforming simulations of $\bar{B}_{conv}$ from Eq. 2.9 utilized exactly the same frequencies, even though the mid-frequency signal bandwidth was larger.

Wavefront arrival angles at each receiver were available directly from the BELLHOP output. The uncertainty of each wavefront arrival angle was determined from the slopes of lines fitted to the impulse-response peaks of the various arrivals to account for wavefront curvature. A sample

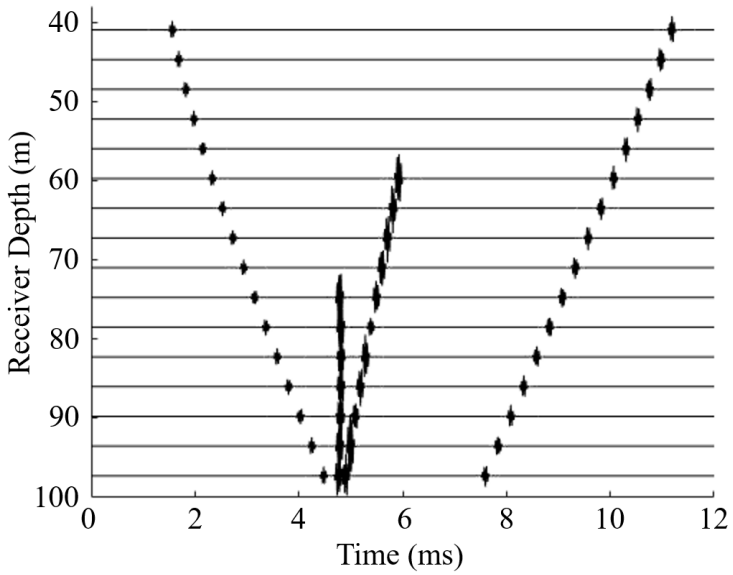

Figure 4.4: Waterfall plot of the simulated impulse response for 16 receivers for the downward-refracting sound speed profile shown in Fig. 4.2 using a 90 m source depth. The horizontal lines intersect the vertical axis at the depth of the corresponding receiver. The simulation parameters were chosen to only generate four wavefront arrivals for this case..

impulse response is shown in Fig. 4.4, constructed from BELLHOP outputs and Eq. 4.2 with four wavefront arrivals for a source depth of 90 m.

Figure 4.5 shows sample beamformed outputs for the simulation data leading to the channel impulse response (CIR) shown in Fig. 4.4 for three beamforming techniques: $\bar{B}_{conv}$ incoherently averaged over 11.2 kHz $\leq f \leq$ 32.8 kHz (dotted black line), $\bar{B}_{conv}$ incoherently averaged over 11.2kHz $\leq f \leq$ 32.8 kHz (dashed blue line), and $\bar{B}_{\Delta}$ computed from the high-frequency signal and incoherently averaged over 1.7 kHz $\leq f \leq$ 2.3 kHz (solid red line). The dashed vertical lines in Fig. 4.5 mark the locations of the expected arrival angles based on a weighted average of the BELLHOP arrival angle outputs for each receiver. The dynamic range of $\bar{B}_{\Delta}$ is reduced compared to $\bar{B}_{conv}$ because of the combined effects of the quadratic nonlinearity inherent in Eq. 2.10, multipath propagation, and incoherent averaging. However, Fig. 4.5 clearly shows that $\bar{B}_{\Delta}$ from the high-frequency signal and $\bar{B}_{conv}$ from the mid-frequency signal both successfully indicate the CIR wavefront arrival directions, while $\bar{B}_{conv}$ obtained from the high-frequency signal does not. The lack of performance of $\bar{B}_{conv}$ using the high-frequency signal shown in Fig. 4.5 was

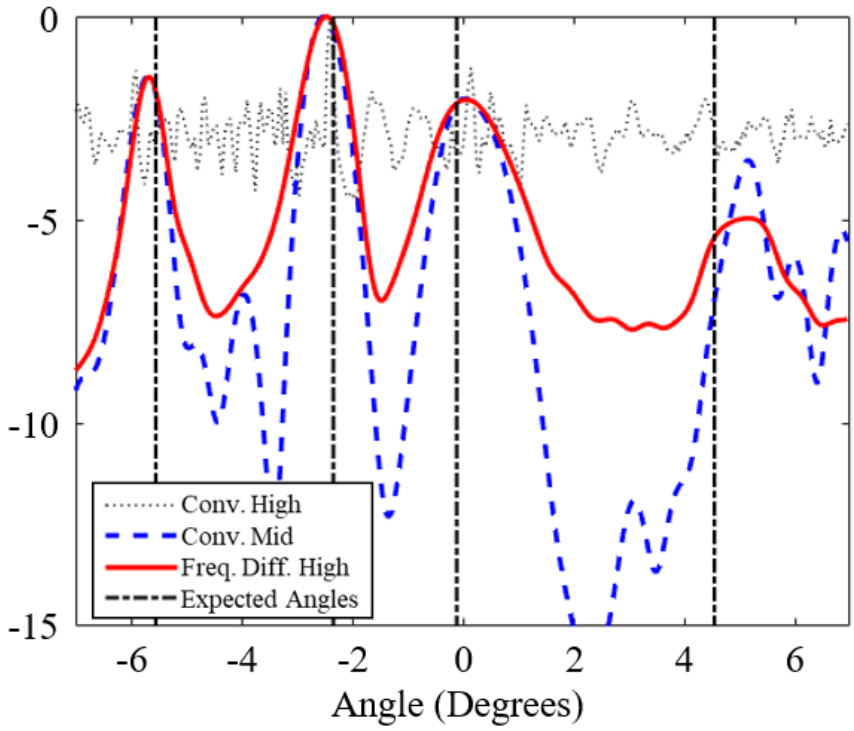

Figure 4.5: Beamforming output for the simulation data leading to the channel impulse response shown in Fig. 4.4. The vertical dashed lines correspond to the BELLHOP-determined arrival angles (5.55°, 2.34°, 0.11°, 4.55°). The frequency-difference result (solid red curve) is calculated using the 11.2 to 32.8 kHz signal. Conventional beamforming results (dotted black curve) from this signal and from the 1.12 to 3.28 kHz signal (dashed blue curve) are plotted for direct comparison.

pervasive in these simulations, so it was not considered further. Here, $\bar{B}_{conv}$'s lack of performance when using the high-frequency signal is readily anticipated because the KAM11 array's receivers are approximately 54 center-frequency (22 kHz) wavelengths apart, making it an extremely sparse array.

The results shown in Fig. 4.5 are typical for all source depths considered in this study when there are four wavefront arrivals. Here, the root-mean-square (RMS) difference between the CIR angles and the angles indicated by $\bar{B}_{conv}$ from the mid-frequency signal and by $\bar{B}_{\Delta}$ from the high-frequency signal are just a few tenths of a degree. The influence of the number of wavefront arrivals on these RMS angle differences across all source depths is shown for the KAM11 environment in Fig. 4.6(a) for a constant sound speed of 1535 m/s, and in Fig. 4.6(b) for the downward refracting sound speed profile shown in Fig. 4.2. In the constant sound speed case, the two beamformers

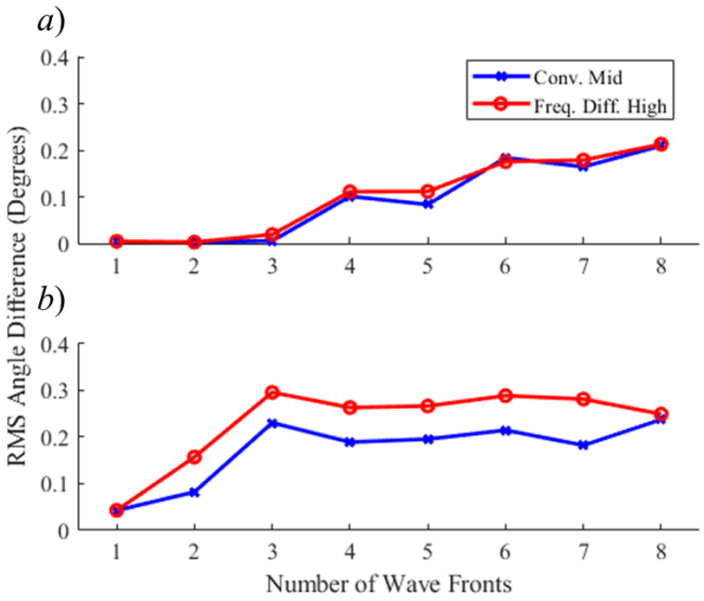

Figure 4.6: Comparison of RMS differences between BELLHOP-determined arrival angles and those determined from $\bar{B}_{\Delta}$ from the high frequency signal (circles) and $\bar{B}_{conv}$ from the mid-frequency signal (crosses) in the KAM11 environment with a constant sound speed profile (a), and with the downward refracting profile shown in Fig. 4.2(b). The results from both techniques are comparable with refraction and more wave fronts both typically leading to greater RMS angle differences.

behave almost identically with increasing RMS angle difference as wavefront arrivals are added. With a refracting sound speed profile, both techniques are less accurate with frequency-difference beamforming showing larger RMS angle differences in all cases except for 1 and 8 wavefront arrivals. Here, the loss of performance when refraction is present, compared to when it is not, can be traced to the greater prevalence of wavefront curvature and the more frequent occurrence of incomplete wave fronts that do not reach every array element.

Figure 4.7 provides a further comparison of the performance of $\bar{B}_{conv}$ from the mid-frequency signal and $\bar{B}_{\Delta}$ from the high-frequency signal. It shows the wavefront arrival angles determined from the two beamformers vs. the BELLHOP-determined angles for all eight source depths when refraction is present and four or five CIR wavefront arrivals were included. The diagonal lines in both panels of Fig. 4.7 have a slope of unity and pass through the origin. Here the uncertainty in the beamformed angles is taken to be 0.35° based on the beam width calculation provided above for a 3 dB below-the-peak specification. This beam width is chosen since this corresponds to

the level required for 1° resolution for two uncorrelated arrival (despite the arrivals most likely being correlated here). The uncertainty in the BELLHOP-determined angles was typically less than ° and was determined for each wavefront from the statistics of the linear fit to that wavefront to account for wavefront curvature [73]. The correspondence of the beamformer angles to the BELLHOP-determined angles is visually and statistically good in both cases. The reduced-χ^2 value, a statistical measure of goodness of fit [147], for the plotted data is 0.362 for Fig. 4.7(a) and is 0.609 for Fig. 4.7(b). In both cases the reduced-χ^2 value is less than unity, and this indicates that the deviations from a perfect match between beamformer angles and BELLHOP-determined angles are explained by the known uncertainties of the data. When taken together, the results in Figs. 4.5–4.7 indicate that the performance of $\bar{B}_\Delta$ using the high-frequency signal is superior to that of $\bar{B}_{conv}$ using the same signal, and that it is comparable to the performance of $\bar{B}_{conv}$ using the mid-frequency signal.

Table 4.1 provides a summary of the BELLHOP simulation results. In total, eight cases are shown, using constant and refracting sound speed profiles, conventional and frequency-difference beamforming of mid- and high-frequency signals, respectively, and varying numbers of wavefront arrivals. As expected, performance is reduced with an increase in the number of wavefront arrivals and with a more complex (refracting) sound speed profile. However, in all cases, the reduced-χ^2 value is well below unity, indicating robust beamforming performance in the simulated environments. The quadratic nature of the autoproduct leads to increased suppression of weaker arrivals in frequency-difference beamforming due to the squaring of the arrival amplitudes and an increase in undesirable cross-terms as the number of wavefront arrivals increases.

4.2.2 Horizontal Arrays

Many shallow-water applications utilize horizontal arrays rather than vertical, either for practical implementation (it is difficult to deploy and maintain a vertical array from a moving ship) or application. Often, a horizontal array is towed behind the ship that deployed it, meaning it is likely in motion while recording a signal. Due to factors such as ship maneuvering, surface conditions,

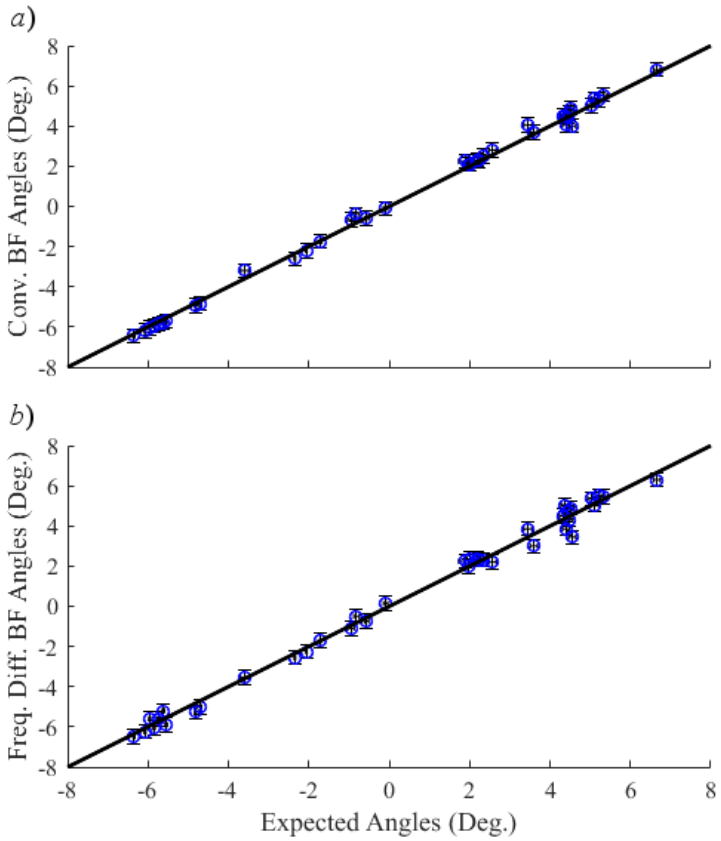

Figure 4.7: Comparison of BELLHOP-determined angles to conventional beamforming angles determined from the lower frequency signal (a) and to frequency-difference beamforming angles determined from the higher frequency signal (b). Both are for the downward-refracting sound speed profile shown in Fig. 4.2 with 4–5 wavefront arrivals for each of the 8 source depths. The diagonal lines have a slope of unity and the error bars correspond to the 68% confidence interval.

Table 4.1: Summary of results of conventional beamforming at the low frequency range and frequency-difference beamforming at the high frequency range. Two different sound speed profiles are used and each profile is examined with a small and large number of arrivals. The reduced chi-squared metric is calculated by comparing the error for each arrival angle with the uncertainty. Uncertainty is determined by the linear curve fits to the arrivals identified in the impulse response, to account for curvature, and the beam width of the frequency difference ranges. Weaker arrivals are sometimes missed and not included in the analysis, the number of missing arrivals for each case is listed in the final column.

Sound Speed Profile	# of Arrivals	Beamforming Method	Total # of Arrivals	RMSE(°)	Reduced χ^2	Missing Arrivals
Constant	4–5	Conventional	37	0.100	0.082	0
Constant	4–5	Freq. Diff.	37	0.100	0.084	0
Constant	7–8	Conventional	56	0.139	0.160	1
Constant	7–8	Freq. Diff.	56	0.153	0.194	1
Refracting	4–5	Conventional	37	0.215	0.362	1
Refracting	4–5	Freq. Diff.	33	0.277	0.609	5
Refracting	8–10	Conventional	61	0.234	0.433	6
Refracting	8–10	Freq. Diff.	56	0.241	0.466	11

and doppler effects, beamforming with towed horizontal arrays may prove challenging in some scenarios. In addition to these factors, ocean depth is no longer a limitation on the array length, so longer arrays are possible, which could lead to improved precision and resolution with increased aperture, but also can promote array designs that are sparse or incoherent.

Continuing from the previous section, simulations are completed using an environment based on the parameters measured during the KAM11 experiment. The geometry for these simulations is shown in Fig. 4.8. The same channel depth and downward refracting sound speed profile used previously is carried over. In addition, 3 km is once again used as a range, but it is measured along the horizontal line extending broadside from the array to the vertical plane passing through the source and parallel to the receiver array. The source is placed at 90 m depth and the receiving array at 50 m depth - neither of which are special, but are chosen because they yield a meaningful level of multipath propagation.

The simulations are run for four source-receiver configurations. For two of these, the receiver array is a 16 element, 5 m spaced linear array, and for the other two, the spacing is 50 m. For each array, the source is placed at both 5° and 55° relative to broadside. The goal of the four geometries is to consider the performance with varying levels of sparseness, and considering near-broadside

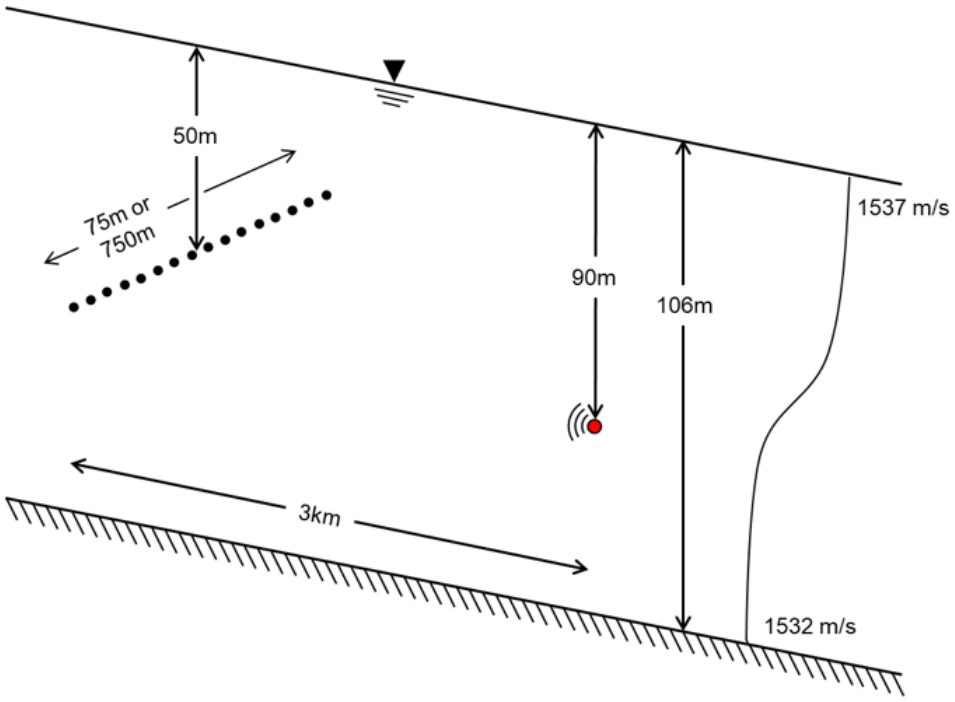

Figure 4.8: Layout for horizontal array simulations using the KAM11 water channel parameters. The source is place 3 km away (along a line extending from the array at broadside and parallel to both surfaces) in a 106 m deep channel with a downward refracting SSP. The array is at a 50 m depth and has 16 elements spaced either 5 m or 50 m apart. The source is placed to have a DOA of either 5° or 55°.

angles as well as more extreme arrival angles. The propagation is simulated once again using Bellhop, but Kraken (available from HLS Research, Inc.), a mode-based propagation code, is also utilized for the lower-frequency signals used for comparison. A 100 ms, 1-3 kHz linear frequency sweep is broadcast to each array and is analyzed using conventional beamforming (Eq. 2.9) and frequency-difference beamforming (Eq. 2.14) with Δf = 150 Hz for the 5 m spaced array, and Δf = 15 Hz for the 50 m spaced array. The signal center frequencies yield d/λ = 6.7 and 67.7 for in-band methods for the 5 m and 50 m spaced arrays, respectively, and $d/\Delta\lambda$ = 0.49 for both frequency-difference cases. In addition, genuine 15 Hz and 150 Hz signals are broadcast for use with conventional beamforming to compare directly to the out-of-band frequency-difference result. Because the wavelength at 15 Hz is comparable to the channel depth, a mode-based propagation model (Kraken) was required. The impulse response results from each of the four cases is shown in Fig. 4.9, 5 m spacing with 5° DOA (a), 5 m spacing with 55° DOA (b), 50 m spacing with 5° DOA (c), and 50 m spacing with 55° DOA (d). The variation in the spread in arrival times is clear between each scenario, and the number of arrivals increases significantly for the 55° DOA case.

Figure 4.10 shows a sample beamforming output from each of the four cases. Each plot displays the frequency-difference result (red), the in-band conventional result (dotted black), the conventional result with a frequency matching the difference frequency (blue), and an indication of the expected DOA (dashed black). Several notable observations can be made from these plots, the first is that the conventional in-band method clearly struggles as the sparseness increases. For the 5 m spaced cases, the conventional results are actually quite nice since the data is simulated and a large bandwidth is available to aid in sidelobe suppression, but in the 50 m spaced case, especially with a 55° DOA, the peak-to-sidelobe ratio drops to a point where any added uncertainty could significantly harm the method's success. A major takeaway of these plots is from the comparison between the frequency-difference conventional cases where the in-band frequency matched the out-of-band frequency used in frequency-difference beamforming. In each case, the peaks are closely aligned (and in the worst case, 5 m spacing and 55° DOA, both peaks have comparable error) and the grating lobes are in strong agreement. The frequency-difference method loses some dynamic range

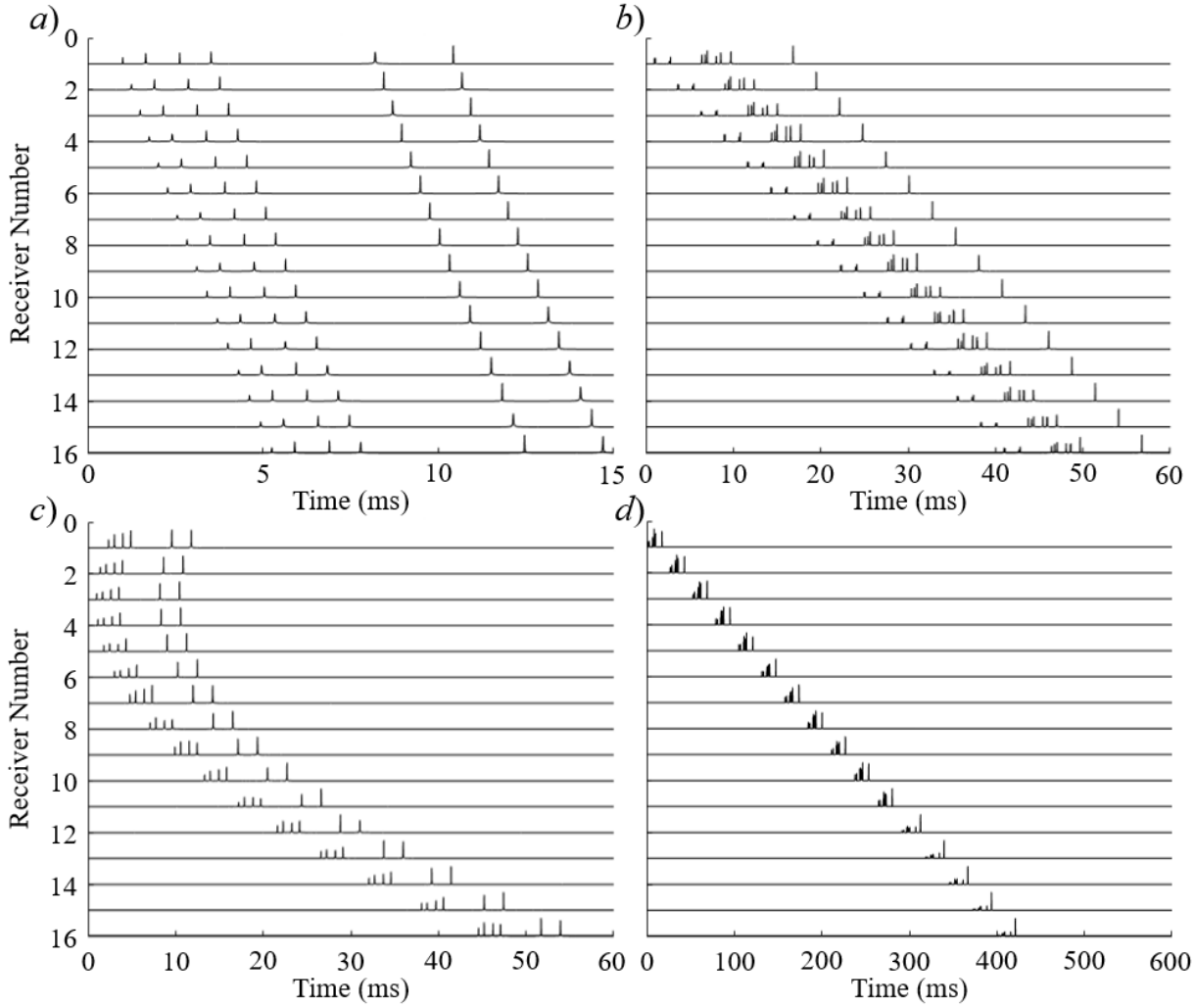

Figure 4.9: Sample impulse responses for each of the four scenarios, 5 m spacing with 5° DOA (a), 5 m spacing with 55° DOA (b), 50 m spacing with 5° DOA (c), and 50 m spacing with 55° DOA (d). Note that each plot has a difference scale on the x-axis.

in some cases, which is especially pronounced in the 50 m spaced examples, but still maintains significantly improved peak-to-sidelobe ratio compared with the conventional output on the high frequency signals.

4.2.2.1 Random Error

While these plots clearly demonstrate frequency-difference beamforming's capability to deal with sparseness, another important consideration is dealing with experimental uncertainty and variation. Such variation could be caused by imperfectly known receiver geometry and locations, variations to the sound channel over time, or the relative motion of the sources or receivers. In order to study this, uncertainty was added to the simulations by randomly varying the path lengths of each ray in the impulse response. Here, simulations were repeated in which every ray on each receiver was delayed by a random value from a Gaussian distribution centered on 0, with increasing standard deviation. For each standard deviation, 100 simulations were run and the peak DOA for each method recorded. Figure 4.11 shows scatter plots for the error in each peak from all trials (panels (a)-(d)) and for each of the four geometries (same order as above), with each point representing absolute DOA error. Clearly, the frequency-difference (red) method results in minimal error at the lower standard deviations, particularly when compared with conventional in-band (blue). Once a certain threshold is passed, frequency-difference's error starts to vary significantly more than conventional, but at this point both methods are already failing. To simplify the visualization, box plots are shown for each method as well, panels (e)-(h) show the corresponding frequency-difference plots, and (i)-(l) show the conventional in-band results. For the lower standard deviations, frequency-difference's errors are barely visible, while conventional methods yield errors of multiple degrees, with many outliers up to and beyond 20 degrees. In the worse case, 50 m spacing with 55° DOA, the median error is significantly higher and half of the points approach double digit errors before frequency-difference beamforming begins to fail. However, once frequency-difference starts to fail, the box plots make it appear as if the output here is seemingly random.

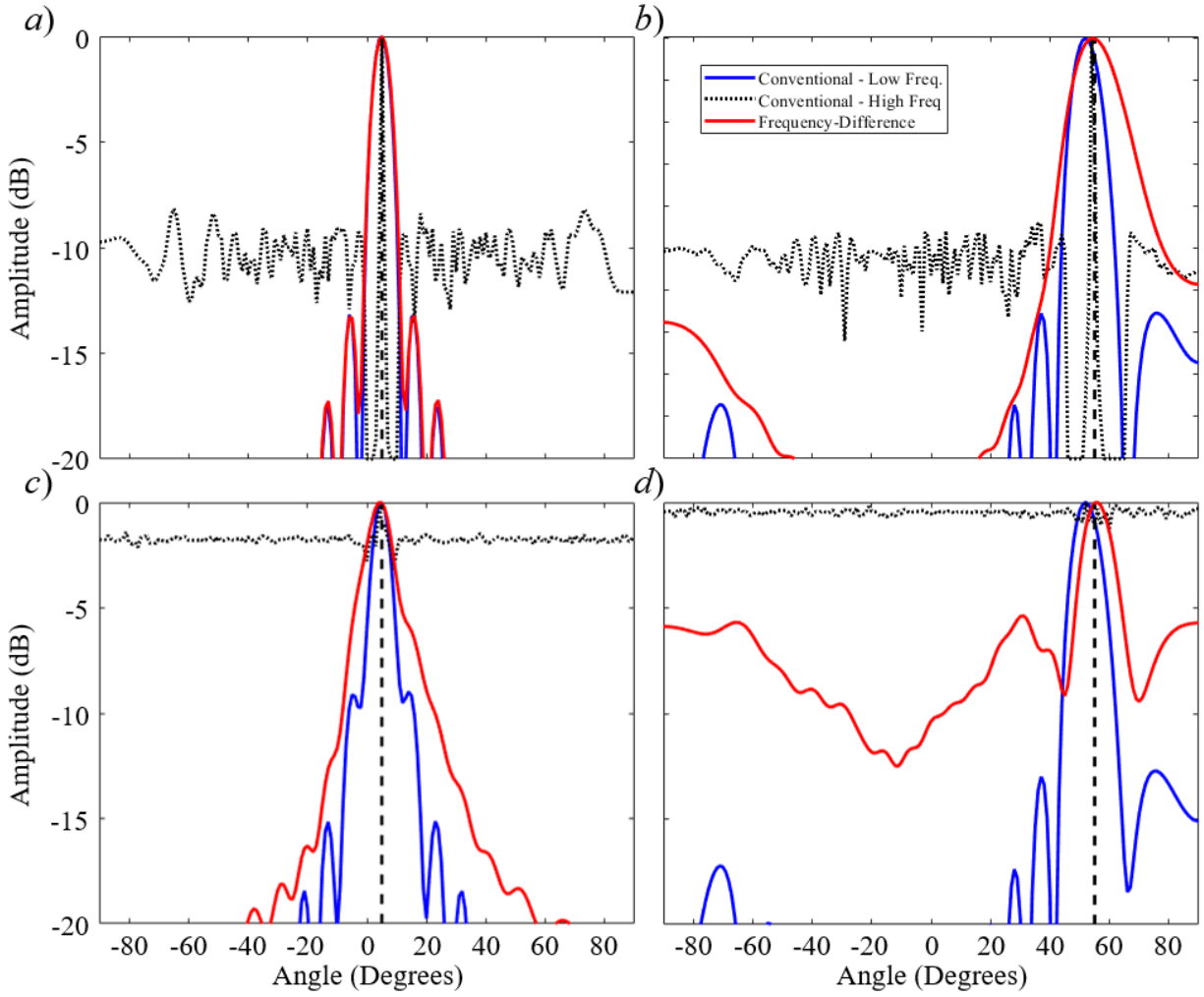

Figure 4.10: Sample beamforming outputs for conventional beamforming with the low frequency signals (blue), conventional beamforming with the high frequency signals (dotted black), and frequency-difference beamforming with the high frequency signals (red) with Δf matching the low frequencies. The vertical dashed line indicates expected arrival angles. The four cases shown are 5 m spacing with 5° DOA (a), 5 m spacing with 55° DOA (b), 50 m spacing with 5° DOA (c), and 50 m spacing with 55° DOA (d).

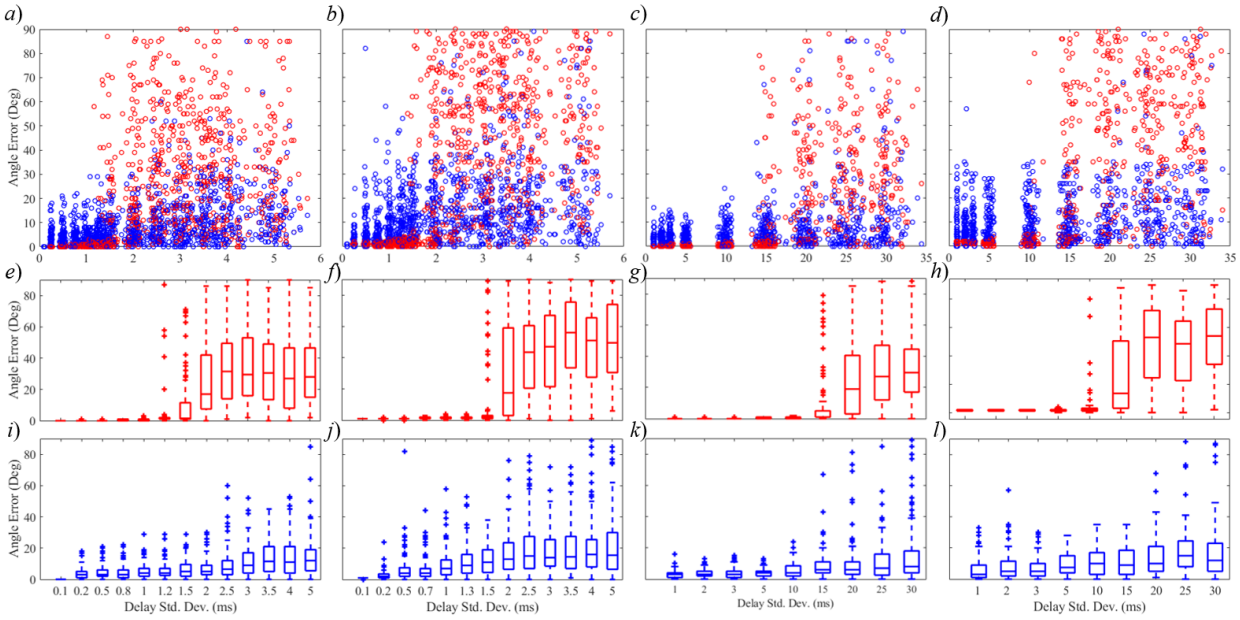

Figure 4.11: Scatter plots of DOA error for frequency-difference beamforming (red) and conventional beamforming (blue) vs. standard deviation of the imposed errors, both using the high frequency signals. Each standard deviation has 100 simulated trials with randomly generated, Gaussian-distributed errors. Each case is shown: 5 m spacing with 5° DOA (a, e, i), 5 m spacing with 55° DOA (b, f, j), 50 m spacing with 5° DOA (c, g, k), and 50 m spacing with 55° DOA (d, h, l). Below each plot are the corresponding box plots for both methods, for easier visualization of the data.

An interesting finding in examining these plots is that frequency-difference beamforming starts to fail at a threshold around when the dimensionless parameter $\Delta f \sigma$, the difference frequency wavenumber times the standard deviation of the error (expressed in units of distance), is equal to 0.40π. This result implies that the distributions of errors that have standard deviations of approximately one-fifth of a wavelength introduce too much uncertainty for the method to consistently determine the correct DOA, and is consistent with the results found in [67]. For a high-frequency signal like the 1-3 kHz signal used with conventional beamforming, one-fifth of the center frequency corresponds to less than 1 meter of uncertainty - a very feasible level of error in some applications, but difficult to avoid in others. Over 3 km, a 1 m fluctuation corresponds to a difference of about 0.5 m/s average sound speed, small depth variations relative to the 106 m deep channel, or moderate variation in receiver position, particularly in the array spaced 50 m, where 1 m is only a small fraction of the aperture. For the difference frequencies used here, one-fifth wavelength corresponds to 10.2 m and 100.2 m for Δf = 150 Hz and 15 Hz, respectively. Errors are much less likely to occur on this scale, especially for the given the geometry. A 10.2 m variation could potentially be introduced by water channel variation (particularly in depth), but variations of 100 m are unlikely in such a shallow channel with only 3 km propagation. In scenarios where information is known about array uncertainty and some basic water channel information is available, it is feasible that an intelligently predicted uncertainty could inform frequency-difference beamforming decisions.

4.2.2.2 Biased Error

In addition to random variations in path length, error in receiver locations during a turn may be of interest. Here, the error isn't random, as in the previous section, but rather is structured and biased. A simplification of a turning scenario is considered here, where the deformed array is assumed to follow an arc with a varying radius of curvature, but the array used for processing is assumed straight and is fit to the curved array. Figure 4.12 shows this fit, with the curved array shown in red, and the straight array geometry relative to the curved array shown in black. The

Figure 4.12: Curved horizontal array (red) and the assumed straight array (black) used for beamforming during a turn.

curved array is assumed to lie along a circular arc, and the straight array is the best fit line for this curved array.

The same four cases are considered once again, for increasing radius of curvature (and thus increasing error), and the DOA evaluated for conventional beamforming with the in-band signal, as well as frequency-difference beamforming with the in-band signal, using either Δf = 150 Hz (5 m spaced array) or Δf = 15 Hz (50 m spaced array). Figure 4.13 shows a sample output for the 5 m, 5° case with a radius of curvature to array aperture ratio of 2 (a), and for 50 m, 5° with a radius of curvature to array aperture ratio of 5 (b). In both cases, the dramatic difference in peak-to-sidelobe ratio between the two methods is clear, and despite conventional methods indicating a correct DOA, the robustness of the technique is compromised by the sidelobes and lack of dynamic range.

Figure 4.14 shows the DOA error and the peak-to-sidelobe ratio for each of the four cases, with the 5 m spaced cases (a,c) and 50 m spaced cases (b,d) plotted together, as a function of radius of curvature relative to array aperture. When the DOA error is large, the peak-to-sidelobe ratio is reported as 0 dB. The error in the two techniques is not dramatically different due to the data being simulated, particularly in the 5 m spaced case, but the peak-to-sidelobe ratio obtained by frequency-difference methods is dramatically larger than the conventional methods, suggesting any additional uncertainty would be challenging to deal with. Interestingly, as this geometry varies, some of the errors result from the frequency-difference beam splitting into two, indicating that the output is characteristic of two separate arrays more than a single array. Similar to the prior results, the $\Delta k * \sigma$ value at the point where frequency-difference beamforming begins to fail varies from

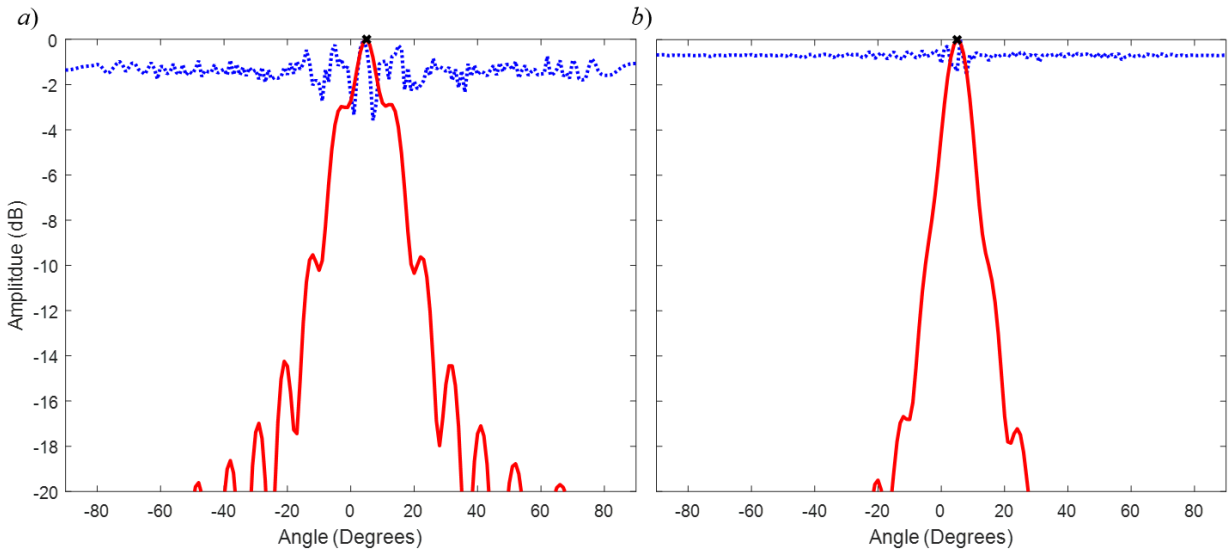

Figure 4.13: Beamformer outputs for the 5 m, 5° case with a radius of curvature to array aperture ratio of 2 (a), and for 50 m, 5° with a radius of curvature to array aperture ratio of 5 (b). Frequency-difference beamforming output is shown in red, and the conventional beamforming in blue.

about 0.25π to 0.45π, depending on the case. In some cases, the biased error leads to failure earlier than random error, without adjustments to account for the uncertainty.

4.3 Shallow-Water Experiments

4.3.1 Sparse Vertical Array

The simulation results presented in Sec. 4.2.1 suggest that frequency-difference beamforming may be successful with signal recordings collected during the KAM11 experiment. The KAM11 data considered here were collected from eight different source depths on two separate days, leading to 16 different data sets. The depths of the sources varied by 2 m between the days, with the first day corresponding to Fig. 4.2, while on the second day sources were 2 m shallower.

In order to evaluate the performance of frequency-difference beamforming, lower-band impulse responses were constructed for use with conventional beamforming methods. To do this, an in-band impulse response was determined using a matched filter with the known broadcast signal.

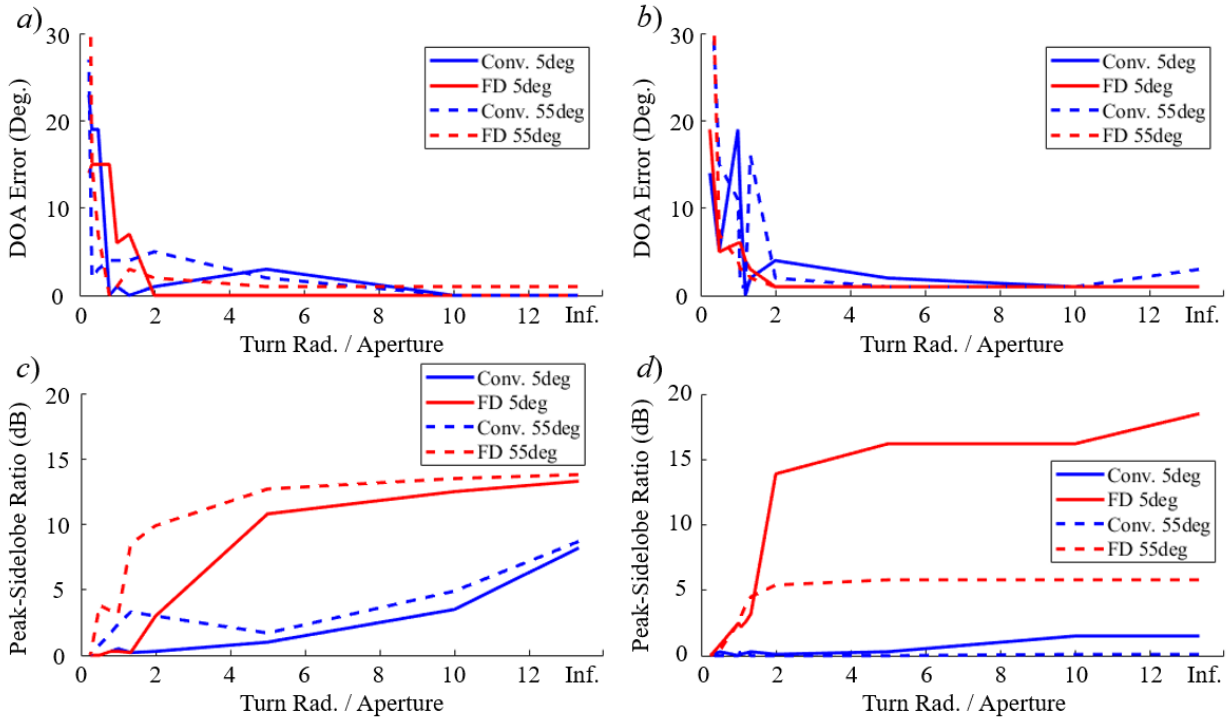

Figure 4.14: DOA error and peak-to-sidelobe ratio for conventional (blue) and frequency-difference (red) beamforming, for each of the four cases. The 5 m spaced cases (a,c) and 50 m spaced cases (b,d) are plotted together, and the array curvature increases towards the left of the plot. When the DOA is indicated by the incorrect peak, the peak-to-sidelobe ratio is plotted as 0 dB.

The envelope of this real impulse response was calculated using a Hilbert transform to find the corresponding complex impulse response and then the magnitude of the complex data. With this envelope function, all peaks above 10% the amplitude of the maximum peak in each impulse response were identified and the amplitudes and arrival times recorded. If this criteria yielded less than ten peaks, the strongest ten were kept regardless of amplitude. The amplitudes and arrival times of these paths were used with Eq. 4.2 to construct an impulse response at any user-chosen frequencies (provided the ray approximation is still valid) that yields the same wavefront arrivals as the actual experimental impulse response. Here, a 100 ms, 1.12–3.28 kHz frequency sweep is simulated and combined with this reconstructed impulse response to produce a synthetic mid-frequency signal for use with conventional beamforming.

Before completing this analysis, simulations are used to validate that this impulse-response reconstruction technique is valid. First, the process is performed on a simulated signal, with the expectation being that the original simulated data can be recovered with reasonable accuracy - Fig. 4.15 shows the process that does just this. First, data is simulated at the array using the KAM11 environment's parameters used previously with the high frequency (11.2-32.8 kHz linear frequency sweep) signal (a). A matched filter is used with this data to determine an impulse response and identify four arrival paths (b). A Hilbert transform is then used to generate an envelope function (c), which is smoothed for clarity, so that for each path, the arrival times and amplitudes at each receiver can be recorded. At this step, the absolute phase information is lost, which is not expected to impact the beamformed outputs significantly, but will prevent exact signal recovery, so for these purposes, that information is also saved. Next, the recorded information is used to generate an impulse response function (d), which visually appears to match the original impulse response function (b). Finally, the original source signal is convolved with this impulse response to recover the array data (e). To compare to the original data, the average, normalized cross correlation across the array is taken, using the data in (a) and (e). For this signal, the cross correlation result is 90.7%. It is easy to show that the discrepancy comes primarily from the resolution in time - when the sampling rate is not large relative to the signal frequency (here it is only slightly more than 4 times the center

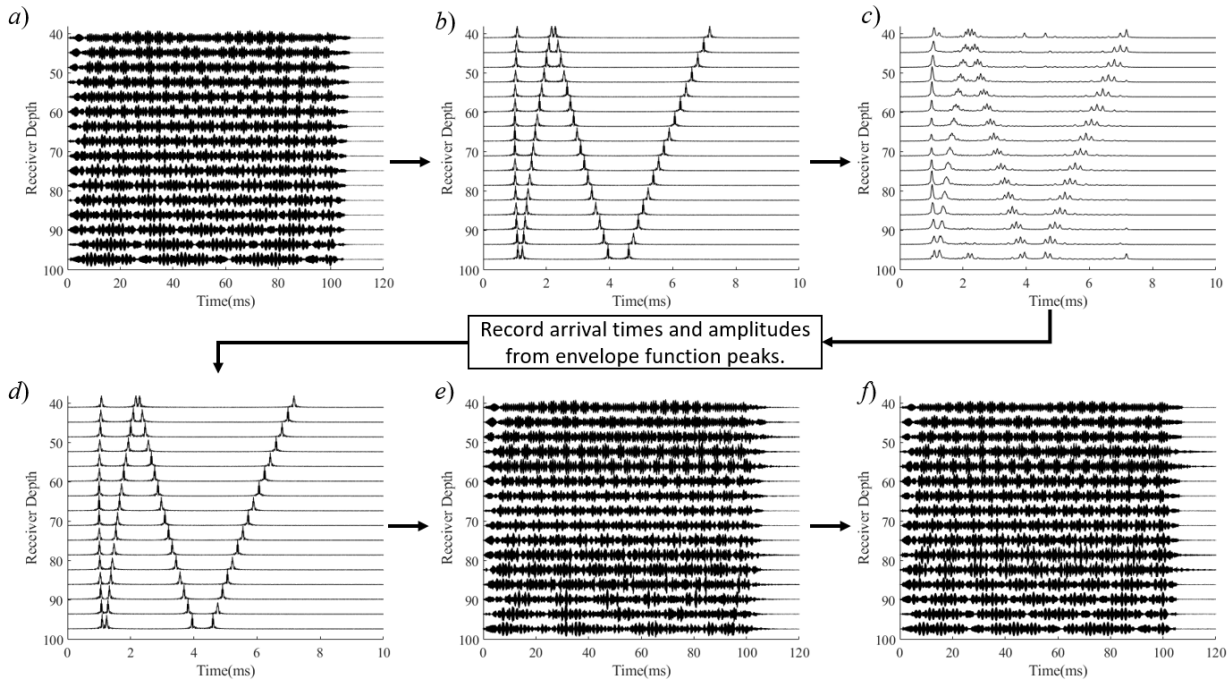

Figure 4.15: Process for calculating a general impulse response from a matched filter output. Array data (a) is turned into an impulse response using a matched filter (b). A Hilbert transform is used to turn the impulse response function into an envelope function (c) and the arrival times and amplitudes recorded. The recorded information is used to generate new impulse response (d), which is convolved with the original signal to recover the array data (e). The result for a sampling frequency 5 times higher than the original is also shown (f). Here, the original phase information is saved for the purposes of returning to the original array data.

frequency), the phase error can actually be quite high when choosing the peak. If the same analysis is completed using a lower frequency, 1.12-3.28 kHz signal, the cross correlation result is 99.3% - nearly a perfect match. If the analysis is repeated with a sampling rate that is 5 times higher, the resulting cross correlations for the high and low frequencies are 96.3% and 99.8%, respectively. The time domain output for this case at the high frequency is shown in (f). This suggests that using the Hilbert transform to generate an envelope function is a valid technique for determining arrival times and amplitudes for a given path, though it may be sensitive for scenarios where the sampling rate is not large relative to the signal frequency (here it is 48 times larger than the center frequency of the low frequency bandwidth of interest).

The loss of absolute phase is an important factor that is not accounted for using the KAM11

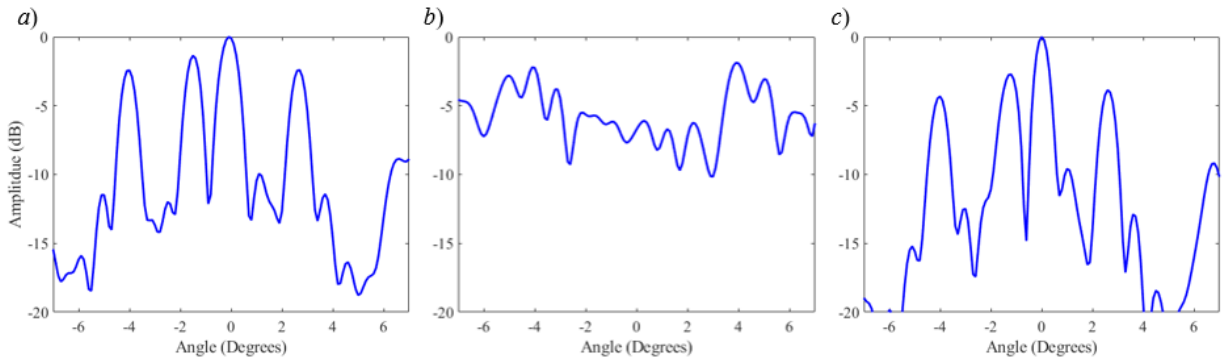

Figure 4.16: Beamformed output for 1.7-2.3 kHz using the impulse response from Fig. 4.15(b). The original beamformed output (a) is corrupted if random phases are applied to each of the impulse response peaks (b), but in phases are applied uniformly across each arrival path, the DOA results are maintained, with only small differences between the two outputs (c).

data. However, for the purposes of beamforming, a change in phase across an arrival path should not impact that arrival's beamformed output, provided that phase shift is constant across the path (i.e. if the path interacts with a surface, leading to a phase shift, it likely won't impact the result provided it occurs over the full arrival path). However, the interaction between multiple paths will be mildly influenced by relative phase shifts between paths, but without loss of DOA information. Figure 4.16 shows a sample beamformed output using the impulse response from Fig. 4.15 but with a lower frequency signal, such that the beamforming is performed from 1.7 to 2.3 kHz. The output from the data with no phase adjustments provides four prominent beams, as expected (a). If random phases are applied to each of the impulse response peaks individually, the beamformed output fails, since phase across each path is important (b). However, when a random phase is chosen and applied uniformly across a single path, the impacts should be much less significant - this was done independently to each of the four identified paths, resulting in a mildly different beamformed output (c), but with consistent DOA results when compared with the original output (a). These two results indicate that this technique for determining beamformed outputs with a lower frequency, synthetic signal, is valid for comparison with frequency-difference techniques.

Figures 4.17 and 4.18 show sample experimental results from these data sets. The measured CIR for a source depth of 90 m is shown in Fig. 4.17(a). Figure 4.17(b) shows the envelope of the

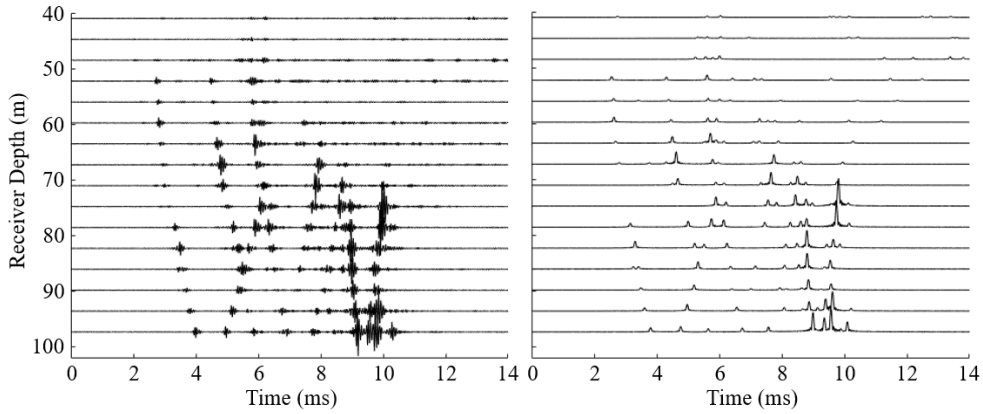

Figure 4.17: Matched filter impulse response from a source at a 90 m depth from the KAM11 experiment. The source signal was an 11.2 to 32.8 kHz linear frequency sweep. The impulse response (a) was enveloped and its peaks identified. After a filtering process, the remaining peaks in the envelope (b) were used to construct an out-of-band impulse response that extended below the signal band to the desired 1.7 to 2.3 kHz band.

peaks obtained from this impulse response after the amplitude filtering process described above. Figure 4.18(a) is the experimental result counterpart of Fig. 4.5. It provides results for $\bar{B}_{conv}$ incoherently averaged over 11.2 kHz $\leq f \leq$ 32.8 kHz (dotted line), $\bar{B}_{conv}$ incoherently averaged over 1.7 kHz $\leq f \leq$ 2.3 kHz using the synthetic signal (dashed line), and $\bar{B}_{\Delta}$ computed from the high-frequency signal and incoherently averaged over 1.7 kHz $\leq \Delta f \leq$ 2.3 kHz (solid line). Figure 10(b) shows the same for second dataset with no corresponding impulse response shown here. As expected, $\bar{B}_{conv}$ fails to indicate wavefront angles using the high-frequency signal because of the receiving array's sparseness. However, $\bar{B}_{\Delta}$ provides peaks closely aligned with those indicated by $\bar{B}_{conv}$ using the synthetic mid-frequency signal. In addition, the two methods provide outputs that have comparable structure, but with less dynamic range in the frequency-difference cases.

When taken together, the 16 experimental data sets provide 62 beamformer peaks for comparison, with each data set contributing between 2 and 6 peaks to the total. To simplify the comparisons of $\bar{B}_{\Delta}$-determined angles using the high-frequency signal and $\bar{B}_{conv}$-determined angles using the synthetic mid-frequency signal, the 62 beamformer peaks considered included only peaks above -6 dB (with the output normalized such that the strongest peak occurred at 0 dB). The -6 dB threshold is chosen since this should correspond to any coherent arrivals with a pressure amplitude larger

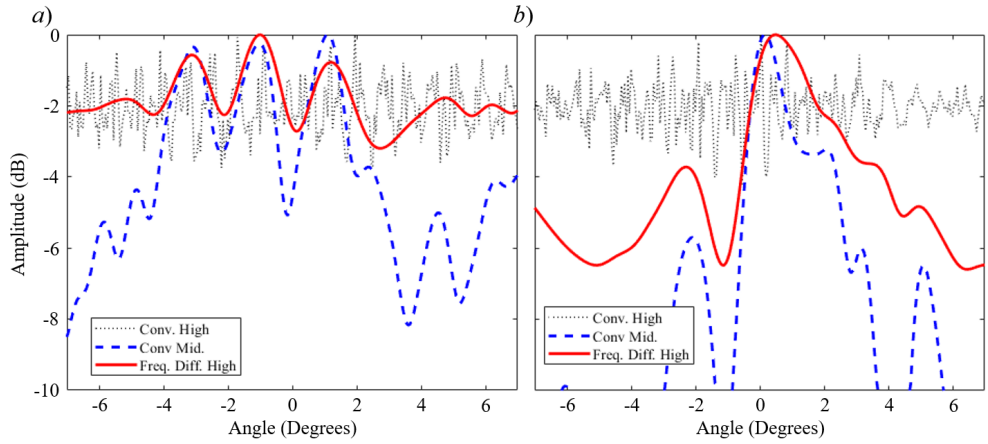

Figure 4.18: Beamforming output from the KAM11 array recordings for source depths of 90 m (a), corresponding to the impulse response shown in Fig. 4.17, and 82 m (b), with the corresponding impulse response not shown. The dotted curve is $\bar{B}_{conv}$ from Eq. 2.9 averaged over 11.2 kHz $\leq f \leq$ 32.8 kHz. The dashed curve is $\bar{B}_{conv}$ from Eq. 2.9 incoherently averaged over 1.7 kHz $\leq f \leq$ 2.3 kHz with data simulated using reconstructed wide-band impulse responses as shown in Fig. 4.17. The solid curve is $\bar{B}_{\Delta}$ from Eq. 2.14 using the high-frequency signal and incoherently averaged over 1.7 kHz $\leq \Delta f \leq$ 2.3 kHz.

than 50% that of the strongest arrival path. Excluding everything below -6 dB leads to roughly 17% of the coherent energy at the array being ignored, based on the 16 available KAM11 data sets, suggesting this is a reasonable (though somewhat ad-hoc) threshold. Overall, three beamforming peaks of -6 dB amplitude or greater were identified in the mid-frequency $\bar{B}_{conv}$ plots that did not appear to have a corresponding peak in the high-frequency $\bar{B}_{\Delta}$; an example of one of these peaks can be seen in Fig. 4.18(a) at approximately 2.5°.

A comparison of $\bar{B}_{\Delta}$-determined and $\bar{B}_{conv}$-determined angles is shown in Fig. 4.19. Here again the diagonal line has a slope of unity and passes through the origin (0,0). The vertical error bars correspond to the array's ideal beam half-width 3 dB below the peak (±0.35°). Here, the data and the ideal line lead to a reduced-χ^2 value of 0.91, indicating that the beam-width uncertainty of the beamformer outputs explains their differences. These experimental results show that frequency-difference beamforming was able to successfully identify wavefront arrival angles in a shallow water ocean environment, despite the array elements being spaced by 54 center-frequency wavelengths apart. Moreover, these results are unlikely to have been obtained by chance. If the 62 $\bar{B}_{\Delta}$-determined angles are replaced by 62 random angles lying uniformly between ±5° and these

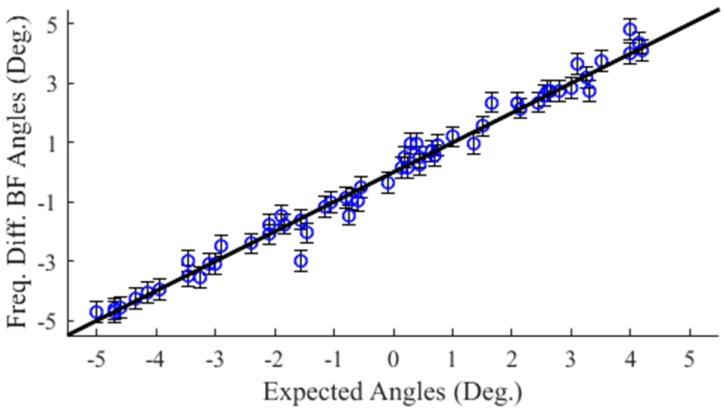

Figure 4.19: Comparison of expected beamforming angles to frequency-difference beamforming outputs for KAM11 data from 16 total experiments (8 sources on two different days). In each case, the conventional beamforming angles were determined from a simulated, lower-frequency signal. Peaks below -6 dB were not considered for this analysis. The two types of angle data produce a reduced-χ^2 value of 0.91, which indicates that their measured differences are explained by the associated uncertainties. The error bars depicted correspond to the 68% confidence interval.

random angles are compared to the $\bar{B}_{conv}$-determined angles, the average reduced-χ^2 value of the resulting data using 30 realizations is approximately 9.8, more than a full order of magnitude higher than the reduced-χ^2 value when the $\bar{B}_{\Delta}$-determined angles are used.

4.4 Conclusions

Frequency-difference beamforming is a potentially useful array signal processing technique for sparse arrays or environments and geometries with significant levels of uncertainty. The performance of frequency-difference beamforming was compared to conventional beamforming in the signal bandwidth and in the frequency-difference bandwidth using shallow ocean simulations and experiments. In all cases, the performance of frequency-difference beamforming was comparable with conventional beamforming at the difference frequency, and much better than conventional beamforming at the in-band signal frequencies.

The following conclusions can be drawn from this research effort. (1) Frequency-difference beamforming provides a useful beamforming output in scenarios where conventional beamforming is unsuccessful due to the sparsity of the receiving array. Here, frequency-difference beamform-

ing was found to be successful with array-element-spacing to signal-center-frequency-wavelength ratios of 6.7, 54, and 67.7 in simulated and experimental environments. (2) Frequency-difference beamforming and conventional beamforming behave similarly when comparing conventional beamforming results at an absolute frequency matching the difference frequency used in frequency-difference beamforming. When formulated for plane waves, both techniques behave similarly when confronted with multiple wavefront arrivals and curved wavefronts. The methods had comparable success in determining wavefront arrival directions, even though they relied on very different signals. However, frequency-difference beamforming was more susceptible to missing weaker wavefront arrivals due to the nature of the quadratic field product, the starting point for the frequency-difference technique. (3) Frequency-difference beamforming is able to withstand uncertainty and variation in propagation path lengths or receiver array geometry, up to when the dimensionless parameter, $\Delta k * \sigma$, approaches 0.40π, implying that roughly one-fifth of a wavelength of error is problematic. The performance of the frequency-difference method in the presence of uncertainty strongly outperformed that of the in-band, higher frequency field, when this constraint was met. (4) Frequency-difference beamforming can successfully identify wavefront arrivals in both simulated and actual shallow ocean environments with many arrival paths, downward refracting sound speed profiles, and range dependence (experiment only). Overall, the comparison between arrival angles determined from frequency-difference beamforming and from conventional beamforming using a synthesized, lower-band signal — combined with the expected uncertainties — yielded a reduced-χ^2 value of 0.91, indicating that the observed differences in the two sets of angles are explained by the uncertainties in these data.

CHAPTER 5

Frequency-Difference Beamforming with Strong Scattering

Acoustic scattering, while sometimes desirable (particularly in active array-based remote sensing applications such as ultrasound imaging), can be detrimental to beamforming in both active and passive scenarios when the source of the scattering is not of interest. Scattering can result from acoustic illumination of rough boundaries (ocean surface or bottom), inhomogeneities in the environment (manmade objects, bubbles, schools of fish, etc.), or changes in medium properties (sound speed, density, salinity, etc.). The resulting scattered fields can vary significantly from the direct-path field in both phase and amplitude. When the scattering features are small relative to the signal wavelength (e.g. $ka < 1$ for a spherical scatterer, where $k = \omega/c$ is the acoustic wave number, c is the medium's sound speed near the scatterer, and a is the scatterer radius) and their impedance contrast is small compared to that of the surrounding fluid, the scattered field is weak and minimally disruptive. However, when ka and the scatterer's acoustic impedance contrast are both large, the scattered field becomes significant and its effects on conventional beamforming methods are no longer negligible. For high ka ($ka >> 1$) and high contrast scatterers, frequency-difference beamforming may provide improvements over in-band conventional beamforming by effectively reducing ka when the difference frequency is chosen such that $\Delta ka = \Delta\omega a/c$ is sufficiently small.

This chapter describes source-localization or source-imaging results obtained with conventional and frequency-difference spherical-wave beamforming, using propagation simulations and water-tank experiments incorporating strong random scattering. The results indicate that even

when strong random scattering causes conventional in-band techniques to fail, below-band source localization or imaging can be robust and successful – albeit with some reduction in precision compared to what is ideally possible at in-band frequencies. Here, the accuracy and robustness of the localization is of interest and is evaluated based on localization error and peak-to-sidelobe ratio over many simulations and experiments.

5.1 Simulation and Experiment Setup

The performance of conventional and frequency-difference beamforming in environments with strong random scattering was simulated and measured using the same geometry and parameters. The robustness of the two methods is examined by varying the number of scatterers, their positions, and the source position. The geometry and coordinate system for the simulations were chosen to nominally match that of the water tank experiments, and are shown in Fig. 5.1(a) for a source positioned at (x, y) = (0.40 m,–0.10 m). The linear receiving array contains 12 elements uniformly spaced 5.08 cm apart along the $y-$axis, with the $x-$axis passing through the array center. The scatterers are placed randomly within the red rectangle shown in Fig. 5.1(a) that covers 2 cm $< x <$ 40 cm and $|y|¡$ 30 cm. All elements of the simulation – receivers, scatterers, and the source – are placed in the $x - y$ plane at least 2 cm away from all other components. Though Fig. 5.1(a) shows the tank walls, reflections from these are not included in the simulations. The setup for the experiment uses the same geometry and is shown in Fig. 5.1(b). In the experiment, reflections from the tank walls, bottom, and water surface were removed by time-gating the recorded signals so that only the direct path and scattered fields were recorded.

In the simulations, the number of scatterers varied from 0 to 30, and for each number of scatterers (except 0), an ensemble of 400 simulations were completed all using the source location shown in Fig. 5.1(a) but with the scatterers in new, random positions within the rectangular region between the source and the array. Two 0.25 ms signals were simulated – a 20 kHz pulse and a 150-200 kHz linear frequency sweep. In addition to these simulations, five additional source locations

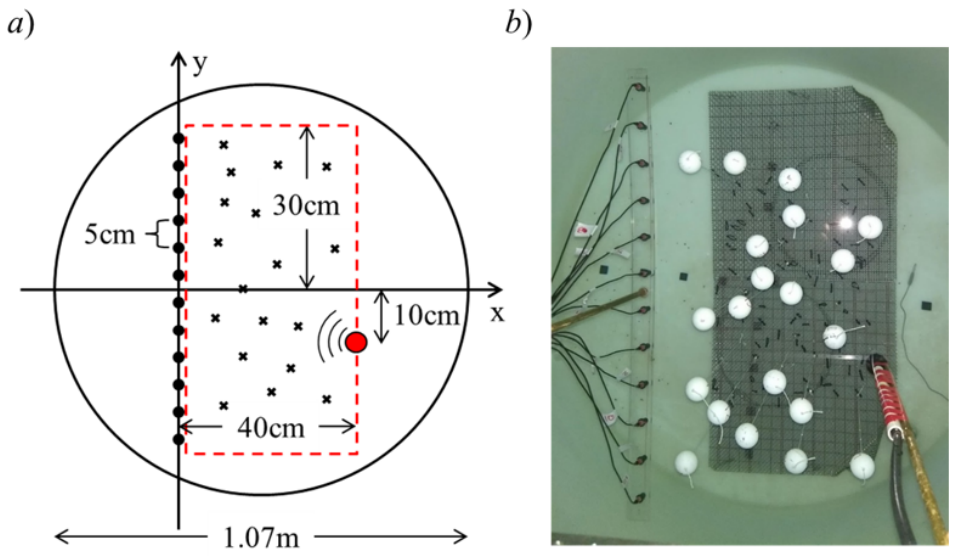

Figure 5.1: Geometry for the simulations (a) and the experiments (b). A 12-element receiving array with 5.08 cm element spacing records signals broadcast from (x, y) = (0.40 m, –0.10 m) relative to the array center. The dashed red line outlines the rectangular region within which the scatterers were placed, with the left edge 2 cm from the receiver array. In both simulations and experiments, reflections from the circular tank wall are not incorporated.

were considered, with 100 simulations completed for each source position with 20 and 30 scatterers. Both soft (pressure release boundary condition) and hard (rigid boundary condition) spherical scatterers with a = 2 cm radius were considered, but only the soft scatterer results are presented here, since both beamforming methods performed better with hard scatterers. Using the center frequencies of the two signals, the scatterers' ka values are 1.7 at 20 kHz and 14.7 at 175 kHz. In addition to the ka values, it is useful to quantify the field as the ratio of mean source-to-receiver distance, $\langle |r_{0j}| \rangle$, and the mean-free-path, l_s. Here, for 1 to 30 scatterers, this ratio varies linearly from 0.1 to 4.3.

For simplicity, only first and second order scattering is considered in the simulations. This is expected to capture nearly all of the scattering physics, and in some cases leads to important corrections to single scattering when near-source scatterers cast shadows on other scatterers. For scattering paths between non-colinear scatterers, higher order scattering will likely be lost in the experiments when the signals are trimmed to remove tank-wall and water-surface reflections. A simple analysis of the geometry shows that the first wall reflection will arrive between 0.65 and

1.0 ms for the source location shown in Fig. 5.1, depending on the receiver, while paths from third order scattering can arrive anywhere between 0.27 and 1.3 ms depending on the three scatterer locations and the receiver. The shorter arrival times correspond to co-linear scatterers, while the longer times correspond to scatterers not lying close to a line. Comparing these arrival times with those of the first reflection indicate that a significant portion of the third order scattering, particularly that which does not correspond to shadow zones and travels significantly longer paths, will be lost in the signal trimming. Thus, considering only first and second order scattering does not yield a significant difference between simulation and experiment. The most notable discrepancies between simulations and experiments will occur when more than two scatterers lie close to a line such that they all have overlapping shadow zones; this is the primary effect of third order scattering that is fully captured in the experiment.

The experimental geometry was nominally the same as that of the simulations. The source, an ITC-1042, broadcasted the same two signals as in the simulation. In addition to the ITC-1042, an ITC-1032 and an ITC-1094a were utilized to obtain cleaner signal outputs, since the broadcast signals fall within the intended frequency range of these sources. However, for consistency, the ITC-1042 alone was used for both signals when doing a direct beamforming comparison between the two to ensure there was no variation in source-array geometry. The scatterers were 2 cm radius table tennis balls suspended from the tank bottom, effectively providing a sphere of air within the water and achieving a nearly pressure release boundary condition due to the impedance difference between the air and water. The receiving array was comprised of 12 Reson TC4013 hydrophones and the time domain recording outputs were trimmed to remove any reflections from the tank wall, tank bottom, or water-surface boundaries. The experiments were all performed at the same source location but with 20 different configurations each of 14, 16, 18, and 20 scatterers.

The source localization or imaging performance of each method was evaluated primarily based on source localization accuracy and peak-to-sidelobe ratio. The beamformer-indicated source location is simply taken as the point in the search field where the maximum occurs in the beamformed output (set to 0 dB in the normalized beamformed outputs). The localization error is then the Eu-

clidean distance between the known source location and the beamformer peak. The search grid for the beamformers is a one meter square, with the array lying on one edge. This size was chosen based on the size of the water tank used in the experiments, but in some cases, a larger beamforming peak may have occurred outside of the search window were it expanded. The results presented below suggest that if the search window were expanded, the overall performance of conventional beamforming would be worse, while that of frequency-difference beamforming would likely stay the same, thus not changing the conclusions drawn from this effort (see Section IV).

The definition of peak-to-side-lobe ratio used in this manuscript is dependent on the beamformer output. In order to calculate peak-to-side-lobe ratio, first a peak-finding algorithm was used to identify and locate all peaks (i.e. local maxima) in the beamformed output. From here, the peak closest to the known source location was identified. If this peak corresponded to the global maximum, the peak-to-sidelobe ratio was computed as the dB difference between this peak and the second highest peak (yielding a positive decibel peak-to-sidelobe ratio), regardless of the second peak's value or location. If only a single peak existed in the output, then the total dynamic range is taken as the peak-to-sidelobe ratio (again, a positive decibel value). Finally, if the beamformed peak closest to the true source location did not correspond to the global maximum, then the difference between this peak and the highest peak is taken as the peak-to-side-lobe ratio (yielding a negative decibel value).

5.2 Mathematical Formulations

The conventional beamforming and frequency-difference beamforming formulations are completed in Chapter 2, and thus are not repeated here. The relevant equations for conventional beamforming are Eqs. 2.6 and 2.9 and for frequency-difference beamforming are Eqs. 2.12 and 2.14. In addition, the same weighting vectors will be used as in Chapter 2, Eqs. 2.7 and 2.8.

The fields resulting from propagation through scatterers can be assumed to be accurately represented as a superposition of the direct and scattered fields (independent of whether the fields are

specified in the time or frequency domains)

$$p = p_{dir} + p_{scat} \tag{5.1}$$

The direct path is simple to calculate in a free-space environment, but the scattered field depends on the number of scatterers and their shapes, sizes, positions, and material properties. For simple shapes, the scattered field is generally well known for a single isolated scatterer. For the work presented here, the scattered field resulting from soft spheres with impinging spherical waves are of interest, with "soft" implying a pressure release boundary condition on at the interface of the scatterer and the propagating medium. The expression for scattering from a soft sphere can be derived analytically, giving

$$p_{scat}(\omega, \vec{r}_s, \vec{r}_l, \vec{r}) = -iA \sum_{n=0}^{\infty} \frac{(2n+1)\mathcal{P}_n(\cos\theta) h_n^{(1)}(k\left|\vec{r}_s - \vec{r}_l\right|) h_n^{(1)}(k\left|\vec{r}_l - \vec{r}_j\right| j_n(ka))}{h_n^{(1)}(ka)} \tag{5.2}$$

Here, A is the source strength, θ is the angle between the incident and scattered directions for a given ray (with $\theta = 0\ ^\circ$ being the backscatter direction), $\vec{r}_l$ is the position of the scatterer of interest, a is the scatterer radius, $h_n^{(1)}$ is a spherical Hankel function of the first kind, j_n is a spherical Bessel function, and $\mathcal{P}_n$ is a Legendre polynomial. The derivation leading to Eq. 5.2 and the corresponding scattered fields for hard and finite impedance spheres can be found in Bowman et al. 1970 [19]. The free-space (or direct-path) field from a source at $\vec{r}_s$ that reaches a receiver at $\vec{r}_j$ is given by

$$p_{j,dir}(\omega) = A \frac{e^{(ik\left|\vec{r}_s - \vec{r}_j\right|)}}{\left|\vec{r}_s - \vec{r}_j\right|} \tag{5.3}$$

where the wave number is $k = \omega/c$. This formula can also be used for the direct-path field at the l^{th} scatterer if $\vec{r}_j$ is replaced with $\vec{r}_l$.

While the calculation of the field from a single scatterer is relatively simple for common shapes, the field resulting from multiple scatterers can be very complicated, particularly when one considers higher order scattering, in which the scattering of the scattered fields is considered. For simplicity, the simulations in this manuscript only consider first and second order scattering. Thus,

the total field at the j^{th} receiver will look like

$$p_j(\omega) = A\frac{e^{(ik\left|\vec{r}_s-\vec{r}_j\right|)}}{\left|\vec{r}_s-\vec{r}_j\right|} + \sum_{l=1}^{L} p_{scat}(\omega,\vec{r}_s,\vec{r}_l,\vec{r}_j) + \frac{1}{A}\sum_{l,m=1,l\neq m}^{L,M}\frac{p_{scat}(\omega,\vec{r}_s,\vec{r}_l,\vec{r}_m)p_{scat}(\omega,\vec{r}_l,\vec{r}_m,\vec{r}_j)}{h_0^{(1)}(k\left|\vec{r}_l-\vec{r}_m\right|)} \tag{5.4}$$

For the purposes of frequency-difference beamforming, the autoproduct of the field is given by Eq. 2.10. Forming the autoproduct using the notation in Eq. 5.1 yields

$$\begin{aligned} AP_j(\Delta\omega,\bar{\omega}) = {} & p_{dir}(\bar{\omega}+\frac{\Delta\omega}{2})p^*_{dir}(\bar{\omega}-\frac{\Delta\omega}{2}) + p_{dir}(\bar{\omega}+\frac{\Delta\omega}{2})p^*_{scat}(\bar{\omega}-\frac{\Delta\omega}{2}) \\ & + p_{scat}(\bar{\omega}+\frac{\Delta\omega}{2})p^*_{dir}(\bar{\omega}-\frac{\Delta\omega}{2}) + p_{scat}(\bar{\omega}+\frac{\Delta\omega}{2})p^*_{scat}(\bar{\omega}-\frac{\Delta\omega}{2}) \\ = {} & \frac{A^2 exp(i\Delta k\left|\vec{r}_s-\vec{r}_j\right|)}{\left|\vec{r}_s-\vec{r}_j\right|^2} + \text{unintended} \quad \text{terms} \end{aligned} \tag{5.5}$$

The expanded form of Eq. 5.5 written in terms of the variables present in Eqs. 5.2 and 5.3 is not presented here for brevity. This expanded equation has nine right-side terms when second-order scattering is included, with only one term (shown in Eq. 5.5) clearly providing the desirable phase structure with dependence only on Δk, which should be useful for the purposes of beamforming. The remaining eight unintended terms arise from the quadratic product and represent source-scatterer-receiver or source-scatterer-scatterer-receiver paths with phases based on k_1 and k_2 (the wave number pairs that make Δk), rather than the direct path and Δk. Fortunately, by averaging through the signal bandwidth, the spread of the unintended term's phases suppresses their negative contributions.

A visualization of the scattered fields from hard and soft spherical scatterers is provided in Fig. 5.2. Here, a source is placed at (x, y) = (-0.20, 0) and the scatterer, either a hard (top) or soft (bottom) sphere with 2 cm radius, is placed at the origin. The $1/r$ range-based decay is not included in this calculation in order to visualize the fields more easily - particularly the phase characteristics. Figs. 5.2(a) and (b) show the same 150 kHz field at two different scales. The field

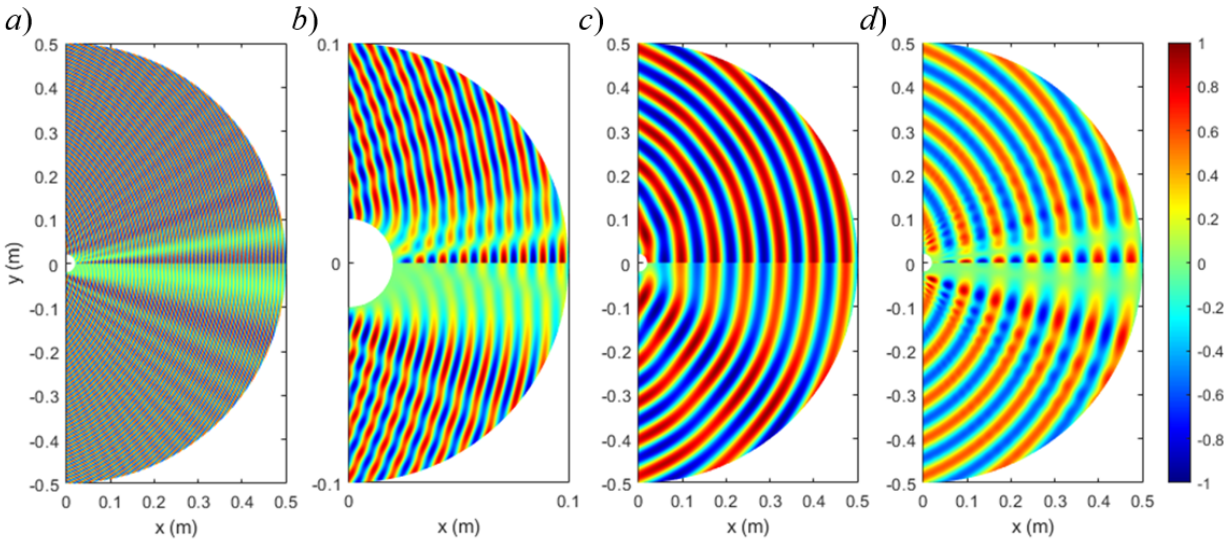

Figure 5.2: Fields resulting from a combined direct path and scattered field. The source is placed 20 cm to the left of the scatterer, which is placed at the origin in each plot. The scatterer has a 2 cm radius and is either hard (top half of each plot) or soft (bottom half). The field is shown for a 150 kHz signal (a) and (b) on two different scales, a 20 kHz field (c), and a 20 kHz autoproduct field generated using 150-200 kHz (d). In all of these cases, the $1/r$ range-based decay is left out in order to more easily visualize the field.

shows non-negligible shifts in phase, indicated by the "wavy" characteristics seen in the lines, and the phase shifts and amplitude variation near the forward scattering angle are more pronounced. Figure 5.2(c) is a genuine 20 kHz field, which shows very little impact resulting from the hard scatterer, and in the case of the soft scatterer, has some amplitude reduction near the forward scattering angle, but the phase shifts are not significant. Finally, Fig 5.2(d) is a 20 kHz autoproduct field generated using 150-200 kHz, but behaves similarly to the genuine 20 kHz field. Throughout most of the field, the energy loss is more significant than the genuine field - a result of the stronger scattering at higher frequencies - but the phase variation is comparable and again, likely negligible in most applications, including beamforming.

A simulation case with 20 ideal soft spherical scatterers with radius $a = 2$ cm is provided here to illustrate how each method's performance is affected by strong random scattering. The simulation setup is that shown in Fig. 5.1 and the broadcast signal is a 150-to-200 kHz frequency sweep. Unlike the matching experiments where only the total field is measured, the simulations allow the

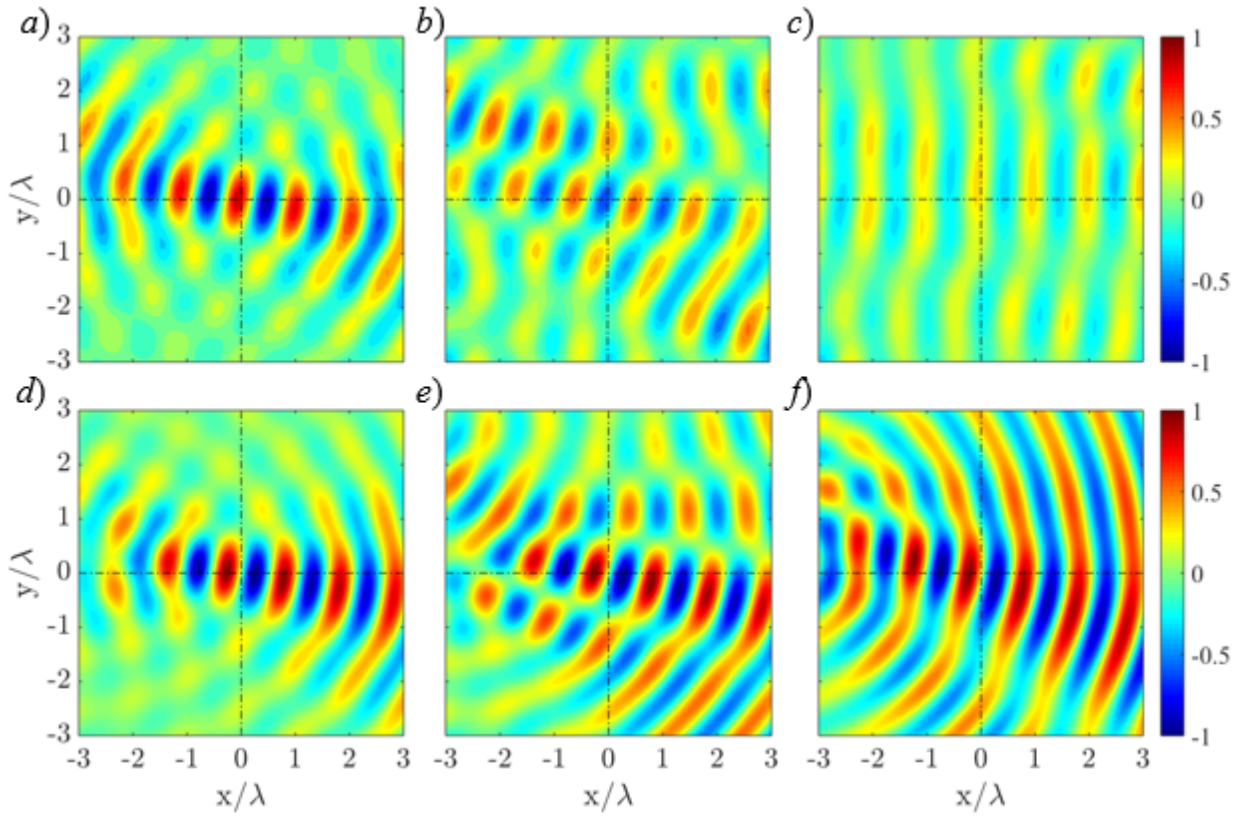

Figure 5.3: The output of the real part of b_{conv} in Eq. 2.6 for conventional beamforming at f = 150 kHz for the direct path field (a), the scattered field (b), and the combined fields (c). The output of the real part of Eq. 2.14 is shown using 150 kHz $\leq f \leq$ 200 kHz at Δf = 15 kHz for the $p_{dir}(\omega_2)p^*_{dir}(\omega_1)$ field (d), the field with all of the scattering influenced terms (e), and the total combined field (f). The axes are multiples of the signal wavelength corresponding to f (a-c) or Δf (d-f), with the source placed in the center of the window.

direct and scattered fields to be beamformed separately to determine their contribution(s) to the total field results. Furthermore, to assess the importance of in- and out-of-phase contributions, the real parts of the complex beamformed outputs are shown in Fig. 5.3 when the source is located at (x_s, y_s) = (40 cm, –10 cm) and the broadcast signal has a Fourier spectrum of unity, $S(\omega) = 1$. Here, red indicates increasingly positive values, while blue indicates increasingly negative values, and the known source location (x_s, y_s) is at the center of each panel.

The upper row of Fig. 5.3 presents conventional beamforming results at frequency f = 150 kHz and shows the real part of Eq. 6.9 near the source location using the direct path field [Fig. 5.3(a)], the scattered field [Fig. 5.3(b)], and the total field [Fig. 5.3(c)]. The lower row of Fig. 5.3 presents

frequency-difference beamforming results for difference frequency Δf = 15 kHz and shows the real part of Eq. 2.14 near the source location for the direct-path autoproduct term [Fig. 5.3(d)], the autoproduct terms that include the scattered field [Fig. 5.3(e)], and all autoproduct terms [Fig. 5.3(f)]. Here, the autoproduct is coherently averaged through the full 150-200 kHz bandwidth. In all six panels of Fig. 5.3, the coordinates are wavelength scaled using the frequencies f or Δf, as appropriate, and centered around the known source location; thus, when compared to the upper row, the lower row shows physical areas that are 10 times larger in both dimensions. Dashed lines are provided along the axes for easier comparison between figure panels. It should be noted that the frequency-difference cases incorporate signal bandwidth (a requirement for the technique), but the in-band cases are only showing a single frequency, since b cannot be averaged, except in coherent beamforming cases not discussed here.

5.3 Results and Discussion

The performance of frequency-difference beamforming was examined using simulations in which the number of scatterers, the scatterer positions, and the source locations varied. The simulations were matched to the geometry of the experiments shown in Fig. 5.1, where the source location is (x_s, y_s) = (0.40 m, -0.10 m). Here, ideal soft scatterers were illuminated by both 20 kHz pulse and 150-200 kHz linear frequency sweep signals. Additional simulations with five other source locations, hard scatterers, and lower signal frequencies were also completed. The performance of all methods improved with hard scatterers and lower signal frequencies; thus, for brevity, those results are not presented here.

The performance of conventional and frequency-difference beamforming was evaluated using several types of processing. Other beamforming techniques, such as MVDR, MUSIC, or compressive beamforming are not considered, based on their performance in Chapter 2. First, conventional spherical-wave beamforming was applied to the 20 kHz and 150-200 kHz signals to establish the capabilities and limitations of conventional methods in the presence of strong random

scattering for different in-band frequencies. Here, results for the higher frequency signal were incoherently averaged through the stated bandwidth with 1 kHz increments. Second, frequency-difference beamforming was applied to the 150-200 kHz signal with incoherent averaging through the full signal bandwidth using difference frequencies of $\Delta f = 10$ kHz and 20 kHz and using an incoherent average of difference frequencies from 5 kHz to 25 kHz in 1 kHz increments. Each of these possibilities was considered with and without scatterers present.

5.3.1 Increasing Number of Scatterers

The first simulation study involved varying the number of scatterers present in the region indicated in Fig. 1a). Fig. 3 shows sample conventional beamforming results for the two signals with and without 20 ideal soft spherical scatterers ($\frac{\langle |r_{0j}| \rangle}{l_s} = 2.9$). Figures 5.4(a) and (b) show no-scatterer results for the 20 kHz and the 150-200 kHz signals, respectively, while Figs. 5.4(c) and (d) show the corresponding results for the same two signals and the same source location but with 20 scatterers placed randomly within the rectangular region indicated in Fig. 5.1(a). In each panel of Fig. 5.4, the source location is indicated by a black 'x', the beamformed peak is indicated with a black circle, and the receiver positions are indicated by black dots. When scatterers are absent, Fig. 5.4(a) and (b) show – as expected – that conventional spherical-wave beamforming locates the source perfectly and with higher precision when using the higher frequency signal. When 20 randomly-placed ideal soft spherical scatterers are present, Fig. 5.4(c) shows that source localization is still possible when $ka = 1.7$, albeit with more prominent side lobes than when scatterers are absent. However, Fig. 5.4(d) shows that conventional spherical wave beamforming may fail at higher signal frequencies where $13 \leq ka \leq 17$ for the same source-scatterer-array geometry. At the higher frequencies, the scattered field is stronger, side lobes are more prominent, and the overall dynamic range is lower.

As previously stated, frequency-difference beamforming is expected to increase beamforming robustness at the expense of decreased precision and resolution via the frequency-downshifting embodied in the frequency-difference autoproduct. More specifically, frequency-difference beam-

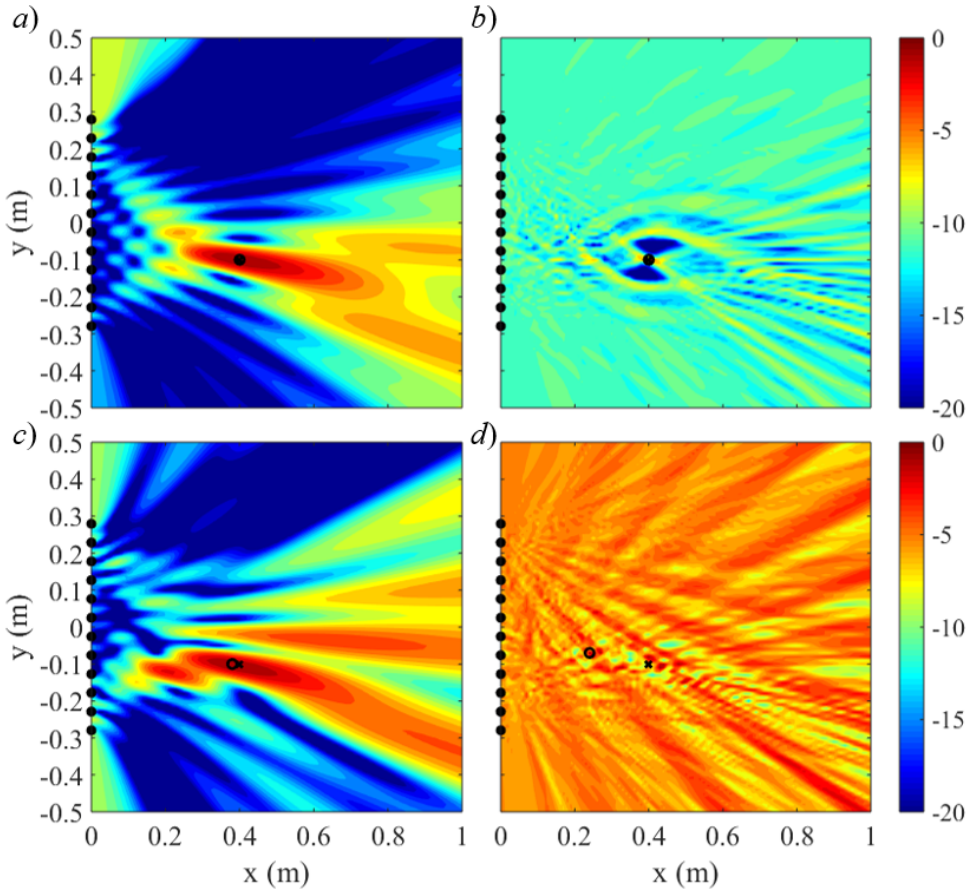

Figure 5.4: Simulated conventional beamforming results with no scatterers for the 20 kHz (a) and 150-200 kHz (b) signals, and for a case with 20 scatterers for the 20 kHz (c) and 150-200 kHz (d) signals. The known source location is indicated with a black 'x', the peak of the beamforming output is indicated with a black circle, and the receiver locations are indicated by black dots.

forming using the 150-200 kHz signal with a difference frequency of 20 kHz should provide results similar to that of conventional beamforming at 20 kHz, shown in Fig. 5.4(c). The results of frequency-difference beamforming using the 150-200 kHz signal with scatterers present are shown in Fig. 5.5(a) for $\Delta f = 20$ kHz and in Fig. 5.5(b) for the incoherent average through difference frequencies, 5 kHz $\leq \Delta f \leq$ 25 kHz. Although the side lobe structures in Fig. 5.4(c) and Fig. 5.5(a) are similar, they are derived from different signals. Thus, the fairest comparisons are between Figs. 5.4(d), 5.5(a), and 5.5(b) since all involve the same 20 scatterers and all are derived from the same signals. For this specific source-scatterer-array geometry, these comparisons show that the frequency-difference methods perform significantly better than the conventional method using the high frequency signal when scatterers are present. Both frequency-difference techniques produce a robust main lobe that surrounds the known source location. When $\Delta f = 20$ kHz alone, as in Fig. 5.5(a), non-negligible side lobes exist that reduce the peak-to-sidelobe ratio, but they do not overwhelm the main lobe. However, by incoherently averaging results from different difference frequencies as in Fig. 5.5(b), some overall dynamic range is lost, but all side lobes are suppressed such that only one notable main lobe exists, an unambiguous source localization or imaging result, especially when compared to the conventional result in Fig. 5.4(d).

Experimental results for the same nominal scenarios and geometry are shown in Figs. 5.6, 5.7, and 5.8. The broadcast signals were a 20 kHz Gaussian-windowed pulse and a 150-200 kHz Gaussian-windowed frequency sweep, both having 0.25 ms duration. Figure 5.6 shows the recorded waveforms for both signals without and with 20 scatterers ($\frac{\langle |r_{0j}| \rangle}{l_s} = 2.9$) placed between the source and the array. Figures 5.6(a) and (b) show the recorded waveforms without scatterers for the 20 kHz and 150-200 kHz signals, respectively. Figures 5.6(c) and (d) show the recorded waveforms with scatterers for the same two signals. The vertical scales are the same for both low frequency array outputs and for both high frequency array outputs, but the high frequency signals are scaled by a factor of five relative to the low frequency signals, for aesthetic purposes. A key observation from these waveform plots is that the tank experiments include some receiver-to-receiver and mounting-hardware-to-receiver scattering, which is most evident in the variable signal en-

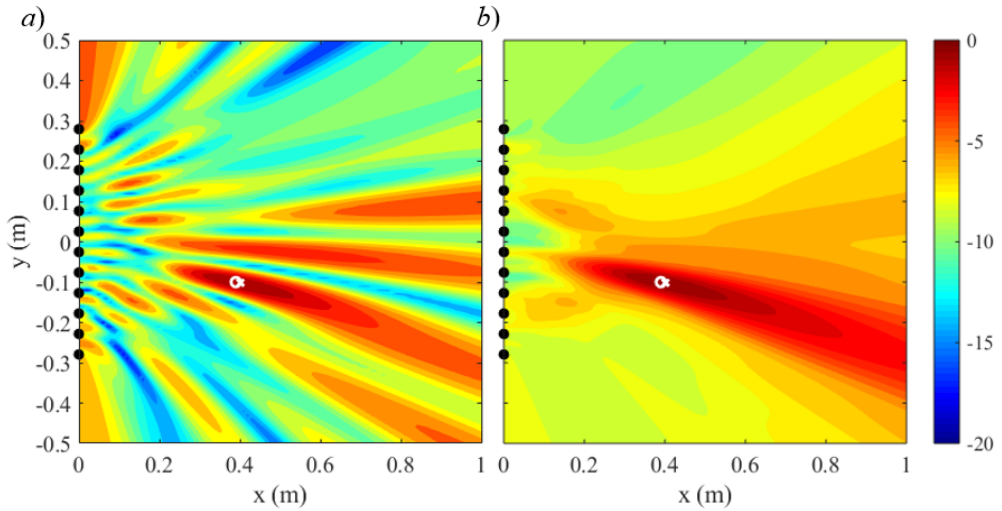

Figure 5.5: Simulated frequency-difference beamforming results with 20 scatterers for the 150-200 kHz frequency sweep using Δf = 20 kHz (a), and averaging Δf outputs from 5 to 25 kHz at 1 kHz increments (b). The known source location is indicated with a white 'x', the peak of the beamforming output is indicated with a white circle, and the receiver locations are indicated by black dots.

velopes displayed in Fig. 5.6(b). This artifact scattering cannot be removed from the experimental recordings, but is presumed to be mild enough to not alter the conclusions drawn from examination and comparison of the various beamformed results shown in Figs. 5.7 and 5.8. A second notable observation is the signal amplitude reduction and envelope distortion that occurs when the scatterers are present. As a nominal specification of the strength of this scattering, the array recorded signal energy is reduced by 10.1 and 5.0 dB for the 20 kHz and 150-200 kHz signals, respectively, when the scatterers are present.

Conventional beamforming results using the Fig. 5.6 signals are shown in Fig. 5.7. The signal processing and figure layout here is exactly the same as in Fig. 5.4: a) 20 kHz signal without scatterers, b) 150-200 kHz signal without scatterers, c) 20 kHz signal with scatterers, and d) 150-200 kHz signal with scatterers. When comparing equivalent conventional-beamforming experimental (Fig. 5.7) and simulation (Fig. 5.4) results without scattering, the effects of experimental imperfections appear to cause a mild decline in performance. When the scatterers are added, some side lobes for the 20 kHz case are altered, but a strong main lobe still exists surrounding the expected source location. For the 150-200 kHz signal, the dynamic range is reduced to only a few decibels

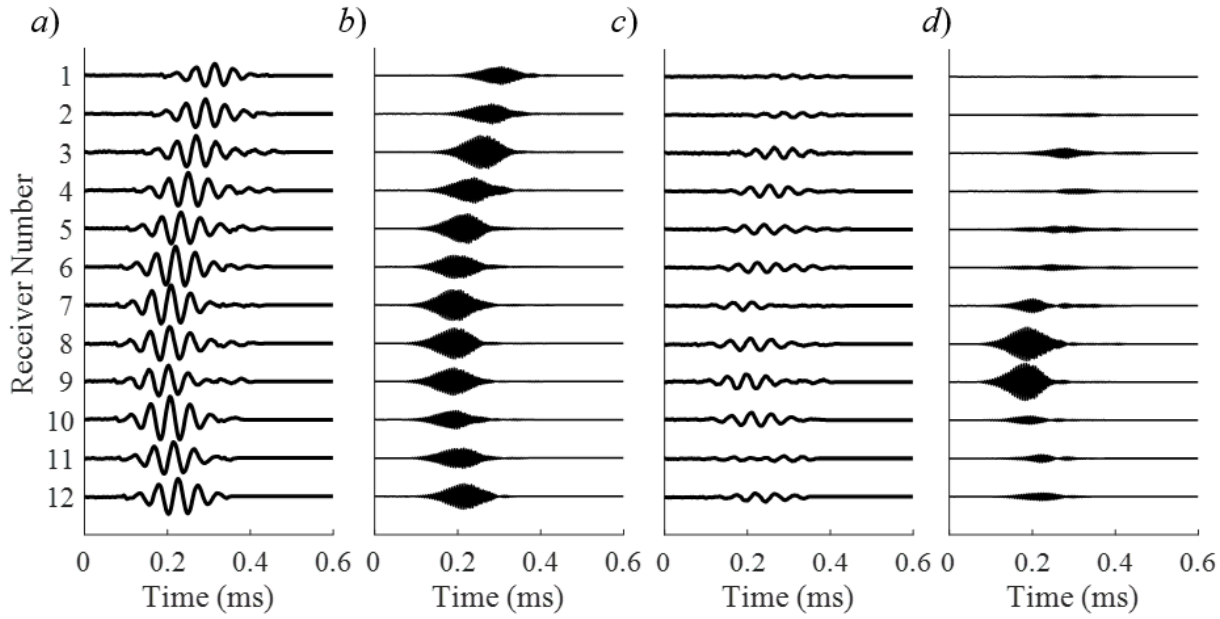

Figure 5.6: Recorded waveforms for the two 0.25 ms signals after time windowing to remove reverberation. The 20 kHz (a) and 150-200 kHz (b) signals without scatterers show predictable signals with some evidence of experimental-artifact scattering in the high frequency signal. The 20 kHz (c) and 150-200 kHz (d) signals with 20 ping-pong-ball scatterers in the tank, with notable amplitude reductions and envelope distortion compared to when the scatterers are absent.

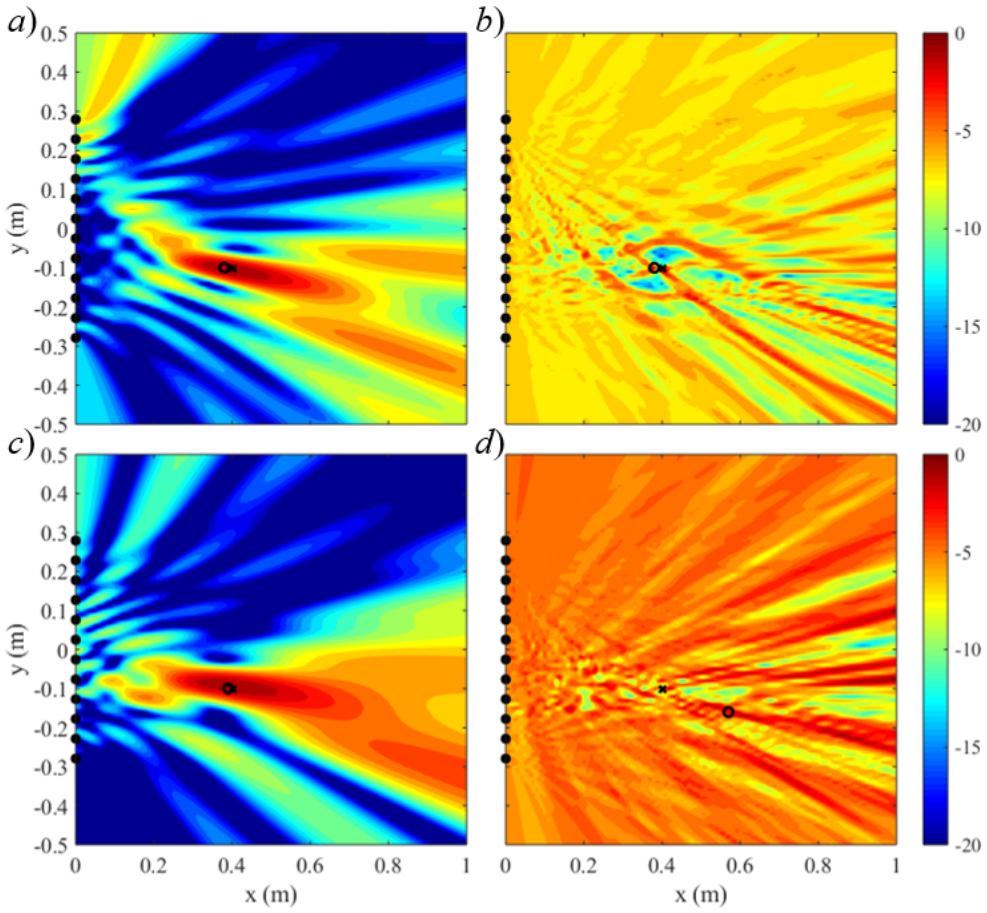

Figure 5.7: Same as Fig. 5.4 except these results are for the signal recordings shown in Fig. 5.6

throughout much of the plot, and again the beamformed peak does not coincide with the source location.

Frequency-difference beamforming results using the 150-200 kHz signal recordings with scatterers present are shown in Fig. 5.8(a) for $\Delta f = 20$ kHz and in Fig. 5.8(b) for the incoherent average through 5 kHz $\leq \Delta f \leq$ 25 kHz. For the $\Delta f = 20$ kHz case, a strong, prominent lobe once again exists around the expected source location, with minimal error in the peak location. In the case with difference frequency averaging, the peak moves slightly closer to the expected location and sidelobes are reduced, though some of the dynamic range is lost again. When comparing Fig. 5.8(b) to conventional beamforming with the high frequency signal [Fig. 5.8(d)], it is clear that frequency-difference beamforming yields the preferred result when the scatterers are present. Not only is the source location more accurate, but the dynamic range is improved, the peak-to-sidelobe

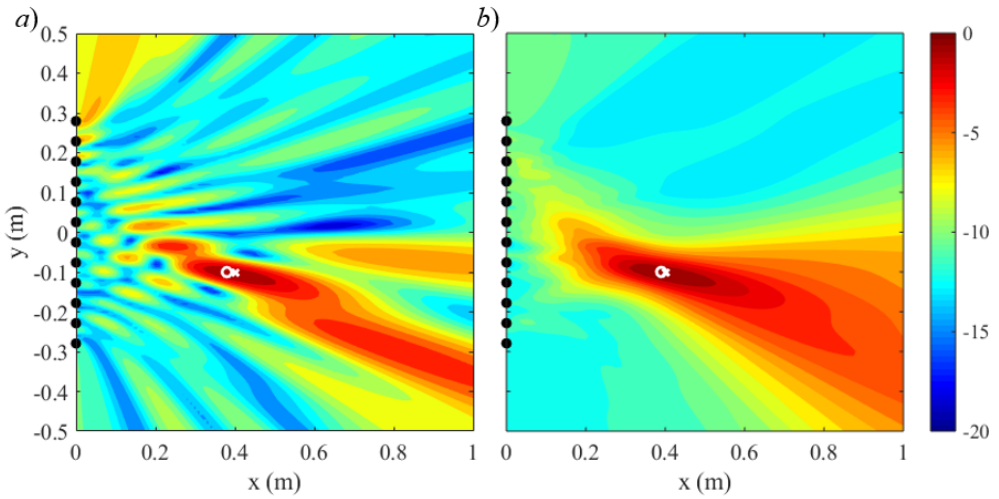

Figure 5.8: Same as Fig. 5.5 except these results are for the signal recordings shown in Fig. 5.6(d)

ratio is greater, and the number of sidelobes is significantly reduced.

The figures above show compelling results from single realizations of the random scattering with and without 20 scatterers ($\frac{\langle|r_{0j}|\rangle}{l_s} = 2.9$). To extend these results, simulations were conducted for the geometry shown in Fig. 5.1 with the number of scatterers varied from 1 to 30. For each scatterer count, 400 different random scatterer configurations were simulated to determine the average performance of the various beamforming techniques. The average localization error (Euclidian distance) and peak-to-side-lobe ratio determined from these simulations are shown in Fig. 5.9 as a function of the number of scatterers for four different types of spherical wave beamforming: conventional (black dotted curve), frequency difference with $\Delta f = 10$ kHz (red dashed curve), frequency difference with $\Delta f = 20$ kHz (green dash-dot curve), and frequency difference averaged through 5 kHz $\leq \Delta f \leq$ 25 kHz (solid blue curve). All four of these signal processing schemes uses the full 150-200 kHz signal bandwidth. For clarity, an additional figure, Fig. 5.10, is provided with only the simulated results, showing the 95% confidence interval error bars for each case.

As expected from Figs. 5.4 through 5.8, the average errors from the frequency-difference methods are significantly lower than that from the conventional method, a difference that becomes more dramatic as the number of scatterers increases. The error does appear to begin leveling off between 20 and 30 scatterers, perhaps indicating that as the recorded field becomes saturated with like scat-

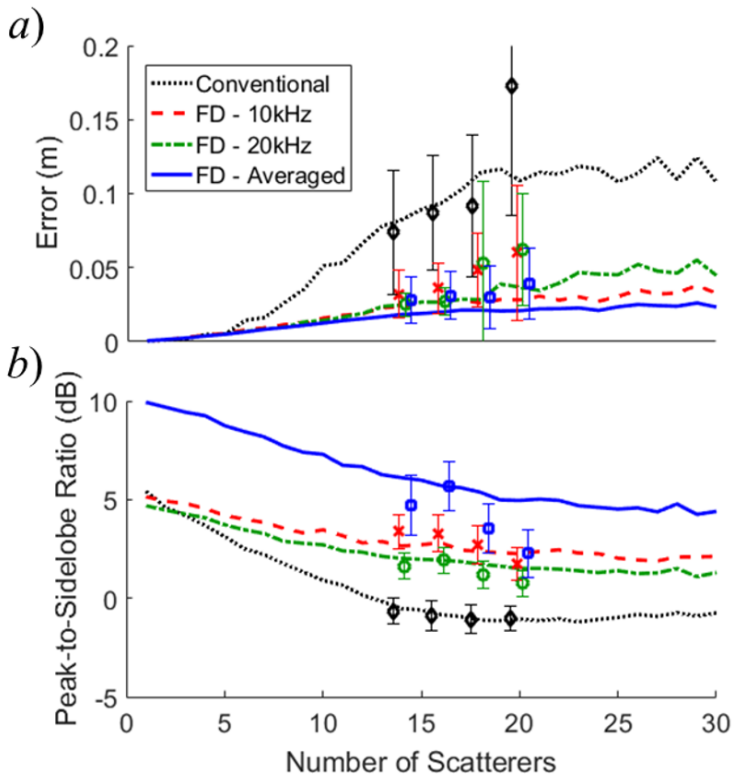

Figure 5.9: Average source localization error (a) for four techniques using the 150-200 kHz linear frequency sweep, increasing from 1 to 30 scatterers, with 400 simulated trials for each number of scatterers (curves) and 20 experimental trials for 14, 16, 18, and 20 scatterers (data points): conventional beamforming (dotted black, black diamond), and frequency-difference beamforming with Δf = 10 kHz (dashed red, red 'x'), Δf = 20 kHz (dash-dot green, green circle), and Δf averaged from 5 to 25 kHz at 1 kHz increments (solid blue, blue square). Peak-to-sidelobe ratio for the same four cases (b). Error bars indicate the 95% confidence interval.

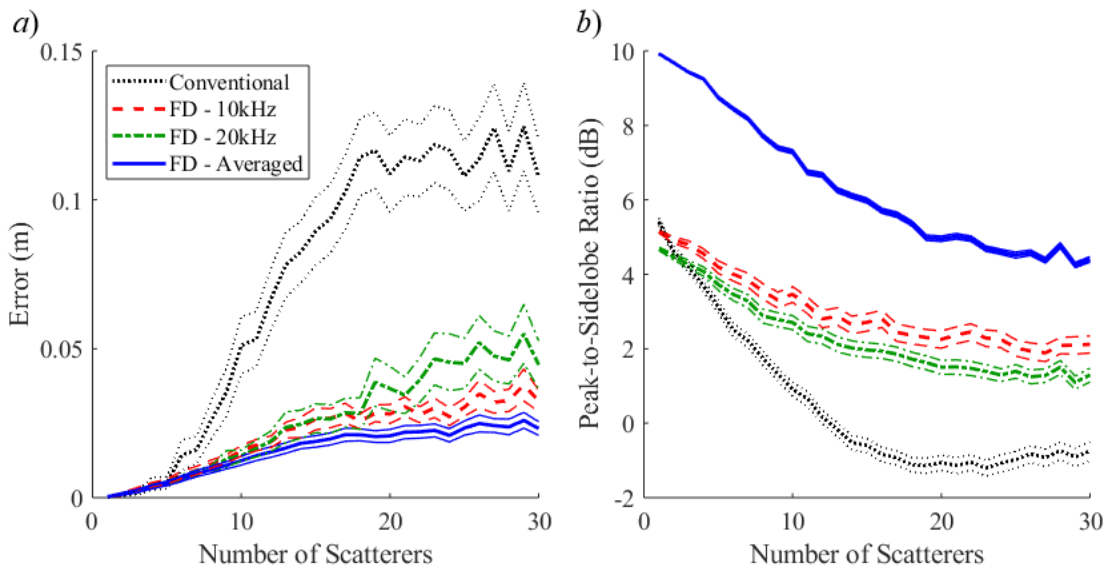

Figure 5.10: Same as Fig. 5.9 but with only the simulated results, showing the 95% confidence interval error bars.

terers so the performance stops degrading as more are added. Another key finding is that the Δf = 10 kHz case appears more accurate than the Δf = 20 kHz, despite the higher precision expected with the Δf = 20 kHz processing. Although 20 kHz is, in general, slightly more accurate than the 10 kHz case, sidelobes are more likely at the higher frequency, occasionally leading to a false peak much further from the known location than is typical at lower frequencies, thereby increasing the average error from only a few cases. The best performance comes by averaging difference frequencies, which reduces the impact of sidelobes, but potentially with some precision and dynamic range loss due to combining beamformed results from low and high difference frequencies.

In addition to varying the scatterer configurations in simulation, the same was done in experiments but only 20 different scatterer configurations were considered for 14, 16, 18, and 20 scatterers. Here, scatterer numbers were increased by simply adding scatterers to the previous configuration – i.e. 14 scatterers are placed initially, then two are added in succession to reach 16, 18, and finally 20. This process was repeated 20 times starting with new configurations of 14 scatterers, and the results are included in Fig. 5.9 as discrete data points with 95% confidence-interval error bars. Here, the conventional beamforming output is indicated with a black diamond, and the

frequency-difference outputs with a red 'x' (Δf = 10 kHz), a green circle (Δf = 20 kHz), and a blue square (Δf averaged). In addition, the experimental data are horizontally offset for visual clarity; in truth, they correspond to the integer scatterer numbers listed above. The experimental localization error results in Fig. 5.9(a) generally agree with the simulated results and follow a comparable trend as the number of scatterers increases, but with a slightly larger error on average, as might be expected from experiments with a low level of artifact scattering. However, in each case, the simulated curve falls within the experimental error bars.

Peak-to-sidelobe ratio is also an important factor in beamforming robustness, since it provides means for predicting the likelihood of failure. Figure 5.9(b) provides the average peak-to-sidelobe ratio for the same cases analyzed in Fig. 5.9(a), for both the simulated and experimental results, and shows that frequency-difference beamforming also outperforms conventional beamforming for peak-to-side-lobe ratio in these simulations and experiments. In the cases with few scatterers, where conventional beamforming performs well, the peak-to-sidelobe ratios are comparable for the single-difference-frequency implementations. However, as the number of scatterers increases and localization error increases, all methods lose peak-to-side-lobe ratio. Conventional beamforming eventually drops to a negative average peak-to-side-lobe ratio when many scatterers are present, but this ratio remains positive for all three frequency-difference methods, with the single-difference-frequency results steadily leveling out in the 1-2 dB range between 20 and 30 scatterers, similar to the behavior in Fig. 5.9(a). Interestingly, averaging across difference frequencies yields a peak-to-sidelobe ratio average of 2-7 dB higher than all other methods. This averaging works to suppress undesired peaks in the beamformer output, significantly improving peak-to-sidelobe ratio in spite of the expected loss in dynamic range.

Another interesting finding is that, in general, the experimental peak-to-sidelobe performance is very comparable to the simulated cases, except for some notable discrepancy in the difference frequency averaging case. This could be the result of incomplete statistical convergence, since 20 experimental cases are being compared to 400 simulated cases, or could indicate an effect from higher order scattering, especially in fields dense with scatterers where multiple shadow zones may

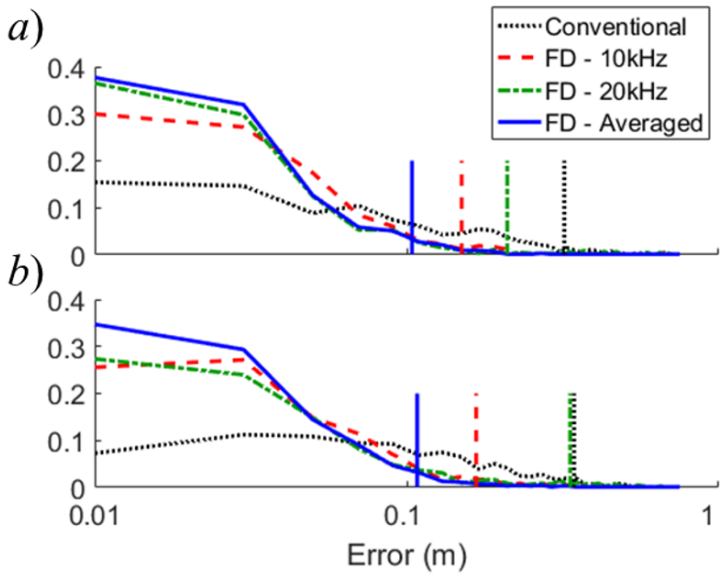

Figure 5.11: Source localization error histograms for five different source locations with 20 scatterers (a) and 30 scatterers (b). For each source location, 100 simulations are performed with random scatterer placement. The plots above are generated from histogram outputs of the source location error, thus the y-axis corresponds to the fraction of samples that fall within a window of error of 2 cm, with the data point centered in each bin. For clarity, the x-axis is plotted as a log scale. The vertical bars indicate the points where 95% of the errors have been accounted for.

be expected to overlap.

5.3.2 Different Source Locations

Simulations were also used to determine if the observed localization and imaging performance for (x_s, y_s) = (40 cm, –10 cm) persists at other source locations. Thus, for six different source locations within the geometry defined in Fig. 1, a similar analysis to that above was conducted via simulation, with fewer trials (100 instead of 400), and for only two scatterer counts (20 and 30) placed in the same region identified in Fig. 1a). With fewer trials, the results are not quite as robust an indicator, but it is unlikely that a dramatic change in performance would be observed by increasing the number of cases from 100. The localization performance of frequency-difference beamforming methods relative to conventional methods for various source locations is comparable to the results presented above and is shown in Fig. 5.11. This figure provides histogram outputs

for location error using 2 cm wide bins starting at 0 cm (and plotted at the bin centers). The localization error is plotted with a log scale on the x-axis while the y-axis is the fraction of cases that fall within that error bin. The vertical lines indicate the point where 95% of the samples are accounted for. In both cases, the difference frequency averaging yields the best results, while the two difference frequency cases still perform better than the conventional method, indicated by the spread of the error away from 0.

5.3.3 Multiple Realizations

The final consideration involves averaging the beamforming outputs from multiple realizations of the random scatterers. Such averaging would be possible in some practical scenarios where the scatterers are not stationary, but an array of receivers is still being used to locate or image a remote source using multiple signal samples, perhaps obtained by segmenting a longer signal recording.

For the study performed here, groupings of 2, 5, and 10 realizations with 20 scatterers ($\frac{\langle|r_{0j}|\rangle}{l_s}$ = 2.9) were considered with the groupings chosen randomly from the 400 simulated cases or the 20 experimental cases. The compiled results of this effort are summarized in Table 5.1. Here, the average error is shown in bold for each case, and the error bound containing 95% of the results below that number, providing the same information as the vertical lines in Fig. 5.11. As expected, the trend of decreasing error and decreasing variability of the error as more realizations are added is apparent in both the simulated and experimental results. For all frequency-difference beamforming cases in both simulation and experiment, combining up to 10 realizations yielded an average error of less than 2 cm and as low as 0.4 cm, with the 95% thresholds within 3 cm of the average. The difference in error between the simulated and experimental results is easily accounted for with experimental uncertainty and additional scattering effects between the simulated and recorded experimental components. For conventional beamforming, the absolute improvement in source localization with more realizations is larger, but the proportional improvement is comparable to that seen in frequency-difference beamforming, leaving an error that is 3-6 times larger in all cases. In addition, the 95% threshold for conventional beamforming is anywhere from 8 to 27 times

Table 5.1: Average source localization error and 95% error threshold for multiple realization averaging. Either 2, 5, or 10 realizations are chosen from either 400 different scatterer configurations in simulation or 20 different scatterer configurations in experiments. A total of 200,000 different combinations was considered for each case, except for 2 realizations where the total possible number of combinations was just 159,600 (simulations) or 380 (experiments).

			Absolute Localization Error (cm)			
	Number of Realizations		Conventional f = 150-200kHz	Freq. Diff. Δf = 10kHz	Freq. Diff. Δf = 20kHz	Freq. Diff. Δf = 5-25kHz
Simulation	2	Average	**9.6**	**1.7**	**1.5**	**1.3**
		95%	38.5	4.6	4.3	4.0
	5	Average	**6.7**	**1.0**	**0.7**	**0.7**
		95%	31.0	3.0	2.3	2.2
	10	Average	**3.7**	**0.6**	**0.4**	**0.4**
		95%	21.0	1.8	1.0	1.0
Experiment	2	Average	**13.5**	**2.2**	**2.0**	**1.9**
		95%	57.1	3.8	4.0	3.9
	5	Average	**10.5**	**1.5**	**1.6**	**1.6**
		95%	57.0	2.4	2.3	2.4
	10	Average	**5.9**	**1.2**	**1.6**	**1.6**
		95%	56.0	2.1	2.3	2.2

larger. While all methods improve with additional realizations, the performance of the frequency-difference methods reduces the error to nearly negligible levels as more realizations are included, and the individual outputs tend to be more stable, as indicated by the 95% threshold.

To illustrate the effect of averaging realizations, Fig. 5.12 shows a typical output from averaging 10 beamforming outputs for the same source location, where each data set is from either a simulation or experiment with 20 scatterers. Many combination possibilities exist from the 400 simulated data sets and the 20 experimental data sets, so a combination that produced a result with a localization error close to the average was chosen. Figures 5.12(a) and (b) show simulated data for conventional beamforming using the full 150-200 kHz bandwidth and for frequency-difference beamforming at Δf averaged between 5 and 25 kHz, respectively. Figures 5.12(c) and (d) show the corresponding experimental results for both methods. The most notable feature of these plots is

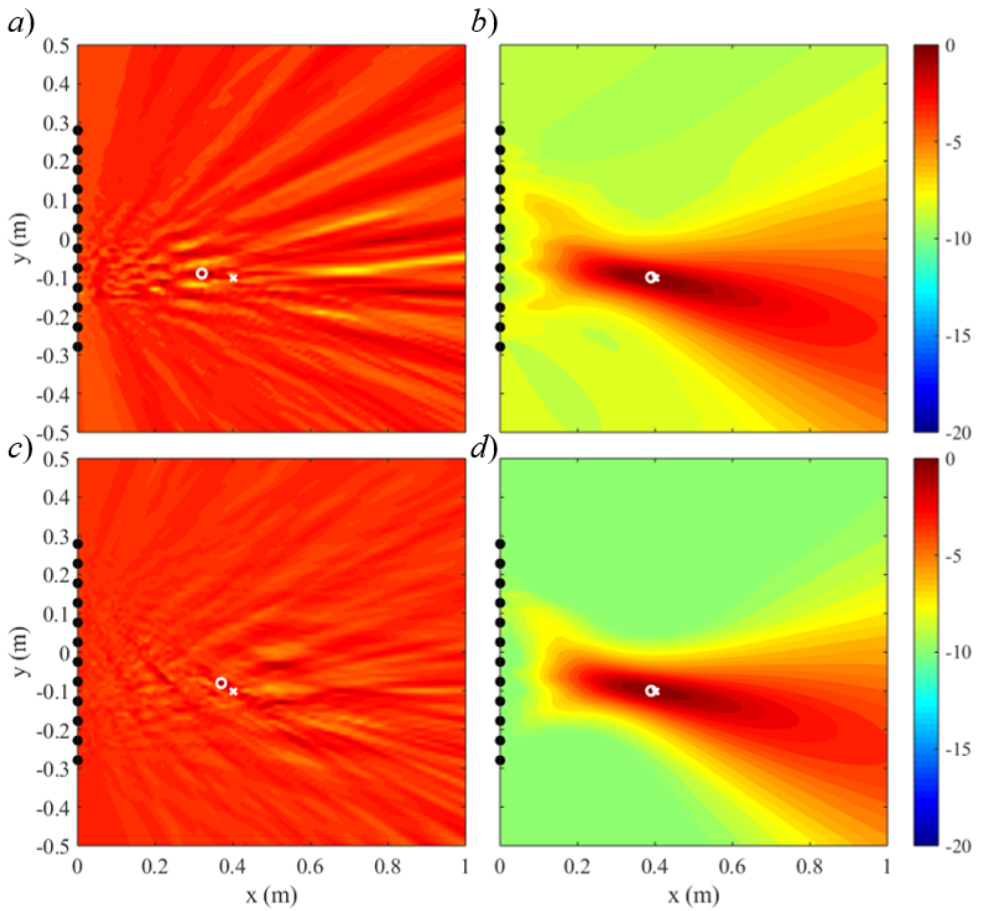

Figure 5.12: Average beamforming outputs for 10 realizations in simulation (a,b) and experiment (c,d) for conventional beamforming between 150-200 kHz (a,c) and frequency-difference beamforming from 150-200 kHz with Δf averaged from 5 to 25 kHz. The expected source location is indicated with a white 'x' and the beamformer peak indicated by a white circle.

the loss in dynamic range in the conventional beamforming output. The highly varying ambiguity surfaces from each realization yield peaks or low dynamic range throughout most of the field when averaged together, causing a drop in dynamic range and a multitude of peaks close to 0 dB. On the other hand, the main lobe in the frequency-difference outputs consistently surrounds the actual source location and provides an accurate localization result while maintaining approximately 8 to 10 dB of dynamic range.

5.4 Summary and Conclusions

Frequency-difference beamforming is a technique for robust beamforming of non-zero bandwidth signals at lower, out-of-band frequencies. It is based on replacing the recorded in-band field with the quadratic frequency-difference autoproduct field in standard beamforming techniques and then evaluating these techniques at the difference frequency. Past investigation of frequency-difference beamforming found it to be viable remedy for sparse arrays [2] [45]. The performance of spherical-wave frequency-difference beamforming was considered here with multiple strong scatterers placed between the source and the receiving array. Results from simulations and experiments both show that frequency-difference beamforming can succeed in the presence of strong scattering when conventional beamforming fails. However, the point spread of frequency-difference beamforming is set by the lower below-band difference frequency wave number (Δk), and not by the higher in-band center-frequency wave number (k). The source localization results here would likely scale to smaller or larger experiments if the wavelengths and scatterers are appropriately scaled as well. Differing scenarios, such as those with many weaker scatterers, continuously varying environments, rough surface reflections, etc., might see similar benefits from frequency-difference beamforming, but the error scaling may differ. In particular, moving to an environment such as the shallow ocean is substantially different from the environment considered here, but may see benefits within the error constraints of such an application.

Five conclusions can be drawn from the results presented here. (1) In cases where strong random scattering causes the in-band, complex, beamformed direct-path field to add destructively with its corresponding scattered field at the source location, the equivalent below-band, complex, beamformed autoproduct fields add constructively at the same location. However, the focal region formed by the autoproduct at the source location has lower precision than that possible with the in-band field; its dimensions are proportional to $1/\Delta k$, and not $1/k$. (2) In the presence of strong random scattering, spherical-wave frequency-difference beamforming provides better localization (imaging) performance than conventional spherical-wave beamforming using the same

high frequency signals. As shown herein, when multiple acoustically-large high-contrast spherical scatterers (ka = 14.7) are placed between a source and a sparse receiving array, the localization error from frequency-difference beamforming was significantly lower on average in both simulations and experiments. (3) Frequency-difference beamforming maintains a positive average peak-to-side-lobe ratio when conventional beamforming of the same array recordings produces a negative one. For the simulations and experiments described here, the peak-to-side-lobe ratio for the frequency-difference methods was typically 2-7 dB better than that of conventional beamforming using the same signal recordings, with the best results involving additional averaging across difference frequencies. (4) The performance of frequency-difference beamforming relative to conventional beamforming is maintained for varying scatterer configurations and varying source locations. (5) Averaging multiple realizations improves the localization performance of all methods, but frequency-difference beamforming maintains a higher dynamic range relative to conventional beamforming – a difference of about 5-10 dB for any given case – when strong random scattering is present. Overall, frequency-difference beamforming provides a lower precision but more robust beamforming output than conventional beamforming in the presence of strong random scattering.

CHAPTER 6

Synthetic Time Reversal for Time-Varying Underwater Communications

Underwater communication applications regularly utilize acoustics as a means of transmitting information, due primarily to the fact that electromagnetic waves, the primary alternative, attenuate quickly in water, particularly at the shorter wavelengths that are feasible for use in underwater applications. As a result, acoustics is generally a more useful method of communicating over long distances in an underwater environment. Many characteristics of underwater sound channels make communications difficult - multipath propagation, frequency-dependent attenuation, noisy backgrounds, doppler effects, time-varying environments, etc. all contribute to errors in communication sequences [154] [131]. Until the early 2000s, most underwater acoustic communication progress with coherent receiver arrays utilized decision feedback equalizers (DFEs) or Phase Locked Loops (PLL) [86].

The use of time reversal (TR) in underwater communications was introduced in 2002 [50] and has seen significant development and progress since [131]. Generally, TR uses a known probe signal to calculate a channel impulse response (CIR), which is used to combine the receiver outputs into a single output. At this point, a DFE is typically used to remove residual inter-symbol interference (ISI). The required probe signal is a potential downside to TR, as it must be known a priori and frequent intermittent probe signals may be required in time-varying environments, interrupting the stream of useful information. However, without a probe signal, the problem becomes an ill-posed blind deconvolution scenario.

Synthetic time reversal (STR) [117] [118] is a blind deconvolution technique that simultaneously estimates the source signal and CIR using only the receiver array outputs by making an assumption about the acoustic wave propagation (ray- or mode-based). This chapter focuses on using STR for communication signals without the need of a probe signal and as a method for adapting to a time-varying CIR by utilizing real-time CIR updates. The goal of this chapter is to successfully demodulate a long-duration signal in a time-varying environment using a blind deconvolution technique. The success of the technique will be evaluated by demonstrating a reduction in bit error rate in the communication signal and an improvement in signal-to-noise ratio (SNR) of the bits received (here, SNR is a measure of average bit error, expressed in dB).

6.1 Mathematical Formulation

6.1.1 Communication Signals

The work presented here will utilize binary phase shift keying (BPSK) communication signals - other types of communication signals will not be thoroughly discussed, but could potentially be useful when combined with STR. Communication system design is a well studied area and references are easily found [113], so only a high level overview is presented here for completeness. First, an M-ary PSK signal waveform $s_m(t)$ is represented in the time domain by

$$s_m(t) = h(t) * \cos\left[2\pi f_c t + \frac{2\pi}{M}(m-1)\right], \tag{6.1}$$

for a single symbol, where m is one of the M possible symbols or bit combinations, $h(t)$ is the signal pulse shape, and f_c is the carrier frequency; the full communication signal is generated as a series of these symbols. For BPSK signals, there are only two possible symbols, either +1 or -1, which correspond to a 0 or 1 bit, respectively, which generate waveforms that are separated in phase by π radians. Higher order PSK sequences form combinations of 0 and 1 for each possible waveform (for example, 00, 01, 10, 11 for QPSK), but aren't considered here. The successful

demodulation of a communication signal is based on two parameters here, the bit error rate (BER) - the percentage of incorrect bits in the signal - and the signal-to-noise ratio (SNR), defined by

$$\text{SNR} = -20\log_{10}\left(\frac{1}{N_{bits}}\sum_{n=1}^{N_{bits}} q(n) - \tilde{q}(n)\right), \tag{6.2}$$

where $q(n)$ and $\tilde{q}(n)$ are the known and estimated demodulated signals, respectively. Note that this definition of SNR is specific to communication signals, and thus is different than that considered in previous chapters and the following chapter. If the average error is less than 1 (which is expected in non-failure cases), the negative sign in Eq. 6.2 generates a positive SNR, indicating the average bit has not crossed into a region where it would be mistaken for the opposite value. Once the communication signal is recovered, it is shifted to baseband (i.e. the carrier frequency is removed from the signal, ideally leaving a signal composed of only +1 and -1 values, for the BPSK case) and samples are averaged together if more than one sample is expected per symbol.

A common tool used in the demodulation of communication signals is the Decision Feedback Equalizer (DFE). A DFE utilizes a training sequence of known bits to determine a set of coefficients, sometimes referred to as "taps", which are utilized to remove inter-symbol interference (ISI). The k^{th} symbol, $\hat{q}_k$, is then given as

$$\hat{q}_k = \sum_{j=-K_1}^{0} v_j z_{k-j} + \sum_{j=1}^{K_2} v_j \tilde{q}_{k-j}. \tag{6.3}$$

This is a combination of undetermined symbols, z_k, previously detected symbols, $\tilde{q}_k$, and their tap coefficients, v_j. The taps fed into the DFE are both feedforward (K_1) and feedback (K_2). This process is summarized in Fig. 6.1.

6.1.2 Synthetic Time Reversal

Conventional TR methods with a probe signal aim to solve Eq. 2.4 by measuring $P(\vec{r}, \omega)$ and using prior knowledge of the portion of $s(t)$ corresponding to the probe signal to calculate $G(\vec{r}_s, \vec{r}_j, \omega)$. $G(\vec{r}_s, \vec{r}_j, \omega)$ is then assumed to be steady throughout the communication portion of the

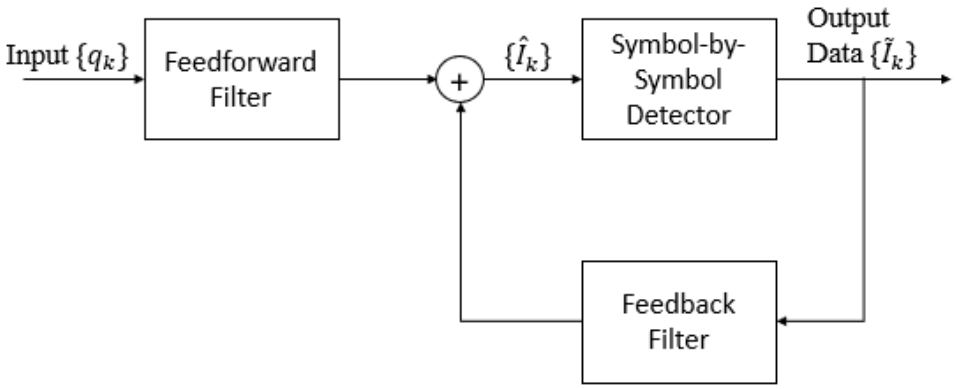

Figure 6.1: DFE process.

signal (until a new probe signal is broadcast), and combined with Eqs. 2.3 and 2.4 to recover the remainder of the signal $s(t)$. With Synthetic Time Reversal (STR), $s(t)$ is completely unknown, so both $G(\vec{r}_s, \vec{r}_j, \omega)$ and $S(\omega)$ are determined simultaneously in order to obtain the communication portion of $s(t)$. The derivation of STR starts by rewriting Eq. 2.4 as

$$S(\omega) = \sum_{j=1}^{N} G(\vec{r}_s, \vec{r}_j, \omega)^* P(\vec{r}_j, \omega), \tag{6.4}$$

with * representing a complex conjugate. Once the Green's function is determined, the source signal is known by default. In the frequency domain, the source term can be rewritten as a combination of frequency-dependent amplitude and phase terms,

$$S(\omega) = |S(\omega)| e^{i\alpha(\omega)}. \tag{6.5}$$

Using Eq. 6.5 to rewrite Eq. 2.4 as

$$P(\vec{r}_j, \omega) = |S(\omega)| e^{i\alpha(\omega)} G(\vec{r}_j, \vec{r}_s, \omega) \tag{6.6}$$

and normalizing, provides

$$\frac{P(\vec{r}_j,\omega)}{\sqrt{\sum_{j=1}^{N}\left|P(\vec{r}_j,\omega)\right|^2}} = \frac{|S(\omega)|\,e^{i\alpha(\omega)}}{|S(\omega)|}\frac{G(\vec{r}_s,\vec{r}_j,\omega)}{\sqrt{\sum_{j=1}^{N}\left|G(\vec{r}_s,\vec{r}_j,\omega)\right|^2}}. \tag{6.7}$$

Since the signal amplitude terms cancel, the equation reduces to one for a normalized Green's function, where the only unknown on the left hand side is the signal phase term, $\alpha(\omega)$

$$\frac{P(\vec{r}_j,\omega)e^{i\alpha(\omega)}}{\sqrt{\sum_{j=1}^{N}\left|P(\vec{r}_j,\omega)\right|^2}} = \frac{G(\vec{r}_s,\vec{r}_j,\omega)}{\sqrt{\sum_{j=1}^{N}\left|G(\vec{r}_s,\vec{r}_j,\omega)\right|^2}}. \tag{6.8}$$

If this phase term can be determined accurately, then a normalized Green's function is easily calculated. Unfortunately, the normalized Green's function removes amplitude information from the propagation, but this is ideally recovered from the array outputs when substituted into Eq. 6.5, though it ignores any frequency-dependent attenuation or dispersion.

The critical piece of the STR technique is the estimation of the signal phase term, $\alpha(\omega)$. Two techniques for this step have been developed, one based on modal propagation models [117] and one based on ray propagation models [118][2][3]. Here, only ray-based propagation will be considered, since communication signals generally utilize higher frequencies (for increased rates of data transmission). The phase term is estimated using conventional plane-wave (or spherical-wave) beamforming techniques. First, a beamformer is used to isolate a ray path (or source location) using Eq. 2.6. Once the direction (or location) is determined, the beamforming output from 2.6, prior to squaring, is utilized, i.e.

$$b_{conv}(\omega) = \sum_{j=1}^{N} P_j(\omega)w_j(\omega). \tag{6.9}$$

Choosing a peak from the output of Eq. 6.9 provides a complex value from which a phase can be calculated. Since this output results from combining all receiver outputs based on a single source direction (or location), influence from other ray paths is minimized in the summing procedure. In addition, a successful beamforming result removes the spatial phase contribution, by nature of the technique. The resulting frequency-dependent phase recovered from Eq. 6.9 is then used to

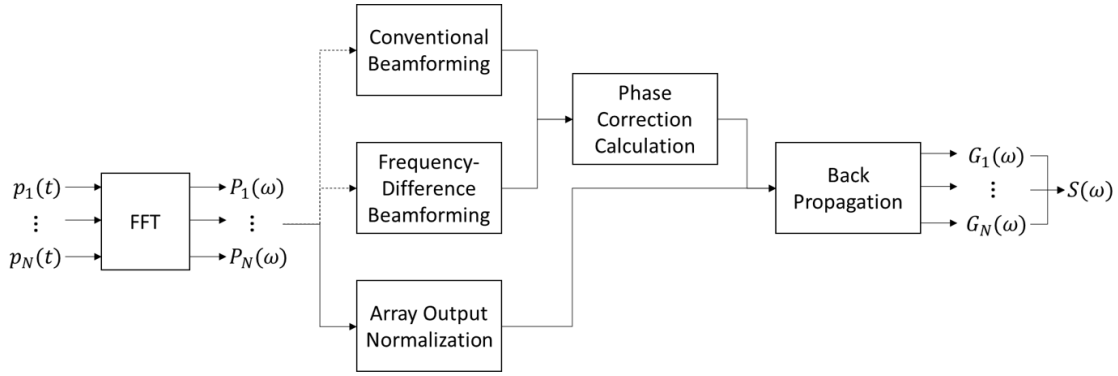

Figure 6.2: STR process.

calculate $\alpha(\omega)$,

$$\alpha(\omega) = arg(b(\theta_m, \omega)). \tag{6.10}$$

Ideally, by removing the geometric phase dependencies through the beamforming process, the source signal phase is recovered. This result is substituted into Eq. 6.8 to calculate the normalized Green's function, and from here, the source signal is determined by

$$S(\omega) = \sum_{j=1}^{N} \left\{ \frac{P(\vec{r}_j, \omega) e^{-i\alpha(\omega)}}{\sqrt{\sum_{j=1}^{N} \left| P(\vec{r}_j, \omega) \right|^2}} \right\}^* P(\vec{r}_j, \omega). \tag{6.11}$$

As previously mentioned, communications can benefit from using higher frequency signals, which can potentially lead to reduced beamforming capabilities if the array is not appropriately designed for the signal's carrier frequency. Thus, in some cases, it is preferential to use frequency-difference beamforming methods, rather than conventional [3]. The STR process with frequency-difference beamforming is similar, with the key difference being the phase term calculation. While an absolute phase can be calculated using Eq. 6.10, only relative phases can be determined with frequency-difference methods. Thus, a reference phase must be chosen at one frequency, and all other phases are determined relative to the reference. The beamforming output from Eq. 6.9

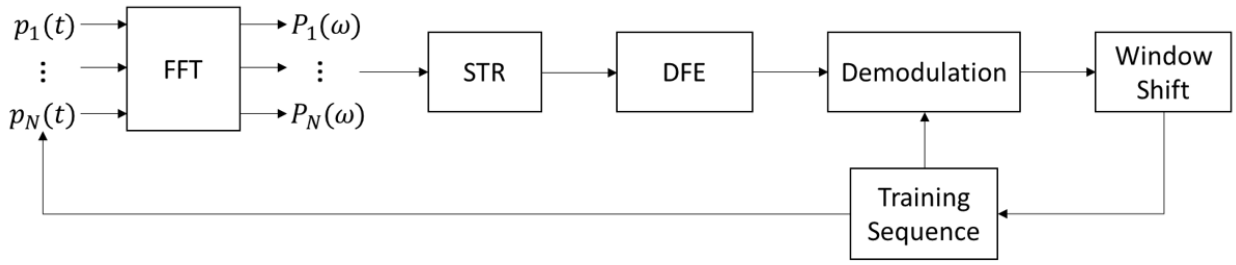

Figure 6.3: OSTR-DFE process.

becomes

$$b_\Delta(\theta_m, \omega_1, \omega_2) = \sum_{j=1}^{N} P^*(\vec{r}_j, \omega_1) P(\vec{r}_j, \omega_2) w_j(\Delta\omega), \tag{6.12}$$

where $\Delta\omega = \omega_2 - \omega_1$. Using this beamforming output for the phase calculation, Eq. 6.10 becomes

$$\alpha(\omega_q) = \sum_{q=2}^{Q} arg(b_\Delta(\theta_m, \omega_{q-1}, \omega_q)) + (Q-1)K. \tag{6.13}$$

Here, Q is the total number of frequencies used from the signal bandwidth and K is an unknown constant phase term that results from not having information about the absolute phase. The linearly-dependent phase term resulting from the constant K leads to an unknown time shift in the signal when using STR, which may not be a concern when considering a whole signal, but can increase difficulty if signal subsets or noisy signals are being considered, since the signal or window starting point may be difficult to identify. The STR process described here for both conventional and frequency-difference beamforming is summarized in Fig. 6.2.

In time-varying environments, STR's capability to estimate the signal and impulse response will degrade as the magnitude and rate of variation increases. This is also a problem with the conventional TR technique, which is solved with impulse response updates that come from re-broadcasting probe signals. However, since STR is capable of estimating the signal without using a probe signal, the impulse response can be updated in real time without disrupting the signal broadcast, and thus the flow of information. For long-duration signals where changes are likely, simply choosing the correct window size - short enough such that the impulse response is roughly

static, but long enough that enough information exists to reconstruct the signal - ideally allows signal recovery at any point in time. This technique, called Overlapping STR (OSTR), simply applies the STR technique to consecutive windows, with overlapping portions that are averaged together, while stepping through the full signal. A single-channel DFE can then be applied either after the full signal reconstruction, using a single training sequence at the beginning, or to each individual STR window, using the overlapping bits as a training sequence. For this work, the DFE will be applied on each individual window and the technique will be referred to as OSTR-DFE. The OSTR-DFE process used here is summarized in Fig. 6.3.

6.2 Water Tank Experiments

The benefits of STR and its applications to underwater communications are initially demonstrated in a controlled laboratory experiment. For this experiment, the same water tank shown in Fig. 2.2 is used. The tank provides a nearly noise-free environment with an abundance of reflected paths, with the strong early paths predictable based on the geometry. In this experiment, a randomly generated 4096-bit BPSK signal is broadcast with a 50 kHz carrier frequency. Each bit consists of four cycles of a sine wave with either a 0° or 180° phase shift, corresponding to a 0 or 1 bit (+1 or -1 symbol), respectively. The receiving array is a 2-D, 4-by-4 element array of Reson TC4013 hydrophones with 1 in. vertical and horizontal spacing. The source, an ITC-1042, is placed approximately 0.39 m from the array center and roughly 26° from broadside, in the horizontal plane crossing the center of the array. Several different experimental conditions are considered - (i) a static but reverberant environment, (ii) a static environment with the same configuration but with an absorbing material placed between the source and array to encourage use of the surface reflection, and (iii) this same case but with a dynamic surface condition, causing a dynamic surface reflection. Figure 6.4 shows the tank geometry, as well as a picture of the experimental setup.

The first case considered is the static, but highly reverberant environment (i). In order to visualize the level of reverberation present in the tank, Fig. 6.5 shows a waterfall plot for a single-bit

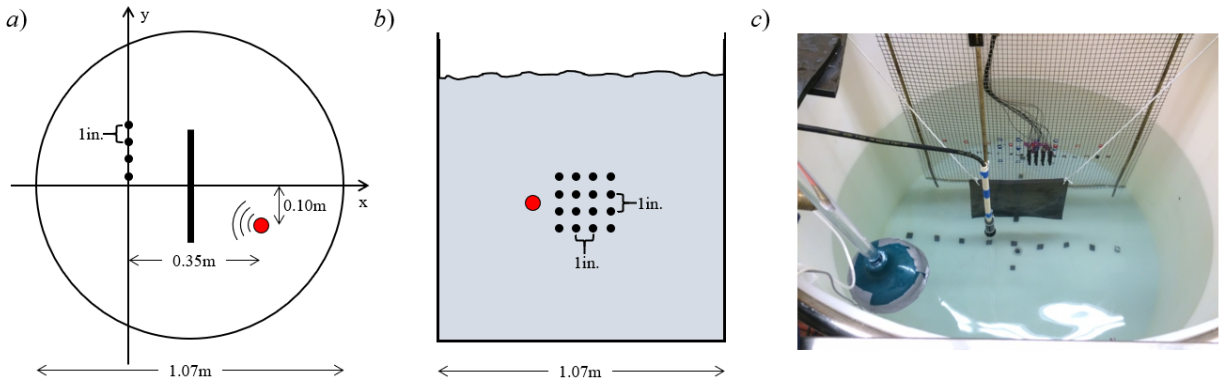

Figure 6.4: Geometry used for water tank experiments. The tank has a 1.07 m diameter and a depth of approximately 0.9 m. A 4-by-4 element receiving array with 1 in. spacing is placed as shown relative to a source lying on the x-y plane that crosses the center of the array along the z-axis. Reflections from the tank walls, bottom, and water surface create significant reverberation in the measurements. In some experiments an absorptive sheet is placed between the source and receiver array (vertical black bar) in order to emphasize the strength of the reflected path relative to the direct path. Here, the geometry is shown from above (a), from the side along the x-axis (b), and with a real picture of the setup (c). A plunger is used to manually generate surface waves to create a time-varying impulse response in one of the experiments.

broadcast (a), which provides a signal that is short enough to visually identify most individual arrivals, particularly the early ones. In addition to the single-bit broadcast, the impulse response determined with STR for the same, known signal is plotted (b) for a more genuine look at the impulse response and for comparison to the single-bit broadcast. From here, it is clear that there are two expected early arrivals - a direct path and a surface reflection, which blend together slightly in the single-bit case. Beyond these two arrivals, at least five additional paths can be easily identified in this window, but likely more. These plots demonstrate that the multi-path in this tank is significant and will potentially harm the deconvolution and demodulation processes. An analysis of the signal energy from this broadcast indicates a signal-to-reverberation ratio of -4.5 dB and a T60 reverberation time of roughly 13 ms.

Two methods will be used in this section for blind deconvolution of the signal - Delay-and-Sum (D&S) Beamforming and STR, both of which rely on an initial, successful beamforming output. Plane-wave beamforming is used in two dimensions here, over angles θ (azimuth angle)

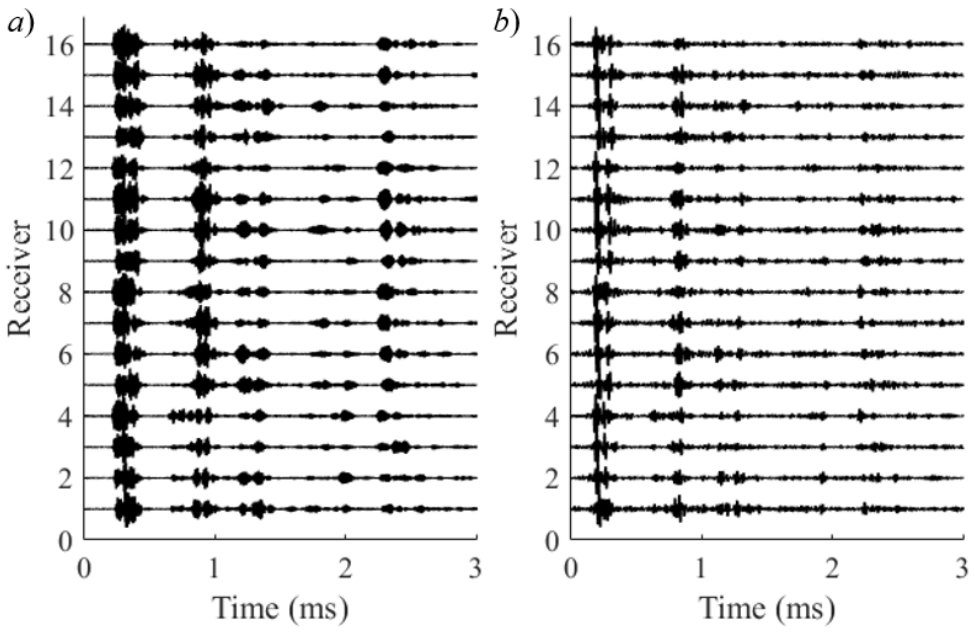

Figure 6.5: Waterfall plots of a single-bit broadcast (a) and the impulse response function determined by STR (b).

and ϕ (polar angle), the output of which is shown in Fig. 6.6. Here, the direct path is at roughly $\theta = 28°$ and $\phi = 3°$, a strong reflection from the negative θ side of the search grid is present with a comparable intensity, a surface reflection directly above the direct path is clear, and several additional weaker paths exist as well. It is noteworthy that the surface reflection doesn't appear to be the second strongest arrival, as one might expect (since it has the shortest travel time of any path except the direct path). This is most likely due to the tank wall's curvature, which causes a non-negligible amount of signal focusing, increasing the intensity along the beam reflected from the wall. The key observation from this output is that several strong beams are available to choose from for both blind deconvolution methods.

The deconvolved and demodulated signal outputs for this first case are shown in the demodulation plots in Fig. 6.7. Here, each blue dot corresponds to a single bit, which is represented as a +1 or a -1 on the real axis, and 0 on the imaginary axis. In both cases, the influence of multipath propagation, interference with experimental components, experimental uncertainty, and non-ideal broadcast signals is clear, since many bits lie quite far from the expected bit location (indicated by

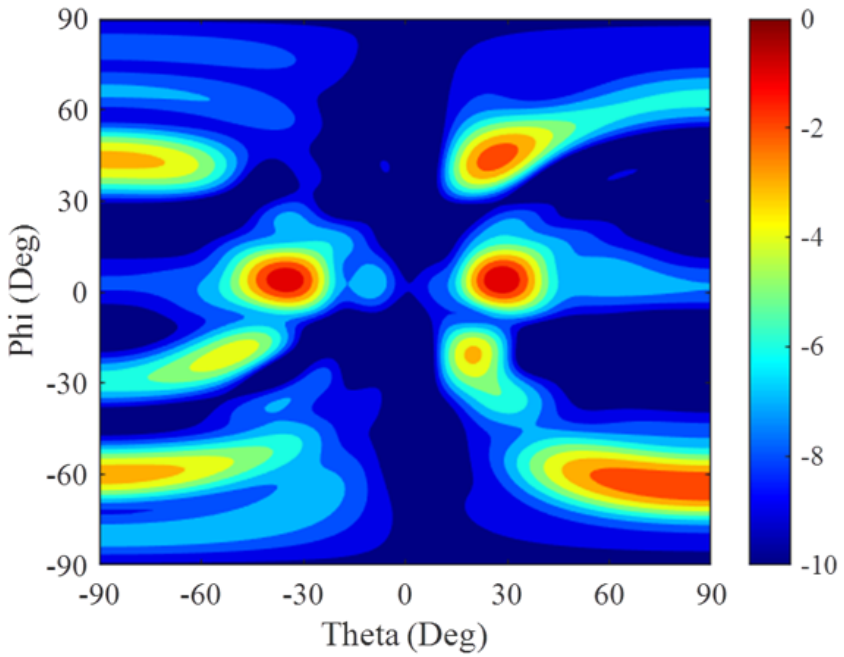

Figure 6.6: Beamforming output for a static environment with an unobstructed direct path, shown on a normalized decibel scale.

the two black 'x's). However, for BPSK, the success of a bit is effectively determined by whether or not it is in the correct half-plane - each red dot shown here indicates a bit lying in the incorrect half-plane. In this experiment, both methods have performed well, with some improvements apparent in the STR case, due to the incorporation of reflected paths in the blind deconvolution step. Here, the BERs and SNRs for the two cases are 0.81% and 5.0 dB (D&S) and 0.098% and 6.4 dB (STR). The SNR improvement in STR can be visually observed by considering the size of the clouds of bits compared with the D&S case, and the BER improvement is shown by the decreased number of red dots (which becomes more challenging to see for higher BERs with many overlapping bits).

With the given experimental setup and the short duration of the communication signal, generating a time-varying direct path is difficult, so instead the conditions of the water's surface can be changed. Here, this is done by manually oscillating a plunger slightly below the water's surface, generating waves at the point(s) of surface reflection. In order to increase the influence of the surface reflection, a sheet of absorbing material is placed between the source and the array to weaken

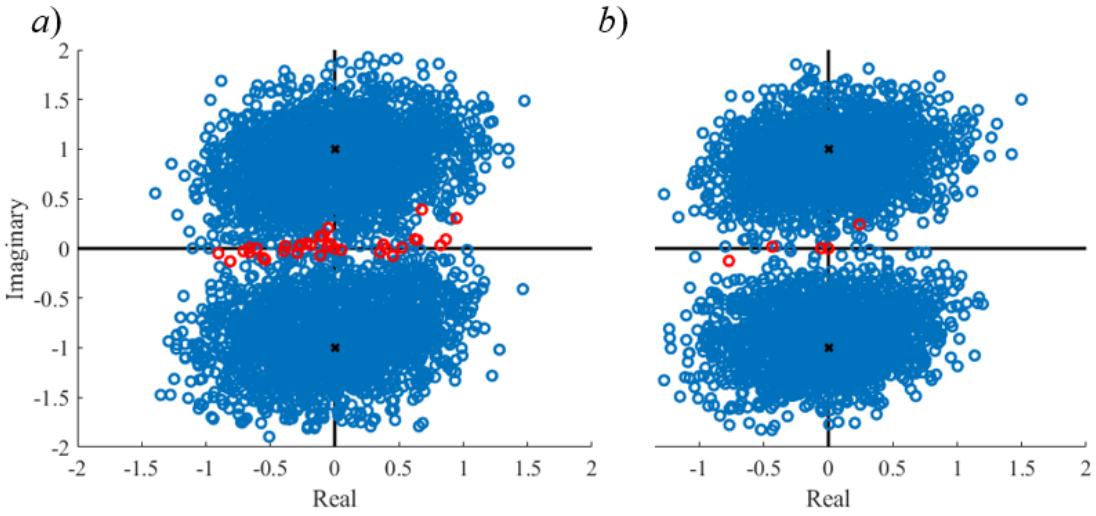

Figure 6.7: Demodulation outputs for Delay-and-Sum (a) and STR (b) for the static case with an unobstructed direct path. Here, D&S has a BER = 0.81% and an SNR = 5.0 dB; STR has a BER = 0.098% and an SNR = 6.4 dB.

(but not totally remove) the direct path. The effects on the impulse response and the beamformer outputs are shown in Figs. 6.8 and 6.9. The weakened direct path amplitude is clearly seen in the impulse responses plots, with the reflected path showing significantly more prominence. This can also be observed in the beamformed output, Fig. 6.9, where the direct path is present but is reduced in amplitude by several dB, while reflected paths from angles of ϕ not aligned with the direct path show an increase in relative amplitude. Another relevant observation is that the amplitude of some later arrivals has been reduced, due to the fact that reflected paths are also interacting with the absorption material, impacting the overall reverberation levels in the tank and bringing the T60 reverberation time down to roughly 8 ms.

Two cases for this experimental setup prior to introducing the time-varying surface conditions. In one case, the beamformer is still forced to use the direct path for deconvolution, and in the other it is allowed to choose a path, which leads to the choice of the surface reflection. When the direct path is chosen, D&S and STR achieve BERs of 0.37% and 0.0073%, and SNRs of 4.8 dB and 7.0 dB, respectively. With the direct path's reduction in intensity, the additional paths have a more significant impact on D&S, which is evident in the demodulation plot shown in Fig. 6.10(a), where the bits have spread significantly (it should be noted that in this figure and all demodulation

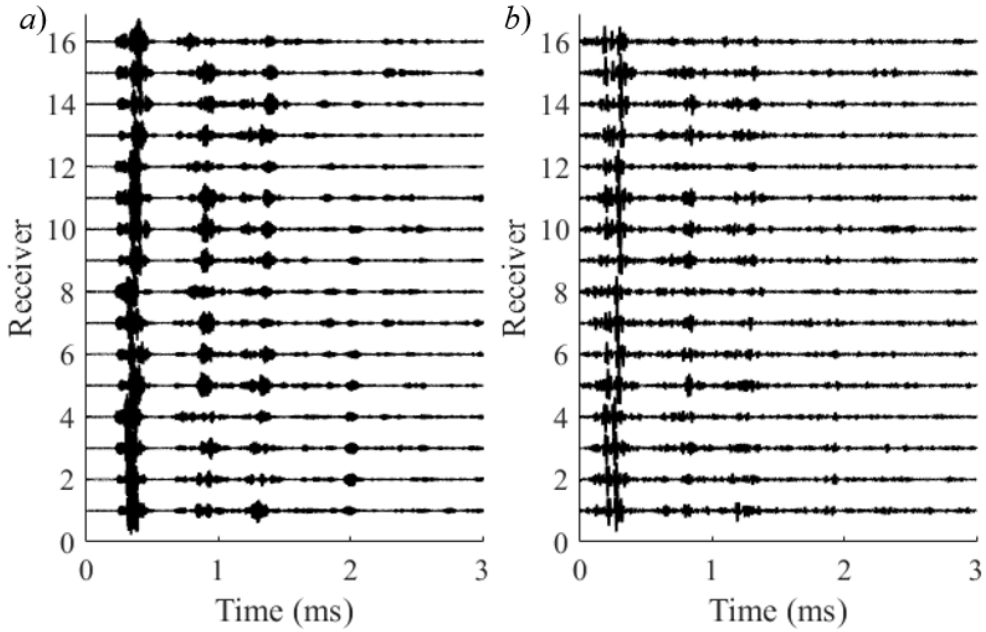

Figure 6.8: Waterfall plots of a single-bit broadcast (a) and the impulse response function determined by STR (b) for a case with a weakened direct path.

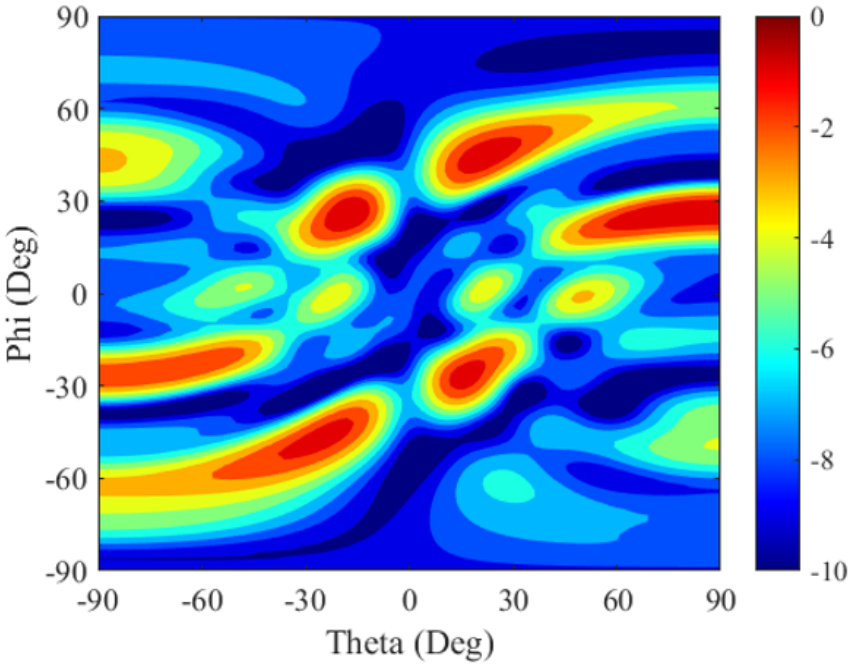

Figure 6.9: Beamforming output for a static environment with a weakened direct path, shown in a normalized decibel scale.

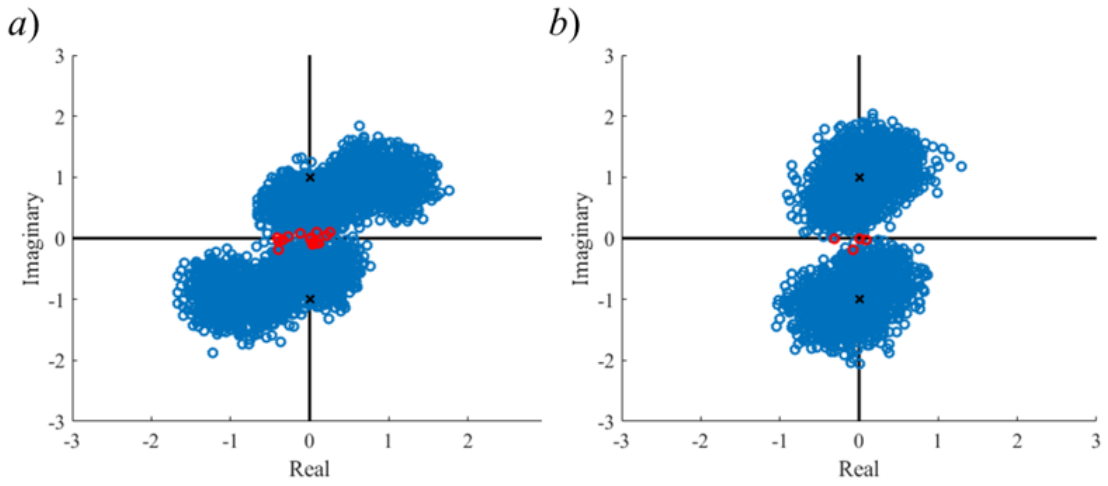

Figure 6.10: Demodulation plots in a static environment with a weakened direct path, using the direct path for blind deconvolution, for D&S Beamforming (a) and STR (b). Here, D&S has a BER = 0.37% and an SNR = 4.8 dB; STR has a BER = 0.0073% and an SNR = 7.0 dB.

plots to follow in this section, the axes have been adjusted to show a larger window). While STR (b) will perform better when using a strong path, it suffers substantially less from the use of the weakened path when compared with D&S, since it utilizes the strong, later-arriving paths as well. Although the weak direct path may hurt the performance of both methods, it is notable that the SNRs are comparable to the case without the obstruction, most likely due to the reduced levels of reverberation that make demodulation easier. When the reflected path is used for the beamforming, as shown in Fig. 6.11, both methods are able to achieve zero bit errors and SNRs of 11.6 dB and 12.4 dB for D&S (a) and STR (b), respectively. Since the reflected path is the strongest in the window, its use leads to better performance, but it is also more susceptible to variations over time. Some indication of this is potentially seen in Fig. 6.11 (particularly in (a)) with the horizontally spread bits, possibly indicating a shift in path length from mild surface motion in the water tank, generating a geometry-dependent phase shift.

The final consideration is that of a time-varying environment and a weakened direct path. In such a case, if the reflected path is strongest, the beamformer may still choose it for blind deconvolution purposes, despite it providing a poor choice due to its variation. The dynamic impulse response from this experiment is shown in Fig. 6.12, where STR is performed on short, 6.4 ms

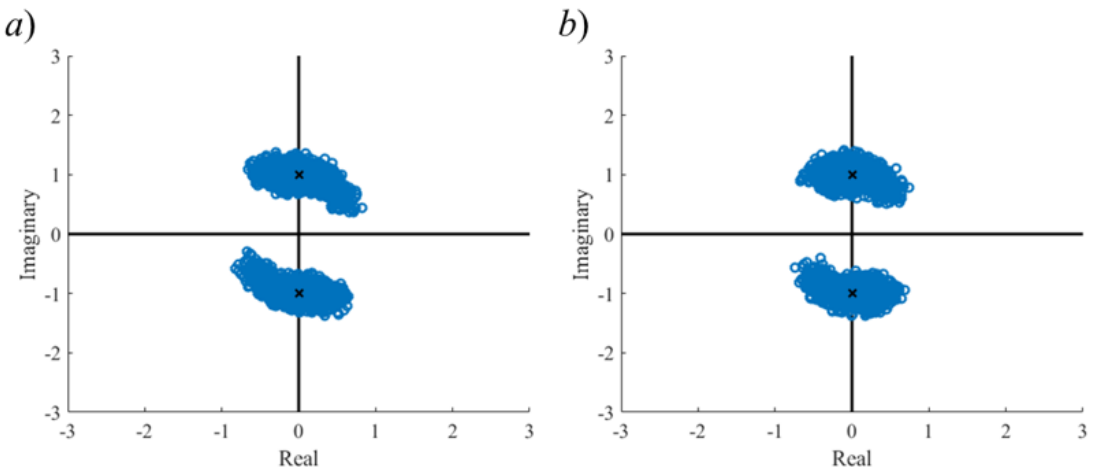

Figure 6.11: Demodulation plots in a static environment with a weakened direct path, using the surface reflected path for blind deconvolution, for D&S Beamforming (a) and STR (b). Here, D&S has a BER = 0.0% and an SNR = 11.6 dB; STR has a BER = 0.0% and an SNR = 12.4 dB.

time windows, and the CIR outputs are stacked on top of one another, shifting through the signal by 1.6 ms increments (STR is forced to use the direct path throughout the signal for this purpose). The figure only shows approximately 1.2 ms of each window for clarity, and the y-axis indicates the start time of each window with respect to the full signal. A direct path is clearly visible here, though its intensity varies throughout the signal duration. Several strong reflected paths are visible as well, and these vary substantially throughout the signal duration, sometimes combining into fewer paths and varying in intensity. From this figure, it is clear that a single impulse response determined by STR is potentially problematic, especially if it is generated using the reflected path. As a result, OSTR will be used here in order to calculate a different impulse response for each window as it shifts through the array output. In addition, an overlapping version of D&S (OD&S) will be implemented for comparison.

The first case considered forces the beamforming to locate the known direct path again, despite it being weaker than many of the other arrivals. Figure 6.13 shows the D&S (a) and STR (b) outputs for this case. The performance of the two cases are quite reasonable despite the dynamic nature of the environment, with BERs of 0.17% (D&S) and 0.37% (STR), and SNRs of 7.8 dB (D&S) and 7.2 dB (STR). The fact that D&S performs better than STR here is not surprising, since

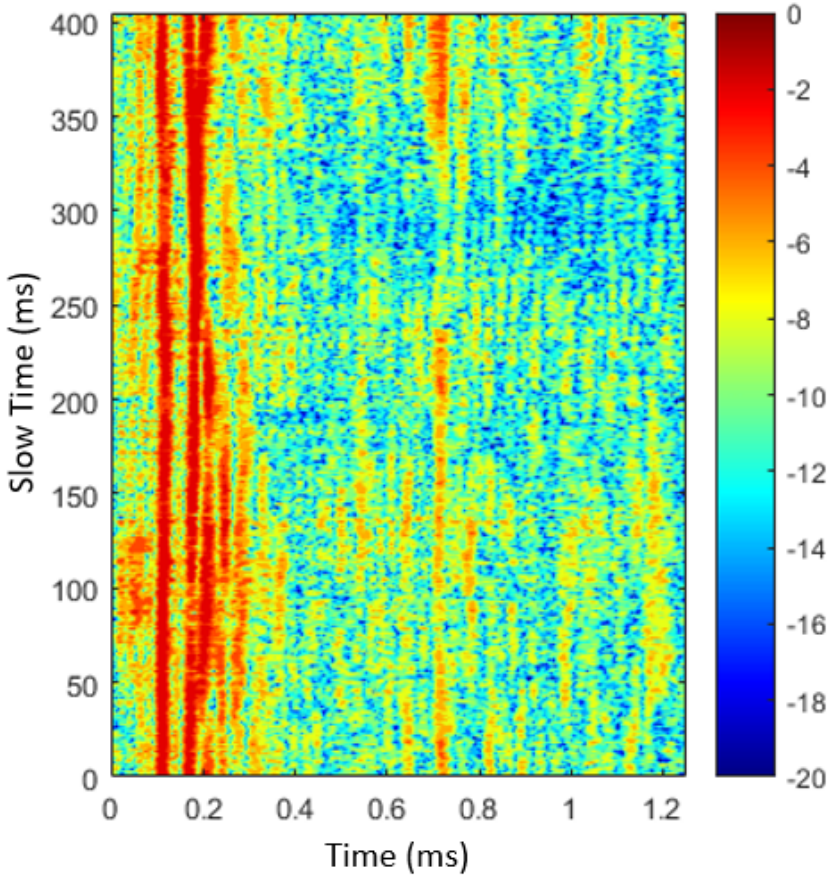

Figure 6.12: Time-varying impulse response determined by STR using 6.4 ms windows, shifted through the signal by 1.6 ms. The x-axis indicates time within each window under consideration, while ”slow time” on the y-axis indicates the start time for each window.

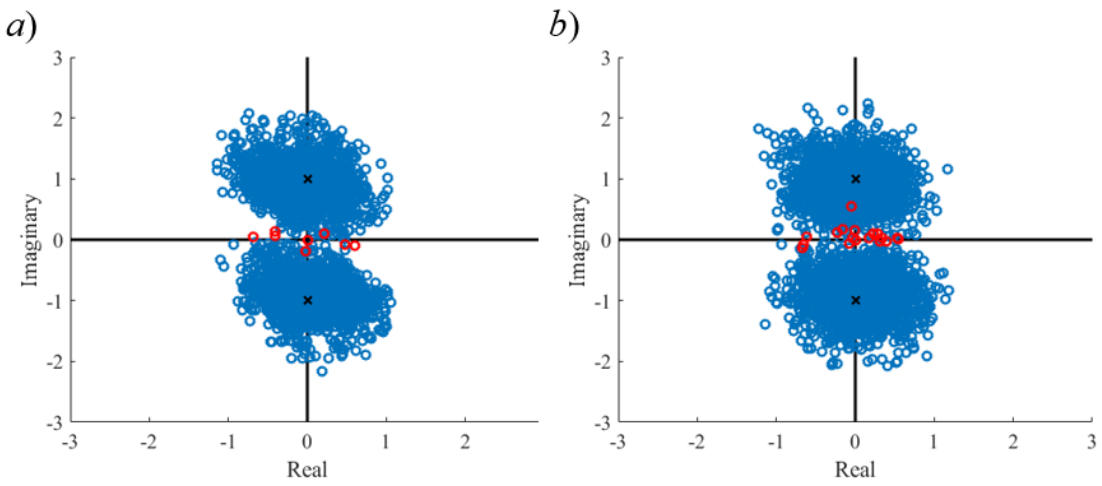

Figure 6.13: Demodulation plots in a dynamic environment with a weakened direct path, using the direct path for blind deconvolution, for D&S Beamforming (a) and STR (b). Here, D&S has a BER = 0.17% and an SNR = 7.8 dB; STR has a BER = 0.37% and an SNR = 7.2 dB.

STR is attempting to use the strong surface reflection as part of its deconvolution process, which can hurt the result since this path is so variable. When the overlapping versions are used on the direct path, the improved results yield BERs of 0.12% (OD&S) and 0.0073% (STR), and SNRs of 7.2 dB (D&S) and 8.0 dB (STR). The overlapping addition isn't of much help to D&S, however it improves STR with a slight increase in SNR and a significant reduction in the already low BER by allowing it to adapt to the varying reflected path with each overlapping window.

When the reflected path is used for beamforming, the performance changes dramatically. This result is important, because if given the full range of possible angles to choose from, the beamformer will choose the surface reflection as the strongest path, despite its variability. Since this path is significantly varying with time, neither method performs well when not using an overlapping technique. Figure 6.15 shows the results without overlapping techniques, yielding BERs of 13.4% (D&S) and 12.67% (STR), and SNRs of 1.3 dB (D&S) and 1.5 dB (STR). This poor performance is not only due to the dynamics of the reflected path, but the fact that a steady reflected path doesn't exist. When overlapping schemes are used, there is a slight improvement in OD&S (BER = 10.69%, SNR = 1.5 dB) and a more substantial one in OSTR (BER = 4.35%, SNR = 3.6 dB), shown in Fig. 6.16. Unfortunately, a robust reflected path doesn't exist in all time windows,

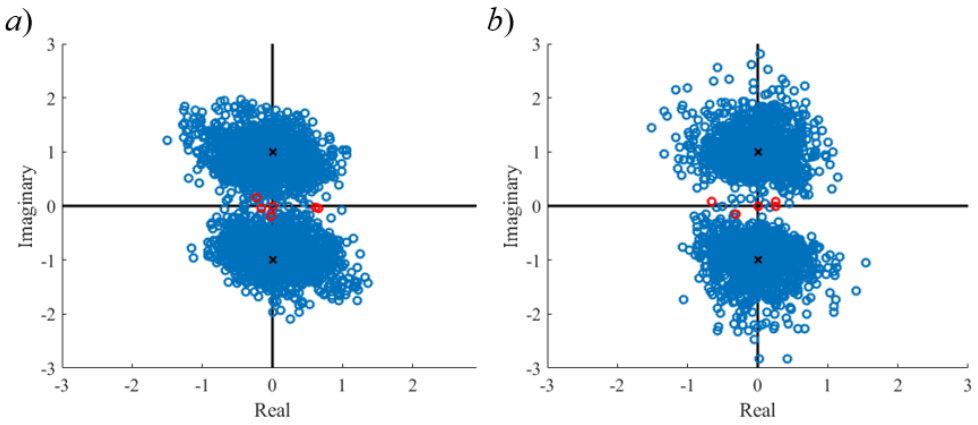

Figure 6.14: Demodulation plots in a dynamic environment with a weakened direct path, using the direct path for blind deconvolution, for OD&S Beamforming (a) and OSTR (b). Here, D&S has a BER = 0.12% and an SNR = 7.2 dB; STR has a BER = 0.0073% and an SNR = 8.0 dB.

meaning that sometimes OSTR still fails to deconvolve the signal successfully, particularly when no path is available.

When OD&S and OSTR are used and are allowed to choose a new arrival path with each time window, the result is improved over the reflected-path-only case. With the full search window available during beamforming, the techniques will regularly switch between the direct path and the reflected path, based on the current window's impulse response. The OD&S technique does not manage this variation well, since the impulse response information is not included and only information about the chosen path is considered. OSTR includes the full impulse response and thus a time-of-arrival can be extracted with more ease and each piece of the reconstructed signal is more robust, thus it is capable of adjusting for the use of different paths. In Fig. 6.17, this difference is clear. Here, OD&S actually performs worse than in the previous case, with BER = 15.26% and SNR = 0.84 dB. OSTR still does not perform like the direct-path only case, but improves over the reflected-path only case to BER = 2.47% and SNR = 2.6 dB, demonstrating the capability to mitigate many of the challenges of dynamic environments.

The water tank experiments provide a controlled environment to validate the OSTR method. Unfortunately, interesting dynamics are hard to achieve in the tank, and are only easily implemented over such short time scales using the surface reflection. Nevertheless, STR and OSTR

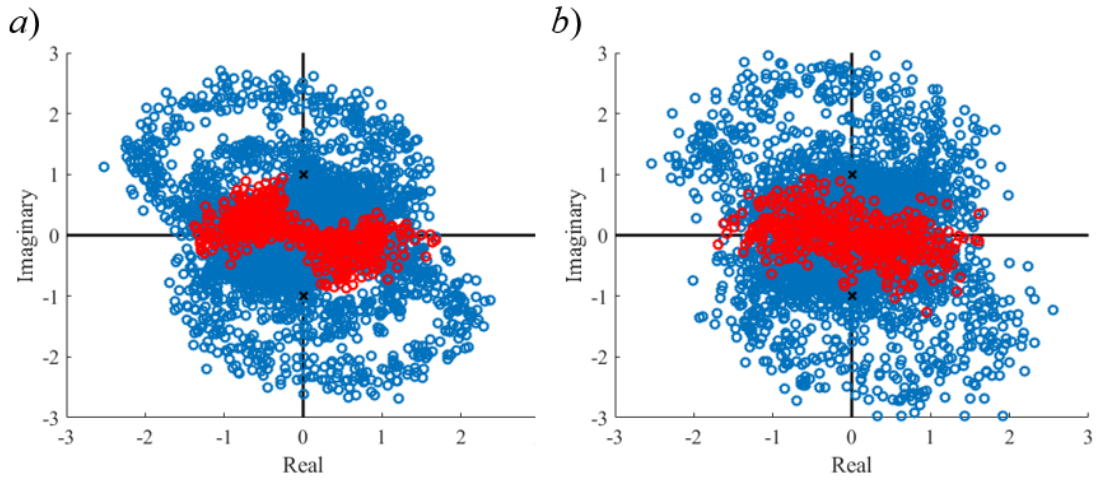

Figure 6.15: Demodulation plots in a dynamic environment with a weakened direct path, using the surface reflected path for blind deconvolution, for D&S Beamforming (a) and STR (b). Here, D&S has a BER = 13.4% and an SNR = 1.3 dB; STR has a BER = 12.67% and an SNR = 1.5 dB.

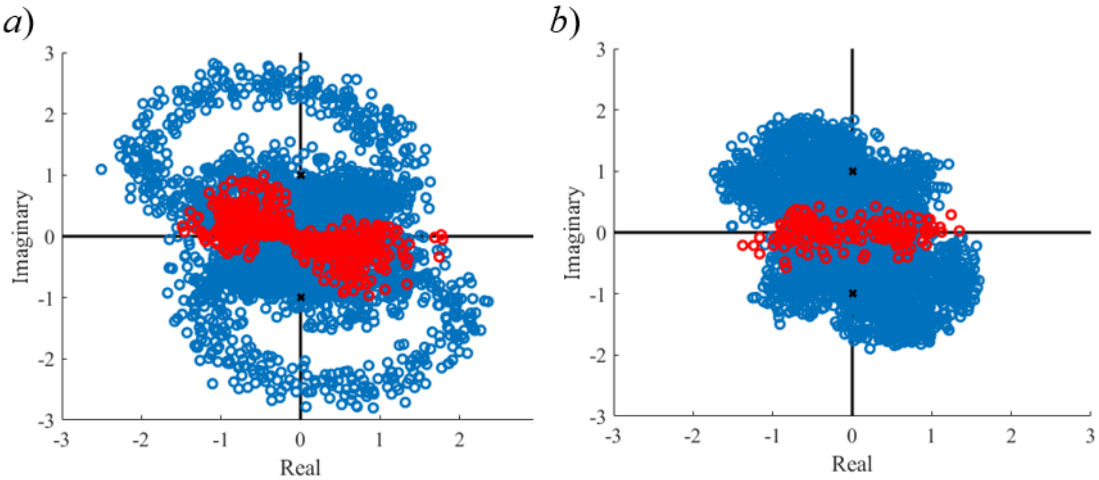

Figure 6.16: Demodulation plots in a dynamic environment with a weakened direct path, using the surface reflected path for blind deconvolution, for OD&S Beamforming (a) and OSTR (b). Here, OD&S has a BER = 10.69% and an SNR = 1.5 dB; STR has a BER = 4.35% and an SNR = 3.6 dB.

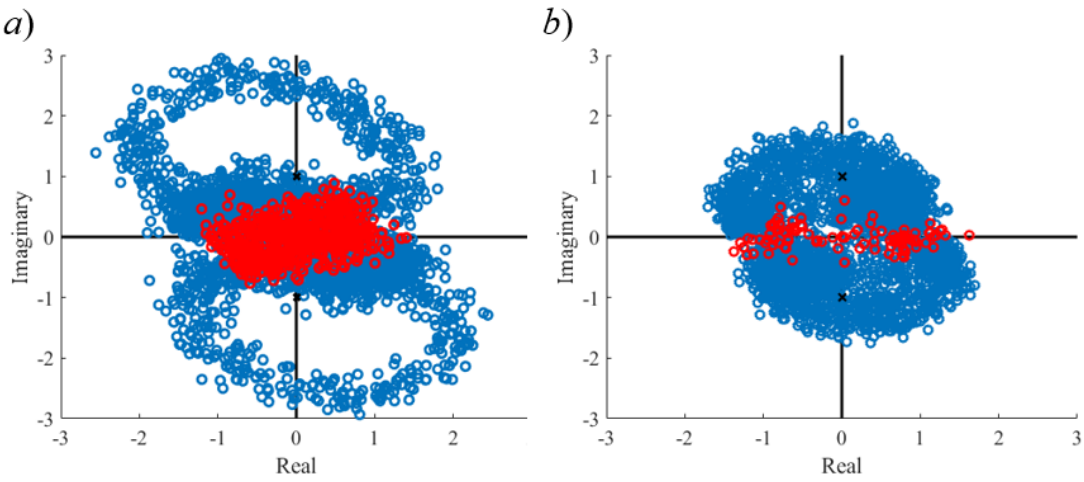

Figure 6.17: Demodulation plots in a dynamic environment with a weakened direct path, using both the direct and surface reflected paths for blind deconvolution, for OD&S Beamforming (a) and OSTR (b). Here, OD&S has a BER = 15.26% and an SNR = 0.84 dB; STR has a BER = 2.47% and an SNR = 2.6 dB.

were shown to be useful for acoustic communication signals in reverberant and dynamic environments, generally performing better than a simple D&S technique, and improving in dynamic environments when the overlapping version was implemented.

6.3 Shallow Water Experiments

The water tank results discussed above demonstrate the potential for OSTR to mitigate some of the challenges present in an ocean environment, but real shallow-ocean communication data is considered here to explore an actual case with these challenges. The performance of two blind deconvolution techniques for use in underwater communication is examined in this section. Data from the KAM11 experiment, which is laid out in detail in Chapter 4, is utilized, with the same geometry as that shown in Fig. 4.2. In the experiment of interest, a 22 kHz center frequency, 12k bit-per-second, BPSK signal is broadcast for 9.4 s with a 39.0625 kHz sampling rate from source 1 shown in Fig. 4.2 to the 16 receivers placed 3 km away on JD 183. Prior to the broadcast of the BPSK signal, a 100 ms linear frequency sweep from 11.2 to 32.8 kHz is broadcast as a probe signal. This probe signal can be used to estimate the channel impulse response (CIR) using

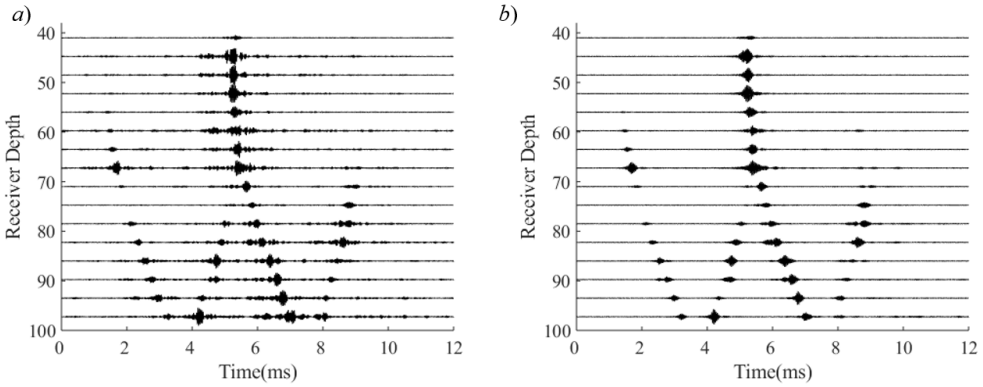

Figure 6.18: KAM11 CIR generated using STR with the received probe signal (a) and using a matched filter with a modeled probe signal for comparison (b). The normalized cross correlation between the two outputs is 0.872.

a matched filter with a modeled probe signal or with the STR technique - but STR can also use the communication signal itself to determine a CIR estimate in real time. The duration of the signal provides the opportunity for a time-varying CIR, which is when the OSTR-DFE technique is expected to be of the most use.

The KAM11 environment has an average depth of roughly 106 m and has a downward-refracting sound speed profile, which leads to substantial multipath propagation. Figure 6.18 shows the CIR prior to broadcast of the communication signal using the two methods mentioned above for comparison - STR is with the probe signal (a), and a simple matched filter is used with a simulated ideal probe signal (b). The two CIRs show how significant the multipath propagation is in the channel, with at least four prominent paths that are easily identifiable, none of which appear to be a simple direct path, and some of the paths don't extend across the full array. The figure also demonstrates STR's capability to determine the CIR well, with a 0.872 cross correlation coefficient between the two results.

Over the course of the broadcast, a successful beamforming output is critical for the success of STR. Due to the sparsity of the array, conventional beamforming methods don't yield a useful result (see Chapter 4) and thus frequency-difference methods are used with STR, utilizing Eq. 6.13. Here, the smallest available difference frequency is chosen for the phase estimation step, providing relative phase for each frequency bin. Since conventional D&S beamforming isn't usable, the

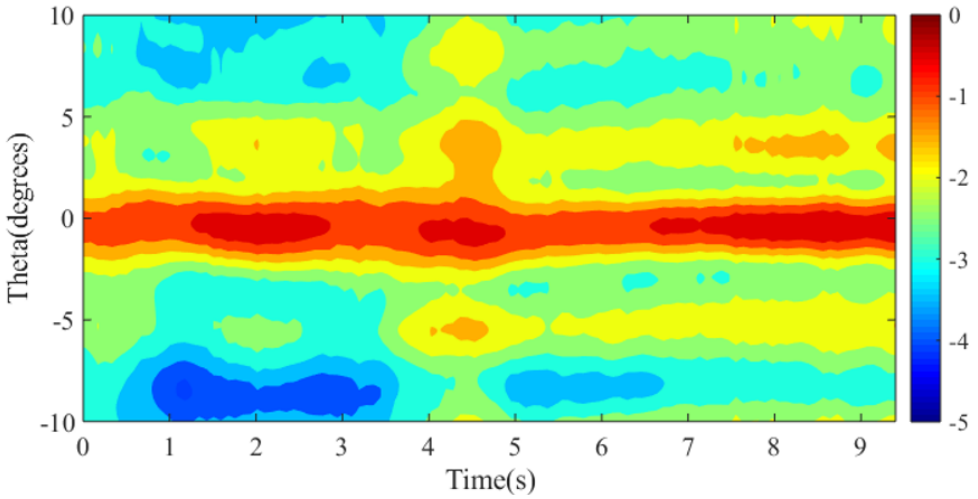

Figure 6.19: Frequency-difference beamforming output using a difference frequency of 1.0 kHz over a 13.6 kHz bandwidth centered around 22 kHz, with 0.33 s time windows overlapped by 0.11 s. Color scale is in decibels.

comparison in this section is between time reversal using the probe signal with a single channel DFE and OSTR with a single channel DFE on each overlapping window. A frequency-difference beamforming output is shown in Fig. 6.19 over the length of the communication signal for the purpose of demonstrating some of the time-varying results. Each frequency-difference beamforming step here is performed on a 0.33 s window, shifted by 0.11 s between windows, and uses a 13.6 kHz bandwidth centered around 22 kHz to generate a 1.0 kHz difference frequency field. Between 3 and 4 individual paths are visible, with the path close to 0° dominant. Over the full length of the signal, the paths vary in amplitude substantially, particularly those further from 0°.

When the probe signal is used to generate a CIR to use with TR, the variation in the CIR is not captured, since this provides only a single 100 ms snapshot in time. The demodulation output using conventional TR is shown in Fig. 6.20 for the full 112,000 bit signal. Here, the DFE uses a 1000 symbol training sequence, 90 feedforward taps, 10 feedback taps, and a recursive least squared fitting technique with a 0.99 forgetting factor. The first plot shows the full demodulation output with real-imaginary axes (note that this is 90° rotated from previous plots, which is simply a function of the BPSK signal design and does not impact the results) (a), while the second shows the bit output vs. time (b), providing insight into the time-dependent variation. In this result, the

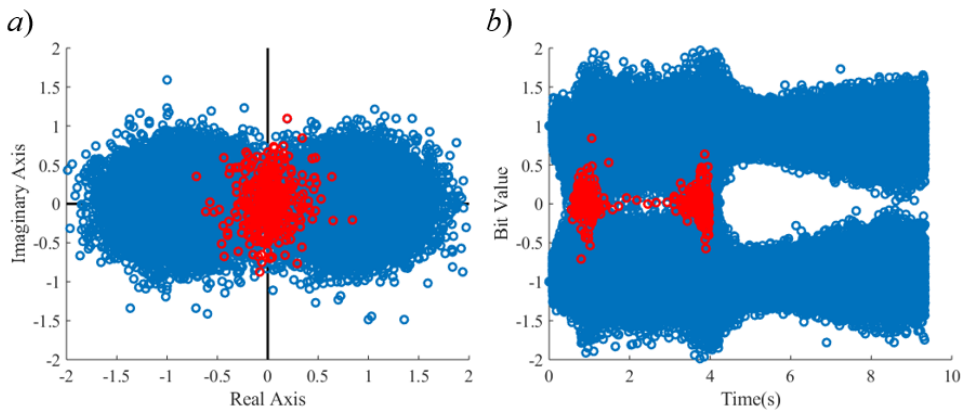

Figure 6.20: Demodulation of the 9.4 s communication signal using TR on the probe signal and a DFE utilizing an initial 1000 symbol training sequence, 90 feedforward taps, 10 feedback taps, and a recursive least squared fitting technique with a 0.99 forgetting factor. The demodulation is shown on a real-imaginary axis plot (a), as well as vs. time (b). The resulting BER is 0.34% and the SNR is 8.5 dB.

SNR of the output is 8.5 dB and the BER is 0.34%. While the DFE is able to remove enough ISI in some of the signal to achieve successful demodulation, other sections of the signal fail to demodulate reliably and increase the BER.

When OSTR-DFE is implemented, the result is significantly improved. Here, the probe signal is not used at all. Instead, an initial 164 ms window of the communication signal is used for STR, and a DFE with the same parameters as above is applied. At this point, the window is shifted forward by one third of the window size (54.6 ms) and STR is performed on the new section. A DFE is applied again, using the first third of the new window (which is the middle third of the previous one) as the training sequence for the remainder of the new window. This process continues throughout the duration of the signal, using the previously demodulated bits as training sequences for each DFE performed after each STR implementation. The results of this OSTR-DFE implementation are shown in Fig. 6.21 and yield 0 bit errors and an SNR of 12.2 dB. The performance of the method does not vary with time, clearly shown by the time-dependent demodulation result (Fig. 6.21(b)). Since STR is updating the impulse response with each window, and the overlapping portions are available for DFE training sequences, the variability with time is less significant. If the time varies slowly enough that the CIR can be considered nearly steady

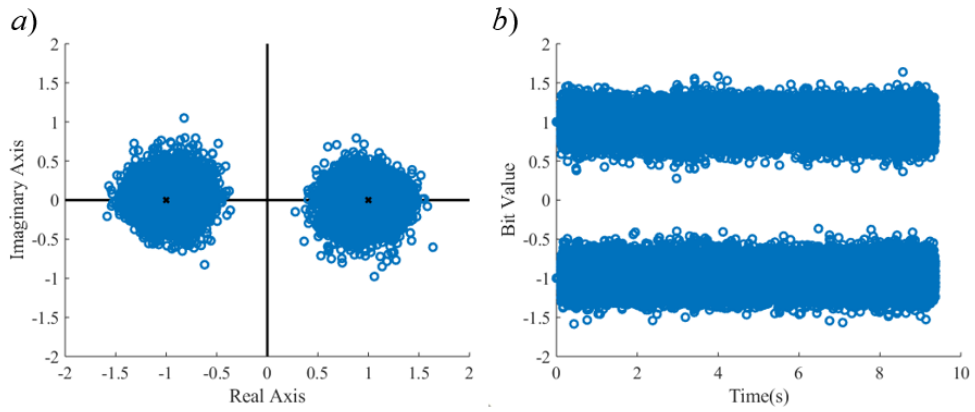

Figure 6.21: Demodulation of the 9.4 s communication signal using the OSTR-DFE technique with a DFE utilizing an initial 1000 symbol training sequence, 90 feedforward taps, 10 feedback taps, and a recursive least square forgetting factor of 0.99 on the initial window. The following DFEs use the overlapping window portions as training sequences, with all other parameters remaining the same. The demodulation is shown on a real-imaginary axis plot (a), as well as vs. time (b). The resulting BER is 0% and the SNR is 12.2 dB.

within each sub-window, then the OSTR-DFE method is expected to perform well, as it does.

6.4 Summary and Conclusions

This chapter demonstrated the capabilities of D&S beamforming, OD&S, TR, STR, and OSTR-DFE for the purposes of blind deconvolution of a communication signal. Lab experiments with both steady and time-varying impulse responses were considered, as well as shallow ocean data with a real, time-varying channel impulse response.

In the water tank experiments, the effects of multipath were mitigated with the use of D&S beamforming and, to a larger extent, with STR. STR showed improvements over D&S due to its capability to account for some of the reverberation in the tank, though by choosing a strong path, D&S also performs well. When the impulse response of the tank varied, and particularly when the reflected path from the dynamic surface was used, the performance of both methods degraded significantly. However, OSTR is able to partially adapt to the changing impulse response by choosing different paths as available and update the impulse response specific to the window in consideration.

In the shallow water experiments, the dynamics of an actual environment are considered. The TR method, despite using a probe signal, is unable to account for the varying impulse response, even when followed by a single channel DFE. As a result, the demodulated output has a higher BER than desired. The OSTR-DFE method is able to estimate a nearly-real-time impulse response, which, when combined with a DFE, is able to demodulate the signal without a single bit error, despite the dynamics, multipath, and noise present in the environment.

The primary conclusion shown herein is that the STR, OSTR, and OSTR-DFE methods are potentially useful techniques for blind deconvolution of long duration, time-varying signals, such as those encountered in typical underwater communication applications, as the overlapping implementations can adapt to time-varying environments and do not require a probe signal. The main requirements for success with this method are that the CIR is roughly static for the sub-windows of interest, that conventional beamforming or frequency-difference beamforming can be used successfully (unless mode-based STR is used, which is not discussed here), and that a training sequence is available, if a DFE is needed (if a DFE is not needed, the first bit is required to be known for the frequency-difference OSTR case, to be sure that the initial phase is aligned properly).

CHAPTER 7

Source Level Estimation and Localization Using a Noise Reference

In many areas of acoustics, measurements of a field of interest may be characterized by low SNRs. In both field applications or experimental and R&D applications, these noisy fields can be problematic for source detection, localization, characterization, etc. In some of these cases, a reference measurement of the noisy field without the source of interest may be available. If the noise field is statistically slowly varying (or the field is reasonably similar between two experimental trials), this noise reference can potentially be used to reduce or remove the influence of noise on the signal-plus-noise measurement. The motivation for this work is the use of a noise reference in an experimental setting where changes to an object in a flow field are of interest. A measurement of an acoustic field present in a wind tunnel is made with an object placed in the flow, then a second measurement is taken after implementing a change to the object (in the case considered here, the change is to the object's geometry). The detection and localization of the new feature and its contribution to the source level from the flow past the object is of interest. Several techniques will be considered for the task, but they will first be considered for a discrete source broadcasting in two types of noise fields to understand their behavior with straightforward sources. Then, they will be extended to wind tunnel experiments in an attempt to quantify the effects of a small physical change to a plate. The goal here is to demonstrate that the influence of noise can be significantly reduced when a reference measurement is available, despite very low SNRs. Success in this work is determined by accurate localization of a source or a geometric feature change, as

well as accurate estimation of the source level, in noisy environments.

7.1 Background and Theory

The quantification of source level, source level increments, direction of arrival (DOA) of sources, and localization of source changes will be investigated in this chapter with several techniques. Each technique involves determining a cross spectral density matrix (CSDM) that is ideally free of noise by exploiting a reference measurement of the noisy field, and this CSDM is processed using an additional signal processing step to determine source location and source level. In some cases, these techniques are also be compared to the techniques with no noise removal. The techniques considered herein include source level estimation from a CSDM's diagonal elements, Conventional Beamforming (CBF), the Spectral Estimation Method (SEM) [18], and Robust Principal Component Analysis (RPCA) [25], each with a corresponding noise removal method described below. For the RPCA technique, the output is a CSDM, which can be used with either CBF or SEM to obtain the DOA or localization output, as well as source level.

Each of the techniques discussed below rely on the use of a CSDM, which is defined for a given frequency as

$$K_{mn}(\omega) = P_m(\omega)P_n^*(\omega), \tag{7.1}$$

where $P_m(\omega)$ is the frequency-domain output of the acoustic pressure measured by the m^{th} receiver at frequency ω, and * indicates a complex conjugate. The CSDM is an N-by-N complex, Hermitian matrix, where N is the total number of receiver elements. Each element of the CSDM is a correlation between two receiver elements at frequency ω, with real numbers lying along the diagonal (since $m = n$ here). In this chapter, the CSDMs will generally be incoherently averaged over many signal snapshots. The construction of the CSDM removes the source phase from the measurements, but maintains measured field amplitudes. As a result, the source phase should not impact the CSDM for a stationary and discrete source, rather it should depend on only source amplitude and the source-to-receiver impulse response functions. If the field contains isotropic white

noise, or if the coherence length across an array is smaller than the receiver element spacing, the variation in phase between receiving elements should drive the off-diagonal CSDM terms towards 0, leaving only the diagonal magnitude terms.

When uncorrelated acoustic fields are present, such as a discrete source in the presence of an independent noise field, the CSDM can ideally be decomposed into a simple sum of the source CSDM and noise CSDM, provided enough snapshot averaging or subarray averaging is available. Without averaging, cross terms between the source and noise fields will persist, but their variation across snapshots or subarrays drives them towards zero, relative to the source-source and noise-noise terms. That is,

$$\langle K^{tot}(\omega) \rangle \approx \left\langle K^{sig}(\omega) \right\rangle + \left\langle K^{noise}(\omega) \right\rangle \tag{7.2}$$

where $\langle\rangle$ indicates CSDM averaging, which will be limited to snapshot averaging herein. As a result, if a noise reference is available that provides an accurate estimate of the $K^{noise}(\omega)$ component of $K^{tot}(\omega)$, it can ideally be removed to yield an accurate estimate of $K^{sig}(\omega)$. The CSDM can be used for directly estimating field levels at the array based on the diagonal terms - in a signal-only field it can be used to determine the source level at the array, when the diagonal terms, $K_{nn} = |P_{rms}|^2$, with

$$\text{SPL} = 20 \log_{10} \left(\frac{\frac{1}{N} \sum_{n=1}^{N} \sqrt{K_{nn}}}{P_0} \right), \tag{7.3}$$

where P_0 is a reference pressure, equal to 20 μPa in air [88]. Unfortunately, this doesn't take into account multipath propagation or multiple sources, and doesn't utilize the structure of the off-diagonal CSDM terms, and thus may not be ideal for estimating a single source's level, unless that source's acoustic signal propagates in a free-space environment with no other sources present.

7.1.1 Beamforming

Conventional beamforming, described previously in Chapter 2, will be used as one of the techniques for localization and source level estimation below. Eq. 2.6 is reformulated as

$$B_{conv}(\omega) = \frac{1}{N^2} w(\omega) K(\omega) w^H(\omega), \tag{7.4}$$

where the weighting vectors are the same as those given in Eqs. 2.7 and 2.8 and the $1/N^2$ is included so that the output will also yield a source level. Although the source amplitude at the array should be a direct output of Eq. 7.4, influence from other arrivals, particularly those with similar DOAs, will potentially impact the source level estimation in a multipath environment, and the source level calculation from a distributed source is more complex (discussed in Section 7.3). The main difference between the source level output from conventional beamforming and the simple CSDM formulation in Eq. 7.3 is the utilization of off-diagonal terms, which are particularly influential in a multipath environment.

In general, conventional beamforming has been shown to be a robust method of source localization and source level estimation, but in the cases considered herein, it will be explored with the addition of CSDM subtraction. The subtraction described above ideally yields a signal-only CSDM, which would be equivalent to beamforming in a noise-free field.

7.1.2 Spectral Estimation Method

The Spectral Estimation Method (SEM) and SEM With Additive Noise (SEMWAN) are parametric methods that introduce an optimization step for the purposes of localization and source level estimation (Blacodon and Elias, 2004; Blacodon 2010), which is its primary differentiator from CBF. Here, a CSDM is formed from the signal-plus-noise measurement and compared directly to a modeled CSDM (SEM). The inputs to the modeled CSDM are optimized to minimize the error between the two using an L_2-Norm minimization procedure. SEMWAN includes a CSDM subtraction step when a noise reference is available, as described in Eq. 7.2. For consistency with other

methods considered here, this work will refer to SEMWAN as "SEM with CSDM subtraction" from here on. The modeled CSDM used for SEM can be written as

$$K_{mn}^{mod}(\omega) = \sum_{j=1}^{J} G_{m,j}(\omega) A_j(\omega) G_{n,j}^{*}(\omega) \tag{7.5}$$

where $G_{m,j}(\omega)$ is the Green's function between the j^{th} test source location and the m^{th} receiver and $A_l(\omega)$ is a vector of source level magnitudes squared for each DOA (θ_j) or each source location ($\vec{r}_j$). For this technique, the set of possible Green's functions does not vary - instead, a solution for $A_j(\omega)$ is sought for the given basis of Green's functions. The measured, modeled, and optional reference CSDMs are subtracted from one another and a minimization algorithm determines the solution $A_j(\omega)$, constrained such that $A_j(\omega) > 0$, that minimizes the error

$$\min(E(A_l(\omega))) = \min(\sum_{m,n=1}^{N} \left| K_{mn}^{tot}(\omega) - K_{mn}^{ref}(\omega) - K_{mn}^{mod}(\omega) \right|^2). \tag{7.6}$$

For the basic SEM implementation that doesn't utilize a noise reference, $K^{ref}(\omega)$ is simply set to 0. The output $A_l(\omega)$ provides both a source level and a source location output, and in most cases, the solution will be nearly 0 for almost the entire vector output except where sources (or potentially sidelobes or false localizations), are expected. Since this output provides a source level squared, no phase information is available from the output.

SEM with CSDM subtraction provides a potentially high-precision and high-resolution solution to a source localization problem in a noisy environment. However, like many high resolution methods, this technique has some inherent instability that significantly increases with uncertainty in the experimental setup, residual noise, or decreasing spatial resolution in the localization search region. In addition, because of the CSDM subtraction step, the assumption that the signal and noise sources are uncorrelated is critical to its success in noisy environments. Finally, bandwidth averaging with SEM is difficult, as the outputs of high-precision methods may not easily combine if slight variation occurs in the localization, and because incorporating a meaningful bandwidth

dimension into the solution of Eq. 7.6 significantly increases computational complexity.

7.1.3 Robust Principal Component Analysis

Principal component analysis (PCA) is a technique that reduces a matrix into its "principal components", which in this case refer to a set of eigenvalues and corresponding eigenvectors. PCA relies on the fact that a CSDM can be rewritten as

$$K = X\Lambda X^H, \tag{7.7}$$

where X is a matrix of eigenvectors and Λ is a diagonal matrix of eigenvalues. Eigenvalue decomposition techniques can be used to determine X and Λ with no additional information about K. Ideally, each independent source results in a corresponding eigenvalue and eigenvector. Robust Principal Component Analysis (RPCA) [25] is an extentsion to PCA that is useful for scenarios where a matrix, M, can be decomposed into a low rank matrix, L_0, and a sparse matrix, S_0, such that

$$M = L_0 + S_0. \tag{7.8}$$

For the purposes of this work, M is the CSDM generated by the recording that consists of both signal and noise, K^{tot}. The low-rank matrix, L_0, is assumed to correspond to the source CSDM, K^{sig}, which is ideally low rank if the number of sources in the field is small relative to the number of receivers (i.e. the matrix is composed of a small number of nonzero eigenvectors and eigenvalues). The sparse matrix, S_0, is assumed to correspond to the noise CSDM, K^{noise}, which ideally is equal to K^{ref}, when available. With enough snapshot averaging, the noise CSDM will be sparse if the noise field can be accurately modeled as isotropic white noise, or if the noise is uncorrelated across the array, since these scenarios will cause the CSDM to tend towards a diagonal matrix. RPCA is

ideally completed by solving

$$\begin{aligned} &\text{argmin}\left\{\text{rank}(K^{sig}) + \lambda\|K^{noise}\|_0\right\} \\ &\text{subject to } K^{tot} = K^{sig} + K^{noise}, \end{aligned} \tag{7.9}$$

where λ is the regularization parameter, which is discussed in detail in prior works on RPCA [7] [168] [32]. Based on the results of these works, λ is chosen as the inverse of the square root of the number of receivers in the array. The above equation is nonconvex and difficult to solve as is, but prior work [25] has shown that these constraints can be relaxed to a nuclear norm and an l_1 norm,

$$\begin{aligned} &\text{argmin}\left\{\|K^{sig}\|_* + \lambda\|K^{noise}\|_1\right\} \\ &\text{subject to } K^{tot} = K^{sig} + K^{noise}. \end{aligned} \tag{7.10}$$

Equation 7.10 is solved here using an Accelerated Proximal Gradient algorithm (APG) [151]. The APG algorithm is iterative, and herein 1000 iterations are used for each solution - this was enough that additional iterations did not yield changes to the solutions, but took minimal time from a computational standpoint.

Unfortunately, in many applications, the existence of correlated noise will hurt the performance of this RPCA implementation, since it will yield significant off-diagonal terms in the noise CSDM. If a noise reference exists, the influence of correlated noise can be partially mitigated by using a denoising technique described here. Rather than CSDM subtraction, this method aims to diagonalize the CSDM prior to the RPCA operation by projecting onto a noise basis (defined by the reference matrix), and returning to the original basis after the RPCA implementation [14] [7]. This process consists of using the reference noise CSDM, K^{noise}, to generate a temporary CSDM,

$$K^{tot,X} = (X^{ref}\Lambda^{-1/2})^H K^{tot}(X^{ref}\Lambda^{-1/2}), \tag{7.11}$$

where X is the matrix of eigenvectors determined from the principal component analysis of K^{noise}, and Λ is the diagonal matrix of eigenvalues. Since X and Λ are determined from the reference

measurement, ideally Eq. 7.11 will result in

$$(X^{ref}\Lambda^{-1/2})^H(K^{sig'} + K^{ref})(X^{ref}\Lambda^{-1/2}) = K^{sig',X} + I, \tag{7.12}$$

where I is the identity matrix, which can easily be subtracted to obtain $K^{sig',X}$, which is ideally equal to $K^{sig,X}$. Here, RPCA is implemented on $K^{sig',X}$ to separate any remaining noise from the signal CSDM. The outputs of RPCA, ideally $K^{sig,X}$ and $K^{noise,residual,X}$ can then be used to determine K^{sig} with

$$K^{sig} = ((X^{ref}\Lambda^{-1/2})^H)^{-1}K^{sig,X}((X^{ref}\Lambda^{-1/2}))^{-1}. \tag{7.13}$$

Another potential implementation for RPCA is possible that is not considered here. Generally in image processing applications, an M by N matrix - N snapshots of M data points - is decomposed into a stationary image (the low rank matrix), and a foreground image that only appears in some small number of snapshots (the sparse matrix). In this case, N noise CSDMs could be considered, with a small number containing the signal-plus-noise measurement. In this implementation, the source signal is the sparse case, while the noise is the low-rank. However, in such an implementation, the signal is likely to be both sparse and low-rank, and the noise is likely either low-rank (for a coherent noise field) or sparse (isotropic white noise or incoherent noise), potentially causing problems with the technique. In addition, it specifically requires that a small number of signal-plus-noise measurements are used (to achieve sparseness), despite many more potentially being available.

7.2 Source in a Noisy Field

The goal of the experiment considered in this section is to evaluate the performance of each of the above methods in a case with a discrete noise source in the presence of two different types of noise. These two types of noise will consist of a simulated, isotropic white noise field, and a spatially-coherent measured noise field generated by a compressed air flow from a wall-mounted

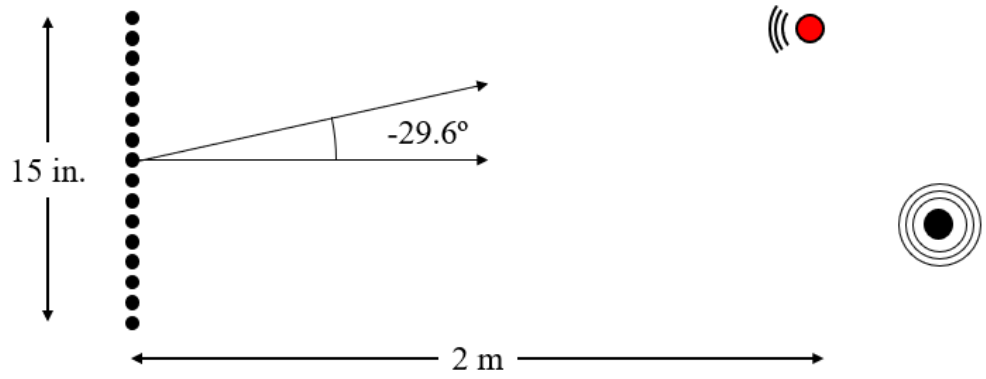

Figure 7.1: Setup for laboratory experiments. A 16-element array with 1 in. spacing is placed roughly 2 m from a source (red) broadcasting a 2 ms, 2.5-3.5 kHz sweep (far field). A noise source (black), also in the far field, is a compressed air nozzle which reverberates throughout the lab.

nozzle. The performance of each method as a function of SNR in the two types of noise fields is considered in order to understand the potential applications, advantages, and disadvantages of each method and to inform success in other types of experiments and acoustic fields.

7.2.1 Experimental Setup

The experiment considered in this section consists of a discrete source broadcasting a 2 ms, 2.5-3.5 kHz Gaussian-enveloped linear frequency sweep to a far-field vertical receiving array of 16 elements with uniform 1 inch spacing. A compressed air nozzle mounted to a wall in the lab was opened to act as a broadband noise source and allowed to reverberate throughout the room. The geometry of this experiment is shown in Fig. 7.1. For the broadcast signal measurement, the direct path of the signal is isolated by removing any reverberation occurring after the direct path reaches the array (the most prominent secondary arrival being the initial floor reflection). A sample measured signal is shown in Fig. 7.2 for the same case shown in Fig. 7.1 with only unintended lab noise present (which is nearly non-existent in this frequency range) after the signal trimming process.

Measuring the signal and noise simultaneously would make trimming the source signal's reverberation challenging, so instead a single signal broadcast is recorded independently, as is a 60

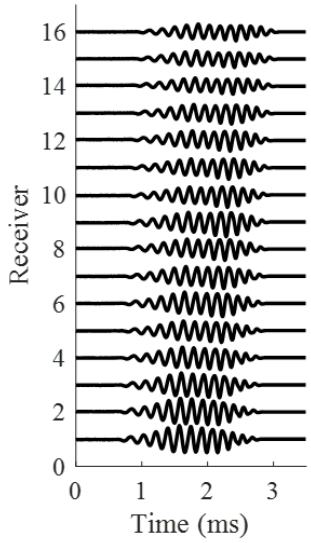

Figure 7.2: Waterfall plot of the source signal of interest for the case shown in Fig. 7.1, a 2 ms 2.5-3.5 kHz Gaussian-enveloped linear frequency sweep with reverberation trimmed from the end of the signal.

s measurement of a noise-only field, or a 60 s simulation of an isotropic white noise field. The noise field is split into the desired number of snapshots in the time domain and each snapshot is individually combined with the same signal measurement, thus the signal portion in each snapshot is identical, for simplicity, while the noise is time-varying. The white noise spectrum provides roughly the same noise magnitude across all frequencies, but the noise from the compressed air flow is likely less uniform and propagates from a fixed point in space, adding spatial coherence to the field. Figure 7.3 shows the signal spectrum (a) and the compressed air noise spectrum (b) measured at one receiver, both with amplitudes normalized to lie between 0 and 1 (linear scale). The noise field here is very wideband, with sufficient information in a region overlapping with that of the broadcast signal.

Signals broadcast from roughly 6.6° and -29.6° were considered here in order to provide a source location with a DOA close to that of the noise source (6.6°) and one where they are well separated (-29.6°). The outputs of the signal-only and noise-only measurements are shown on a dB scale in Fig. 7.4 for the -29.6° case. The isotropic white noise case is not shown since this will yield roughly uniform directionality. The amplitudes here are not corrected for range, thus they

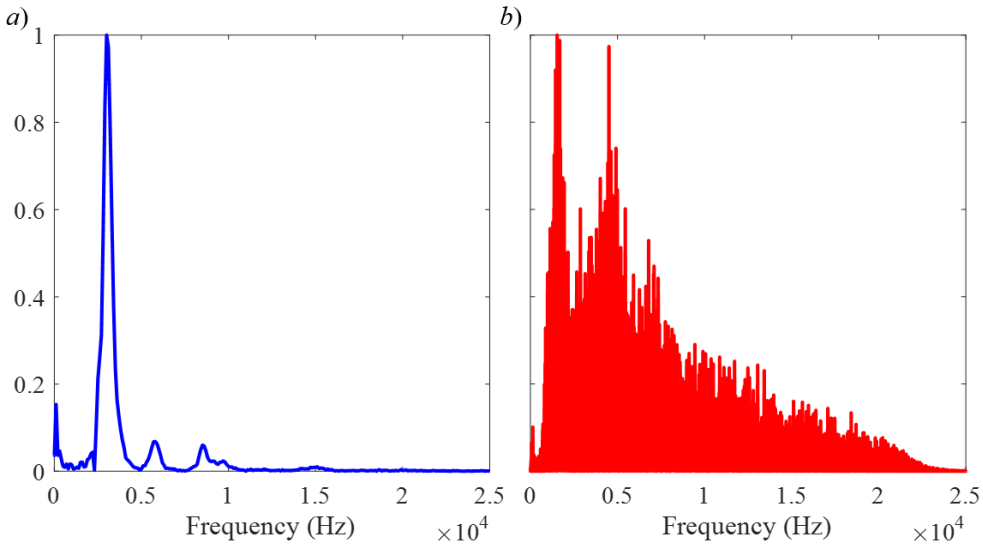

Figure 7.3: Frequency spectrums of the source signal (a) and the compressed air noise field (b). Both spectrums are normalized to have a maximum amplitude of 1 and are shown on a linear scale.

provide Sound Pressure Levels (SPL) at the array.

7.2.2 Results

In this section, source localization will be considered for CBF with and without CSDM subtraction, SEM with and without CSDM subtraction, and RPCA with and without denoising, followed by a CBF step (RPCA-CBF). For conciseness and clarity, only the RPCA-CBF results are shown here, since the performance of RPCA-SEM relative to RPCA-CBF was comparable to that of SEM relative to CBF, thus no additional insights were obtained. In all results, 10 ms snapshots will be utilized, leading to 3000 noise-only snapshots and 3000 signal-plus noise snapshots. The first 30 s of each noise measurement will be used for the noise-only reference, and the latter 30 s for the signal-plus noise measurement.

7.2.2.1 Isotropic White Noise

The first case considered here is that of isotropic white noise. Here, localization methods are expected to handle low SNRs well since the noise field does not have any significant directionality inherent to it. Sample localization outputs at 3 kHz are provided in Fig. 7.5 for three different

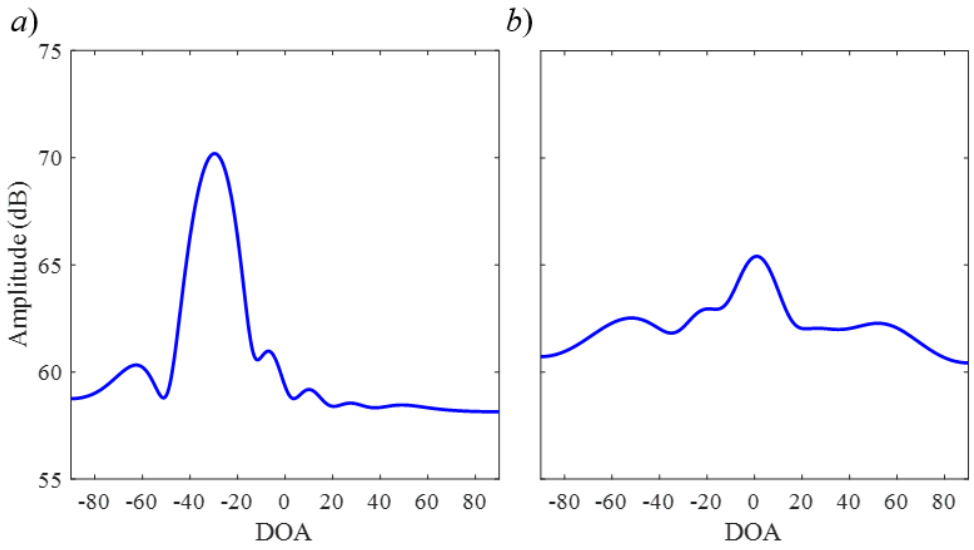

Figure 7.4: Beamformed outputs of the signal-only measurement (a) and the noise-only measurement (b) over a 2.5-3.5 kHz bandwidth. The signal appears at -29.6° and the noise source appears close to 0°, with significantly reduced dynamic range relative to the signal, most likely due to the strong reverberation in the room.

SNRs: 0 dB (top row), -10 dB (middle row), and -20 dB (bottom row). In each row, the results from CBF with and without CSDM subtraction (first column), SEM with and without CSDM subtraction (middle column), and RPCA-CBF with and without denoising (last column), are shown. In each case, the blue curve is the result from the technique without a noise reference, and the red curve is the result when utilizing a noise reference. The black 'x' indicates the expected peak location, providing both a DOA and a SL estimate. At the SNR = 0 dB case, each method is successful both with and without a reference, though with notable improvements to dynamic range for CBF and SEM when a reference is available. When the SNR drops to -10, the benefit of utilizing the noise reference becomes clearer in the CBF case (d) with several dB of SL error, but notably SEM and RPCA still perform well without a noise reference (though SEM's dynamic range is significantly reduced). When dropping to SNR = -20 dB, both CBF and SEM provide very poor results, which are recovered with the noise reference (though in the case of SEM with CSDM subtraction (h), the SL estimate is now quite poor). Interestingly, in all three cases, RPCA performs comparably with and without a noise reference - a predictable result based on the discussion in the Background and Theory section. With a sufficient amount of snapshot averaging (or other types of averaging),

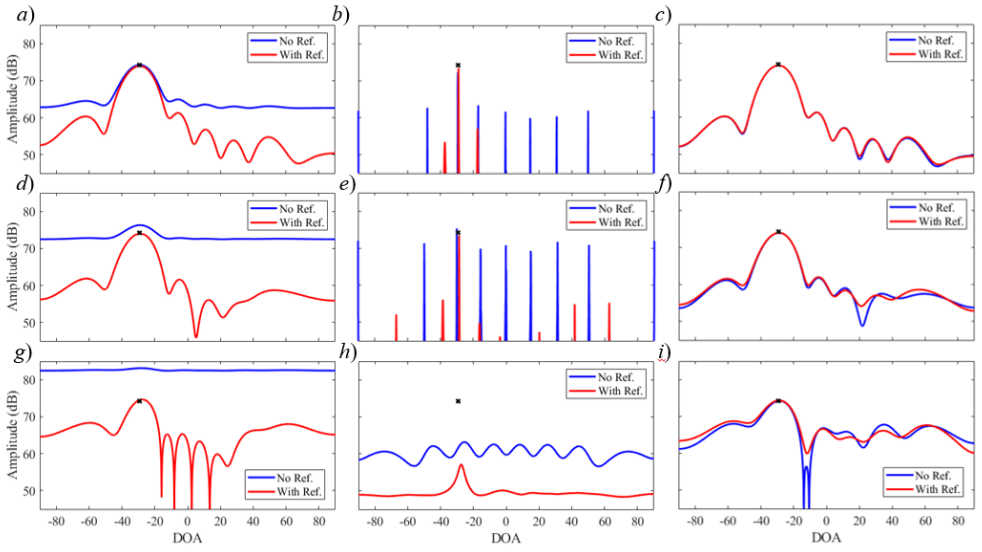

Figure 7.5: Outputs of conventional beamforming with and without a noise reference (a, d, g), SEM and SEMWAN (b, e, h), and RPCA with and without denoising (c, f, i). Performance is shown for three SNRs, 0 dB (first row), -10 dB (second row), and -20 dB (third row).

isotropic white noise will tend towards a diagonal CSDM, since no correlation exists between receivers in the field. As this happens, the CSDM becomes sparse (only N of the N^2 matrix elements will be significantly non-zero), while the signal contribution to the CSDM is low-rank since only a single source exists in the field. Thus, without the noise reference, RPCA is still able to successfully reduce the CSDM into a sparse and a low-rank matrix, implying that in cases with noise that is spatially incoherent, RPCA provides superior performance.

The performance of both DOA and SL estimation as a function of SNR is summarized in Figs. 7.6 and 7.7, again for 3 kHz. For the case not shown in Fig. 7.5, where DOA = -6.6° (top row), the use of a noise reference makes little difference to CBF and RPCA until SNRs as low as roughly -20 dB are reached, and even here the improvement is minimal (this is likely a function of the close DOAs). However, SEM shows significantly more stability below SNR = 0 dB when a noise reference is introduced. For the second case, DOA = -29.6° (bottom row), the performance is similar, with improvements below SNR = -20 dB, particularly for RPCA with a reference. Here, SEM shows some instability below SNR = -10 dB, which is improved significantly with the reference. Conventional beamforming doesn't have a major change in performance with the use of a refer-

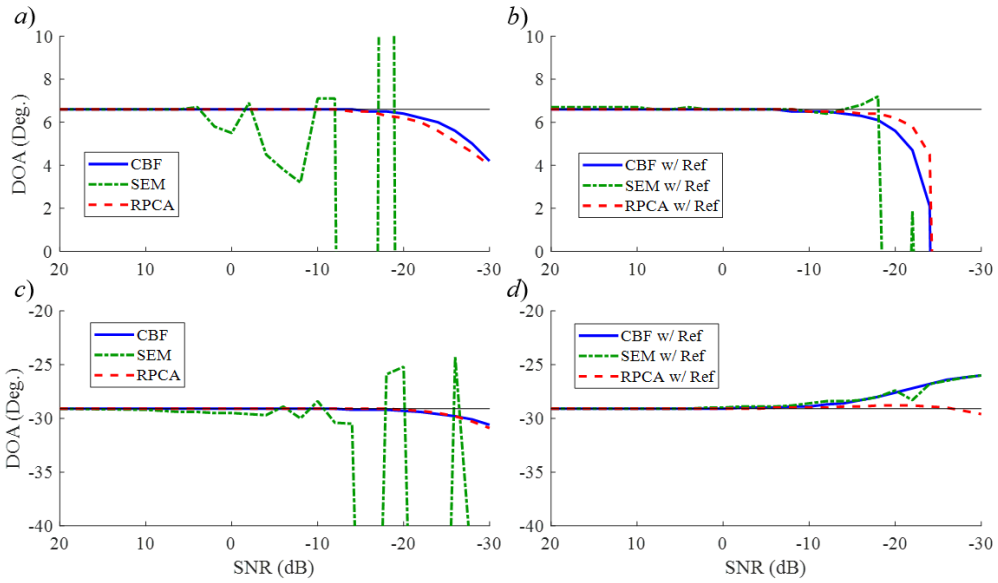

Figure 7.6: Direction of Arrival as a function of SNR for CBF (blue), SEM (Green), and RPCA-CBF (Red) for two cases, DOA = -6.6° (a,b) and DOA = -29.6°, with (b,d) and without (a,c) noise references. Here, the noise is isotropic, Gaussian white noise.

ence, likely because the isotropic nature of the noise allows it to almost always locate the source, even at very low SNRs.

Figure 7.7 shows source level estimation behaves very similarly between the two cases, with notable improvements in the cases utilizing a noise reference. SEM tends to underestimate the source level, both in cases with and without a noise reference, possibly due to the higher precision allowing the technique to assign portions of the source's radiated field to lower amplitude peaks not corresponding precisely to the source location (but close to it). Using the CSDM diagonal for estimation is notably worse than using the identical CSDM with CBF, likely because the diagonal contains all of the signal and noise energy in the no-reference case, and contains residual energy in the case with a reference, which is partially reduced when processed through a beamformer due to the exploitation of between-receiver correlations and directionality of the source. Overall, when a reference is available, all methods perform reasonably well, with instability in SEM and errors building below SNR -20 dB. RPCA once again performs best without a reference, again since the noise-only CSDM likely reduces to a nearly-sparse matrix.

The result shown in Fig. 7.8 provides the source spectrum obtained from each method, ex-

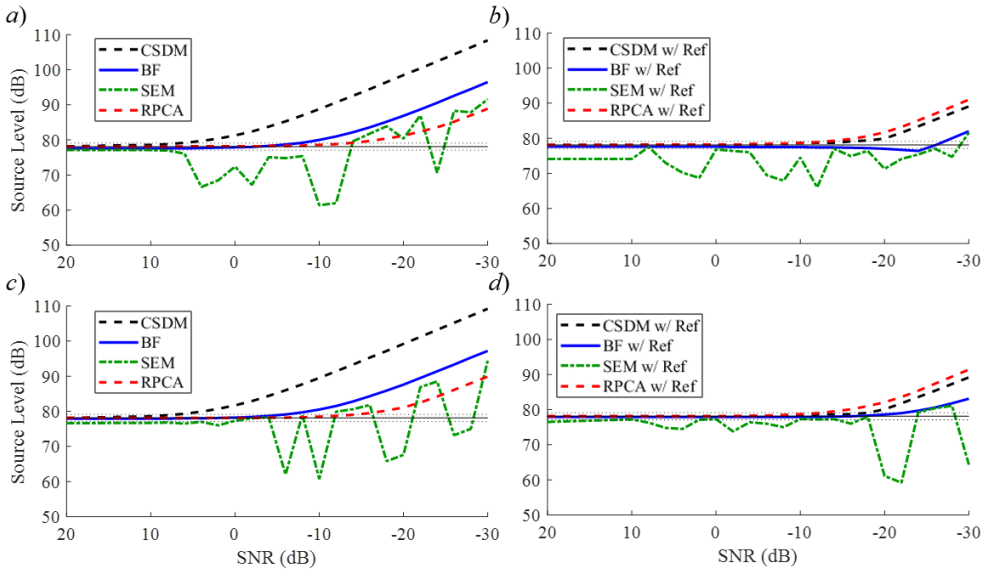

Figure 7.7: Source Level as a function of SNR for unprocessed CSDMs (black), CBF (blue), SEM (Green), and RPCA (Red) for two cases, DOA = 6.6° (a,b) and DOA = -29.6°, with and without a noise reference. Here, the noise is isotropic, Gaussian white noise.

tending slightly outside of the intended bandwidth, and helps in demonstrating the significance of including a reference. The dotted black line is the reference for the correct spectrum. The dashed black line is the straight CSDM SL calculation, the blue line is CBF, the green is SEM, and the red is RPCA. It is clear that when a reference isn't available, the capabilities quickly decline even at 0 dB (particularly for the quieter frequencies, since this SNR is calculated as an average across the spectrum considered here) and the results start to level out since the white noise is of approximately equal amplitude at all frequencies. When a reference is available, all techniques still do reasonably well at SNR = 0 dB, with CBF and SEM performing best here and at SNR = -10 dB. At SNR = -20 dB, all methods have reduced to the point of failure at the quieter frequencies, but still do well at the loudest frequencies (where the peak-frequency SNR is higher than the wideband SNR of -20), particularly CBF and SEM.

This portion of the experiment leads to several conclusions. First, in the presence of white noise, beamforming and RPCA are both very robust for DOA estimation, while SEM behaves slightly more unpredictably. When utilizing a noise reference, the improvements in robustness for SEM are significant, but minimal for the other techniques. For source level estimation, RPCA is

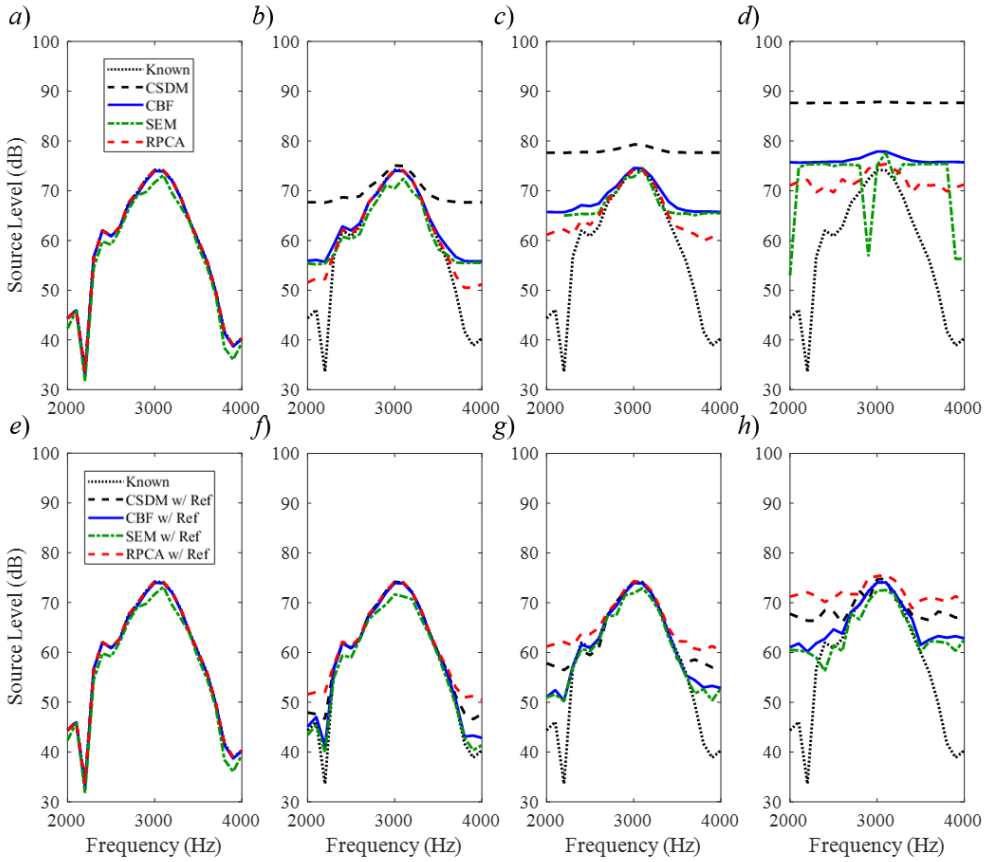

Figure 7.8: Reconstructed signal spectrums in the presence of white noise with four techniques without a reference (top row) and with a reference (bottom row) for no added noise (a,e), SNR = 0 dB (b,f), SNR = -10 dB (c,g), and SNR = -20 dB (d,h). The five lines show the correct reference spectrum (dotted black), using the CSDM diagonal (dashed black), CBF (blue), SEM (green), and RPCA (red). Note that SNRs are calculated across the full bandwidth here, and thus do not directly correspond to the cases shown in the previous three figures.

clearly the preferred method when a noise reference isn't available. Again, SEM shows some instability, though on average follows a reasonable trend. Processing a CSDM with a beamformer rather than simply using the CSDM diagonals to estimate source level provides a notable improvement, likely due to imperfect CSDM subtraction.

7.2.2.2 Spatially Correlated Noise

The second case considered is that of coherent noise generated by airflow from a compressed air nozzle. Here, localization methods are expected to perform worse at low SNRs than in the previous section when the noise is present, since the source of the noise has a discrete location in space. Sample localization outputs at 3 kHz are provided for this case in Fig. 7.9 for the same SNRs as Fig. 7.5 and for the same techniques (laid out in the same manner). At the SNR = 0 dB case, each method performes well both with and without a reference, except SEM, which gets the DOA correct, but significantly underestimates SL. Similar to the white noise case, a notable improvement in dynamic ranges comes with using a noise reference. With SNR = -10 dB, all methods fail without a noise reference, which is expected since now, a discrete source exists in the field and is 10 dB louder than the source of interest (though much of this SNR comes from reverberation, so the peak is not expected to actually be 10 dB higher). Despite this failure, with a reference included, each method performs well. It is also notable that, although the no-reference case doesn't find the source with the largest peak, the correct peak still exists in the window, often with a decent source level estimate. At SNR = -20 dB, the difference between the cases with and without noise references is much more dramatic. While all methods have clearly failed without the reference, including a reference saves the performance of CBF and SEM, and RPCA locates the DOA correctly (by a slim margin) but with several dB of error in source level.

In this case, since the noise is spatially coherent, the off-diagonal elements of the noise CSDM will be populated, meaning the assumption that the noise CSDM is sparse no longer holds for RPCA. However, the denoising technique described previously allows one to diagonalize the CSDM when performing the RPCA operation, prior to returning it to the original domain, hence

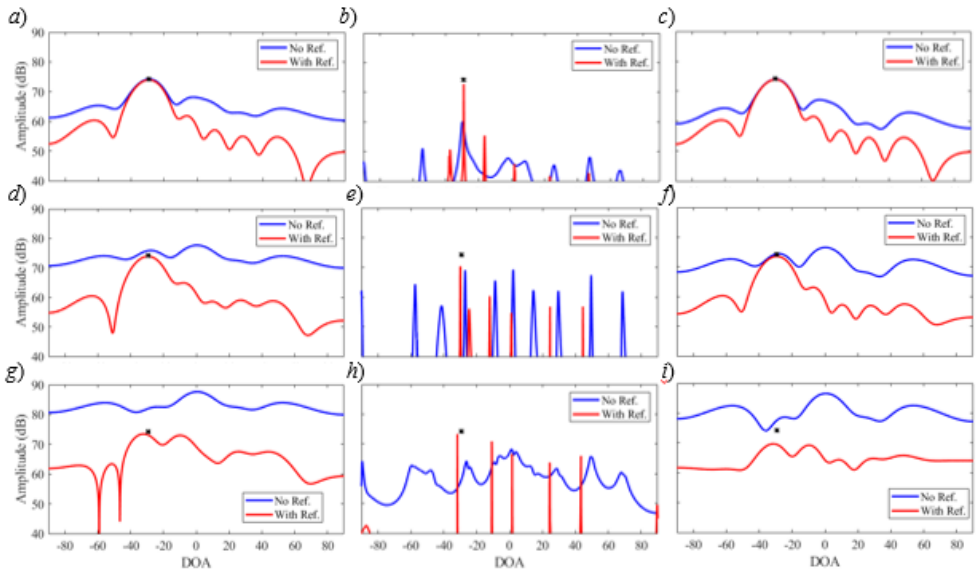

Figure 7.9: Same as 7.5 for the spatially coherent noise case.

the improvements from using a noise reference.

The performance of both DOA and SL estimation as a function of SNR is summarized in Figs. 7.10 and 7.11, again for 3 kHz. In the 6.6° case (top row), the lack of a reference simply means that the noise source slowly dominates the localization as SNR drops below 0 dB, and with the reference, a much lower SNR is achieved successfully for all methods, but with a sharp reduction in performance roughly at SNR = -20 dB. In the -29.1° case, similar results occur but with a sharper error shift in the no reference case, due to the larger difference in DOAs of the two sources. Interestingly, when the SNR drops below -20 dB and a reference is available, the localization methods choose an angle not corresponding to either source - this is likely a result of the imperfect noise reference, maybe indicating that the characteristics of the noise produced from the airflow change with time (perhaps the pressure drops, air temperature changes, or another physical property is slowly varying).

The SL error behaves as expected for both cases. At very high SNRs, the estimate is accurate (except once again, SEM underestimates without a reference), and as SNRs drop below 0 dB, the error begins to increase for all methods without references. Once a reference is added, all methods are able to achieve success down to roughly SNR = -20 dB. Here, there is no consistently preferred

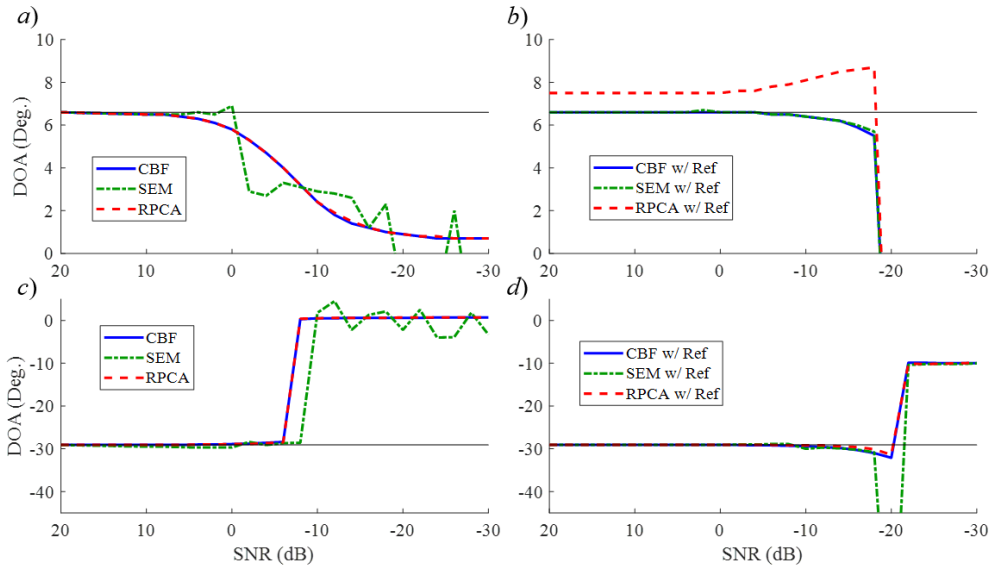

Figure 7.10: Direction of Arrival as a function of SNR for CBF (blue), SEM (Green), and RPCA (Red) for two cases, DOA = 6.6° (a,b) and DOA = -29.6°, with and without a noise reference. Here, the noise is spatially coherent.

method, though CBF seems to have the lowest error overall, combined with a robustness not seen in SEM. Since the noise is spatially correlated, the noise CSDM does not tend towards a sparse diagonal matrix, and thus RPCA does not perform any better than the other methods when a noise reference is not available.

Again, the source spectrums are considered over a 2 kHz bandwidth for varying SNR, shown in Fig. 7.12 for each method. The results are similar to the white noise case, with a relatively uniform distribution across the bandwidth as the noise is increased without a reference. When a reference is available, the performance of all methods improves significantly, particularly at the louder frequencies where the SNR is higher.

From this portion of the experiment, the difference in how each method behaves in the presence of coherent noise, rather than isotropic white noise, is demonstrated. RPCA is no longer successful without a noise reference, and each method struggles more at lower SNRs relative to the direction-less white noise case. However, the ability to subtract a noise reference still drastically improves source level estimation here, particularly if the structure of the noise CSDM is relatively constant over time.

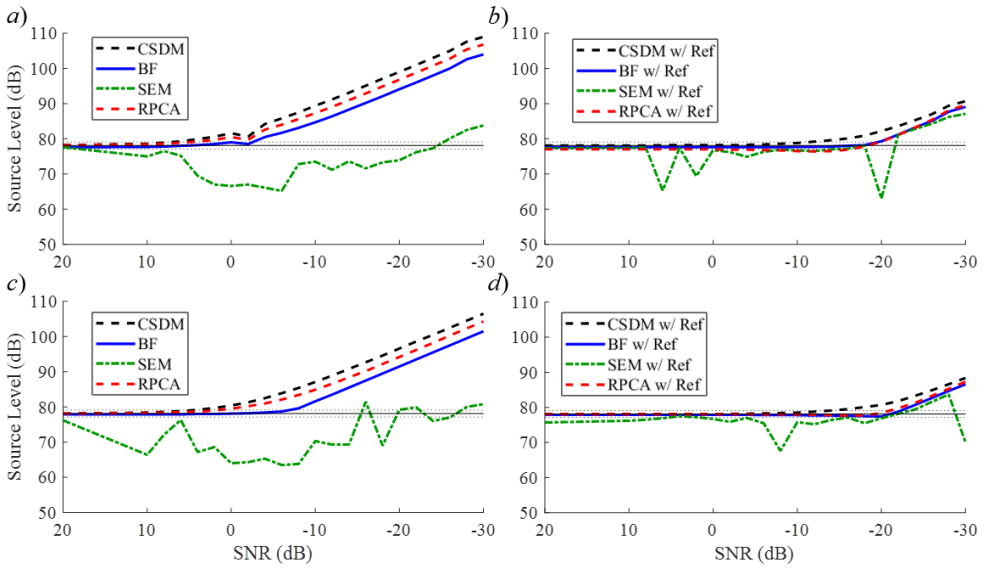

Figure 7.11: Source Level as a function of SNR for CBF (blue), SEM (Green), and RPCA (Red) for two cases, DOA = 6.6° (a,b) and DOA = -29.6°, with and without a noise reference. Here, the noise is spatially coherent.

7.3 Wind Tunnel Noise

This section considers a practical implementation of noise subtraction techniques for a specific laboratory experiment. This data was measured in the Anechoic Flow Facility at the Naval Surface Warfare Center - Carderock and was provided by Dr. Natasha Chang and Dr. Jason Smoker for research conducted as a part of the Naval Engineering Education Consortium. Here, noise is generated in a wind tunnel as a result of air flow interactions with the tunnel itself and with an object placed in the flow. An identical experiment is repeated with a small change to the object of interest's geometry, with the goal of exploiting measured changes to the acoustic field to localize the change and determine its contribution to the overall source level. Although the application in mind is that of a research and development experiment, the use of these techniques for detection, localization, classification, and tracking in field applications is a possible area for future investigation.

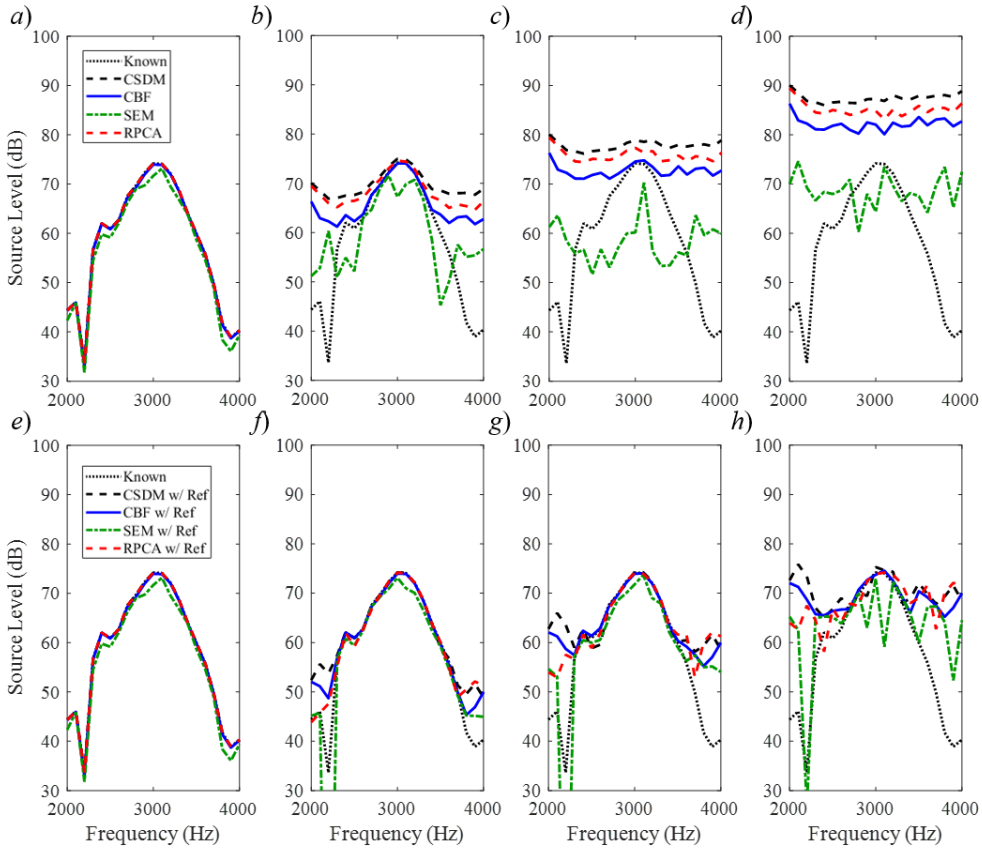

Figure 7.12: Reconstructed signal spectrums in the presence of coherent noise with four techniques without a reference (top row) and with a reference (bottom row) for no added noise (a,e), SNR = 0 dB (b,f), SNR = -10 dB (c,g), and SNR = -20 dB (d,h). The five lines show the correct reference spectrum (dotted black), using the CSDM diagonal (dashed black), CBF (blue), SEM (green), and RPCA (red).

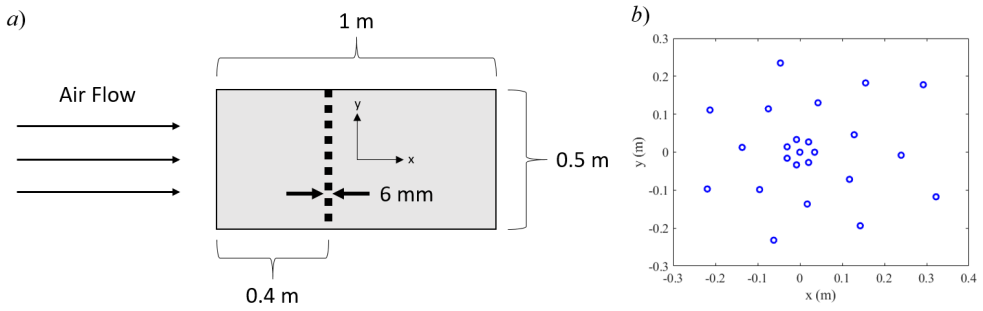

Figure 7.13: Geometry of the wind tunnel experiment. A 1.0 m by 0.5 m plate is aligned along the flow direction with and without a 6 mm gap along the y-axis, located at 0.4 m from the plate's leading edge (a) and centered below a spiral receiving array (b). Air flow is in the positive-x direction.

7.3.1 Experimental Setup

The experiments considered here are performed in a wind tunnel with a 2-D receiving array measuring aeroacoustic noise generated from air flowing over a flat plate. Figure 7.13 shows the geometry used in the experiment for both the plate layout (a) and the array (b). While the wind tunnel's exact geometry is unavailable, the plate is known to lie along the flow path, unobstructed, parallel to the flow. The plate itself is 1 m by 0.5 m, with the larger dimension aligned along the flow direction. The array is a 24-element, spiral array and is centered approximately 1.24 m above the plate, spanning nearly 0.6 m in diameter. Between the source and the array is an assumed acoustically transparent material meant to shield the array from the flow and placed within several inches of the array (the precise location is not known but is estimated to be between 2 and 5 inches). The second half of the experiment is conducted with the exact same setup, except with a 6 mm gap introduced to the plate, perpendicular to the flow direction, spanning the full 0.5 m plate width, and located 0.4 m downstream from the plate's leading edge. In this analysis, the gap is the feature of interest which can ideally be located by utilizing measurements of the plate with and without the gap, and its source level contribution estimated.

This experiment was repeated for five different wind tunnel fan speeds (including one in which the fan was off), with all other parameters ideally unchanged. Table 7.1 summarizes the ten experiments (2 for each fan speed, each with and without the gap) and the measured parameters during

each. Flow speed discrepancies of 0.1 m/s exist between experiments (determined by pitot tube measurements), as well as several degrees variation in temperature (Fahrenheit). In addition, runs 0-4 were completed consecutively, without making changes to the experimental setup, for each plate. However, many components of the experiment were disassembled and reassembled in order to switch between the plate with and without the gap, and an unknown amount of time passed between the two sets of experiments, providing the potential for significant experimental deviations unrelated to the presence of the gap. Roughly five minutes of data is taken in each of the cases, with the flow providing a wide-band frequency response for use in the analysis to be performed here.

Figure 7.14 shows the acoustic power spectrum output from each run with 100 Hz resolution. Here, non-overlapping 0.01 s windows were taken over the full five minutes of each data set and the frequency-domain magnitudes are averaged over these windows. The three figure panels show the spectrums for each run for the plate with a gap (a), the plate without the gap (b), and the difference between the two spectrums (c). In Figs. 7.14(a) and 7.14(b), runs 0-2 roughly overlap, indicating that the aeroacoustic field in these cases is dominated by noise inherent to the experimental environment and/or equipment, and suggesting that the contributions from aeroacoustic noise are negligible. Runs 3 and 4, however, provide a significant increase in amplitude over the apparent background noise levels. The third panel (c), shows the difference between the curves in (a) and (b) for each case. Again, for runs 0-2, the uniform and low-dB differences suggest that the aeroacoustic noise contributions are negligible, and any difference seen here can be attributed to non-repeatability between experiments. The difference curve for run 3 shows significant deviation from the prior cases, suggesting that some influence from the addition of the gap now exists. However, these differences still have comparable SPL to the differences in runs 0-2, suggesting that separating the gap contributions from the experimental non-repeatability contributions may be challenging. Finally, run 4 shows even more significant deviation with the gap added, and an increase in SPL significantly larger than that of the other curves, suggesting that source level quantification may be successful here. The dashed portions of the lines in panel (c) indicate regions of

Table 7.1: Measured characteristics for the 10 experiments considered herein. For each flow speed, two sets of data were taken - one for the plate without a gap and one for the plate with a gap.

Run	Plate	Impeller RPM	Temp (°F)	Flow Speed (m/s)
0	No Gap	0	77.9	0
	Gap	0	81.3	0
1	No Gap	38.6	78	4.3
	Gap	38.6	81.3	4.2
2	No Gap	75.2	77.9	9.2
	Gap	75.5	81	9.1
3	No Gap	150.7	77.7	19.5
	Gap	150.7	80	19.4
4	No Gap	225.8	77.3	29.8
	Gap	225.6	79.1	29.7

the signal bandwidth where the plate without a gap was louder, perhaps indicating some influence from experimental non-repeatability.

7.3.1.1 Flow and Shear Layer Correction

Before considering the gap localization results, the impact of the flow on the acoustic propagation must be considered. The mean flow of the waves as they propagate between the source and the array, as well as the shear layer refraction when the wave passes into the no-flow region closer to the receiving array, will both affect the measured fields. Both of these effects were considered previously in Amiet (1978) [8], however this analysis assumed that the receiver was in the far field, and also did not consider cases where h/D (h being the source-to-shear-layer separation, D being

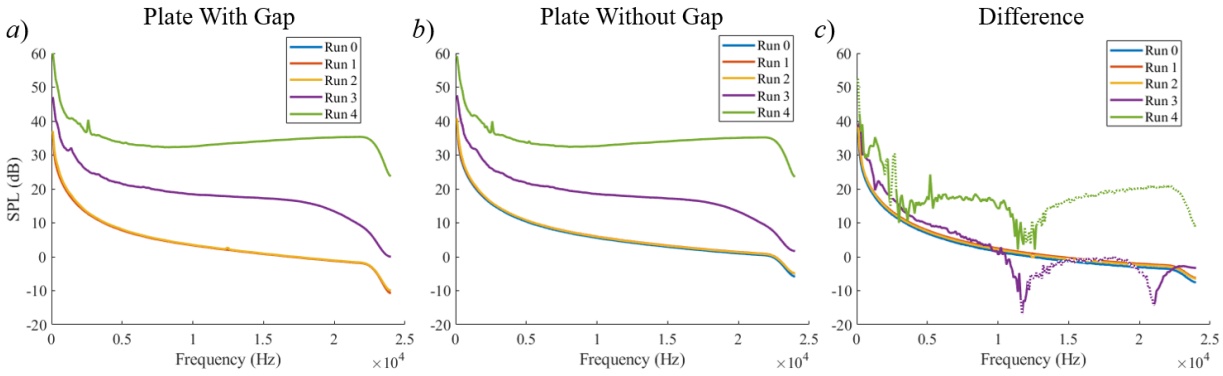

Figure 7.14: Frequency spectra for the plate with a gap (a), the plate without a gap (b), and the differences between the two curves (c), for each run. The dashed portions of the difference curves indicate regions where the plate without the gap was louder than the plate with the gap.

the source-to-receiver-plane separation) was close to unity. Thus, direct application of this analysis for the full geometry is not applicable, but calculations from this result can be used to determine the effect on each individual ray path, and ultimately the relative phase shift at each receiver. The geometry for this setup is shown in Fig. 7.15, where r_m is the actual source-to-receiver range, θ_m is the actual angle between the source and receiver, θ is the apparent angle of the arrival path, and θ_c is the propagation angle of the ray that eventually arrives at a given receiver. For a case that isn't in the far field, the apparent source shift is difficult to calculate analytically, since it varies between receivers. Here, the apparent phase shift at each receiver was calculated for the flow speeds in runs 3 and 4, using

$$\tan\theta_c = \frac{\zeta}{\beta^2\cos\theta + M}, \tag{7.14}$$

and

$$r_m\cos\theta_m = h\cot\theta_c + (r_m\sin\theta_m - h)\cot\theta, \tag{7.15}$$

where,

$$\zeta^2 = (1 - M\cos\theta)^2 - \cos\theta^2, \tag{7.16}$$

and

$$\beta^2 = 1 - M^2, \tag{7.17}$$

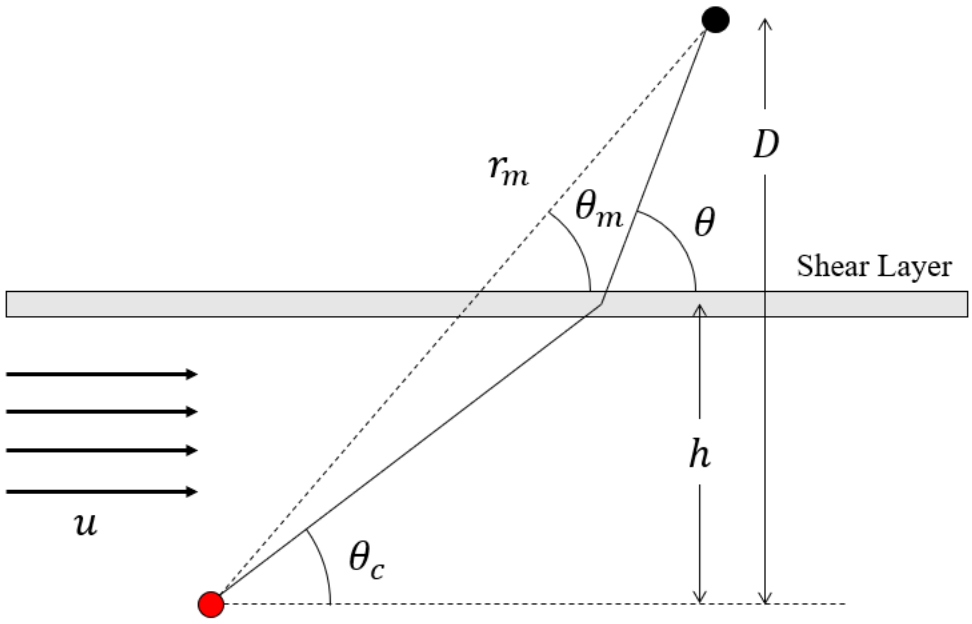

Figure 7.15: Schematic for calculating the effects of flow and shear layer refraction on apparent source localization.

where M is the Mach number [8]. Here, h is not known (it was not recorded at the time of the experiment), but is estimated to be 1.15 m. With this result, a simple point source simulation with identical AFF geometry and the source placed at the expected gap center was used to determine the expected shift. The results of this simulation are shown in Fig. 7.16 for an 8.5 kHz source, which shows a beamformed output with no flow (a), and with the flow speeds from runs 4 (b) and 3 (c). Here, an expected shift of roughly 7 cm is shown for run 4, and 4 cm for run 3. For the purposes of the gap localization, these corrections will be incorporated into the beamformed outputs in the next section.

7.3.2 Results

The first consideration in this section is whether or not the acoustic energy coming off of the plate or from the gap can be detected in a large field using one of the source localization techniques described above (i.e. assuming the plate location is unknown, can the search window be narrowed from a much larger region?). The actual wind tunnel geometry is unavailable, so a large 5 m

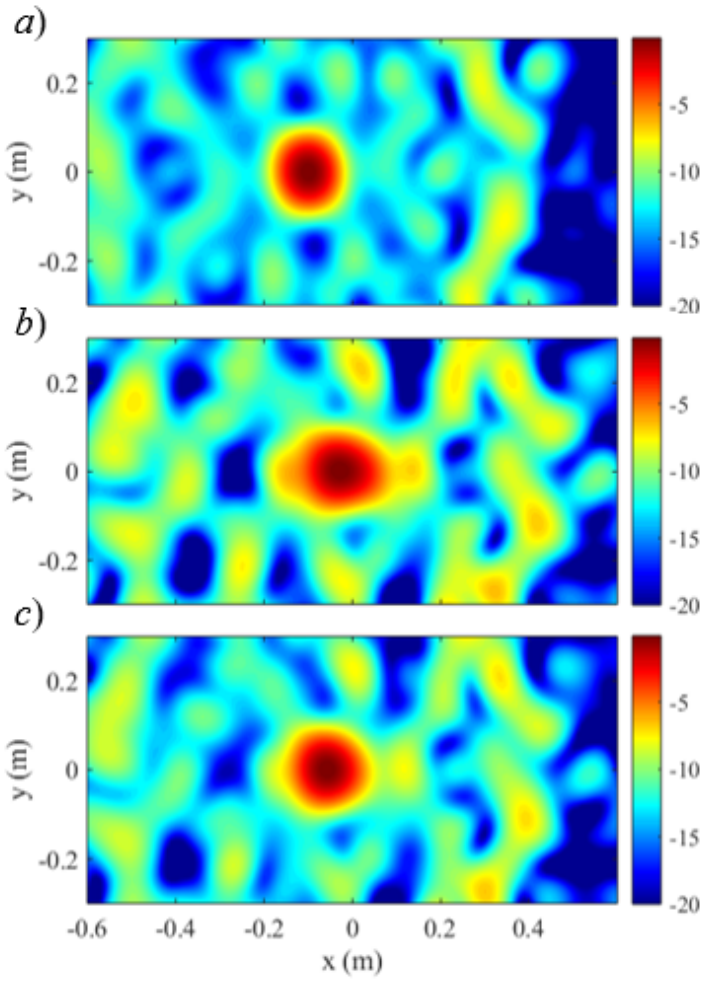

Figure 7.16: Simulated beamformed output for a point source using the AFF geometry with no flow (a), and the flow speeds from runs 4 (b) and 3 (c), including a correction for the flow speed and shear layer refraction. The known source location (a) is 7 cm upstream from the apparent location using a flow speed from run 4 (b) and 4 cm upstream from the apparent location using a flow speed from run 3 (c).

by 5 m window is chosen to consider with each technique, with the expected plate midpoint at the center of the window, to determine if the acoustic energy source is localized in this region. Rather than a three dimensional beamforming operation, the beamforming is performed on the plane defined by the plate's surface. Figure 7.17 shows the outputs of each of the four methods described in section 7.1, CBF (a), SEM (b), RPCA-CBF (c), and RPCA-SEM (d), all processed at 8 kHz, for run 4. In addition, CBF and SEM with CSDM subtraction (e,f respectively) and RPCA-CBF and RPCA-SEM with denoising (g,h respectively) are shown. In each window, some indication of the gap can be seen before removing the reference measurement, but it is difficult to distinguish from other characteristics in the field. After removing the reference measurement, the focus of acoustic energy towards the plate center is much more apparent. In each column, the dynamic range matches before and after the reference is removed, highlighting the effectiveness of this procedure. The same results for run 3 are also shown, with the same configuration, in Figure 7.18. Again, the results are shown for 8 kHz and in some cases indicate a finer region where the plate can be expected, but it is much less clear in this case, particularly with the RPCA methods. This is likely due to the result from Fig. 7.14(c), that suggests the gap contribution is not easily separated from other experimental differences. For runs 1 and 2, no indication of a finite region was obtained from the beamformer output, supporting the conclusion that the slow flow speeds did not generate significant aeroacoustic noise, particularly at the gap location.

Given that acoustic energy coming from the plate and gap in run 4 (and run 3, to a lesser degree) is significant and allows for some refinement of the plate's location when the reference is utilized, each method is considered over a much smaller window, slightly larger than the plate's actual dimensions, for the purposes of localizing the gap. The same four methods are considered again in Figs. 7.19 (run 4) and 7.20 (run 3), again for 8 kHz, with the first column corresponding to CBF, the second to SEM, and third to RPCA-CBF, and the fourth to RPCA-SEM. In each case, the corresponding flow corrections have been incorporated, as determined in Section 7.3.1.1. Three cases are considered in Fig. 7.19 - the plate with the gap (first row), the plate without the gap (second row), and the result from each method when the reference measurement is removed from

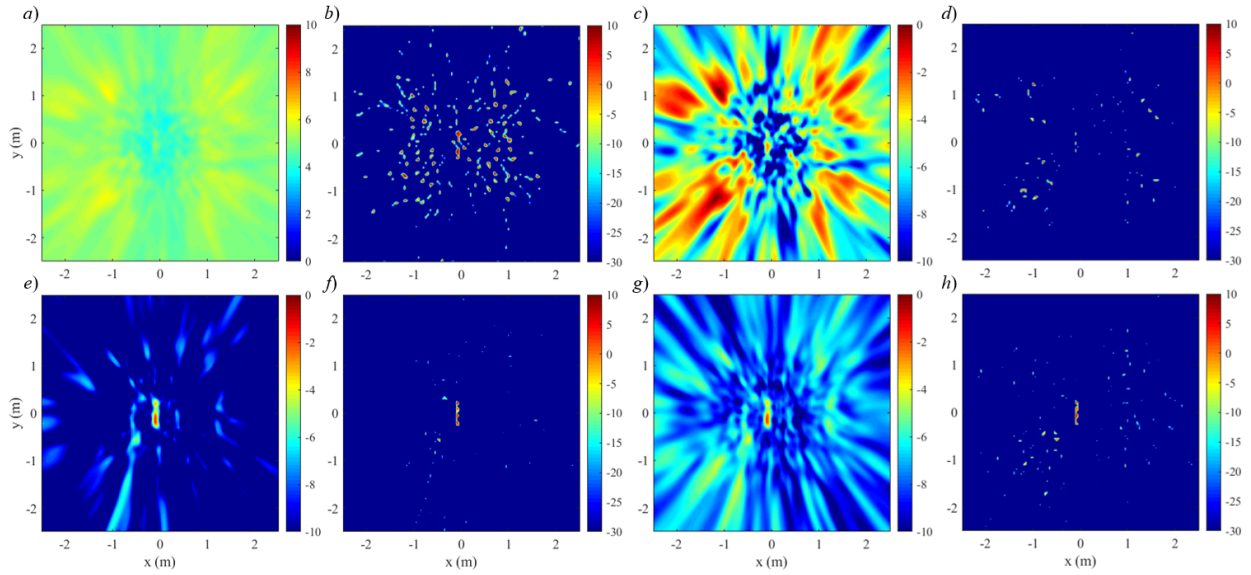

Figure 7.17: The output of the plate-with-gap at 8 kHz using CBF (a), SEM (b), RPCA-CBF (c), and RPCA-SEM (d), and CBF with CSDM subtraction (e), SEM with CSDM subtraction (f), RPCA-CBF with denoising (g), and RPCA-SEM with denoising (h) over a 5 m by 5 m window with 5 cm resolution. All results for run 4.

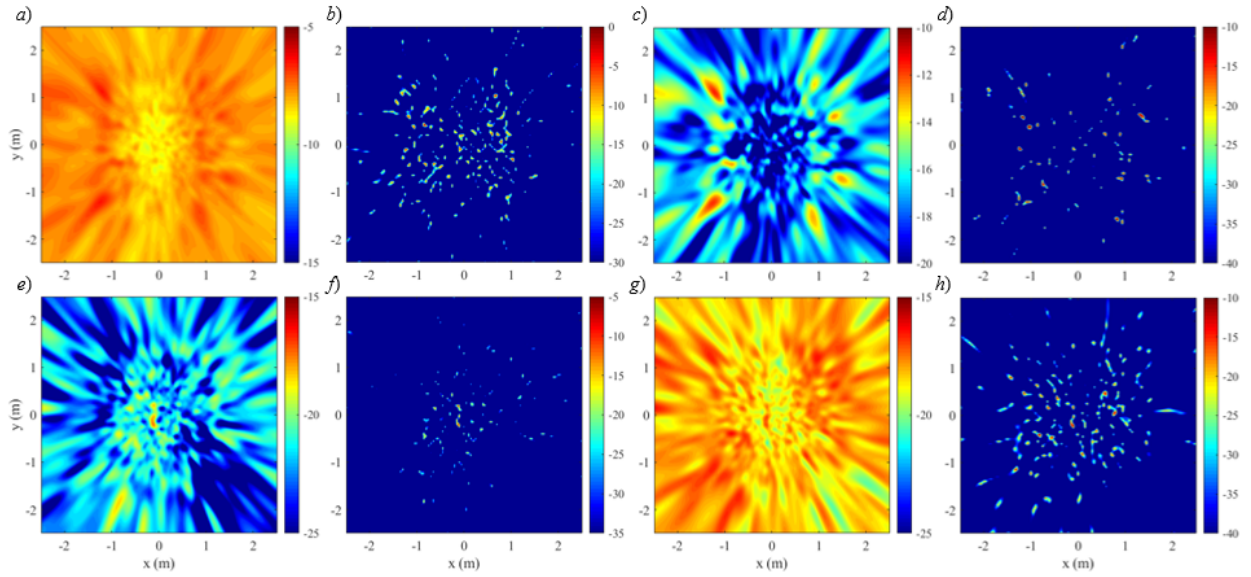

Figure 7.18: The output of the plate-with-gap at 8 kHz using CBF (a), SEM (b), RPCA-CBF (c), and RPCA-SEM (d), and CBF with CSDM subtraction (e), SEM with CSDM subtraction (f), RPCA-CBF with denoising (g), and RPCA-SEM with denoising (h) over a 5 m by 5 m window with 5 cm resolution. All results for run 3.

the plate-with-gap measurement (third row). For Fig. 7.20, only the output after the noise removal step is shown, for brevity. In these plots, the dashed white line corresponds to the expected plate boundaries, and the dashed black or red lines correspond to the expected gap location (note that the gap is not present in the second row measurements). Conventional beamforming shows some indication of what is likely to be the gap in 7.19(a), but the low dynamic range does not yield much certainty. When removing the reference measurement (7.19(e)) with CSDM subtraction, a much more robust result is obtained with nearly 30 dB of dynamic range (7.19(i)). SEM does not provide any useful indication of the gap location in 7.19(b), but SEM with CSDM subtraction (7.19(f)) indicates the gap position along both axes with much higher precision. RPCA-CBF again provides some indication of the gap location without any subtraction, similar to CBF, but with a much larger dynamic range. With the denoising process (7.19(k)), some of the other misleading points that don't correspond to the known gap location (dark red) are removed, improving the overall result, but without improvement over CBF. Finally, RPCA-SEM actually provides some reasonable indication of the gap prior to denoising, especially when compared with SEM. After the denoising process, RPCA-SEM does indicate a gap position well, but it includes more uncertainty in the full field than SEM does. For Fig. 7.20, the results are similar for the CBF and RPCA-CBF methods, though with significantly reduced source levels (expected) and significantly reduced dynamic range. While the SEM and RPCA-SEM methods both provide some peaks along the gap, other artifacts are prevalent throughout the window, leading to more uncertainty than in the previous case. In all of the cases shown, there is a discrepancy of approximately 6 cm in the expected gap location, and the locations determined by the four methods considered here. However, the location is consistent between the different two runs, suggesting the flow correction was implemented correctly.

Of these four methods, SEM with CSDM subtraction clearly provides the most precise indicator of the gap position in run 4, and CBF likely works best in run 3. However, both RPCA techniques provide a stronger indication than CBF and SEM when the noise reference isn't utilized in run 4. This indicates that perhaps the field potentially has some behavior that is mathematically

similar to a coherent source (the gap) in an isotropic white noise field, though not enough to make this method alone a feasible solution.

Each method provides an indication of the gap when processing at frequencies between 5 and 11 kHz. This may be expected based on Fig. 7.14(c), given that this region has higher SPL in the plate-with-gap case. Below 5 kHz, some indication of the gap is possible, but the reduction in beam width makes it challenging to localize with certainty without prior knowledge of the gap location, and does not provide good indication of the y-direction gap length. Frequencies above 11 kHz don't appear to localize the gap at all, suggesting the aeroacoustics generated by the gap are frequency dependent. Prior work [70] indicated that the acoustic energy from flow over a gap begins to decay when $f\delta/U_0$ is greater than unity, where δ is the boundary layer thickness and U_0 is the free stream velocity. Considering laminar (Blasius) boundary layer of flow over a plate yields a result of $f \approx 10^4$, suggesting that difficulty beamforming above 11 kHz may be predictable.

To localize the gap more robustly, an average of beamformed outputs over the full 5-11 kHz bandwidth is considered. Figure 7.21 shows this result for the four methods - CBF with CSDM subtraction (a), SEM with CSDM subtraction (b), RPCA-CBF with denoising (c), and RPCA-SEM with denoising (d) - for run 4. The same layout with the same parameters for run 3 is shown in 7.22. Again, the flow correction is included in this result. In run 4, all four methods clearly indicate an estimated gap location, and run 3 is also successful, but with significantly less dynamic range and more uncertainty in the window. Due to the precision limitations of CBF, a robust indication of a gap location is provided, but with reduced precision. The results using SEM-based methods provide not only a more precise indicator of the gap location, but also indicate the gap's width well, with the output intensity quickly dropping by >20 dB within 1-2 cm of the plate's y-direction edge on either side. The imaging capabilities of SEM with CSDM subtraction and RPCA-SEM with denoising provide a precise imaging of the gap and indicate that noise is generated along the full 0.5 m, with some emphasis towards the edges.

All of the localization results thus far have provided strong indications of the gap's presence. However, the localization results are consistently showing the gap about 6 cm upstream from the

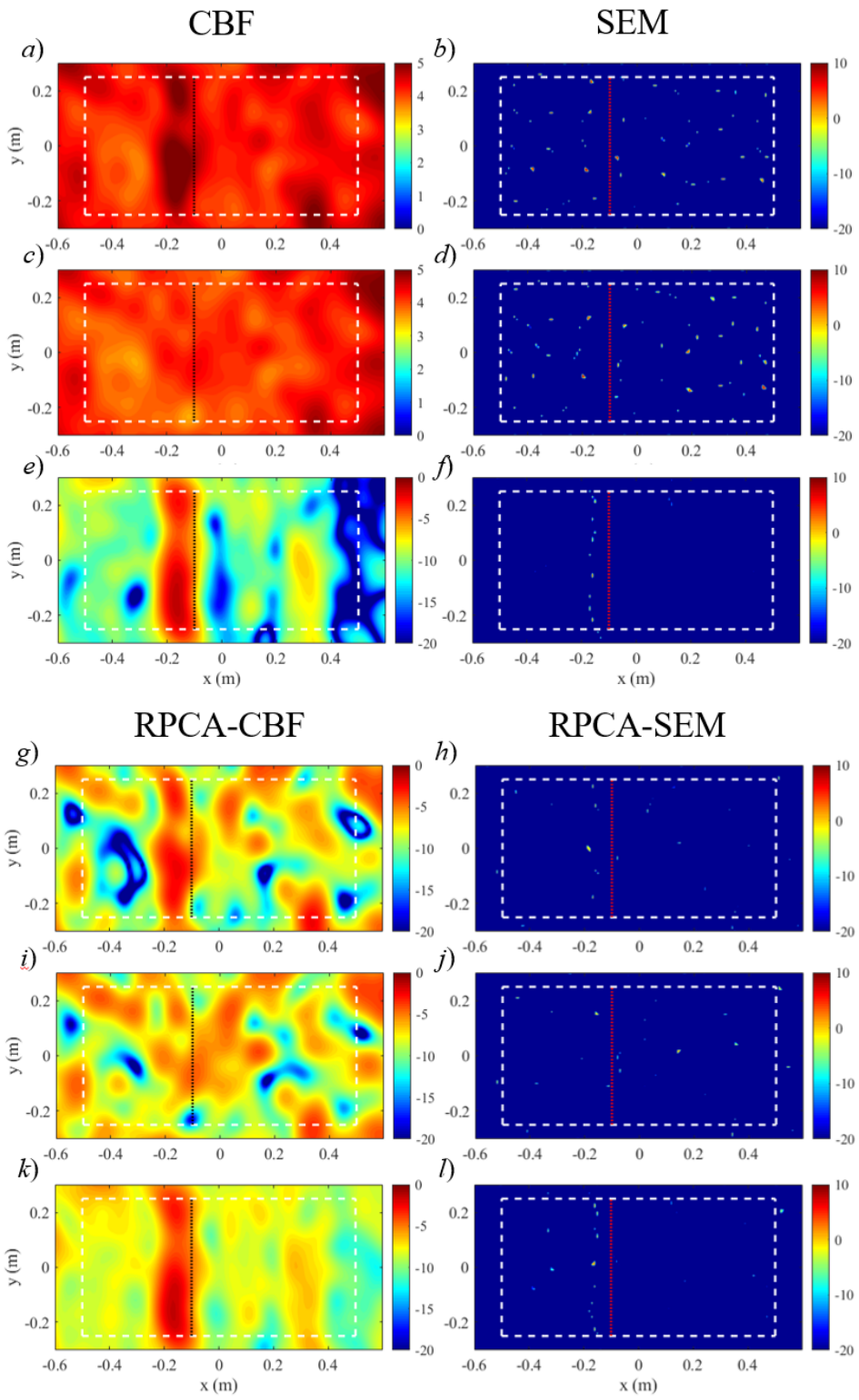

Figure 7.19: The CBF (a,e,i), SEM (b,f,j), RPCA-CBF (c,g,k), and RPCA-SEM (d,h,l) outputs for the plate-with-gap (first row), plate without a gap (second row), and the gap-only output (final row) obtained from removing the second row from the first row. All results are for run 4. The plate edges are indicated by a dashed white line and the expected gap location by a dotted red or black line.

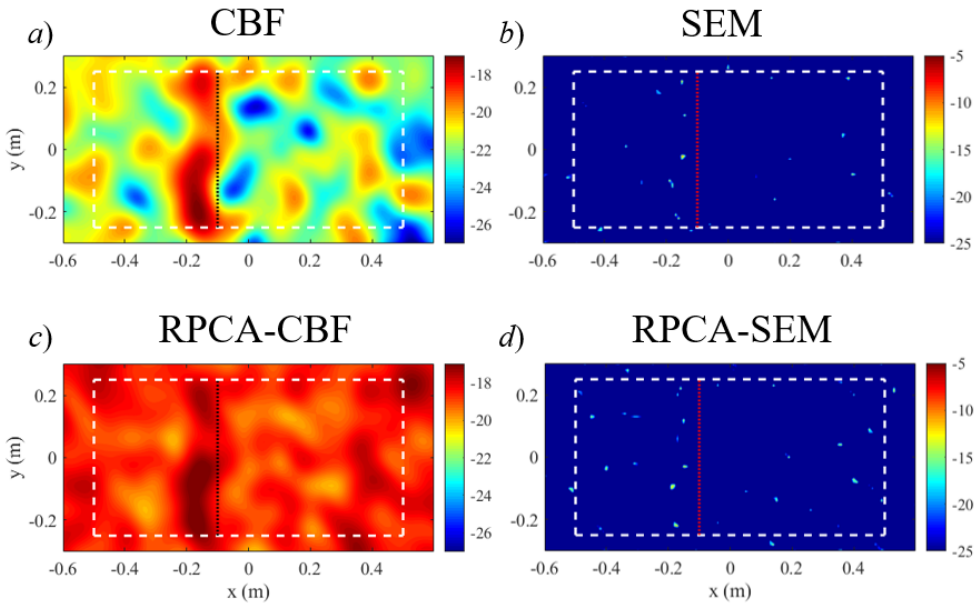

Figure 7.20: The CBF (a), SEM (b), RPCA-CBF (c), and RPCA-SEM (d) the gap-only output (same as third row in Fig. 7.19, but for run 3).

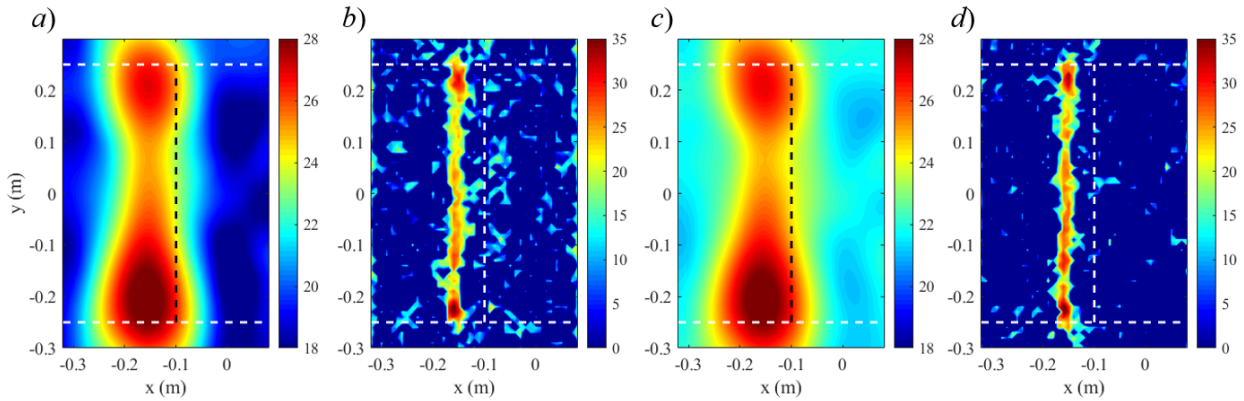

Figure 7.21: Beamformed output for run 4 averaged over a bandwidth of 5-11 kHz. CBF with CSDM subtraction (a), SEM with CSDM subtraction (b), RPCA-CBF with denoising (c), and RPCA-SEM with denoising (d) are each shown. Note that the expected gap location is now either a black or white vertical dashed line, chosen for visual clarity.

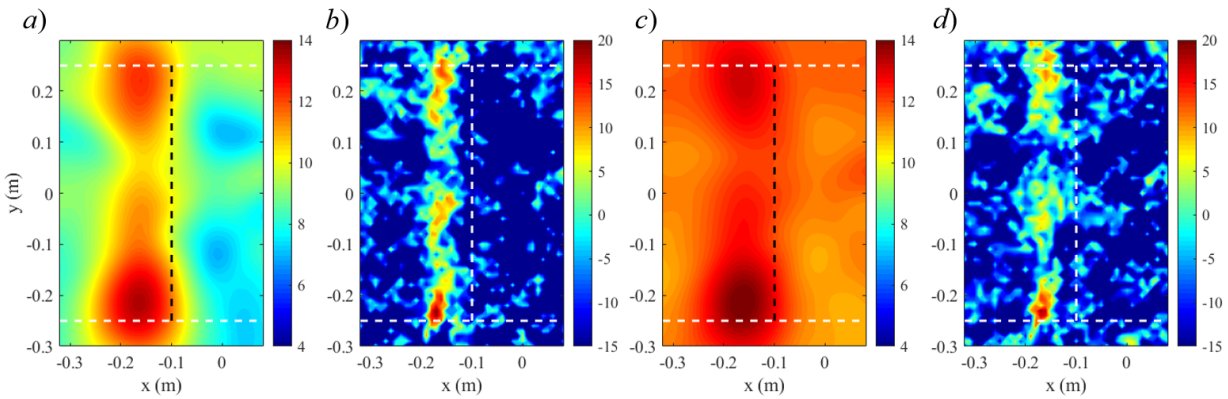

Figure 7.22: Same as Fig. 7.21 for run 3.

expected gap location, when the flow correction is included. The strong agreement between the gap locations in Figs. 7.21 and 7.22 suggest two things - that the flow correction has been implemented correctly and that a consistent feature is being located between the two runs (likely the intended gap). Several factors are potentially contributing to the localization bias present in these results. First, the flow correction may not be implemented perfectly and the flow barrier may be at a different location that assumed here - though the agreement between the two results suggests that this has been done correctly. Second, significant levels of experimental uncertainty exist, particularly since it wasn't originally intended as a source localization experiment. Potential sources of uncertainty include the horizontal position of the array relative to the plate (which is estimated to be several cm in magnitude), changes occurring between the setup of the plate with no gap and the plate with the gap experiments and the environments between the two days, the position of the flow barrier used in the flow correction, or the relative planes of the plate and the receiver array (if the receiving array were tilted by 1°, this would correspond to an additional 2.2 cm error). Thus, the potential sources of uncertainty may be enough to explain this discrepancy.

The final parameter of interest is the source level increment that results from the addition of the gap to the plate. The results thus far suggest that the addition of the gap provides enough increase acoustic energy to distinguish it between the two experiments and localize it well when the reference measurement is exploited. The reference source level for the gap to be used here is

that shown in Fig. 7.14(c) (but will be expressed as a source level increment here). The success of each technique will be measured against this curve and appropriate error bars determined from the standard deviation of the mean of the curves in Figs. 7.14(a) and 7.14(b) at each frequency, over the consecutive 0.01 s windows. The source level increment is calculated as the ratio of the measurements with the gap present to those without, expressed in decibels, and adjusting for the $1/r$ term, providing source level increment from the standard 1 m reference distance.

For the beamforming-based methods (CBF with CSDM subtraction and RPCA-CBF with denoising), the ambiguity surface output along the line previously determined to represent the gap is summed and the influence of the point spread function for a point source using this experimental configuration (determined via simulation of a point source) is accounted for with the double integral over the gap length. The expression for the beamforming output can be written

$$\int_{-l/2}^{l/2} B(y)dy = \int_{-l/2}^{l/2}\int_{-l/2}^{l/2} \mathrm{SL}_{CBF}(y)\mathrm{PSF}(y-y')dydy', \tag{7.18}$$

where $\mathrm{PSF}(y)$ is the point spread function of the beamformer, $\mathrm{SL}_{CBF}(y)$ is the spatially-dependent source level along the gap, $B(y)$ is the beamformer output along the gap (with a $1/r$ correction included), and l is the plate width in the y-direction. For the analysis here, the source level is treated as a mean source level distributed evenly across the gap, rather than each point having a unique value (which is potentially more accurate, but more difficult to calculate). This approximation allows Eq. 7.18 to be rewritten as

$$\mathrm{SL}_{CBF} = \frac{\int_{-l/2}^{l/2} B(y)dy}{\int_{-l/2}^{l/2}\int_{-l/2}^{l/2} \mathrm{PSF}(y-y')dydy'}. \tag{7.19}$$

For the SEM-based methods (SEM with CSDM subtraction and RPCA-SEM with denoising), the technique specifically aims to model a CSDM that accounts for as much of the signal energy as possible (and as accurately as possible with respect to localization or DOA). Thus, the output of the SEM-based methods ideally includes the total source level along the gap and the values from

the ambiguity surface outputs can simply be combined to estimate the total source level of the gap, i.e.

$$\mathrm{SL}_{SEM} = \int_{-l/2}^{l/2} A_l(y)dy. \tag{7.20}$$

The results of this analysis are shown in Fig. 7.23 for 500 Hz increments between 5 and 11 kHz for both runs 3 (a) and 4 (b). The dashed lines indicate the error bars corresponding to the 95% confidence interval, determined by the variation of the signal energy at each frequency over the full five minutes. The results from all four techniques are shown, CBF (blue 'x'), SEM (green circle), RPCA-CBF (black 'x'), and RPCA-SEM (black circle). For run 3, the source levels determined using the four methods of interest do not agree with the red curve. However, as was previously discussed based on Fig. 7.14(c), the aeroacoustic effects of the gap do not generally exceed the background noise differences and experimental non-repeatability expected, thus a poor result is not surprising here. For run 4, each method typically provides a source level within the error bars, indicating that each method is potentially useful for this task. However, CBF and SEM in particular lie very close to the desired curve and have very few points (primarily on the bandwidth edges) outside of the error bars. This result indicates that, for this experimental case, a straightforward CSDM subtraction technique does a better job of removing the reference measurement from the plate-with-gap measurement. In general, the CSDM subtraction method relies on sources in the field that are incoherent with one another, providing few unwanted cross terms in the CSDM calculation when averaged over a significant number of snapshots, which is likely the case here. For the RPCA methods, the goal is to separate a sparse and low-rank matrix. Since the noise field in the reference likely can't be modeled as isotropic white noise, and the distributed noise source may not provide a low-rank source CSDM, the method's performance declines. While the performance of run 3 is unclear, the agreement in source level increment between the markers in runs 3 and 4 suggests that there is potentially some success in the result of run 3.

Overall, the average SL error across the spectrum considered in run 4 was 0.006 dB for CBF with CSDM subtraction, 0.010 dB for SEM with CSDM subtraction, 0.013 dB for RPCA-CBF

with denoising, and 0.010 dB for RPCA-SEM with denoising. Despite the sub-0.15 dB source level increments considered here, all methods, particularly the CSDM subtraction methods, successfully estimate the source level increment.

7.4 Conclusion

This chapter demonstrated the capability of four techniques, CBF with CSDM subtraction, SEM with CSDM subtraction, RPCA-CBF with denoising, and RPCA-SEM with denoising, for the purposes of locating an acoustic source in a noisy field with the use of a noise reference. The first half of the chapter focused on a discrete source in two types of noisy fields, while the second considered a distributed source with noise generated by air flow (which was also the source of the background noise).

In the laboratory experiments with a discrete source, all techniques demonstrated the ability to localize the source and estimate its source level at SNRs well below 0 dB. In the white noise case, methods without utilizing a reference were successful down to at least -5 dB SNR before the SL error exceeded 1 dB and the localization began locating the noise source instead of the source of interest. Notably, SEM showed some erratic behavior that significantly reduced its accuracy and robustness, and RPCA demonstrated the ability to estimate source level at SNRs below -10 dB without a reference, since the white noise could be assumed to yield a sparse CSDM. With a reference available, all methods performed well down to roughly -15 dB, with CBF using CSDM subtraction, the simplest of these techniques, generally performing best.

When the noise was generated by a physical source in the room, the methods generally only succeeded slightly below 0 dB SNR without a reference, with error increasing at higher SNRs than in the white noise case (and when the noise source was placed close to the discrete source, the localization error increased at higher SNRs, but did so more slowly). With the noise reference available, all methods saw localization success at nearly -20 dB SNR, and source level success at slightly lower than -20 dB SNR. In these cases, a single method didn't clearly outperform the

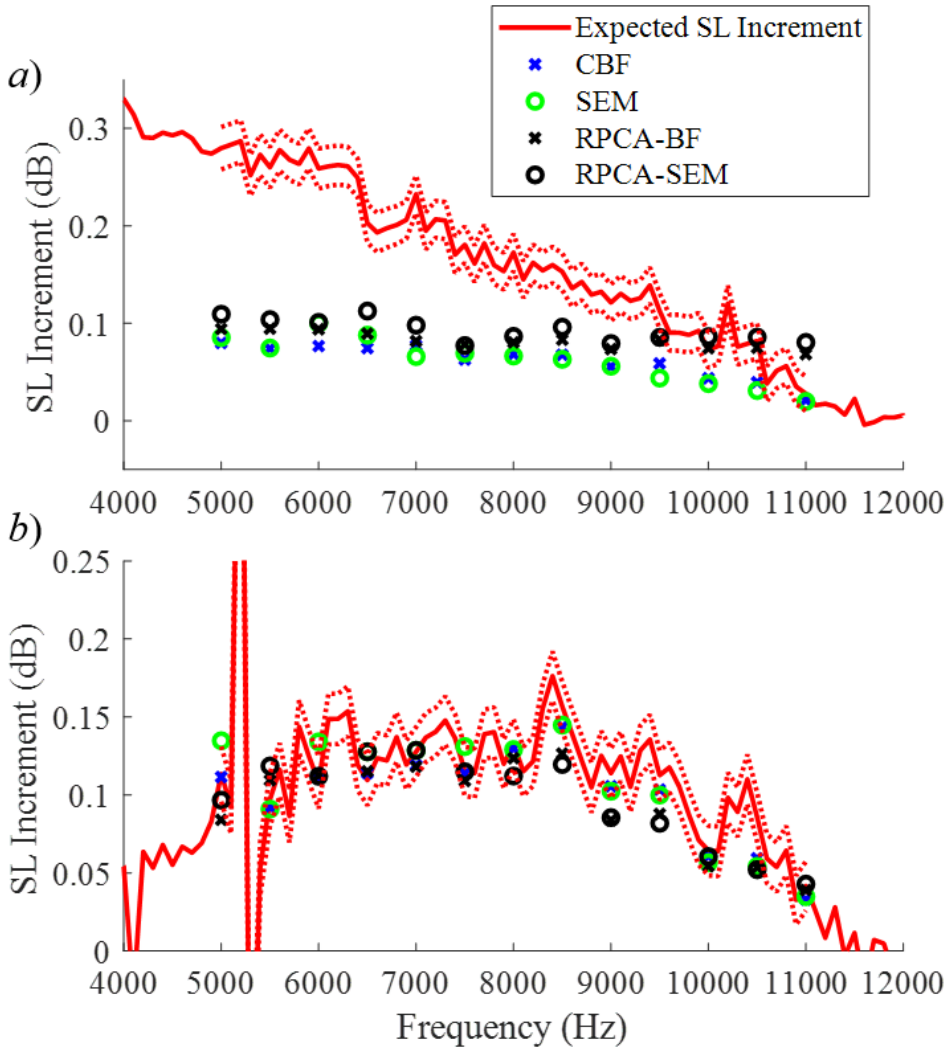

Figure 7.23: A comparison of the SL increment determined by CBF (blue 'x'), SEM (green 'o'), RPCA-CBF (black 'x'), and RPCA-SEM (black 'o') and the expected increment (red curve). The dashed red lines indicate the error bars corresponding to the 95% confidence interval, determined based on the standard deviation of the energy at each frequency over consecutive 10 ms windows through the full 5 minute signals.

others, but this demonstrated that a discrete noise source generally works better as a reference than a white noise source when trying to remove its influence from the CSDMs used in these signal processing techniques.

In the wind tunnel experiments, all techniques showed the ability to locate a small change to a plate when using a reference measurement of the plate prior to implementing the change. Here, the SEM-based methods, particularly SEM with CSDM subtraction, provided the most precise imaging of the gap, especially when incorporating bandwidth into the result. The localization from the CBF-based methods provided a robust result, but the lack of precision leaves additional ambiguity, as expected. Unfortunately, specific experimental uncertainty was not available to fully quantify the localization success, particularly after making adjustments for flow effects, and an overall bias of approximately 6 cm cannot be confidently attributed to this uncertainty, though it is likely the explanation. Once again, all four methods showed the ability to estimate the source level increment expected from the addition of the gap, with particularly strong performance when using the methods with CSDM subtraction. In run 4, average errors of 0.006 dB (CBF w/ CSDM subtraction), 0.010 dB (SEM w/ CSDM subtraction), 0.013 dB (RPCA-CBF w/ denoising), and 0.010 dB (RPCA-SEM w/ denoising) were achieved despite the minimal source level increments of less than 0.15 dB.

Four key conclusions were determined from the work in this chapter. (1) For a discrete source in an isotropic white noise field, RPCA can locate the source and estimate source level without the use of a reference measurement down to an SNR of roughly -15 dB, while other methods typically cannot drop below -10 dB. (2) All techniques utilized here with a noise reference are successful in localization and source level estimation down to SNRs of roughly -20 dB when the noise field is spatially coherent. (3) SEM-based methods with CSDM subtraction or denoising provide strong imaging capabilities for changes to an object in a flow field when a reference is available, though all techniques utilizing a noise reference were capable of indicating a consistent, expected gap location. (4) All techniques utilizing a noise reference were able to determine SL increment of a change to an object in a flow-field, with the methods based on CSDM subtraction performing best,

when the SL increment from that change is more significant than the non-repeatability differences between experiments.

CHAPTER 8

Conclusions

8.1 Summary

Acoustic array signal processing is a wide area of research with many applications, several of which have been considered here, with a focus on applications to underwater acoustics. Array signal processing of underwater acoustic fields easily becomes complex due to the propagation characteristics in the ocean and difficulties associated with deployment of receiving arrays. Underwater environments are characterized by ocean floor and surface interactions, refraction from depth- and range-dependent sound speed profiles, frequency-dependent attenuation, low SNRs, and interactions with rough surfaces or other underwater objects. In addition, receiver arrays are subject to spatial uncertainty, particularly during ship maneuvering for a towed array, and geometric designs not suitable to the frequency of interest or the coherence length of a given environment. These challenges provide difficult scenarios and environments for completing desired tasks, such as source detection, localization, classification, tracking, signal recovery or deconvolution, navigation, and mapping, among others. In this work, the applications focused on source localization and beamforming, blind deconvolution of long-durations signals, and general array signal processing parameters - namely coherence length. The work in Chapters 2-6 focused on areas of acoustics specific to or applicable to underwater acoustics. Chapter 7 shifts the focus to array signal processing in an experimental environment characterized by flow-induced noise, but still utilizes many of the same signal processing techniques.

Chapter 2 provides a brief overview of some fundamental acoustic concepts, a thorough overview of conventional beamforming techniques, and the extension of these techniques to out-of-band beamforming methods. Free-space simulations and experiments using an underwater source and receiving array in a 1.07 m diameter and 0.90 m deep laboratory water tank were used to demonstrate the outputs and behavior of out-of-band methods. Below-band beamforming using a high frequency signal was compared to conventional beamforming using both the same high frequency signal, as well as genuine low frequency signals matching the below-band difference frequencies. Above-band beamforming was also compared with conventional beamforming, again using the same in-band signal as well as genuine signals matching the above-band sum frequency.

Chapter 3 utilizes ocean data obtained from the COAST 2012 experiment with an 8 km, 636 element towed horizontal array and a source array of airguns to evaluate the coherence length of genuine in-band fields and out-of-band fields generated using the frequency-difference and frequency-sum autoproducts. Here, repeated firings of the airguns were considered while the array was towed on along a nearly straight path with some depth variation. The coherence is calculated by comparing the phase between pairs of receivers and many experimental trials along a single tow line.

Chapter 4 extended frequency-difference beamforming to a shallow ocean sound channel in simulations and experiments. Here, data from the KAM11 experiment was used as both a model for the simulated portions, and for the experimental analysis, to compare frequency-difference beamforming outputs to expected sound propagation directions. This experiment consisted of high-frequency signals broadcast to a sparse array placed roughly 3 km away in a 106 m average depth channel. Horizontal array simulations were also completed with identical channel characteristics, but with a 16-element horizontal array with varying element spacing, source position, and uncertainty.

Chapter 5 examined the capability of frequency-difference beamforming for mitigating the effects of strong scattering by broadcasting a high frequency signal through a field of scatterers with large *ka* values of up to 14.7, utilizing the same laboratory tank as in Chapter 2. By processing

at lower difference frequencies, where Δka yielded more desired values between 0.8 and 1.7, the ability to localize the source of interest is considered.

Chapter 6 considers an Overlapping Synthetic Time Reversal (OSTR) technique for use in underwater communications, specifically as a means of mitigating the effects of time-varying environments on the deconvolution and demodulation of these signals. The first experiment considers a 50 kHz center frequency BPSK signal in a highly reverberant environment provided within the laboratory water tank used previously. Time variation is incorporated by generating surface waves and using the surface reflection for deconvolution, which is compared directly to Delay-and-Sum (D&S) methods. The next section returns to the KAM11 experiment, using the same geometry as in Chapter 4, but examining communication signals. Here, a 9.4 s duration, 22 kHz center frequency BPSK signal is broadcast over the 3 km range in a shallow ocean channel, which contains some variation over the 9.4 s. In this case, OSTR is compared directly to time reversal techniques.

Chapter 7 shifts the focus onto an experimental application, not specific to underwater acoustics (though with potential extensions and applications in underwater acoustics). Here, conventional beamforming, the Spectral Estimation Method (SEM), and Robust Principal Component Analysis (RPCA) are all considered for use in detecting and locating sources in noisy fields. In the first section, a discrete source is placed in a noisy, broadband field, generated by flow from a compressed air valve. A reference measurement of the noise field is used to reduce the noise's influence on source detection, localization, and source level estimation. The second section considers wind tunnel tests in which the noise is a result of the flow interacting with the tunnel, the test cavity, and the objects within the test region. Here, another reference measurement is used to remove the noise influence and allow for the detection, localization, and source level estimation of a small change to a plate lying in the tunnel.

8.2 Conclusions

The work presented in this thesis has led to nine major conclusions, which are summarized below.

1. **Out-of-band beamforming methods behave similarly to conventional beamforming methods in a free-space environment.** In Chapter 2, frequency-difference beamforming and frequency-sum beamforming were compared with genuine in-band fields where the difference frequencies and sum frequencies matched the in-band frequencies of a conventional field. A frequency-difference beamforming output at Δf = 15 kHz generated by a 60 kHz bandwidth signal centered at 165 kHz was compared to a conventional beamforming output using a genuine 15 kHz field. A frequency-sum beamforming output at Σf = 30 kHz generated by a 10 kHz bandwidth signal centered at 15 kHz was compared to a conventional beamforming output using a genuine 30 kHz field. In both cases, the out-of-band beamforming results were qualitatively and quantitatively comparable to the in-band results when considering localization performance and beam width. The results of this study are summarized in Tables 2.1 and 2.3 for the frequency-difference and frequency-sum cases, respectively. The average range errors for frequency-difference beamforming across 9 simulations were only 0.1 cm larger than the genuine field error and the average angle error matched. In 9 experiments, frequency-difference beamforming yielded 0.8 cm additional ranging error and 0.6° less arrival angle error. Similarly, for the same experimental setups but with different signals, frequency-sum beamforming resulted in an additional 0.4 cm range error and 0.2° arrival angle error in simulations, and 0.4 cm less range error and 0.3° less arrival angle error in experiments.

   Once again, the primary emphasis here is on the fact that the out-of-band results are comparing beamforming capabilities at frequencies generally not available from the in-band signal, and the performance is being compared with the genuine field at these frequencies. Comparisons with the genuine in-band fields, particularly for frequency-difference beamforming,

provide a more dramatic view of the benefits of out-of-band methods, discussed further in conclusions below. These results serve as a baseline for further exploration of these techniques, confirming that in a simple environment, the out-of-band methods can be expected to behave like a genuine field, and thus could potentially extend to more difficult applications.

2. **Frequency-difference and frequency-sum beamforming can mitigate the negative effects associated with using an in-band frequency with a non-ideal array geometry - specifically spatial aliasing and beam width.** A free-space environment with a sparse array is considered in Chapter 2, with sample results shown in Figs. 2.4 and 2.6, and the frequency-difference results summarized in Table 2.1. Frequency-difference beamforming is performed on sparse arrays, both in simulation and experiments, in a laboratory water tank with a nominal receiver-spacing-to-signal-wavelength ratio of 5.7. In simulation, the ability to localize a 165 kHz signal with a 16-element linear receiving array with 2 inch spacing worked well, but when extended to experiments, the additional uncertainty and interaction with experimental components reduced the performance, often resulting in substantial localization error. The frequency-difference beamforming output using the same signal at $\Delta f = 15$ kHz consistently located the source with minimal error, though with notably less precision.

   Frequency-sum beamforming in a free-space environment is considered in Chapter 2 as well, with the precision-enhancing capabilities demonstrated in Figs. 2.8 and 2.9, resulting from increasing the frequency used for beamforming. Frequency-sum beamforming was performed in both simulation and experiments, again in a laboratory water tank, with a 15 kHz signal. The bandwidth of this signal extending from 10 to 20 kHz was used to generate frequency-sum fields between 22 and 38 kHz. Fortunately, the signal contained enough signal energy at 30 kHz for direct comparison with a genuine field without having to run additional experiments, possibly introducing other experimental differences. Frequency-sum beamforming does struggle in the presence of multiple sources due to undesired cross term effects, though this can be partially mitigated when coherent beamforming is possible.

3. **Autoproducts can extend coherence lengths predictably below and above the signal band, as well as increase coherence length, on average, within the signal bandwidth.** Coherence length is an important factor in determining the performance of array signal processing techniques such as beamforming. In general, the coherence length describes the length of an array that can be used for coherent processing. When extending above or below the signal band, it is important that coherence is maintained. The work shown in Chapter 3 demonstrates that both frequency-difference and frequency-sum fields can extend coherence length above and below the signal band, following a similar trend as would be expected with genuine in-band frequencies. Figure 3.7 shows the coherence length determined from ocean propagation measurements at 1 Hz increments for a genuine field, the frequency-difference autoproduct, and the frequency-sum autoproduct, over most of the available frequencies in each field. In addition, at many in-band frequencies, the added robustness that results from bandwidth averaging to generate the autoproduct yields a higher coherence length than the genuine field at the same frequency. Furthermore, dips in coherence that result from experimental artifacts can potentially be mitigated with the use of autoproducts, despite the frequency being in-band. Over the frequency ranges considered in Fig. 3.7, conventional fields yielded an average coherence of 7.0 wavelengths, frequency-difference autoproducts an average of 12.4 wavelengths, and frequency-sum autoproducts an average of 8.6 wavelengths.

   These coherence length results suggests that out-of-band beamforming techniques maintain a comparable coherence to genuine in-band fields in the shallow ocean, supporting their usefulness for underwater applications. Figures 3.9 and 3.10 demonstrate the ability to beamform using out-of-band frequencies when substantial coherence is available.

4. **Frequency-difference beamforming is robust in multipath, shallow ocean environments with sparse arrays.** In Chapter 4, frequency-difference beamforming is considered in simulated and experimental shallow ocean environments. Beamforming in the shallow ocean introduces additional challenges that include not only sparseness, but also multipath propa-

gation, refraction, or significant geometric uncertainty. These are investigated in both simulations and experiments in Chapter 4. In the vertical array case, frequency-difference beamforming is shown to determine DOAs with comparable performance to that of conventional beamforming, when comparing to in-band frequencies that matched the out-of-band difference frequencies (and much better performance when compared to the in-band frequencies for the signal used to create the frequency-difference autoproduct). The comparison between the two methods yields reduced-χ^2 values between 0.082 and 0.194 for constant sound speed simulations and between 0.362 and 0.466 for downward-refracting sound speed simulations, with the full results shown in Fig. 4.7. In experiments, the reduced-χ^2 value was 0.91 - these results are shown in Fig. 4.19.

An additional contribution to this conclusion is the qualitative comparison of the conventional beamforming outputs of the high-frequency fields that are used to generate the frequency-difference beamforming output. In general, these outputs provide no indication of the expected DOAs. The dotted lines in Figs. 4.5 and 4.18 show the conventional outputs from these high frequencies, with no prominent peaks or significant dynamic range.

These results demonstrate the capability of frequency-difference beamforming for use in the shallow ocean, particularly in cases with sparse arrays and multipath propagation. The comparison with in-band fields that match the difference frequencies suggest that the behavior of frequency-difference methods is comparable to a genuine field when Δf matches an in-band frequency, thus the capabilities and limitations of conventional methods are potentially a reasonable guideline for the use of frequency-difference beamforming.

5. **Frequency-difference beamforming mitigates the effects of uncertainty due to fluctuations in propagation paths or receiver array geometry.** Horizontal array simulations in Chapter 4 (section 4.2.2) showed that frequency-difference beamforming has significantly improved robustness to experimental uncertainty over the in-band conventional beamforming outputs that utilized the same fields used to generate the frequency-difference output.

Simulations were performed here with similar geometry to the KAM11 channel, but with receivers aligned horizontally and spaced either 5 m or 50 m, with a source placed at 5° or 55° relative to broadside. The signal broadcast is a 1-3 kHz frequency sweep, providing receiver-spacing-to-signal-wavelength ratios of 6.7 and 67.7. Here, it is shown that frequency-difference beamforming can perform robustly in the presence of random ray propagation time variations that correspond to $\Delta k * \sigma = 0.40\pi$ or less (where σ is the standard deviation of the time variations), indicating that a geometric uncertainty standard deviation of roughly one-fifth of a wavelength provides the threshold for robust performance in the presence of uncertainty. These results are summarized in Fig. 4.11 for four cases considered. This result suggests that in practical scenarios where geometric or environmental uncertainty is significant (such as during a turn with a towed array), frequency-difference methods may recover some of the signal processing capabilities that are lost.

6. **Frequency-difference beamforming mitigates the effects of strong scattering when high frequency fields propagate through regions dense with scatterers.** Water tank experiments were performed where a 150-200 kHz signal was broadcast to a 12 element receiving array with between 0 and 30 strong scatterers (ka = 14.7 at the center frequency) placed randomly in the field between the source and receiver. Simulations and experiments show that processing the signal at difference frequencies between 5 and 25 kHz (Δka = 1.26 at 15 kHz) can yield an average localization performance improvement of up to 10 cm when many scatterers are present (400 simulations were performed for each number of scatterers, 1 to 30, and 20 experiments for 14, 16, 18, and 20 scatterers). In addition, a 2-7 dB improvement in peak-to-sidelobe ratio is observed. Both of these results are shown as a function of the number of scatterers in Fig. 5.9. Furthermore, averaging of frequency-difference outputs over multiple snapshots where scatterer positions are randomly varied provides robust localization where conventional methods are unable to recover the correct source location, or yield very poor dynamic range, as shown in Fig. 5.12 and summarized in Table 5.1.

7. **Overlapping Synthetic Time Reversal provides a means of successful blind deconvolution for long-duration and time-varying signals.** Water tank experiments show that the Synthetic Time Reversal (STR) technique provides a better means of blind deconvolution of a communication signal than a basic Delay-and-Sum (D&S) beamformer when multipath exists, with anywhere from 0.8 to 2.2 dB signal-to-noise ration (SNR) improvement in static, reverberant environments, as shown in Figs. 6.7, 6.10, and 6.11. When dynamics are introduced to the environment and the direction-of-arrival (DOA) of the signal is assumed unknown, Overlapping STR (OSTR) adapts to changing DOA and time-varying impulse response functions, providing a nearly 13% improvement in bit error rate (BER) and nearly 2 dB improvement in SNR over similar D&S methods, highlighted in 6.16.

   OSTR was also extended to the KAM11 experiment described above for a 9.4 s, 12k bit-per-second binary phase shift keying (BPSK) signal, and utilized a decision feedback equalizer (DFE) on overlapping windows. The duration of the signal and the ocean environment provided some time-varying characteristics that a standard time reversal (TR) implementation was unable to adapt to without additional probe signals. For the same signal, TR followed by a single channel DFE yielded a BER of 0.34% and an SNR of 8.5 dB, while OSTR with a DFE on each window was able to achieve a BER of 0% and an SNR of 12.2 dB, with consistent performance across the full signal duration. This result is shown in Figs. 6.20 and 6.21. This indicates that OSTR may be of use for underwater communications that may be difficult in underwater environments with significant multipath, and particularly, with a time-varying channel impulse response.

8. **When a noise reference is available, discrete sources are detectable in noisy fields down to SNRs of roughly -20 dB.** Three techniques, Conventional Beamforming (CBF) with cross spectral density matrix (CSDM) subtraction, the Spectral Estimation Method (SEM) with CSDM subtraction, and Robust Principal Component Analysis (RPCA) with CBF (RPCA-CBF) with denoising, were examined for use in localizing and estimating source levels in noisy fields when a noise reference is available. All of these results are found in Section 7.2,

particularly in Figs. 7.5 through 7.12 Here, RPCA proved best in the white noise background case, in that it was successful at SNRs well below -10 dB without the use of a reference, exploiting the sparsity of the white noise CSDM. When a reference was available, particularly when the noise couldn't be assumed to be isotropic white noise, all methods were capable of localization and source level estimation down to roughly -20 dB SNR with only 1-2 degrees and 1-2 dB of error. In general, in the presence of coherent noise, the CSDM subtraction techniques performed best and the improvements to the robustness of SEM with the introduction of CSDM subtraction confirm the results of Blacadon (2011) [17]. Even in the coherent noise case, RPCA still generally performed best when not utilizing a reference, suggesting that a portion of the field could perhaps be modeled as white noise, which RPCA could mitigate.

9. **Changes to objects in noisy flow fields are detectable when a reference is available. A geometric change to an object in flow was detected and its source level increment was determined at experimental SNRs less than -15 dB.** The three techniques mentioned above, plus RPCA-SEM with denoising, were examined in Section 7.3 for the localization and estimation of source level increment resulting from a change to the acoustic field generated by the flow over a plate. Here, a measurement was taken for a flat plate as reference, and another measurement was taken with a gap present in the plate, perpendicular to the flow direction. All four methods showed the ability to localize a feature likely corresponding to the gap, though the SEM-based methods, particularly SEM with CSDM subtraction, performed most precisely at localizing and imaging the full gap. A bias of approximately 6 cm placed the gap image upstream, possibly due to a combination of experimental uncertainties and non-repeatability between experiments. Figures 7.21 and 7.22 shows the imaging capabilities of each technique, with strong agreement between the two runs when a flow correction is included.

   Each method also successfully estimated the source level increment when the aeroacoustic noise was above the experimental noise and non-repeatability levels, with the CSDM sub-

traction techniques providing a more consistently accurate result, summarized in Fig. 7.23. A source level increment of less than 0.15 dB was successfully estimated within the 95% confidence interval in most cases, with an average error of 0.006 dB for CBF with CSDM subtraction, 0.010 dB for SEM with CSDM subtraction, 0.013 dB for RPCA-CBF with denoising, and 0.010 dB for RPCA-SEM with denoising.

8.3 Suggestions for Future Work

The research presented in this document covered several different areas of acoustic array signal processing with the goal of improving on existing methods of localization, detection, and source level estimation, and understanding the performance and behavior of the frequency-difference and frequency-sum autoproduct. Though much of this effort has led to new and impactful results, each area has the potential for additional exploration. Possible extensions to this work are summarized here.

- Out-of-band beamforming methods were examined in multiple scenarios and applications, but thorough SNR studies have not been completed. Many of the applications of beamforming, particularly in underwater acoustics, must deal with low SNRs, and thus an understanding of performance in noisy fields, both from a theoretical and applied perspective, is important. In particular, the quadratic nature of the autoproduct could lead to undesired amplification of the noise.

- Frequency-sum beamforming is challenging to use in environments with multiple sources or multipath propagation, due to the cross terms that behave like additional, nonexistent sources in the field. This was only briefly discussed and examined here, but is a critical piece of the technique to understand if implementation is to be successful in the future.

- Coherence length for out-of-band fields was considered relative to comparable in-band fields. However, coherence length is still studied extensively to understand the influence of various environmental factors. Similar studies should be extended to out-of-band coherence

lengths if the methods are to be implemented in underwater environments, in order to understand how the environmental characteristics of interest influence out-of-band methods, and whether this influence is any different than their influence on conventional fields.

- The case used here for coherence length was a very specific experiment that contained some challenging features that made the coherence length study non-ideal - such as the endfire nature of the experiment and the downward-focused acoustic energy. Ideally, a similar study would be repeated in a scenario where a source is placed in a near-broadside position to the array to obtain coherence length measurements that have less dependence on the experimental artifacts.

- The performance of frequency-difference methods in the presence of random uncertainty was considered, but often the uncertainty encountered in real applications has a bias. One key example of this is processing with a horizontal array during a turn. It is expected that frequency-difference beamforming will be more robust to performing source localization during a turn than conventional methods, but a thorough study hasn't been undertaken that considers realistic array variations against estimated array element positions.

- Frequency-difference beamforming in the presence of strong scatterers showed significant improvement in source localization over conventional methods, but only a single scatterer type and size was considered. Additional simulations or experiments for inhomogeneous environments that have continuous variations, many small scatterers, account for 3-D propagation, or have a greater variety of scatterer geometries and configurations should be considered to obtain a full picture of the frequency-difference beamforming benefits. In addition, scattering from rough surface boundaries is of interest in many applications.

- The capability of frequency-difference beamforming to handle scattered fields more robustly may also provide improved capabilities for scatterer detection and localization, possibly even classification. In particular, this might prove useful in an active scenario where the scatterer, or information about the scatterer, is desired.

- OSTR was shown to be useful for blind deconvolution of long-duration signals in time-varying environments. Here, a communication signal was considered, but other long-duration signals of interest could be studied. OSTR provides the benefit of real-time CIR estimation, but other methods have been developed that may perform similarly or better. Despite this, OSTR can likely still contribute to underwater communications applications, possible by combination with some of these other methods or by considering ways to enhance the CIR estimation. In addition, only two underwater experiments were considered here, which could contain characteristics favoring one method over another. Ideally, other simulations or experiments would be considered to understand the environmental or geometric influences.

- The frequency-difference STR technique loses absolute phase information and requires frequency-difference beamforming at the lowest available difference frequency, potentially reducing the capability to resolve a single, useful path. Exploration of techniques for determining absolute phase and for implementing the technique with higher difference frequencies may yield improved success for scenarios like the one presented here.

- Four methods were used for the localization and source level estimation of sources in noisy fields. This list of methods is not a complete list of potential signal processing methods for use here, and thus others could be considered or combined with these ideas. For example, CSDM subtraction combined with other advanced beamforming techniques, such as the Minimum Variance Distortionless Response (MVDR) or Multiple Signal Classification (MUSIC) beamformers. Other techniques to consider are diagonal removal, which has been improved upon using oblique projection methods [21] or eigenvalue-based subtraction methods [14]. In addition, varying the experimental setups and geometries may provide more insight into the limitations of these methods, particularly the SNRs where success is possible, the effects of distributed vs. discrete changes to an object, or the influence of multiple changes.

- The wind tunnel experiment utilized in Chapter 7 included a single gap perpendicular to the

flow, providing a single, continuous source to detect, localize, and quantify. However, practical implementation may include cases with multiple changes to detect, which may introduce some interaction or coherence between the sources, potentially being problematic. A simple extension to this experiment would be a plate with two gaps, with varying separation, and eventually extending to more complex geometries.

BIBLIOGRAPHY

[1] S. H. Abadi, K. J. Haworth, K. P. Mercado-Shekhar, and D. R. Dowling. Frequency-sum beamforming for passive cavitation imaging. *The Journal of the Acoustical Society of America*, 144(1):198–209, 2018.

[2] S. H. Abadi, D. Rouseff, and D. R. Dowling. Blind deconvolution for robust signal estimation and approximate source localization. *J. Acoust. Soc. Am.*, 131(4):2599–2610, 2012.

[3] S. H. Abadi, H. C. Song, and D. R. Dowling. Broadband sparse-array blind deconvolution using frequency-difference beamforming. *J. Acoust. Soc. Am.*, 132(5):3018–3029, 2012.

[4] S. H. Abadi, M. J. Van Overloop, and D. R. Dowling. Frequency-sum beamforming in an inhomogeneous environment. 19(2013):055080–055080, 2013.

[5] M. Agmon, B. Rafaely, and J. Tabrikian. Maximum directivity beamformer for spherical-aperture microphones. *IEEE Workshop on Apps. of Sig. Proc. to Audio and Acoust.*, pages 153–156, 2009.

[6] D. L. Alon and B. Rafaely. Beamforming with optimal aliasing cancellation in spherical microphone arrays. *IEEE/ACM Transactions on Speech and Language Processing*, 24(1):196–210, 2016.

[7] S. Amailland, J. H. Thomas, C. Pezerat, and R. Boucheron. Boundary layer noise subtraction in hydrodynamic tunnel using robust principal component analysis. *J. Acoust. Soc. Am.*, 143(4):2152–2163, 2018.

[8] R. K. Amiet. Refraction of sound by a shear layer. *J. Sound and Vibration*, 58(4):467–482, 1978.

[9] B. Amizic, L. Spinoulas, R. Molina, and A. K Katsaggelos. Compressive blind image deconvolution. *IEEE Trans. Image Processing*, 22(10):3994–4006, 2013.

[10] R. K. Andrew, B. M. Howe, and J. A. Mercer. Transverse horizontal spatial coherence of deep arrivals at megameter ranges. *The Journal of the Acoustical Society of America*, 117(3):1511, 2005.

[11] E. J. G. Arcondoulis, C. J. Doolan, L. A. Brooks, and A. C. Zander. A modification to logarithmic spiral beamforming arrays for aeroacoustic applications. *17th AIAA/CEAS Aeroacoustics Conference*, 17, 2011.

[12] A. B. Baggeroer, W. A. Kuperman, and P. N. Mikhalevsky. An overview of matched field methods in ocean acoustics. *IEEE J. Ocean. Eng.*, 18:401–424, 1993.

[13] A. B. Baggeroer, W. A. Kuperman, and H. Schmidt. Matched field processing: Source localization in correlated noise as an optimum parameter estimation problem. *J. Acoust. Soc. Am.*, 83(2):571–587.

[14] C. J. Bahr and W. C. Horne. Advanced Background Subtraction Applied to Aeroacoustic Wind Tunnel Testing. *21st AIAA/CEAS Aeroacoustics Conference*, 2015.

[15] A. J. Barabell. Improving the resolution performance of eigenstructure-based direction-finding algorithms. *IEEE International Conference on Acoustics, Speech, and Signal Processing*, pages 336–339, 1983.

[16] Kristine L. Bell, Yariv Ephraim, and Harry L. Van Trees. A Bayesian approach to robust adaptive beamforming. *IEEE Trans. Signal Proc.*, 48(2):386–398, 2000.

[17] D. Blacodon. Spectral estimation method for noisy data using a noise reference. *Applied Acoustics*, 72(1):11–21, 2011.

[18] D. Blacodon and G. Elias. Level estimation of extended acoustic sources using a parametric method. *Journal of Aircraft*, 41(6):1360–1369, 2004.

[19] J. J. Bowman, T. B. A. Senior, and P. L. E. Uslenghi. *Electromagnetic and Acoustic Scattering by Simple Shapes*. North-Holland Publishing Company, Amsterdam, Netherlands, 1970.

[20] H. P. Bucker. Use of calculated sound fields and matched field detection to locate sound sources in shallow water. *J. Acoust. Soc. Am.*, 59(2):368–373, 1976.

[21] J. Bulte. Acoustic Array Measurements in Aerodynamic Wind Tunnels: a Subspace Approach for Noise Suppression. *13th AIAA/CEAS Aeroacoustics Conference*, 2007.

[22] S. H. Byun, C. M. A. Verlinden, and K. G. Sabra. Blind deconvolution of shipping sources in an ocean waveguide. *J. Acoust. Soc. Am.*, 141(2):797–807, 2017.

[23] C. A. Cabrelli. Minimum entropy deconvolution and simplicity: A noniterative algorithm. *Geophysics*, 50(3):394–413, 1984.

[24] A. Caiti, A. Garulli, F. Livide, and D. Prattichizzo. Localization of autonomous underwater vehicles by floating acoustic buoys: A set-membership approach. *IEEE J. Ocean. Eng.*, 30(1):140–152, 2005.

[25] E.J. Candés, X. Li, Y. Ma, and J. Wright. *J. ACM*, 58(3):1–37.

[26] J. Capon. High-resolution frequency-wavenumber spectrum analysis. *Proceedings of the IEEE*, 57(8):1408–1418, 1969.

[27] W. M. Carey. Transverse coherence lengths, processing limits and implications. *Proc. of Meetings on Acoustics*, 6(005001).

[28] W. M. Carey. Sonar array characterization, experimental results. *IEEE Journal of Oceanic Engineering*, 23(3):297–306, 1998.

[29] W. M. Carey. The determination of signal coherence length based on signal coherence and gain measurements in deep and shallow water. *J. Acoust. Soc. Am.*, 104(2):831–837, 1998.

[30] M. Carlin and P. Rocca. A Bayesian compressive sensing strategy for direction-of-arrival estimation. *Proc. of 6th European Conference on Antennas and Propagation*, pages 1508–1509, 2011.

[31] G. C. Carter, C. Knapp, and A. H. Nuttall. Statistics of the estimate of the magnitude-coherence function. *IEEE Transactions on Audio and Electroacoustics*, 21(4):388–389, 1973.

[32] V. Chandrasekaran, P. Sanghavi, P. A. Parrilo, and A. S. Willsky. Sparse and low-rank matrix decompositions. *Proc. 47th Conf. on Comm., Control, and Computing (October 2009)*, 50, 2002.

[33] J. C. Chen, R. E. Hudson, and K. Yao. Maximum-likelihood source localization and unknown sensor location estimation for wideband signals in the near-field. *IEEE Transactions on Signal Processing*, 50(8):1843–1854, 2002.

[34] X. Chen. Multiple signal classification method for detecting point-like scatterers embedded in an inhomogeneous background medium. *The Journal of the Acoustical Society of America*, 127(4):2392–2397, 2010.

[35] Y. Chen, J. Huang, and J. Han. A novel beamspace algorithm for direction of arrival based on compressive sensing. *Proceedings of International Conference on Signal Processing*, pages 394–397, 2012.

[36] P. Chiariotti, M. Martarelli, and P. Castellini. Acoustic beamforming for noise source localization - reviews, methedology and applications. *Mech. Syst. and Sig. Proc.*, 120:442–448, 2019.

[37] C. Cho, H. C. Song, and W. S. Hodgkiss. Robust source-range estimation using the array/waveguide invariant and a vertical array. *J. Acoust. Soc. Am.*, 139(1):63–69, 2016.

[38] S. E. Cho, H. C. Song, and W. S. Hodgkiss. Multiuser acoustic communications with mobile users. *J. Acoust. Soc. Am.*, 133(2):880–890, 2013.

[39] M. Ciaurriz, Y. Tawk, and C. G. Christodoulou. Adaptive Beamforming for Random Planar Arrays. *IEEE Antennas and Propagation Society International Symposium*, pages 1728–1729, 2014.

[40] A. Cigada, M. Lurati, F. Ripamonti, and M. Vanali. Moving microphone arrays to reduce spatial aliasing in the beamforming technique: theoretical background and numerical investigation. *J. Acoust. Soc. Am.*, 124(6):3648–3658, 2008.

[41] M. D. Collins and W. A. Kuperman. Focalization: Experimental focusing and source localization. *J. Acoust. Soc. Am.*, 90(3):1410–1422, 1991.

[42] H. Cox. Line array performance when the signal coherence is spatially dependent. *J. Acoust. Soc. Am.*, 54(54):1743–2360, 1973.

[43] H. Cox, Zeskind R. M., and M. Myers. A subarray approach to matched-field processing. 87(87):168–178, 1990.

[44] A. Das, W. S. Hodgkiss, and P. Gerstoft. Coherent multipath direction-of-arrival resolution using compressed sensing. *IEEE J. Ocean. Eng.*, 37(1):35–44, 2012.

[45] A. S. Douglass, H. C. Song, and D. R. Dowling. Performance comparisons of frequency-difference and conventional beamforming. *The Journal of the Acoustical Society of America*, 142(3):1663–1673, 2017.

[46] D. R. Dowling. Revealing hidden information with quadratic products of acoustic field amplitudes. *Phys. Rev. Fluids*, 3:110506 (17 pages), 2018.

[47] D. R. Dowling and K. G Sabra. Acoustic Remote Sensing. *Annual Review of Fluid Mechanics*, 47:221–243, 2015.

[48] G. L. D'Spain and W. A. Kuperman. Application of waveguide invariants to analysis of spectrograms from shallow water environments that vary in range and azimuth. *J. Acoust. Soc. Am.*, 106(5):2454–2468.

[49] T. F. Duda, J. M. Collis, Y. T. Lin, A. E. Newhall, J. F. Lynch, and H. A. DeFerrari. Horizontal coherence of low-frequency fixed-path sound in a continental shelf region with internal-wave activity. *The Journal of the Acoustical Society of America*, 131(2):1782–1797, 2012.

[50] G. F. Edelmann, T. Akal, W. S. Hodgkiss, S. Kim, W. A. Kuperman, and H. C. Song. An initial demonstration of underwater acoustic communication using time reversal. *IEEE J. Ocean. Eng.*, 27(3):602–609, 2002.

[51] G. F. Edelmann and C. F. Gaumond. Beamforming using compressive sensing. *J. Acoust. Soc. Am.*, 130(4):EL232–EL237, 2011.

[52] A. El-Keyi, T. Kirubarajan, and A. B. Gershman. Robust adaptive beamforming based on the Kalman filter. *IEEE Trans. Signal Proc.*, 53(8):3032–3041, 2005.

[53] B. G. Ferguson. Time-delay estimation techniques applied to the acoustic detection of jet aircraft transits. *The Journal of the Acoustical Society of America*, 106(1):255, 1999.

[54] A. Finez, A. Pereira, and Q. Leclere. Broadband mode decomposition of ducted fan noise using cross-spectral matrix denoising. *Proc. of Fan Noise*, 2015.

[55] R. G. Fizell. Application of high-resolution processing to range and depth estimation using ambiguity function methods. *The Journal of the Acoustical Society of America*, 82(2):606–613.

[56] L. Flax, P. K. Raju, J. George, and H. Überall. Resonating fields inside elastic scattering objects. *The Journal of the Acoustical Society of America*, 68:973–979, 1980.

[57] J. A. Flynn, J. A. Ritcey, D. Rouseff, and Warren L. J. Fox. Multichannel equalization by decision-directed passive phase conjugation: Experimental results. *IEEE J. Ocean. Eng.*, 29(3):824–836, 2004.

[58] L. L. Foldy. The multiple scattering of waves. I. General theory of isotropic scattering by randomly distributed scatterers. *Physical Review*, 67(3-4):107–119, 1945.

[59] O. L. Frost, III. An algorithm for linearly constrained adaptive array processing. *Proceedings of the IEEE*, 60(8):926–935, 1972.

[60] K. L. Gemba, W. S. Hodgkiss, and P. Gerstoft. Adaptive and compressive matched field processing. *The Journal of the Acoustical Society of America*, 141(1):92–103, 2017.

[61] K L. Gemba, S. Nannuru, P. Gerstoft, and W. S. Hodgkiss. Multi-frequency sparse Bayesian learning for robust matched field processing. *J. Acoust. Soc. Am.*, 141(5):3411–3420, 2017.

[62] P. Gerstoft, W. S. Hodgkiss, W. A. Kuperman, H. C. Song, M. Siderius, and P. L. Nielsen. Adaptive beamforming of a towed array during maneuvering. *IEEE J. Ocean. Eng.*, 28(1):44–54, 2003.

[63] P. Gerstoft, C. F. Mecklenbräuker, W. Seong, and M. Bianco. Introduction to compressive sensing in acoustics. *J. Acoust. Soc. Am.*, 143:3731–3736, 2018.

[64] P. Gerstoft, A. Xenaki, and C. F. Mecklenbräuker. Multiple and single snapshot compressive beamforming. *J. Acoust. Soc. Am.*, 138(4):2003–2014, 2015.

[65] J. Gomes, A. Silva, and S. Jesus. Adaptive spatial combining for passive time-reversed communications. *J. Acoust. Soc. Am.*, 124(2):1038–1053, 2008.

[66] G. A. Grachev. Theory of acoustic field invariants in layered waveguide. *Acoust. Phys.*, 39(1):33–35, 1993.

[67] C. A. Greene and R. T. Moller. The effect of normally distributed random phase errors on synthetic array gain patterns. *IRE Trans. on Military Electronics*, pages 130–139, 1961.

[68] A. C. Gürbüz, J. H. McClellan, and V. Cevher. A compressive beamforming method. *Proceedings of IEEE International Conference on Acoustics, Speech and Signal Processing*, pages 2617–2620, 2008.

[69] T. R. Hahn. Low frequency sound scattering from spherical assemblages of bubbles using effective medium theory. *The Journal of the Acoustical Society of America*, 122(6):3252–3267, 2007.

[70] J. Hao, M. Wang, M. Ji, and k. Wang. Flow noise induced by small gaps in low-Mach-number turbulent boundary layers. *Physics of Fluids*, 25:110821, 2013.

[71] G. Haralabus, V. Premus, D. Alexandrou, L. W. Nolte, and A. M. Richardson. Source localization in an uncertain acoustic scattering environment. *The Journal of the Acoustical Society of America*, 94:3379–3386, 1993.

[72] K. D. Heaney. Shallow water narrowband coherence measurements in the Florida Strait. *The Journal of the Acoustical Society of America*, 129(4):2026–2041, 2011.

[73] J. Higbie. Uncertainty in the linear regression slope. *Am. J. Phys.*, 59(2):184–185, 1990.

[74] W. S. Hodgkiss and J. C. Preisig. Kauai ACOMMS MURI 2011 (KAM11) experiment, 2012.

[75] S. Holbrook, G. Kent, K. Keranen, P. Johnson, A. Trehu, H. Tobin, J. Caplan-Auerbach, and J. Beeson. COAST: Cascadia Open- Access Seismic Transects. *GEOPrisms Newsletter*, 29, 2012.

[76] I. K. Holfort, F. Gran, and J. A. Jensen. Broadband Minimum Variance Beamforming for Medical Ultrasound Imaging. *IEEE Trans. Ultrason., Ferroelec., Freq. Contr.*, 56(2):314–325, 2009.

[77] S. Hosseini, Y. Deville, and H. Saylani. Blind separation of linear instantaneous mixture of non-stationary signals in the frequency domain. *Signal Process.*, 89(5):819–830, 2009.

[78] E. Huang, D. R. Dowling, T. Whelan, and J. L. Spiesberger. High-sensitivity photoacoustic leak detection. *J. Acoust. Soc. Am.*, 114:1926–1933, 2003.

[79] R. Jagannath, G. Leus, and R. Pribic. Grid Matching for Sparse Signal Recovery in Compressive Sensing. *Proc. 9th European Radar Conference*, pages 111–114, 2012.

[80] F. B. Jensen, W. A. Kuperman, M. B. Porter, and H. Schmidt. *Computational Ocean Acoustics*. AIP, Melville, NY, 2nd edition, 2011.

[81] M. Johnson, L. Freitag, and M. Stojanovic. Improved Doppler tracking and correction for underwater acoustic communications. *Proc. IEEE International Conf. on Acoust., Speech, and Sig. Proc.*, pages 575–578, 1997.

[82] T. Kang, H. C. Song, W. S. Hodgkiss, and J. S. Kim. Long-range multi-carrier acoustic communications in shallow water based on iterative sparse channel estimation. *J. Acoust. Soc. Am.*, 128(6):EL372–L377, 2010.

[83] M. Karaman and M. O'Donnel. Uncertainty in the linear regression slope. *IEEE Trans. on Ultrasonics, Ferroelectrics, and Freq. Control*, 42(3):429–442, 1995.

[84] M. Kaveh and A. Bassias. Threshold extension based on a new paradigm for MUSIC-type estimation. *Proc. IEEE International Conference on Acoust., Speech, and Sig. Proc.*, pages 2535–2538, 1990.

[85] S. Khazaie, X. Wang, and P. Sagaut. Localization of random acoustic sources in an inhomogeneous medium. *Journal of Sound and Vibration*, 384:75–93, 2016.

[86] D. B. Kilfoyle and A. B. Baggeroer. The State of the Art in Underwater Acoustic Telemetry. *IEEE J. Ocean. Eng.*, 25:4–27, 2000.

[87] S. Kim, W. A. Kuperman, W. S. Hodgkiss, H. C. Song, G. F. Edelmann, and T. Akal. Robust time reversal focusing in the ocean. *J. Acoust. Soc. Am.*, 114(1):145–157, 2003.

[88] L. E. Kinsler, A. R. Frey, A. B. Coppens, and J. V. Sanders. *Fundamentals of Acoustics*. Wiley, New York, NY, 4th edition, 2011.

[89] H. Krim and M. Viberg. Two decades of array signal processing research: the parametric approach. *IEEE Signal Processing Magazine*, pages 67–94, 1996.

[90] C. J. Lam and A. C. Singer. Bayesian beamforming for DOA uncertainty: Theory and implementation. *IEEE Trans. Signal Proc.*, 54(11):4435–4445, 2006.

[91] Z. Lei and K. Yang. Sound sources localization using compressive beamforming with a spiral array. *IET Conference Proceedings;*, 2015.

[92] S. G. Lemon. Towed-array history, 1917-2003. *IEEE J. Ocean. Eng.*, 29(2):365–373, 2004.

[93] D. Li and Y. H. Hu. Energy-Based Collaborative Source Localization Using Acoustic Microsensor Array. *J. on App. Sig. Proc.*, 4:321–337, 2003.

[94] J. E. Lipa, B. M. Worthmann, and D. R. Dowling. Measurement of autoproduct fields in a Lloyd's mirror environment. *J. Acoust. Soc. Am.*, 143:2419–2427, 2018.

[95] A. A. Lunkov and V. G. Petnikov. The coherence of low-frequency sound in shallow water in the presence of internal waves. *Acoustical Physics*, 60(1):61–71, 2014.

[96] D. Malioutov, M. Çetin, and A. S Willsky. A sparse signal reconstruction perspective for source localization with sensor arrays. *IEEE Trans. Signal Proc.*, 53(8):3010–3022, 2005.

[97] W. Mantzel, J. Romberg, and K. Sabra. *J. Acoust. Soc. Am.*

[98] E. A. Marengo, F. K. Grüber, and F. Simonetti. Multiple signal classification method for detecting point-like scatterers embedded in an inhomogeneous background medium. *J. Acoust. Soc. Am.*, 127:2392–2397, 2007.

[99] G. D. Martino and A. Iodice. Passive beamforming with coprime arrays. *IET Radar Sonar and Navigation*, pages 964–971, 2017.

[100] N. Martins, S. Jesus, C. Gervaise, and A. Quinquis. A time-frequency approach to blind deconvolution in multipath underwater channels. *Proc. IEEE International Conf. on Acoust., Speech, and Sig. Proc.*, pages 1225–1228, 2002.

[101] J. Maynard, E. Williams, and Y. Lee. Nearfield acoustic holography: I. Theory of generalized holography and the development of NAH. *J. Acoust. Soc. Am.*, 78(4):1395–1413, 1985.

[102] J. Meyer and G. Elko. Nearfield acoustic holography: I. Theory of generalized holography and the development of NAH. *Proc. of IEEE Intl. Conf. on Acoust., Speech, and Sig. Proc.*, 2:1781–1784, 2002.

[103] D. R. Morgan and T. M. Smith. Coherence effects on the detection performance of quadratic array processors, with applications to large-array matched-field beamforming. *The Journal of the Acoustical Society of America*, 87(2):737–747, 1990.

[104] P. M. Morse and K. U. Ingard. *Theoretical Acoustics*. McGraw Hill, New York, NY, 1968.

[105] E.S. Nadimi, V. Blanes-Vidal, and P.M. Johansen. Bayesian-based localization in inhomogeneous transmission media. *Proceedings of the 2013 Research in Adaptive and Convergent Systems, RACS 2013*, pages 226–231, 2013.

[106] A. Nehorai and E. Paldi. Acoustic vector-sensor array processing. *IEEE Trans. Signal Proc.*, 42(9):2481–2491, 1994.

[107] A. M. Norris. Resonant acoustic scattering from solid targets. *J. Acoust. Soc. Am.*, 88:505–514, 1990.

[108] J. M. Ozard. Matched field processing in shallow water for range, depth and bearing determination: Results of experiment and simulation. *J. Acoust. Soc. Am.*, 86(2):744–753, 1985.

[109] A. Paulraj, R. Roy, and T. Kailath. A subspace rotation approach to signal parameter estimation. *Proceedings of the IEEE*, 74(7):1044–1046, 1986.

[110] M. Porter, P. Hursky, M. Siderius, M. Badiey, J. Caruthers, W. Hodgkiss, K. Raghukumar, D. Rouseff, W. Fox, C. de Moustier, B. Calder, B. Kraft, V. McDonald, P. Stein, J. Lewis, and S. Rajan. The Kauai experiment. *High Frequency Ocean Acoustics*, pages 307–321, 2004.

[111] M. B. Porter, R. L. Dicus, and R. G. Fizell. Simulations of matched-field processing in a deep-water Pacific environment. *IEEE J. Ocean. Eng.*, 12(1):173–187, 1987.

[112] J. C. Preisig. Performance analysis of adaptive equalization for coherent acoustic communications in the time-varying ocean environment. *J. Acoust. Soc. Am.*, 118(1):263–278, 2005.

[113] J. Proakis and M. Salehi. *Digital Communications, 5th Ed.* McGraw Hill, New York, NY, 2007.

[114] K. D. Rolt and P. A. Abbot. Littoral coherence limitations on acoustic arrays. *Acoustical Imaging*, 23:537–542, 1990.

[115] D. Rouseff, D. R. Jackson, W. L. J. Fox, C. D. Jones, J. A. Ritcey, and D. R. Dowling. Underwater acoustic communication by passive-phase conjugation: theory and experimental results. *IEEE Journal of Oceanic Engineering*, 26(4):821–831, 2001.

[116] R. Roy and T. Kailath. ESPRIT - Estimation of Signal Parameters Via Rotational Invariance Techniques. *IEEE Transactions on Acoustics, Speech, and Signal Processing*, 37(7):984–995, 1989.

[117] K. G. Sabra and D. R. Dowling. Blind deconvolution in ocean waveguides using artificial time reversal. *J. Acoust. Soc. Am.*, 116(1):262–271, 2004.

[118] K. G. Sabra, H. C. Song, and D. R. Dowling. Ray-based blind deconvolution in ocean sound channels. *The Journal of the Acoustical Society of America*, 127(2):EL42–L47, 2010.

[119] D. Salvati, C. Drioli, and G. L. Foresti. Diagonal Unloading Beamforming for Source Localization. *IEEE/ACM Trans. on Audio, Speech, and Language Proc.*, 25(3):609–622, 2018.

[120] A. G. Sazontov, I. P. Smirnov, and A. L. Matveev. Source localization in a shallow-water channel with a rough surface. *Acoustical Physics*, 61(1):109–116, 2015.

[121] H. C. Schau and A. Z. Robinson. Passive Source Localization Employing Intersecting Spherical Surfaces from Time-of-Arrival Difference. *IEEE Trans. Acoust., Speech, and Sig. Proc.*, 35(8):1223–1225, 1987.

[122] K. Schindler, J. Compressive sensing for sparse arrays. *IEEE International Symposium on Phased Array Systems and Technology*, pages 240–245, 2013.

[123] R. O. Schmidt. A New Approach of Geometry and Range Difference Location. *IEEE Trans. Aerospace and Electronic Systems*, AES-8(6):821–835, 1972.

[124] R. O. Schmidt. Multiple emitter location and signal parameter estimation. *IEEE Trans. Antennas and Prop.*, 34(3):276–280, 1986.

[125] R. O. Schmidt, A. B. Baggeroer, W. A. Kuperman, and E. K. Scheer. Environmentally tolerant beam-forming for high resolution matched-field processing: Deterministic mismatch. *J. Acoust. Soc. Am.*, 88(4):1851–1862, 1990.

[126] Y. Selén, R. Abrahamsson, and P. Stoica. Automatic robust adaptive beamforming via ridge regression. *Signal Processing*, 88:33–49, 2008.

[127] T. J. Shaw and G. C. Valley. Angle of arrival detection using compressive sensing. *Proceedings of 18th European Signal Processing Conference*, pages 1424–1428, 2010.

[128] M. Siderius, D. R. Jackson, D. Rouseff, and R. Porter. Multipath compensation in shallow water environments using. 102(6):3439–3449, 1997.

[129] J. F. Smith III and S. Finette. Simulated annealing as a method of deconvolution for acoustic transients measured on a vertical array. 94(4):2315–2325, 1993.

[130] A. Song and M. Badiey. Time reversal multiple-input/multiple-output acoustic communication enhanced by parallel interference cancellation. *J. Acoust. Soc. Am.*, 131(1):281–291, 2012.

[131] H. C. Song. *IEEE J. Ocean. Eng.*

[132] H. C. Song. Time reversal communication in a time-varying sparse channel. *J. Acoust. Soc. Am.*, 130(4):EL161–EL166, 2011.

[133] H. C. Song. Time reversal communication with a mobile source. *J. Acoust. Soc. Am.*, 134(4):2623–2626, 2013.

[134] H. C. Song. Equivalence of adaptive time reversal and least squares for cross talk mitigation. *J. Acoust. Soc. Am.*, 135(3):EL154–EL158, 2014.

[135] H. C. Song, J. de Rosny, and W. A. Kuperman. Improvement in matched field processing using the CLEAN algorithm. *J. Acoust. Soc. Am.*, 113:1379–1386, 2003.

[136] H. C. Song, W. S. Hodgkiss, W. A. Kuperman, T. Akal, and M. Stevenson. High-rate synthetic aperture communications in shallow water. *The Journal of the Acoustical Society of America*, 126(6):3057–3061, 2009.

[137] H. C. Song, W. S. Hodgkiss, W. A. Kuperman, W. J. Higley, K. Raghukumar, T. Akal, and M. Stevenson. Spatial diversity in passive time reversal communications. *J. Acoust. Soc. Am.*, 120(4):2067–2076, 2006.

[138] H. C. Song, W. S. Hodgkiss, W. A. Kuperman, M. Stevenson, and T. Akal. Improvement of time-reversal communications using adaptive channel equalizers. *IEEE J. Ocean. Eng.*, 31(2):487–496, 2006.

[139] H. C. Song, W. A. Kuperman, and W. S. Hodgkiss. Basin-scale time reversal communications. *J. Acoust. Soc. Am.*, 125(1):212–217, 2009.

[140] H. C. Song, P. Roux, W. S. Hodgkiss, W. A. Kuperman, T. Akal, and M. Stevenson. Multiple-input-multiple-output coherent time reversal communications in a shallow-water acoustic channel. *IEEE J. Ocean. Eng.*, 31(1):170–178, 2006.

[141] J. L. Spiesberger. Geometry of locating sounds from differences in travel time: isodiachrons. *J. Acoust. Soc. Am.*, 116(5):3168–3177, 2004.

[142] P. Stoica and A. Nehorai. Music, maximum likelihood, and Cramer-Rao bound. *IEEE Transactions on Acoustics, Speech, and Signal Processing*, 37(5):720–741, 1989.

[143] P. Stoica and K. C. Sharman. Maximum likelihood methods for direction-of-arrival estimation. *IEEE Transactions on Acoustics, Speech and Signal Processing*, 38(7):1132–1143, 1990.

[144] P. Stoica, Z. Wang, and J. Li. Robust Capon beamforming. *IEEE Signal Processing Letters*, 10(6):172–175, 2003.

[145] M. Stojanovic, J. Catipovic, and J. G. Proakis. Adaptive multichannel combining and equalization for underwater acoustic communications. *J. Acoust. Soc. Am.*, 94(3):1621–1631, 1993.

[146] J. F. Synnevag, A. Austeng, and S. Holm. Adaptive beamforming applied to medical ultrasound imaging. *IEEE Trans. Ultrason., Ferroelec., Freq. Contr.*, 54(8):1606–1613, 2007.

[147] J. R. Taylor. *An Introduction to Error Analysis*. University Science Books, Sausalito, C. A., 2nd edition, 1997.

[148] A. M. Thode. Source ranging with minimal environmental information using a virtual receiver and waveguide invariant theory. *J. Acoust. Soc. Am.*, 108(4):1582–1594, 2000.

[149] A. M. Thode, W. A. Kuperman, G. L. D'Spain, and W. S. Hodgkiss. Localization using Bartlett matched-field processor sidelobes. *J. Acoust. Soc. Am.*, 107(1):278–286, 2000.

[150] K. E. Thomenius. Evolution of ultrasound beamformers. *Proc. IEEE Ultrasonics Symp.*, 2:1615–1622, 1996.

[151] K. C. Toh and S. Yun. An accelerated proximal gradient algorithm for nuclear norm regularized least squares problems. *Pac. J. Optim.*, 6(15):615–640, 2010.

[152] A. Tolstoy. *Matched Field Processing for Underwater Acoustics*. World Scientific, Singapore, 1st edition, 1993.

[153] V. Tourbabin and B. Rafaely. Sub-Nyquist spatial sampling using arrays of directional microphones. *HSCMA '11*, 1:76–80, 2011.

[154] R. J. Urick. *Principles of Underwater Sound*. McGraw-Hill, New York, NY, 3rd edition, 1983.

[155] J. Van Bladel. Low-frequency scattering by hard and soft bodies. *J. Acoust. Soc. Am.*, 44(44):1014–1018, 1968.

[156] B. D. Van Veen and K. M. Buckley. Beamforming: A versatile approach to spatial filtering. *IEEE ASSP Mag*, 5(2):4–24, 1991.

[157] W. Veronesi and J. Maynard. Nearfield acoustic holography (NAH) II. Holographic reconstruction algorithms and computer implementation. *J. Acoust. Soc. Am.*, 81(5):1307–1322, 2005.

[158] M. Viberg, B. Ottersten, and T. Kailath. Detection and estimation in sensor arrays using weighted subspace fitting. *IEEE Trans. Signal Proc.*, 39(11):2436–2449, 1991.

[159] S. A. Vorobyov, A. B. Gershman, and Z. Q. Luo. Robust adaptive beamforming using worst-case performance optimization: A solution to the signal mismatch problem. *IEEE Trans. Signal Proc.*, 51(2):313–324, 2003.

[160] L. Wan, J. X. Zhou, P. H. Rogers, and D. P. Knobles. Spatial coherence measurements from two L-shape arrays in Shallow Water. *Acoustical Physics*, 55(3):383–392, 2009.

[161] X. Wang, S. Khazaie, and P. Sagaut. Sound source localization in a randomly inhomogeneous medium using matched statistical moment method. *The Journal of the Acoustical Society of America*, 138(6):3896–3906, 2015.

[162] Z. Wang, J. Li, and R. Wu. Time-delay- and time-reversal-based robust Capon beamformers for ultrasound imaging. *IEEE Trans. Med. Imag.*, 24(10):1308–1322, 2005.

[163] R. Weber and J. E. Bohme. Adaptive super-exponential methods for blind multichannel equalization. *Proceedings of the IEEE Sensor Array and Multichannel Signal Processing Workshop*, pages 585–589, 2002.

[164] R. A. Wiggins. Minimum entropy deconvolution. *Geoexploration*, 16:21–35, 1978.

[165] B. M. Worthmann and D. R. Dowling. The frequency-difference and frequency-sum acoustic-field autoproducts. *J. Acoust. Soc. Am.*, 141(6):4579–4590, 2017.

[166] B. M. Worthmann, H. C. Song, and D. R. Dowling. High frequency source localization in a shallow ocean sound channel using frequency difference matched field processing. *J. Acoust. Soc. Am.*, 138(6):3549–3562, 2015.

[167] B. M. Worthmann, H. C. Song, and D. R. Dowling. Adaptive frequency-difference matched field processing for high frequency source localization in a noisy shallow ocean. *J. Acoust. Soc. Am.*, 141(1):543–556, 2017.

[168] J. Wright, A. Ganesh, S. Rao, Y. Peng, and Y. Ma. Robust Principal Component Analysis: Exact recovery of corrupted low-rank matrices via convex optimization. *Proc. of Advances in Neural Information Processing Systems*, 22:2080–2088, 2009.

[169] A. Xenaki and P. Gerstoft. Grid-free compressive beamforming. *J. Acoust. Soc. Am.*, 137(4):1923–1935, 2015.

[170] A. Xenaki, P. Gerstoft, and K. Mosegaard. Compressive beamforming. *J. Acoust. Soc. Am.*, 136(1):260–271, 2014.

[171] Z. Xinhua, Z. Anqing, F. Jianping, and Y. Shaoqing. Study on Blind Separation of Underwater Acoustic Signals. *Proc. of ICSP*, 2000:1802–1805.

[172] T. C. Yang. A method of range and depth estimation by modal decomposition. *J. Acoust. Soc. Am.*, 82(5):1736–1745, 1987.

[173] T. C. Yang. Temporal resolutions of time-reversal and passive-phase conjugation for underwater acoustic communications. *IEEE J. Ocean. Eng.*, 28(2):229–245, 2003.

[174] T. C. Yang. Correlation-based decision-feedback equalizer for underwater acoustic communications. *IEEE J. Ocean. Eng.*, 30(4):865–880, 2005.

[175] T. Yardibi, J. Li, and P. Stoica. Nonparametric and sparse signal representations in array processing via iterative adaptive approaches. *Proceedings of IEEE Conference on Signals, Systems and Computers*, pages 278–282, 2008.

[176] T. Yardibi, J. Li, P. Stoica, M. Xue, and A. B. Baggeroer. Source localization and sensing: a nonparametric iterative adaptive approach based on weighted least squares. *IEEE Transactions on Aerospace and Electronic Systems*, 46(1):425–443, 2010.

[177] T. Yardibi, J. Li, P. Stoica, M. Xue, and A. B. Baggeroer. Source localization and sensing: a nonparametric iterative adaptive approach based on weighted least squares. *IEEE Transactions on Aerospace and Electronic Systems*, 46(1):425–443, 2010.

[178] S. H. Yonak and D. R. Dowling. Photoacoustic detection and localization of small gas leaks. *J. Acoust. Soc. Am.*, 105(5):2685–2694, 1999.

[179] W. J. Zeng, X. Jiang, X.L. Li, and X.D. Zhang. Deconvolution of sparse underwater acoustic multipath channel with a large time-delay spread. *J. Acoust. Soc. Am.*, 127(2):909–919, 2010.

[180] W. J. Zeng, X. Jiang, and H. C. Song. Sparse-representation algorithms for blind estimation of acoustic-multipath channels. *J. Acoust. Soc. Am.*, 133(4):2191–2197, 2013.

[181] C. Zhou, Y. Gu, S. He, and Z. Shi. A Robust and Efficient Algorithm for Coprime Array Adaptive Beamforming . *IEEE Trans. on Vehicular Tech.*, 67(2):1099–1122, 2018.

[182] C. Zhou, Y. Gu, Y. D. Zhang, Z. Shi, T. Jin, and X. Wu. Compressive sensing-based coprime array direction-of-arrival estimation. *IET Communications*, 11:1719–1724, 2017.

[183] L. J. Ziomek and C. D. Behrle. Localization of multiple broadband targets via frequency domain adaptive beamforming for planar arrays. *J. Acoust. Soc. Am.*, 85(3):1236–1244, 1989.

[184] I. Ziskind and M. Wax. Maximum likelihood localization of multiple sources by alternating projection. *IEEE Transactions on Acoustics, Speech, and Signal Processing*, 36(10):1553–1560, 1988.